VISUAL OBSERVATION OF BIOLOGICAL AND

MEDICAL OBJECTS BY A NEWLY DEVELOPED

X-RAY IMAGING TECHNIQUE

Miss Wanwisa Pattanasiriwisawa

A Thesis Submitted in Partial Fulfillment of the Requirements for

the Degree of Doctor of Philosophy in Physics

Suranaree University of Technology

Academic Year 2004

การสังเกตวัตถุทางชีวภาพและทางการแพทย์ด้วยตาโดยเทคนิคการถ่ายภาพ

ด้วยรังสีเอกซ์ที่พัฒนาขึ้นใหม่

นางสาววันวิสา พัฒนศิริวิศว

VISUAL OBSERVATION OF BIOLOGICAL AND MEDICAL

OBJECTS BY A NEWLY DEVELOPED X-RAY IMAGING

TECHNIQUE

Suranaree University of Technology has approved this thesis submitted in

partial fulfillment of the requirements for the Degree of Doctor of Philosophy.

Thesis Examining Committee

_____

(Asst. Prof. Dr.Prapun Manyum)

Chairperson

_____

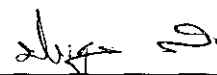(Prof. Dr.Takehiko Ishii)

Member (Thesis Advisor)

_____

(Prof. Dr.Masami Ando)

Member

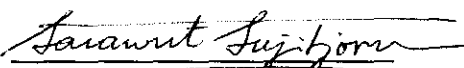_____

(Assoc. Prof. Dr.Prasart Suebka)

Member

_____

(Dr.Prayoon Songsiriritthigul)

Member

_____   _____

(Assoc. Prof. Dr.Sarawut Sujitjorn)   (Assoc. Prof. Dr.Prasart Suebka)

Vice Rector for Academic Affairs   Dean of Institute of Science

วันวิสา พัฒนศิริวิศว : การสังเกตวัตถุทางชีวภาพและทางการแพทย์ด้วยตาโดยเทคนิคการถ่ายภาพด้วยรังสีเอกซ์ที่พัฒนาขึ้นใหม่ (VISUAL OBSERVATION OF BIOLOGICAL AND MEDICAL OBJECTS BY A NEWLY DEVELOPED X-RAY IMAGING TECHNIQUE) อาจารย์ที่ปรึกษา : Prof. Dr.Takehiko Ishii, 226 หน้า. ISBN 974-533-349-2

วิทยานิพนธ์ฉบับนี้ได้นำเสนอการถ่ายภาพดาร์กฟิลด์และไบร์ทฟิลด์ย่านรังสีเอกซ์ในเชิงเรขาคณิตแบบเลาเอ ในการถ่ายภาพได้ใช้ตัวทำแสงเอกรงค์อสมมาตรแบบกรณีแบรกก์ซึ่งสะท้อนรังสีเอกซ์ที่มีไดเวอร์เจน 0.3 ไมโครเรเดียน ฉายผ่านวัตถุ และใช้ตัววิเคราะห์เชิงเรขาคณิตแบบเลาเอในการถ่ายภาพดาร์กฟิลด์ (ดีเอฟไอ) และไบร์ทฟิลด์ (บีเอฟไอ) ขึ้น เทคนิคการถ่ายภาพดีเอฟไอเป็นเทคนิคที่ไม่ได้มีการนำเสนอมาก่อน นั่นคือเส้นสว่างที่อยู่ส่วนกลางซึ่งเป็นไปตามเงื่อนไขของแบรกก์ได้ถูกกำจัดออกด้วยตัววิเคราะห์ผลึก และรังสีพื้นหลังที่เป็นสาเหตุทำให้ภาพไม่ชัดเจนจึงไม่ถูกบันทึกลงบนฟิล์ม แต่ในกรณีบีเอฟไอจะต้องบันทึกรังสีพื้นหลังที่ทำให้ภาพไม่ชัดเจน ด้วยอุปกรณ์เชิงทัศนศาสตร์ย่านรังสีเอกซ์ประกอบด้วยแผ่นเวเฟอร์เลี้ยวเบนแบบกรณีทั้งสองของเลาเอทำงานที่พลังงาน 35 กิโลอิเล็กตรอนโวลต์ ได้ประยุกต์ใช้วิเคราะห์สารตัวอย่างได้แก่ งาช้าง เขา ฟัน และ แบบจำลองมะเร็งเต้านม สำหรับภาพงาช้าง เขา และ ฟัน มีรายละเอียดชัดเจนถึงโครงสร้างภายใน ส่วนภาพของแบบจำลองมะเร็งเต้านมนั้นก็ให้รายละเอียดดีเยี่ยม

สาขาวิชาฟิสิกส์
ปีการศึกษา 2547

ลายมือชื่อนักศึกษา _วันวิสา พัฒนศิริวิศว_
ลายมือชื่ออาจารย์ที่ปรึกษา _____
ลายมือชื่ออาจารย์ที่ปรึกษาร่วม _____

X-ray dark-field and bright-field imaging in the Laue geometry has been successfully demonstrated. Using a Bragg-case asymmetric monochromator which produces an x-ray beam with a 0.3 µrad divergence incident onto an object and a Laue geometry analyzer that can simultaneously provide dark-field imaging (DFI) and bright-field imaging (BFI). The imaging technique of DFI is quite novel one that we did not have before in that the central bright line satisfying the Bragg condition is removed by the analyzer crystal and the background radiation obscuring the image of the object does not come to record film. This is not the case in BFI and the strong background radiation obscures the real image of the object. X-ray optics comprising two Laue case diffraction wafers working at 35 keV has been successfully applied to some biological samples such as ivory, tusk, horn, tooth and a phantom of breast cancer. Images of ivory and others have shown very clear and informative inside structure. All pieces of the breast cancer phantom provide us with very fine images to simulate cancer.

School of Physics

Academic Year 2004

Student's Signature _Wanwisa Pattanasiriwisawa_

Advisor's Signature _____

Co-advisor's Signature _Masai Ando_

Acknowledgements

studies and daily subsistence allowances in KEK and Suranaree University of Technology.

My friends in Japan and Suranaree University of Technology for their friendship.

My mother and family members for their support and love, which cannot be expressed by any words on the earth.

<div align="right">Wanwisa Pattanasiriwisawa</div>

Contents

Chapters

Contents (Continued)

Contents (Continued)

Contents (Continued)

List of Figures

List of Figures (Continued)

Figures

Page

List of Figures (Continued)

List of Figures (Continued)

List of Figures (Continued)

List of Figures (Continued)

Chapter I

Introduction

1.1 Overview of the Study

1.1.1 Introductory Remark

X-rays have been used in modern human life to make it very convenient. Among the applications of x-rays, the observation of materials structures is quite well-known. First, in the medical diagnosis, x-rays that have passed through a body provide a visual image of its interior structure when they strike a photographic plate or a fluorescent screen; the darkness of the shadows produced on the plate or screen depends on the relative opacity of different parts of the body. Another famous medical method is CT (computerized tomography). In this method, we utilize radiowave absorption caused by the proton resonance in order to produce cross-sectional images of the inside of the human's brain. This technique was originally a special application of x-ray absorption (x-ray CT). Similarly, in the industrial applications, x-rays are used to observe the defect structures in materials. X-ray topography is used to detect the defects in semiconductors like stacking faults. Obtaining semiconductor crystals almost without defects is quite important in the semiconductor engineering.

X-ray crystallography is also useful in that we can see atomic arrangements in solid materials. This can be applied to protein crystallography. The protein molecular structures as obtained from the analyses of x-ray diffraction patterns are quite important for biological studies. If the material is a hazardous virus, the information on the structure

of the material is essential for designing the drug for killing the virus or protecting men from the virus. The x-ray diffraction is also applied to industrial investigations of the materials or products. An example is the utilization in the production of x-ray optic equipment such as monochromators, analyzers and filters.

In this thesis, x-ray imaging techniques are developed and tested using 6 kinds of ivory and breast cancer phantom. This new technique is called x-ray dark field imaging which is developed from x-ray interferometer. X-ray dark field imaging is based on Laue diffraction theory which separates a beam to bright and dark filed images by using calculated suitable analyzer blade thickness and x-ray energy. The calculation of the thickness and energy is carried out by the use of program from Professor Ando's group. Then we design three kinds of analyzer which we call 'Owl', the parallel analyzer and the wedge analyzer. They are used for beams with suitable sizes from the upstream beamline station.

In the 1960's and 1970's a number of investigations were published on the identification and theoretical analyses of imaging in diffraction patterns. These images are associated with diffraction by crystals which contain line or plane defects. They are also associated with the successive transmission of an incident beam through two or three crystals separated by nondiffracting lamella. In x-ray imaging one can use three kinds of contrast: The absorption contrast, the phase contrast and the refraction contrast. The absorption contrast has been used since the discovery of x-rays in 1895 by Rontgen. Cosslett and Nixon (1953) made quite pioneering work of edge contrast enhancement in 1953. They called the system they made an x-ray shadow microscope. In their system, images were produced actually by refraction contrast. It was achievable only by illuminating an object with highly coherent light. Bonse and Hart (1965) devised

important an x-ray optics called an x-ray interferometer in 1965. This opened a totally new x-ray research field by showing the possibility of phase contrast imaging. Some years later, Ando and Hosoya (1972) applied this technique to biology and mineralogy. Momose et al. (Momose, Takeda, Itai, Yoneyama and Hirano, 1996. Momose, Takeda, Itai, Yoneyama and Hirano, 1998), developed CT imaging using the phase contrast method to visualize cancer tissues. The refraction contrast was rediscovered and refined by Podurets et al. (Podurets, Somenkov and Shil'stein, 1989), Ingal et al. (Ingal and Beliavskaya, 1995), Wilkins et al. (Wilkins, Gureyev, Gao, Pogany and Stevenson, 1996), Clotens et al. (Clotens, Barrett, Guigay and Shlenker, 1996) and Chapman et al. (Chapman, Thomlinson, Arfelli, Gmuer, Zhong, Menk, Jonston, Washburnn, Pisano and Sayers, 1996). Some of them have achieved enhancement of contrast by adopting the angle resolving nature of an x-ray contrast optics either by the Laue geometry or by the Bragg geometry. In 2001, Ando et al. (Ando, Sugiyama, Zhang, Hyodo, Maksimenko and Pattanasiriwisawa, 2001) discovered that an analyzer in an ordinary x-ray interferometer has the angular resolving power. They named the contrast attained by their method is the angle-resolved contrast.

In this way, x-ray imaging technology has been progressing steadily. However, it has vast problems yet to be solved. This is particularly so if we use synchrotron radiation as probe light. The present thesis is one to challenge this type of problems.

1.1.2   Brief Description of the Principle of the Research

In what follows, the principle of the experimental aspects of the present research is briefly given. In obtaining optical images of materials, we usually utilize two methods. One uses the spatial difference in the absorption intensity. This is the

method used in medical diagnosis that is familiar in a hospital. Live biological materials such as ones composing human bodies consist mainly of water. There the spatial difference of absorbance is not appreciable in many cases. This reduces the contrast of the optical images of materials.

On the other hand, the phase of the electromagnetic wave changes as it proceeds in a material. Even in case where the material has low absorbance and the absorption contrast is low, the phase of the electromagnetic wave changes spatially if the density changes spatially. We define the spatial change in the electromagnetic wave passing through the material as the phase contrast. If we find a method to make the phase contrast visible, we can observe the structure of the material by observing the phase contrast. Since the change of the phase is more appreciable than that of absorbance, the phase contrast method of obtaining optical images of materials is quite promising. The basic principle of this method is described below.

Supposing the phase shift of x-rays suffering while passing through a sample.

$$\phi(x,y:k) \quad = \quad k\int \rho(x,y,z)\,dz \tag{1.1}$$

where $\rho(x,y,z)$ is the electron density of phase media at (x, y, z), k is wave number of x-rays and z is the optical path along the direction of the x-rays. Thus the amplitude modulation leading to the phase contrast becomes

$$\varphi_p(x,y,z) \quad \propto \quad \exp(-i\phi(x,y,k)) \bullet \exp(-ikz). \tag{1.2}$$

The angle deflection leading to the angle-resolved contrast is given as

$$\Delta_{an}(x,y,z) \quad \propto \quad (\partial\phi(x,y,k)/\partial x,\ \partial\phi(x,y,k)/\partial x,\ k). \tag{1.3}$$

The absorption contrast is given as

$$I_{ab}(x,y,z)\,/\,I_0(x,y,z) \quad \propto \quad \exp\left(-\int \mu(x,y,z)z\,dz\right) \tag{1.4}$$

where μ (x, y, z) is absorption coefficient.

Historically, we call images of materials made by x-rays according to the principles described above as the phase-interference or phase contrast images, the refraction images and absorption images. They are explained in more detail in the following:

Phase-interference or phase contrast image: An almost transparent material is made visible through the interference of light caused by the changes in phase that occur when transparent specimens are nonuniformly illuminated with light. While passing through an object light is slowed down and its phase becomes out of that of incident light. In the case where transparent specimens have some spatial structure, light transmitted by them is diffracted. Diffraction must occur if an aperture with a finite size. The diffraction pattern is such that a central intense band occurs and a dark band exists beside the central bright band. Then weaker bands occurs further outside. The diffraction pattern makes a fringe-like profile. A phase change occurring in light outside the central maximum of the diffraction pattern is larger. A phase-contrast microscope is a device to combine this retarded light with that of the central maximum by means of an angular diaphragm and a retardation plate (phase-contrast plate). This device can make changed phase matched only in light giving of the central maximum. This gives greater contrast to the final image, owing to constructive interference between the two sets of light waves produced by the angular diaphragm. This is the bright contrast. In the case where the phase outside the central bright band advances a dark image is produced. In the dark contrast, a different phase-contrast plate is used to make the same object structure appear to be dark by the destructive interference of the same waves. This phase contrast image

is most famous technique but the experimental setup is complicated and its practical construction is not easy. The phase contrast mechanism is present in any kind of edges of object materials. It is not suppressed even in a strongly absorbing material. However, a demerit exists: The phase contrast image enhances the contrast of the edge images too much in some cases. Therefore, a thin object fixed on an other object cannot be distinguished. In case of x-rays, the phase contrast imaging is closely related with x-ray holography.

Refraction image: The refraction is recognized as the change in the propagation direction of a wave when it passes the boundary of two media. If the direction of rays is exactly at right angles to the surface no refraction occurs. In all other cases x-rays are bent away from the surface normal (an imaginary line perpendicular to the surface) when they enter a medium and are bent toward the surface normal when they leave the medium. The angle between the surface normal and the refracted rays is called the angle of refraction. The angle of refraction is related to the angle of incidence by a quantity called the refractive index. This situation is used for the image formation, if the index of refraction is not uniformly distributed in the object material or the surface is not smooth. This situation is some what similar to the case of the diffuse reflection of light by an object material with a surface not smooth. Thus we can recognize the existence of the material. In other words, the image of the object material is formed through non-uniform refraction. This is the refraction imaging. The refraction imaging is suitable to see the real shapes of inner structures because the edge effect is much less appreciable than in the case of phase contrast imaging. The demerit of the refraction imaging is that imaging mechanism by refraction does not work when the boundary of the object material does not make sharp edges; the contrast of images is suppressed in strongly absorbing objects.

Absorption image: A beam passing through a medium may lose its intensity because of the absorption of photons by atoms or molecules in the medium. The absorption imaging is of the poorest quality among three kinds of imaging described here. However, it has a great merit: It is easy to set up the measurement system and radiation dose is low enough for us to avoid hazardous radiation effects by x-rays. Thus, this method can be applied for living animals including human being.

In this way, the usefulness of these three kinds of imaging is dependent on the simplicity of the technique and the total amount of energy absorbed by the objects. Each imaging method has its own merit and demerit. The absorption imaging has been developed ever since x-rays were discovered.

In case of the refraction and phase contrast imaging, x-rays must be highly monochromatized and the wavelength should be variable for obtaining good object images with high contrast. This is different from the case of the absorption contrast imaging where characteristic x-rays are used without monochromatization. Thus, strong parallel x-ray beam is necessary for the refraction and phase-contrast imaging. This problem is overcome by the use of synchrotron radiation. Another problem is that a large crystal is necessary for obtaining a wider monochromatic x-ray beam. Recent progress of the semiconductor technology has made it possible to obtain a large size single crystal of Silicon. Thus, difficulties preventing the practical applications of the refraction and phase-contrast imaging are now being overcome.

1.1.3 Outline of Experimental Methods

Here, the summary of experimental procedure is given. The synchrotron light sources used are storage rings at Photon Factory (PF), KEK (High energy Accelerator Organization) and SPring-8 of Japan Synchrotron Radiation Research Institute. The x-ray optical systems have been designed for experimental stations for

the respective beam lines. In this thesis work, three kinds of x-ray optical system are developed. They are a system named 'Owl', a parallel analyzer system and a wedge analyzer system. 'Owl' is used in BL20B at SPring-8. The practical length of the reflecting crystal is 80-100 cm. The x-ray analyzer of 'Owl' consists of two crystal blades. In this system, absorption and refraction dark field images are taken. The parallel and wedge analyzers are used in PF BL14B in which x-ray beam size is smaller. The crystal length is 40-40 cm. The parallel and wedge analyzers consist of one crystal blade. In these systems, bright and dark field refraction images are taken. It is easy to setup the experimental arrangements. Two images can be clearly separated. In designing the optical system, the determination of the indices of the reflection net planes of the analyzer crystals is an important issue. When they are determined the blades are cut out of the crystal ingot and sliced with a diamond saw. The crystallographic orientations are examined with x-rays. Then the blades are polished and chemically etched. All other details of the preparation of the x-ray optical systems for the experimental setup will be described later.

1.1.4 The Backgrounds of Adopting Samples.

The performance of developed equipment was examined by obtaining images of a few samples. Prior to the description of the real applications of the system, the backgrounds of the use of the employed samples are simply mentioned here. More details will be presented later. Samples used in the present thesis work are ivory and breast cancer phantoms.

Ivory: Male Asian elephants have suffered from the ivory trade, like their African cousins, both male and female in this case. Poaching for meat, hide, and bones occurs in some areas, including upper Burma. Hide is smuggled to Thailand, where it is turned into bags and shoes, and to China, where the ash is used to treat ulcers and wounds and bone ash is prescribed for stomach problems. The trade of elephant ivory and its products is prohibited under the control of the Convention on International Trade in Endangered Species (CITES), known well as the 'Washington convention'. Although ivory has been protected, smugglers still want to import or export it in illegal ways because of a strong demands in the underground commercial market.

The smuggling of ivories is caused by the situation that ivories bring poachers and their associated brokers enormous profit. More than half of ivories brought to the commercial market are consumed in Japan. In Japan, ivories are used for decorates and seals. Seals are used instead of signatures. Ivory is appreciated and used because of its long life as a seal. For decorations, they have been used as raw materials of some arts and crafts such as carvings, scrimshaws, and 'netsuke' which are used to secure a cord carrying personal belongings to the sash (obi) that acts as a belt on a traditional Japanese dress. Traditional Japanese dresses for both men and women have only a few places in which small personal objects are kept. Women keep things in their sleeves, but men have no equivalent places.

It is essential to have methods to identify forbidden materials to be seen among traded products for preventing the movement of the materials banned by the Washington Convention. The research work like one made in this thesis makes an important contribution to this issue. The ivories selected comprise an elephant ivory (hard and soft ivory), a mammoth ivory, a horn of Dutch water buffalo, tooth of sperm whale

and tooth of hippo.

Breast cancer: Other kinds of samples we used in this thesis work are breast cancer phantom. From statistics, breast cancer is not the most prevailing cancer as compared with uterus cervix cancer. However, the number of breast cancer patients is increasing every year over the world. The early diagnosis is quite important. Everyone wishes that cancer is found before it is clearly recognized as cancer. The advance in technology has now made it possible to find cancer with a small size. Surgery is effective for primary breast cancer. Radiotherapy is also effective, where high energy photons are used for killing cancer cells. In chemotherapy, drugs for killing cancer are used but the method is usually used for big breast cancer.

It is quite important to establish the method to find small size breast cancer. We try to use the refraction contrast imaging to observe breast cancer. For this purpose, we use breast cancer phantom specimens in the present thesis work. The breast cancer phantom specimens are composed of a unit of 16 pieces in one box so the image is taken one by one. The details will be described later.

1.1.5 The Basic Concept of the Study

The most important objective of the present study is to establish the method of refraction imaging. For implementing it, we use beam lines in two synchrotron radiation facilities. This part of the study is described in Chapter II. The experiments are carried out to examine the usefulness of the developed method. Thus, the analyses of obtained images from biological and medical materials point of view are not of the first priority in the present thesis work.

1.2 Synchrotron Radiation

In the present thesis, synchrotron radiation is used as light to observe the x-ray images of samples. Therefore, the properties of synchrotron radiation are summarized here.

1.2.1   What is Synchrotron Radiation?

Synchrotron radiation is emitted by electrons traveling with velocities almost equal to the speed of light when their orbits are bent by a magnetic field. This is shown in Fig.1.1 schematically. As it was first observed in a synchrotron in 1947, it was named "synchrotron radiation". In general, the electromagnetic wave is generated by charged particles making accelerated motions. Mathematical analyses show that generated electromagnetic wave is stronger if the particle mass is smaller and the acceleration is large. Thus, in practice, the electromagnetic wave is produced either by electrons or positrons making curved motions. The electromagnetic wave is often referred to as electromagnetic radiation.

This radiation proceeds with a wave front as shown in the upper panel of Fig.1.2. In the lower panel of Fig.1.2 the wave front in the plane containing the tangent of the trajectory of the moving electron and the acceleration direction are shown. The wave fronts are shown only qualitatively in Fig.1.2. The wave fronts are quantitatively or analytically obtained by solving the Maxwell equation expressing the electromagnetic field formed by a moving particle. The solution is proved to be valid by experiments. The analytical treatment is not presented here.
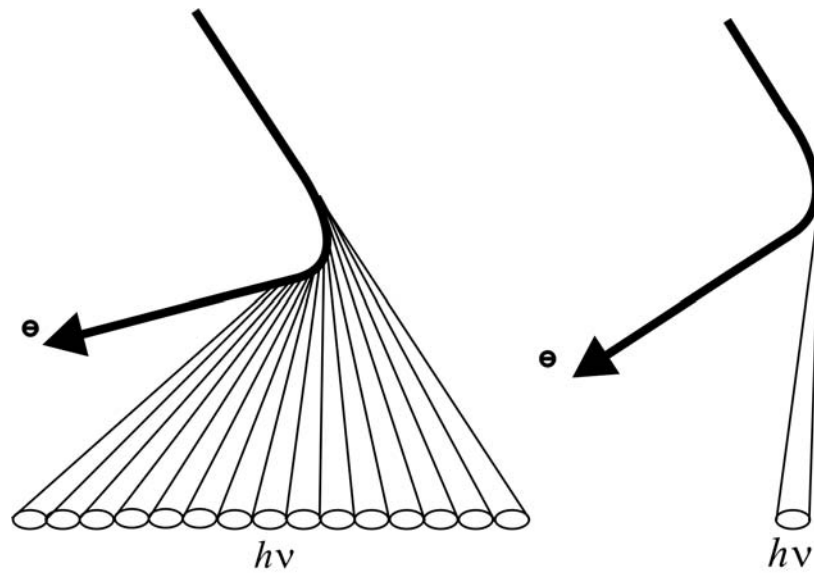
Fig. 1.1 Synchrotron radiation is emitted when electrons proceeding with a velocity almost equal to that of light make a curved motion.

Suppose the electron velocity is large enough to be almost equal to the light velocity. Then, the wave front changes drastically from those shown in Fig.1.2 owing to relativistic effects. This situation can be understood if a line is transformed by the Lorentz transformation.

Let us consider the coordinate, (x', y', z'), that moves with an electron at a speed, **v**, almost equal to light velocity. We assume this electron is also in the coordinate, (x, y, z), fixed in the laboratory. We assume that the x' axis is in the x axis direction and the electron moves along the x axis direction toward the positive direction. In the (x', y', z') coordinate, the electron does not move and rests at the origin. The coordinate systems are illustrated in Fig.1.3. The lengths in the y' and z' direction are the same as those in the y and z direction. Thus we have

$$\left. \begin{array}{l} y' = y \\ z' = z \end{array} \right\} \qquad (1.5)$$
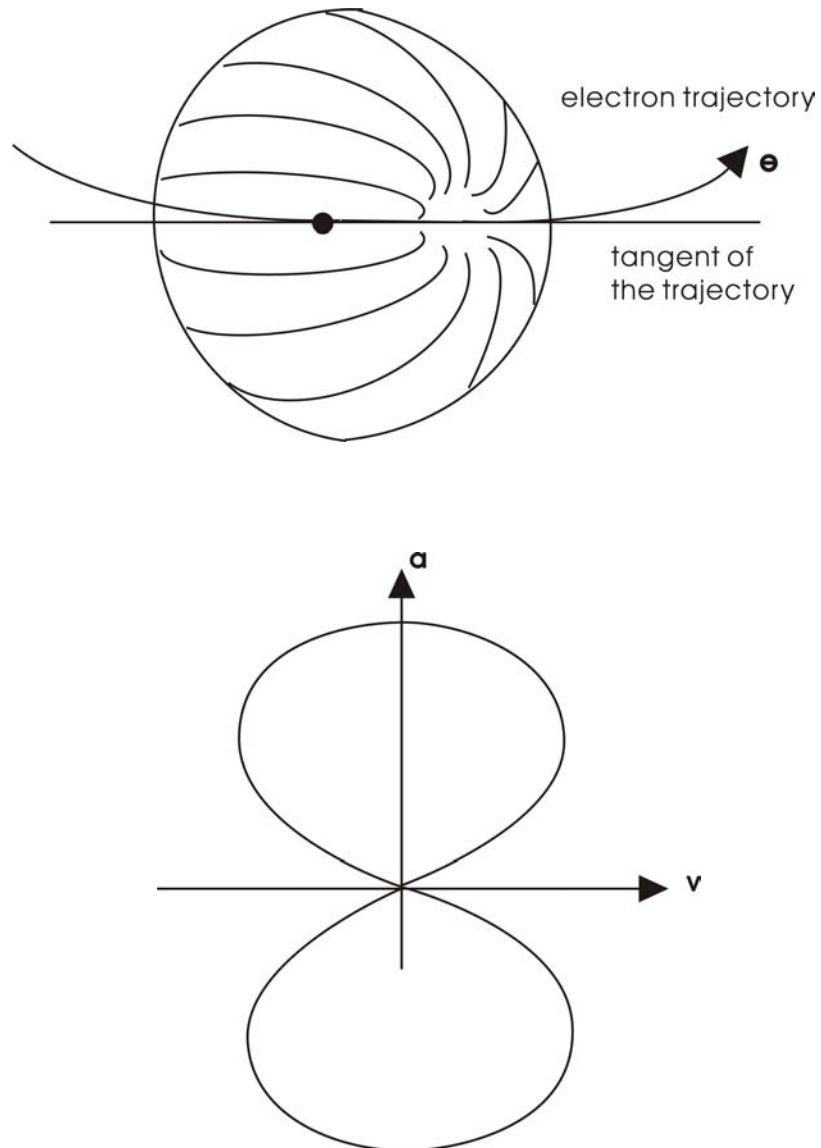
Fig. 1.2 The wave front of the radiation emitted by a moving electron whose trajectory is bent. The electron velocity is small as compared with the speed of light. Upper panel: Wave front. Lower panel: Wave front as shown in the plane including the electron velocity **v** and acceleration **a**.
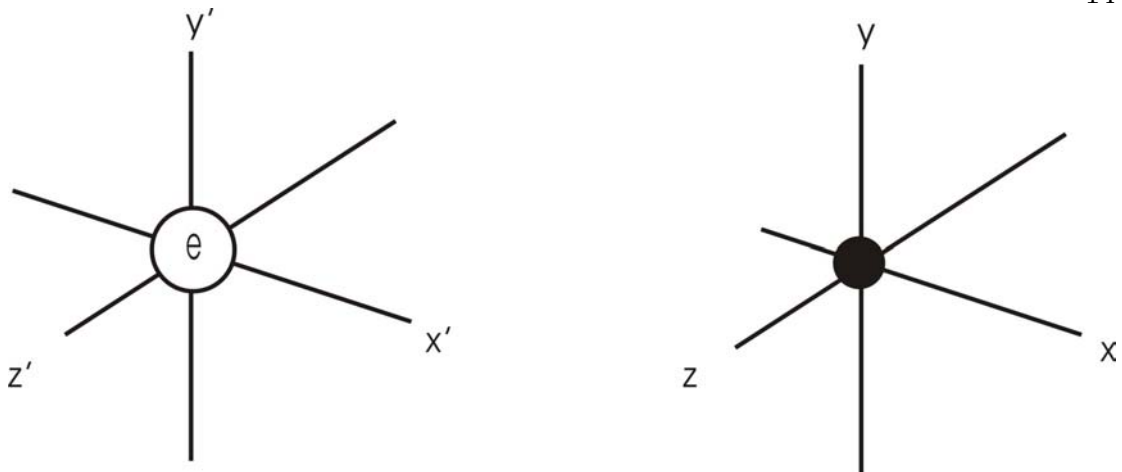
Fig. 1.3 The coordinate system fixed to the moving electron (left) and that fixed in the laboratory (right).

This in turn means that time is the same in the y, y′, z and z′ directions. There, time is the same towards these directions. This is because the relative velocity between the two coordinates in these directions is zero. The electromagnetic wave emitted by an electron propagates in the (x′, y′, z′) system with the ordinary wave front as shown in Fig.1.2.

On the other hand, time progresses differently in the x and x′ directions. If we observe time in the x′ coordinate system, a clock progresses slowly relative to the x coordinate system. While the electromagnetic wave proceeds slightly toward the y or z direction, it appears to proceed for a considerable distance in the x direction.

This situation can be understood by the Lorentz transformation. This is shown in Fig. 1.4. In the figure, ct′ in the upper panel represents the distance of the electronmagnetic wave propagation in the (x′ y′) plane. θ_R is the angle of the electromagnetic wave propagation direction as measured from the x′ axis. ct in the lower panel represents the distance of the electromagnetic wave propagation in the (x y) plane.

θ_L express the angle of the direction of the electromagnetic wave propagation as measured from the x axis. In this case the transformation equations are written as

$$\left.\begin{array}{rcl} z &=& z' = 0 \\ y &=& y' \\ x &=& c\gamma\,(x' + vt') \\ t &=& \gamma\,(t' + x'\beta/c) \end{array}\right\}$$ (1.6)

The parameters in (1.6) are given as

$$\beta = vt'$$ (1.7)

Where c is the light velocity. γ is equal to the ratio of the electron energy to its rest mass energy, E/m_oc^2, and expressed as

$$\left.\begin{array}{l} \gamma = 1/\sqrt{1 - v^2/c^2} \\ = 1/\sqrt{1 - \beta^2} \end{array}\right\}$$ (1.8)

If the velocity of the electron is much smaller than that of the light velocity, (1.6) gives us $x = x'$ and $t = t'$. The relations between the coordinates and angles are represented as

$$\left.\begin{array}{l} x' = ct'\cos\theta_R \\ y' = ct'\sin\theta_R \\ x = ct\,\cos\theta_L \\ y = ct\,\sin\theta_L \end{array}\right\}$$ (1.9)

Using equation (1.6) through (1.9), we obtain the relation

$$\tan\theta_L = \frac{1}{\gamma}\frac{\sin\theta_R}{(\beta + \cos\theta_R)}$$ (1.10)

Since γ is very large and β is near to unity, tan θ_L is small. Then θ_L is a very small quantity. In other words, the emitted radiation is confined in a very narrow cone directed in the direction of the tangent of the electron trajectory if it is observed in the laboratory. This is synchrotron radiation. The property of the radiation just mentioned is one of the observed characteristics of synchrotron radiation that it has a

very small beam divergence. The average vertical angle of the emission cone is calculated to be about $1/\gamma$. By numerical calculation γ has a value equal to

$$\gamma \;=\; 1957\,E \tag{1.11}$$

where E is the electron energy in the unit of GeV.
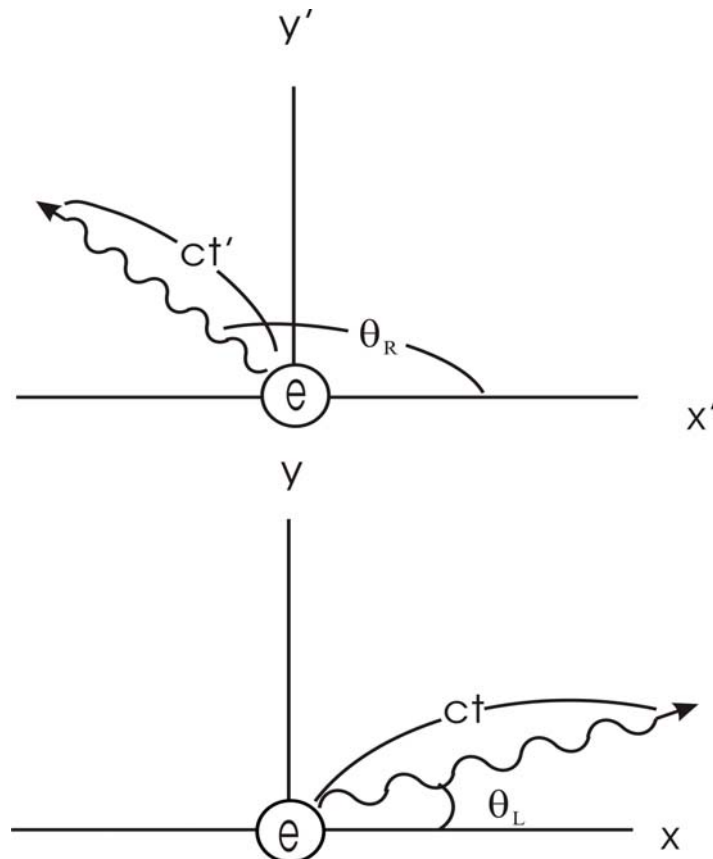
Fig. 1.4 The propagation of the electromagnetic wave in the coordinate fixed to a moving electron $(x'\,y')$ and that in the coordinate fixed to the laboratory $(x\ y)$. The electron is moving along the x axis. ct' and ct are the distances that the electromagnetic wave propagate in the $(x'\ y')$ and $(x\ y)$ coordinate systems, respectively. θ_R and θ_L are the angles of the directions of wave propagation from the x' and x axes, respectively.

Synchrotron radiation is emitted toward the orbital tangential direction. Therefore, synchrotron radiation is emitted in whole tangential direction of the electron trajectory. If a pinhole slit is installed near the electron orbit, the radiation coming out of this hole proceeds in space in a narrow cone. This situation is depicted in Fig.1.1.
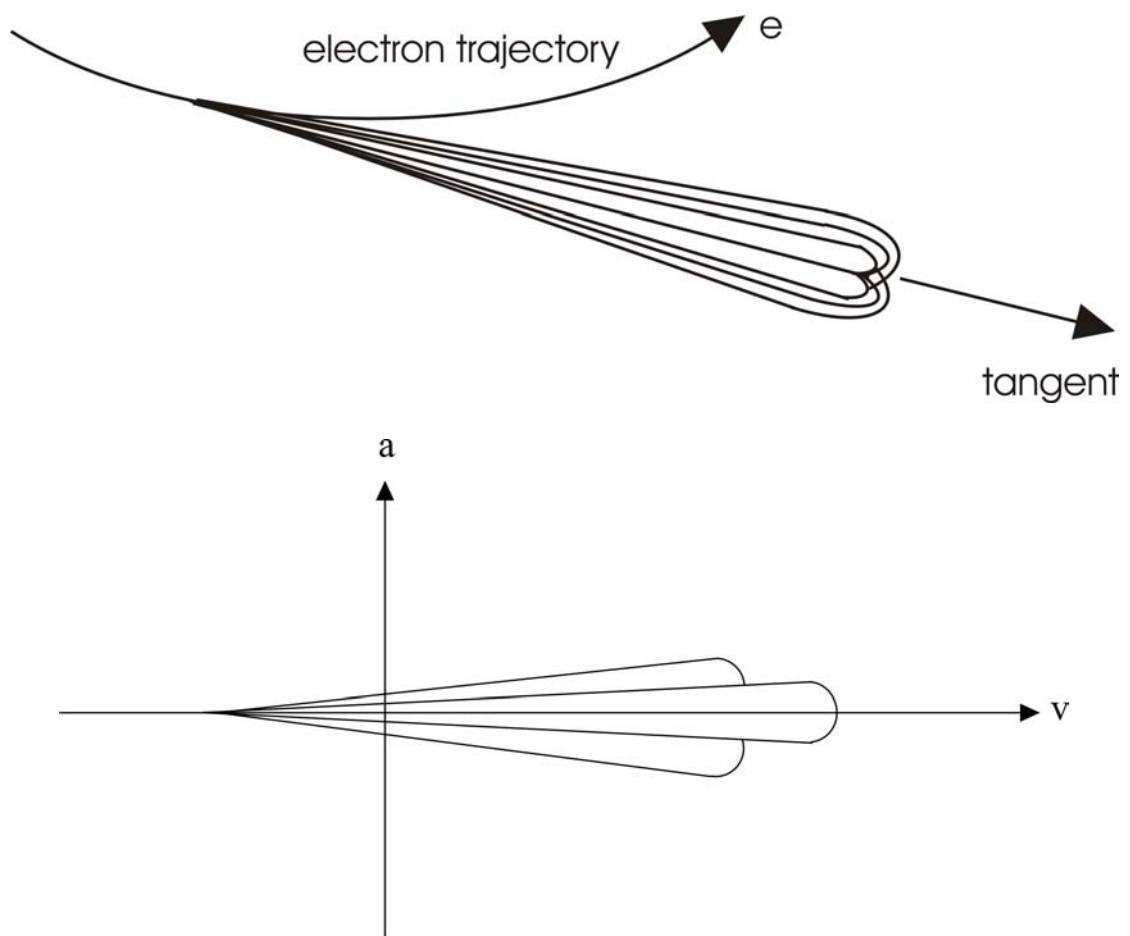
Fig. 1.5 The wave front of the electromagnetic wave emitted by an electron moving with a velocity almost equal to the light velocity as observed by the observer rest at the point in the laboratory. Upper panel: Wave front. Lower panel: The wave front in the plane containing electron velocity, **v**, and its acceleration, **a**.

Because of the relativistic effect described above, the wave fronts of synchrotron radiation as observed in the laboratory system become ones as shown in Fig.1.5. The shapes are very much contrasted with the wave front shape shown in Fig.1.2. As mentioned already, the wave front shapes shown in Fig.1.2 are these of synchrotron radiation seen in the (x' y') coordinate system which is moving with the electron. The wave front shapes shown in Fig.1.5 are those of synchrotron radiation seen in the (x y) coordinate system which is rest in the laboratory. Therefore, we usually call the radiation shown in Fig.1.5 as synchrotron radiation.

Synchrotron radiation source we use is an electron accelerator called a storage ring. In Fig.1.6, a storage ring is illustrated schematically. In the storage ring, electrons accelerated at a high energy are stored. Synchrotron radiation is generated at the bending magnet parts. In the storage ring, not only bending magnets but quadrupole magnets for the beam focusing are installed. In addition to these, sextupole and octopole magnets for finer adjusting of the electron beam are installed. In modern storage rings, different types of radiation sources called insertion devices are installed. A brief description of the insertion devices are presented later. Figure 1.7 shows the magnet arrangement in the storage ring of Siam Photon Source owned by the National Synchrotron Research Center. In the figure, black long rectangles are supposed to be insertion devices.
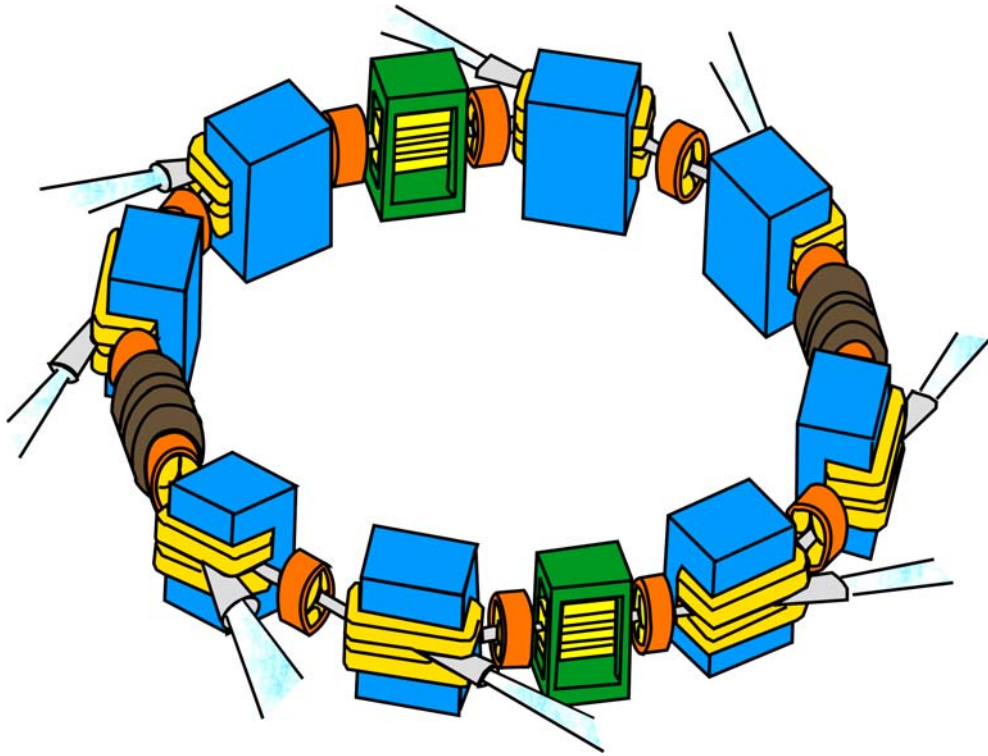
Fig. 1.6 A storage ring illustrated schematically.
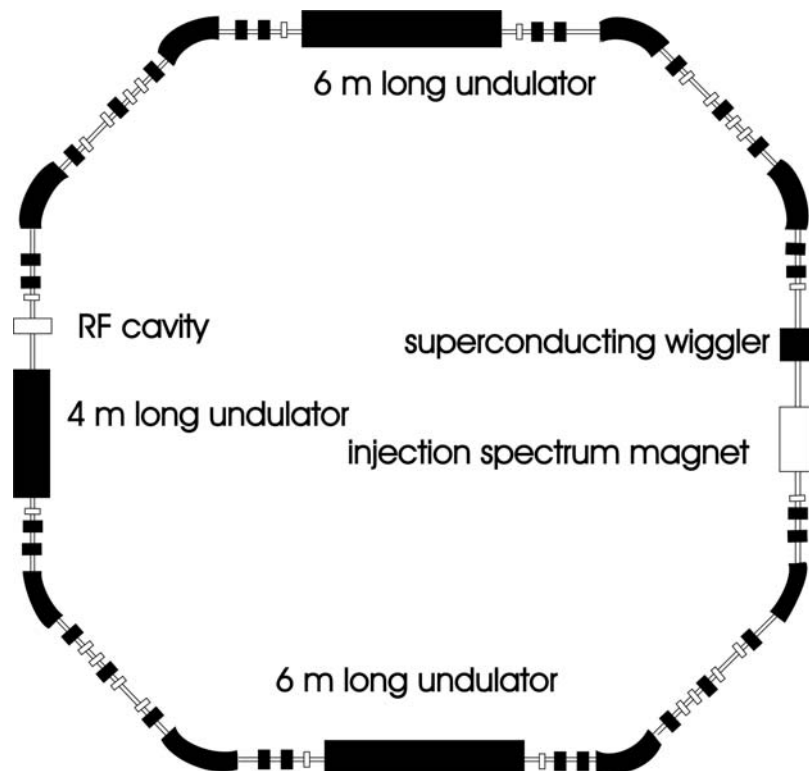
Fig. 1.7 Magnet arrangement in the Siam Photon Source.

Suppose an electron loses the energy in one turn by emitting synchrotron radiation. This energy is compensated by radio frequency (RF) acceleration in an RF cavity. The energy radiated per turn is calculated to be

$$U_o = 4\pi e^2 \gamma^4 / 3\rho \qquad (1.12)$$

where ρ is the radius of curvature of the electron trajectory. U_o is expressed in keV. Some more calculations show the energy (keV) emitted per turn is given as

$$U_o = 2.65 E^3 B \qquad (1.13)$$

E is the beam energy in GeV and B is the field strength of the bending magnet in kilogauss. If we write the radiated power in kilowatts, we have

$$P = 2.65 E^3 BI \qquad (1.14)$$

where I is the beam current in ampare. This is a quite large amount and shows that synchrotron radiation is quite intense light. Synchrotron radiation emitted from the bending portion of the storage ring is illustrated schematically in Fig.1.8.
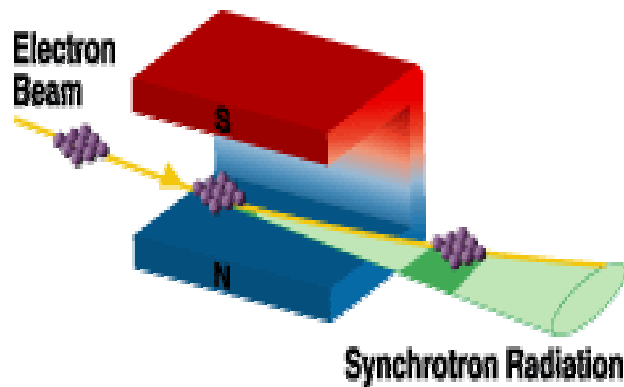
Fig. 1.8   Synchrotron radiation from a bending magnet part.

Suppose that synchrotron radiation emitted by an electron is observed at point, Q, in the plane containing the electron orbit as shown in Fig.1.9. Synchrotron radiation emitted while the electron is moving on an arc $P_1' P_2'$ of the electron trajectory is assumed to be able to be observed. Since synchrotron radiation emitted in

a narrow cone with a small angle, $1/\gamma$, synchrotron radiation can be seen at the point,

Q, far away from the orbit while the electron passes through a very narrow section of

the trajectory. Thus, the arc, $P_1' P_2'$ has its center angle equal to $1/\gamma$. This is because

the light pulses emitted at P_1' and P_2' can not be seen at R if the parts of the two

light cones from P_1' and P_2' do not overlap.
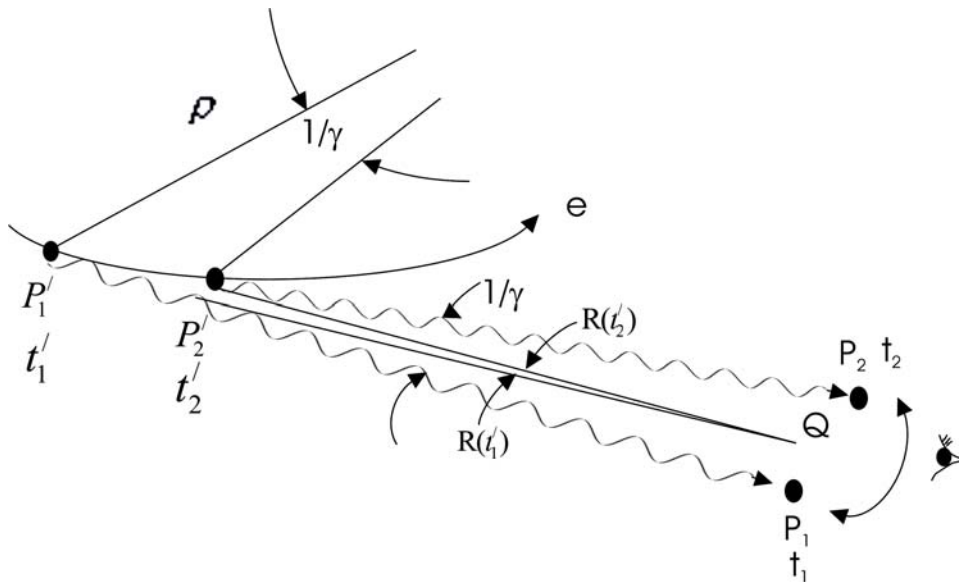
Fig. 1.9 Synchrotron radiation as observed in the laboratory. ρ is the radius of
curvature of the electron trajectory. Synchrotron radiation emitted in the
trajectory section $P_1' P_2'$ can be seen at observers position Q. The electron
passes P_1' at a time t_1' and P_2' at t_2'. Radiation emitted at P_1' at t_1'
reaches Q at t_1. Radiation emitted at P_2' at t_2. $P_1' Q = R(t_1')$, $P_2' Q = R(t_2')$.

Let the time when the electromagnetic wave is emitted at P_1' and P_2' be t_1' and t_2', respectively. Let the time when the two light pulses from P_1' and P_2' arrive at Q be t_1 and t_2, respectively. Let the distances, $P_1' Q$ and $P_2' Q$, be R (t_1') and R (t_2'), respectively. Since the distance between a point on the electron trajectory and the point, Q, changes as time passes, the distance must be written as R (t'), as we have defined here. Obviously, the light pulse can be generated during a period

$$\Delta t' = t_2' - t_1'$$

$$= P_1' P_2' / v$$

$$\Delta t' = \rho / \gamma v \tag{1.16}$$

Here ρ is the radius of curvature of the electron trajectory and v is the electron velocity. The time when the light pulse arrive at Q is given as

$$\left. \begin{aligned} t_1 &= t_1' + \frac{R(t_1')}{c} \\ t_2 &= t_2' + \frac{R(t_2')}{c} \end{aligned} \right\} \tag{1.17}$$

Using (1.16) we have

$$\begin{aligned} R(t_2') &= R(t_1' + \Delta t') \\ &= R(t_1') + \frac{dR}{dt'} \Delta t' \\ &= R(t_1') + \frac{dR}{dt'} \frac{\rho}{\gamma v} \end{aligned}$$

Using the relation given below and noting that the direction of dR/dt' is opposite to that of **v**

$$\frac{dR}{dt} = -\left| \frac{dR}{dt'} \right| = -|\mathbf{v}| = -v$$

we obtain

$$R(t_2') = R(t_1') - \frac{\rho}{\gamma} \tag{1.18}$$

Using (1.16), (1.17) and (1.18), the time duration that synchrotron radiation can be seen at Q is given as

$$\Delta t = t_2 - t_1$$

$$= t_2' + \frac{R(t_2')}{c} - t_1' - \frac{R(t_1')}{c}$$

$$= t_2' - t_1' + \frac{R_1(t_1')}{c} - \frac{\rho}{\gamma c} - \frac{R_1(t_1')}{c}$$

$$= \frac{\rho}{\gamma \mathrm{v}} - \frac{\rho}{\gamma c}$$

$$= \frac{\rho}{\gamma \mathrm{v}} \left(1 - \frac{\mathrm{v}}{c} \right) \tag{1.19}$$

If the velocity of the electron is much lower than the light velocity, (1.16) and (1.19) given as

$$\Delta t = \frac{\rho}{\gamma \mathrm{v}} = \Delta t' \tag{1.20}$$

This can be understood in the following way:

Radiation emitted at P_1' at t_1' arrives at Q in a period much a shorter than that the electron travels to P_2'. Thus,

$$t_1' \, \square \, t_1$$

Similarly we can consider

$$t_2' \, \square \, t_2$$

Therefore we have

$$\Delta t' = t_2' - t_1' = t_2 - t_1 = \Delta t_1$$

If the velocity of the electron is increased to be almost equal to the light velocity, the situation is much complicated. The radiation is emitted at $P_2^/$ at $t_2^/$ before the radiation emitted at $P_1^/$ at $t_1^/$ reaches Q. Here, the situation similar to the Doppler effect is realized. From (1.8),

$$\frac{1}{\gamma^2} = 1 - \frac{v^2}{c}$$
$$= (1 + \frac{v}{c})(1 - \frac{v}{c})$$
$$= 2(1 - \frac{v}{c})$$

Therefore we have

$$1 - \frac{v}{c} = \frac{1}{2\gamma^2} \tag{1.21}$$

Inserting (1.21) into (1.19), we have

$$\Delta t = \frac{\rho}{2v} \left(\frac{1}{\gamma} \right)^3 \tag{1.22}$$

Thus, Δt in (1.22) is far much smaller than that given in (1.20). The time dependence of the radiation field is shown in Fig.1.10 schematically. Suppose this field is formed by harmonic waves, then the spectrum of the radiation is given by the Fourier transformation of the time dependence of the radiation field. Since the width of the radiation pulse is narrow, the Fourier transform is distributed a wide frequency range continuously. The qualitative form of the spectrum is also shown in Fig.1.10.
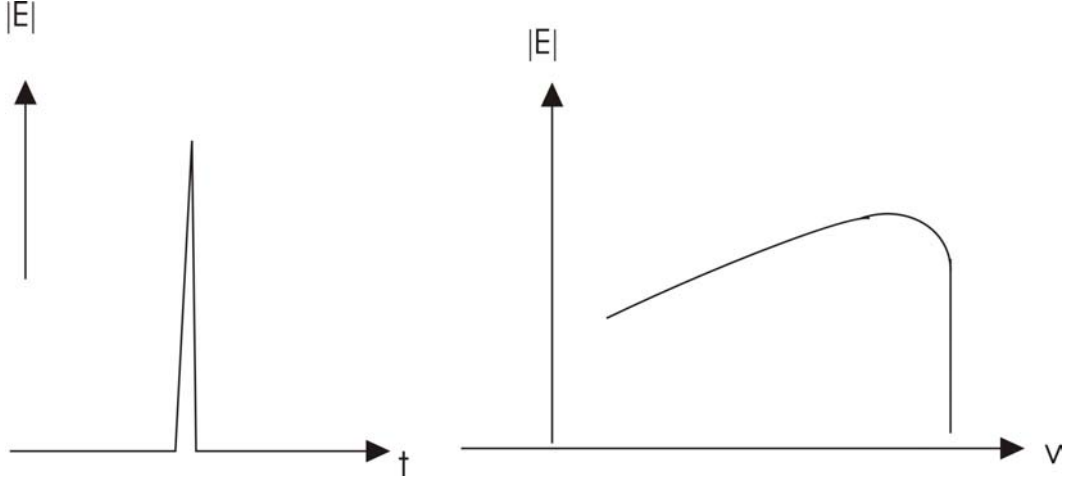
Fig. 1.10 Time dependence of the radiation as observed at a point on the plane containing the electron orbit in the laboratory and the spectrum of synchrotron radiation.

According to a detailed calculation made by taking the relativistic effect into account, the photon density spectrum of synchrotron radiation is given as

$$\frac{dN}{d\Omega} = \frac{4\pi e^2}{3c} \left(\frac{\nu\rho}{\gamma^2 c}\right)^2 \left(1+\gamma\theta^2\right)\left[F_\sigma(\xi) + F_\pi(\xi)\right] \tag{1.23}$$

$$\left.\begin{aligned} F_\sigma(\xi) &= K_{2/3}^2(\xi) \\ F_\pi(\xi) &= \frac{\gamma^2\theta^2}{1+\gamma^2\theta^2} K_{1/3}(\xi) \end{aligned}\right\} \tag{1.24}$$

$$\xi = \frac{2\pi\nu\rho}{3\gamma^3 c}(1+\gamma^2\theta^2)^{3/2} \tag{1.25}$$

Here, ν is the radiation frequency and $K_{2/3}(\xi)$ and $K_{1/3}(\xi)$ are the modified Bessel function. $F_\sigma(\xi)$ is for the radiation whose electric vector is in the plane containing the electron trajectory. $F_\pi(\xi)$ is for the radiation whose electric vector is in the plane normal to the plane containing the electron trajectory. θ is angle between the tangential direction of the trajectory and the radiation propagation direction. Although

the results are not shown practically, the numerical calculation of (1.23) through (1.25) shows that synchrotron radiation is well polarized with its electric vector in the plane containing the electron trajectory.
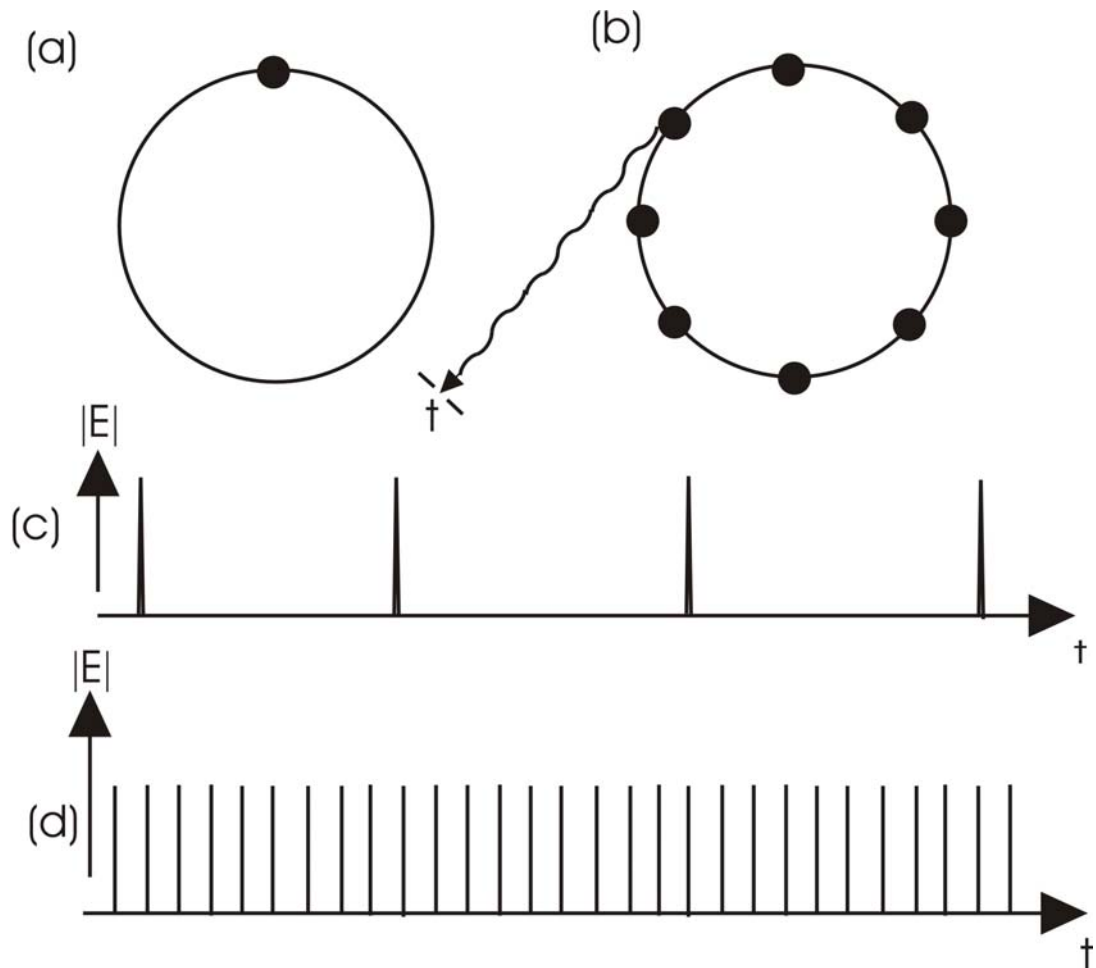
Fig. 1.11 Time structure of radiation from a circular accelerator

(a) An electron circulating in a storage ring.

(b) Electron bunches circulating in a storage ring.

(c) Time structure of the radiation field emitted by an electron circulating in a storage ring.

(d) Time structure of the radiation field emitted by bunches of electrons circulating in a storage ring.

In a storage ring, an RF cavity is installed. The energies of electron lost by emitted synchrotron radiation are compensated by acceleration by RF field in the cavity as mentioned before. Electrons enter the RF field in the acceleration mode can be accelerated and pass through the RF cavity. This makes the electrons in the storage ring are bunched. Synchrotron radiation is emitted from bunches of electrons. This makes the time structure of synchrotron radiation be pulsed. The pulse structure is shown schematically in Fig.1.11.

1.2.2   Insertion Devices

In addition to the bending magnet portion of storage ring, an insertion device which is installed in the straight section is used as a synchrotron radiation source. The insertion device has the structure that many pairs of magnets with different polarity are lined up. The conceptual structure is shown in Fig.1.12. Electrons make a wiggling motion like snake's motion. Synchrotron radiation is generated every time when an electron is wiggled. This is shown in Fig.1.13.
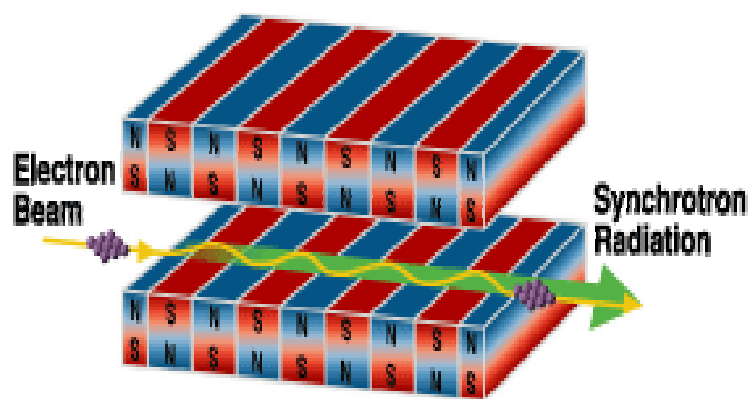
Fig.1.12 The magnet arrays in an insertion device.
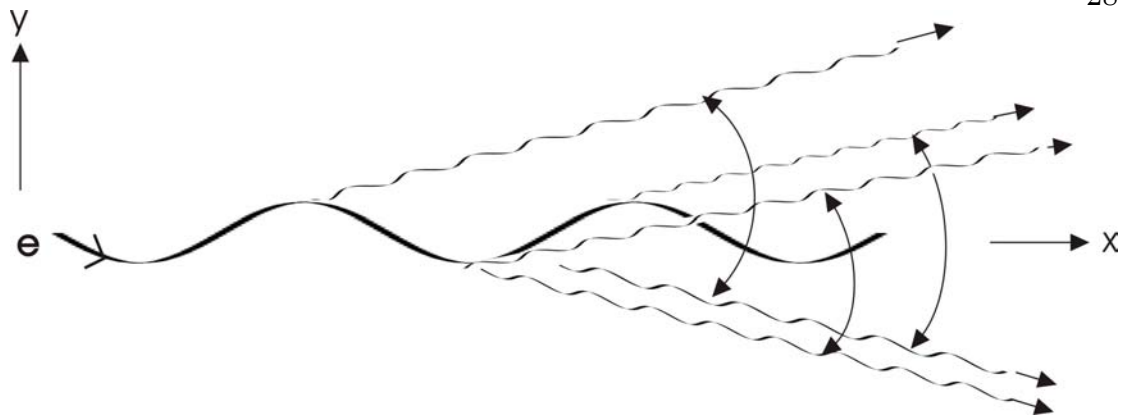
Fig. 1.13 Synchrotron radiation generated by an electron making a wiggling motion.

If the magnetic field is weak and the amplitude of the wiggling is small, emitted synchrotron radiation falls in a small cone with a vertical angle of $1/\gamma$ directed toward the average direction of the electron motion, as is illustrated in the top panel of Fig. 1.14. In the part of the electron trajectory where the radius of curvature, ρ is small, the intensity of emitted radiation is weak. In the part of the electron trajectory where the radius of curvature is large, the intensity of emitted radiation is strong. Therefore the generated radiation field varies as oscillating with time as shown in the middle panel of Fig.1.14. The spectrum of the radiation has a shape of a narrow band with the central frequency decided by the amplitude of the wiggling motion, thus by the strength of the magnetic field. This narrow band appears as a quasi-line spectrum as shown in the bottom panel of Fig.1.14. Because of the overlap of the radiation generated by the wiggling motion, the interference of radiation occurs. Thus, the harmonics of the fundamental line appears. By a detailed calculation, it is shown that the odd order line appears strong.

Synchrotron radiation generated in an insertion device with a weak magnetic filed is very intense because of the confinement of the spectrum in a narrow spectral region and the interference. The insertion device of this type is called an

undulator. Synchrotron radiation from an undulator is often called the undulator

radiation.

In the theoretical analysis of the radiation generation in an insertion

device, a parameter, K, defined as

$$K = \frac{e}{mcv^2} \frac{\lambda_o B_o}{2\pi} \left.\begin{array}{l} \\ \\ \approx \frac{\lambda_o(cm)B_o(kG)}{10} \end{array}\right\} \tag{1.26}$$

plays an important role. If the value of K is not more than 1, the insertion device is an

undulator. Generated radiation is the distinctive undulator radiation.
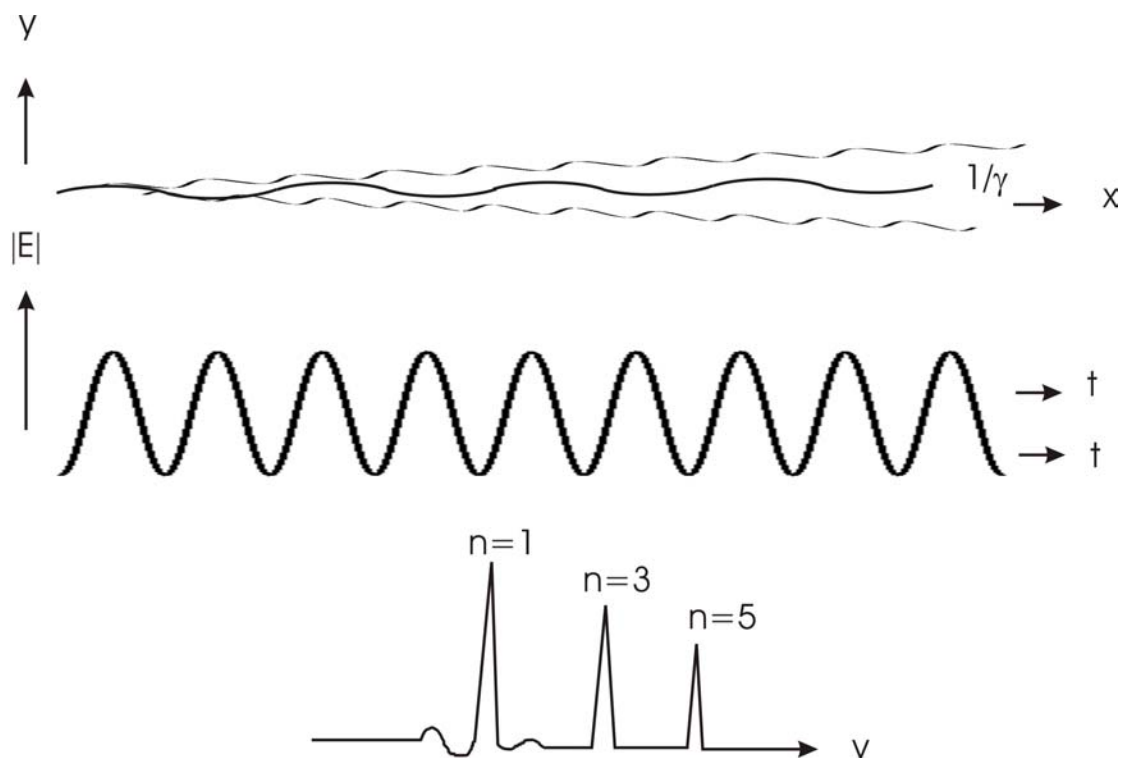
Fig. 1.14 Undulator radiation. Top: The amplitude of the wiggle motion is small and

the generated radiation falls in a small cone direction to the direction of the

average electron motion. Middle: Time structure of the radiation field.

Bottom: Spectrum of the generated radiation.
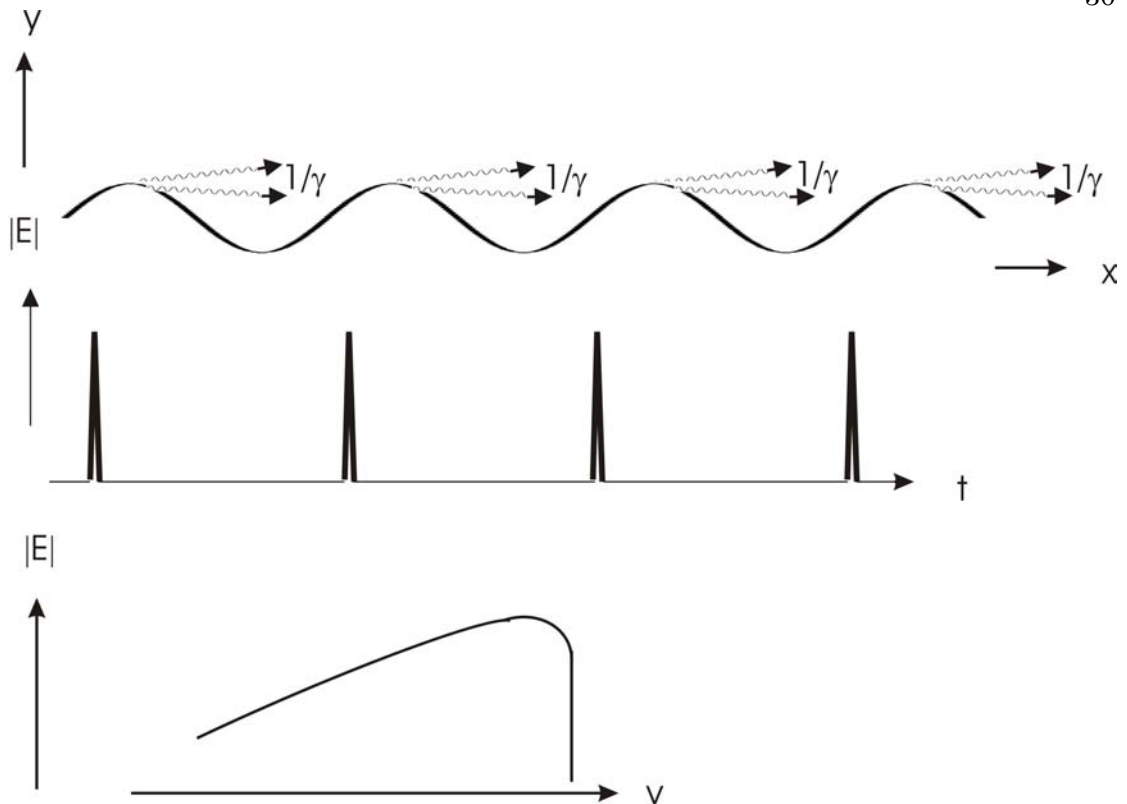
Fig. 1.15 Wiggler radiation. Top: The amplitude of the wiggle motion is large and only a part of generated synchrotron radiation progressing toward the direction of the average electron motion and falling in a narrow cone with a vertical angle of $1/\gamma$ is observable. Middle: Time structure of the radiation field. Bottom: Expected spectrum of the generated radiation.

If the magnetic field of an insertion device is large, synchrotron radiation from wiggling motion is emitted even in the direction in the laboratory system where the emitted radiation is not observable. The radiation is observable only in the narrow cone with a divergence angle of $1/\gamma$ directed toward the direction of the electron motion. This is shown in the top panel of Fig.1.15. In this case, the synchrotron radiation emitted through each electron oscillation is independent of each other. The time structure of the radiation filed is such that shown in the middle panel in Fig.1.15. Thus the spectrum is just

like that of ordinary ring as shown in the lower panel of Fig.1.15. The intensity of

the radiation, however, is high, since the radiation is of the superposition of the source

spectra.
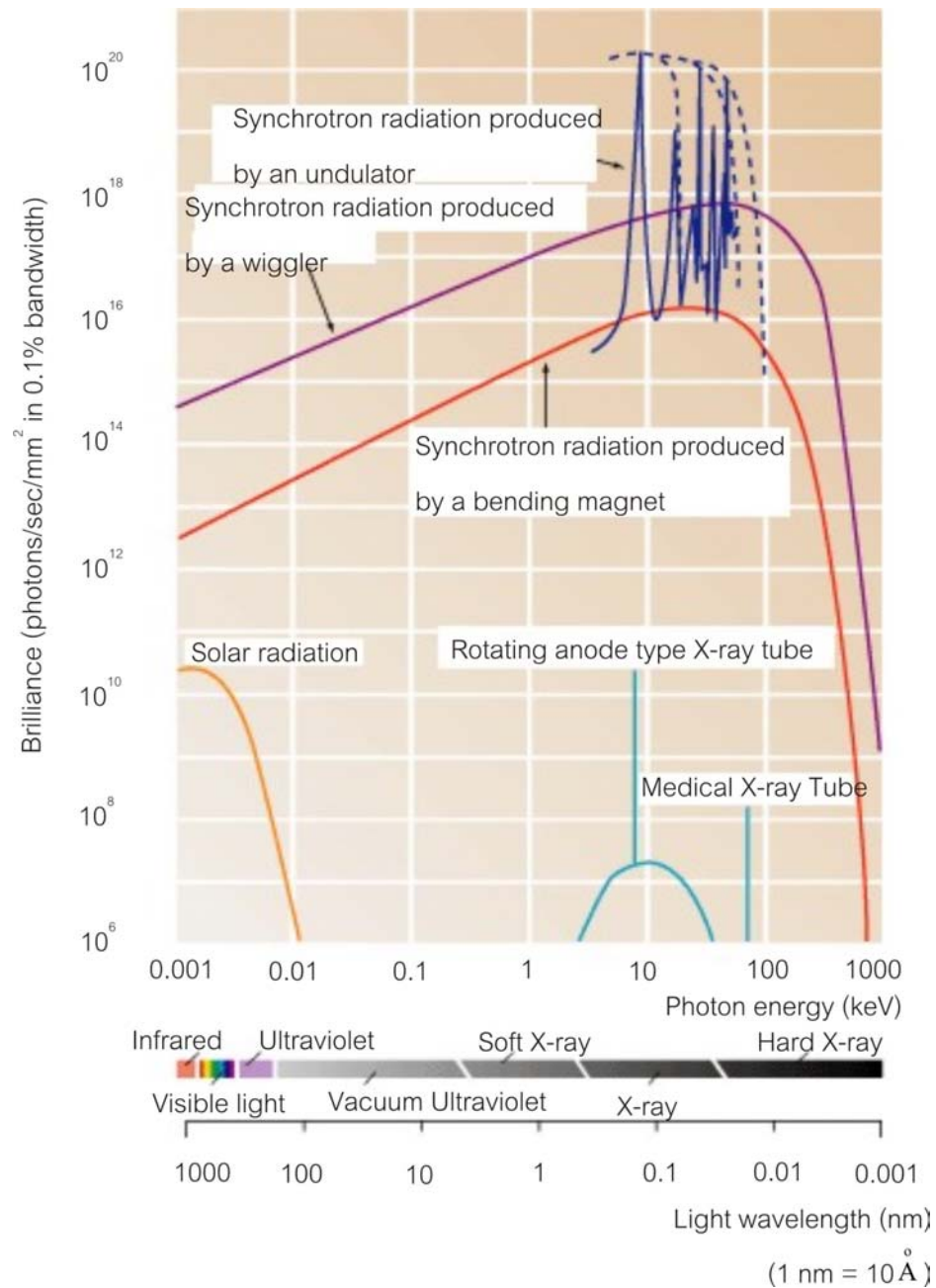
Fig. 1.16 Comparison of the brilliance among various x-ray sources including

SPring-8 source.

The insertion device of the type described above is called the wiggler. The synchrotron radiation from a wiggler is called the wiggler radiation. Practically, the spectrum of the wiggler radiation from a multipole wiggle does not have a shape like one shown in the lower panel of Fig.1.15, but is more like the undulator radiation. However, the bands are wider with stronger satellites.

1.2.3   Summary of the Properties of Synchrotron Radiation

The characteristic properties of synchrotron radiation described in the two proceeding sections are summarized here.

1. High flux: The intensity of synchrotron radiation is very high. The photon flux from a synchrotron light source is much higher than those from conventional sources. This increases magnitudes of signals and reduces measurement time in most experiments. In many cases, the enhanced signals make it possible to carry out experiments that are prohibitively long if conventional laboratory sources are used.

2. High brightness: Synchrotron radiation beam has very low divergence owning to the strong forward emission into a narrow cone of a few hundredth of a degree wide. The low beam divergence combined with the small size of the light beam makes the brightness of the radiation high and allows us to perform experiments with high spectral resolution. In the case of an undulator, the electron trajectory is confined in a narrow beam along the undulator axis. The consequent time structure of the radiation field and interference effect make the brilliance at the peak of the emission band much higher than that of the synchrotron radiation from an ordinary banding magnet portion.

3. Continuous spectrum: Synchrotron radiation comprises a broad and continuous spectrum spanning over an energy range from the far infrared to x-ray

region with the highest photon flux at ultraviolet or x-ray wavelengths depending on the energy of the electron beam in the source. The spectrum of radiation produced by an insertion device is composed of a series of emission bands. By changing the strength of the magnetic field of the insertion device the locations of the bands are shifted smoothly and continuously.

4. Pulsed beam: Since the electron beam in an accelerator consists of a series of bunches, the time structure of emitted synchrotron light is such that very short pulses repeat. Pulsed light makes it possible to observe the progression of a photochemical reaction. A pulse raises the system to an initial excited state and subsequent similar pulses with slightly different energies detect the relaxation of the excited state leading to a chemical reaction.

5. Partial coherence: Synchrotron radiation is partially coherent. Since light produced by the wiggle motion of an electron can cause induced emission of a proceeding wiggling electron, radiation generated by successive wiggling motions can be in phase. This leads to partial coherence of emitted radiation. For more complete coherence we need a resonance cavity as in case of a free electron laser. In case of far infrared light whose wavelength is almost the same as that of bunch length the coherence is higher.

6. Linear or circular polarization: Synchrotron radiation emitted in the plane containing the electron orbit is linearly polarized with its electric vector in the plane of electron orbit. In a specially designed undulator, circularly polarized light is generated. Synchrotron radiation emitted off the electron orbit plane is elliptically polarized. On average, synchrotron radiation is almost linearly polarized with a high degree of polarization. Linearly polarized light can be used to study the orientation of molecules in

matter or on a surface. Circularly polarized light can be used to study the magnitudes of magnetic moments in magnetic materials.

      7. Light intensity standard: The spectral brilliance is completely determined theoretically in a quantitative way through the electron dynamics with relativistic theory. Thus, synchrotron radiation is capable of serving as a light intensity standard, particularly in the region from the vacuum ultraviolet to x-rays where no other appropriate source to be a light intensity standard exists.

      8. Clean light source: Since the electron beam in a storage ring runs in a vacuum chamber evacuated to the ultrahigh vacuum, the light source is clean and does not act as a source of gases contaminating sample surfaces. This is very important in experiments like photoemission spectroscopy.

1.3 Materials

      The purpose of the present thesis work is to develop the technique to make a better x-ray image. Here, the x-ray image means the figure or picture of the material that we inspect for a scientist investigation. A typical example of such x-ray image is the chest x-ray photograph for medical inspection. In the work for developing the technique, we have to examine the performance or quality of the instruments or the methods we have developed. For carrying out this, we have to test the system using some samples. In the technical development work, the properties of the samples should be known to some extent. In the present work, several kinds of materials were used as samples. In this section, the properties of the materials used as samples are described.

1.3.1 Ivory

The word "ivory" was traditionally used for the tusk of an elephant. However chemical structure of the teeth and tusks of mammals is the same regardless the species of origin. The trade of elephant ivories is banned by international treaty. The trade of certain teeth and tusks other than those of elephants is well established and widespread. If the teeth or tusks of some mammals are mechanically processed as carvings or scrimshaws, the products cannot be distinguished from those from elephant teeth or tusks. In the commercial sense, there are many products with different values under the name of "ivory".

Although teeth and tusks have the same origin, teeth have special structures adapted for food mastication. Tusks, which are extremely large teeth projecting beyond lips, have evolved from teeth. In certain species tusks have an evolutionary advantage. Their existence has been useful in their survival in nature. A tooth of a mammal consists of a root and a trunk which is similar to the tusk. The intrinsic structure is affected by the environment and this leads to the evolution. It has been reported that the contents of Sr, C and N in the teeth of the African elephant ivory is influenced by the local geological conditions. It has also been reported that the use of spectroscopic method is quite useful to distinguish different kinds of ivory. Ivory consists largely of collagen and hydroxyapatile $[Ca_{10}(PO_4)_6(OH)_2]$.

Previously ivory meant the tusk of an elephant. A cross section of the tusk reveals a crisscross pattern which is specific to ivory. Along the longitudinal side (long side) of the tusk, the tusk cross section displays a wood grain pattern. It has sheen due to the oils it contains.

The cross sectional views of the ivory of an elephant and a mammoth are shown in Fig.1.17. The ivory cross section of an elephant is illustrated in the left panel and that of a mammoth is shown in the right panel. The Schreger lines are indicated in

the figure. They are lines showing the crisscross features of the patterns on the cross sections as is obvious in the figure. Two Schreger lines cross making an obtuse angle in the ivory of an elephant. Two Schreger lines cross making an acute angle in the ivory of a mammoth. Polished cross sections of elephant and mammoth ivory dentine display Schreger lines which are not specific. Schreger lines are commonly referred to as cross hatchings, engine turnings or stacked chevrons. The angle between the two Schreger lines is called the Schreger angle. If we carefully scrutinize the Schreger lines, we find that they appear to be convex outward. Two kinds of apexes made by two crossing Schreger lines exist. One is convex outward and the other is concave inward. They are shown in Fig.1.17. The Schreger lines are oblique to the radial direction.
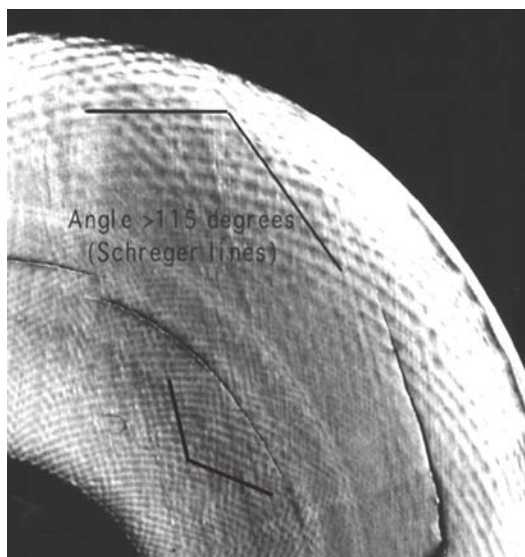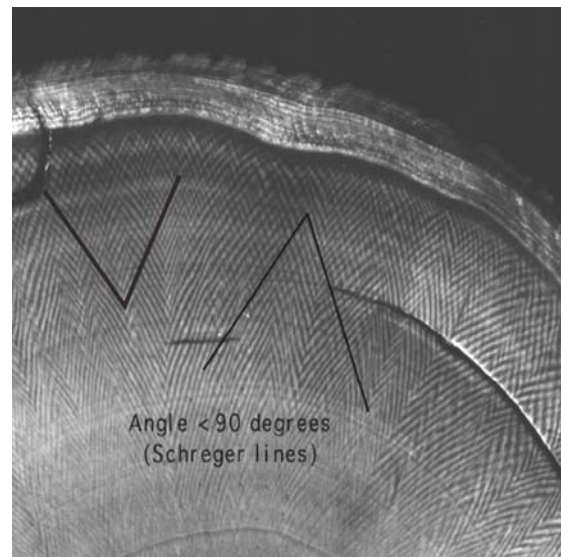
| Elephant Ivory | Mammoth Ivory |

Fig. 1.17 Schreger lines in elephant and mammoth ivories by photocopy machine.

1.3.2   Tusk

-    **Narwhal Tusk:** Narwhal is a kind of dolphin. This belongs to an endangered species. The tusk of narwhal is long and six to eight feet. The cross sectional view of the narwhal tusk is shown in Fig.1.18. From the cross sectional view shown in Fig.1.18, we find that the tusk of narwhal consist mainly of three parts. The outermost layer is the cementum. The inside bulk part is the dentine. Between the cementum and the dentine a layer called the transition ring exists.
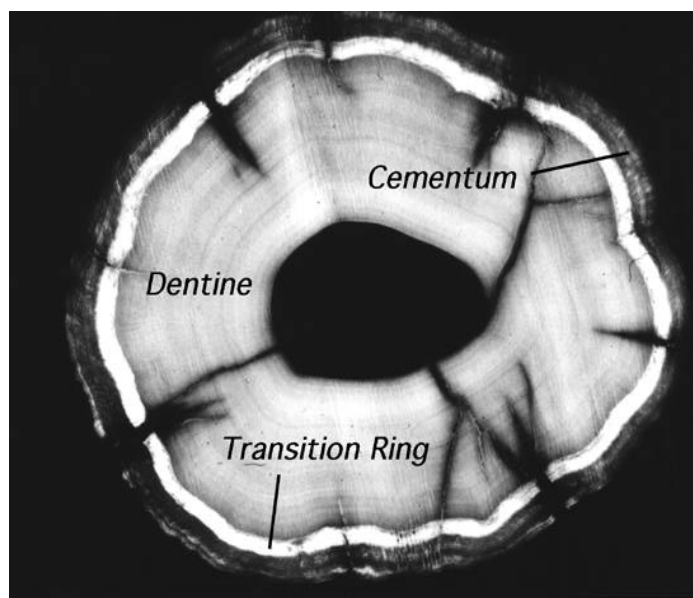
Fig. 1.18   Visual cross section of a narwhal tusk.

This material is seldom cut into sections for the practical use. Instead, it has been used mostly for walking canes as being left intact. If it is cut into small pieces, they are used for kimono-obi (tie) decorations called as "netsuke". The central part of the narwhal tusk is hollow. The tusk has the grain structure resembling that of a tree. Enamel is not found in the trunk part but it may be present at the tip of tusk. The cementum frequently displays longitudinal cracks which follow the depressed

areas of the spiral pattern. Cracks creeps into dentine in some cases. This is recognized in the cross sectional view in Fig.1.18.

- Warthog Tusk: Warthog tusk comes from the animal's upper and lower canine teeth. These tusks are considerably curved. The cross sectional view of the tusk is shown in Fig.1.19. The cross section has more like a square shape. This is contrasted to those of ivory and narwhale. In tusk of warthog, the empty part is very narrow. This part is called the tusk interstitial zone.
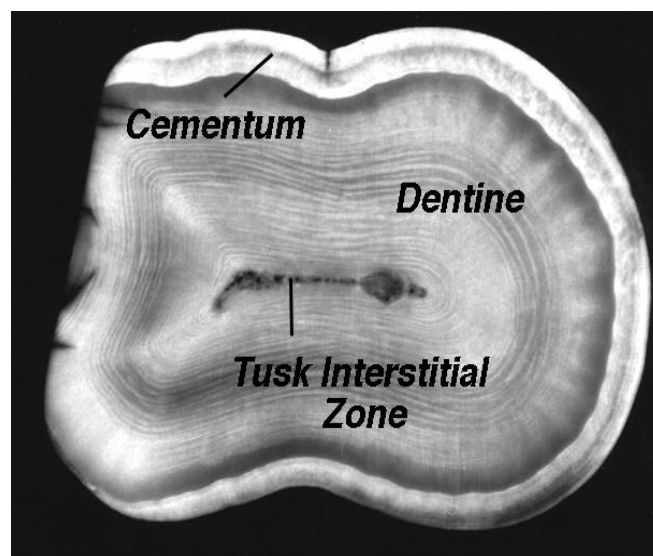
Fig. 1.19   Visual cross section of a warthog tusk.

If we compare three figures, Figs.1.17, 1.18 and 1.19, we find that the structure of ivory is quite distinctive. It is characterized by the existence of the Schreger lines. In the tusks of narwhal and warthog, the Schreger line does not exist but the grain structure is apparent. In the comparison between tusks of narwhal and warthog, the grain structure is not so definite in the tusk of narwhale as that of warthog.

1.3.3 Teeth

Since the tusk can be taken as a special tooth, the structure of a tooth has an

apprecial similarity to that of a tusk. In what follows, we will see the structures of teeth of some selected animals.

- Teeth of Hippopotamus: A tooth of a hippopotamus is the hardest of all ivory-like substances. This is the second most commonly used ivory, after the elephant ivory. Hippo's ivory is often used for flat items, such as buttons and inlays. Those ivories which come from the lower jaw canines and the incisors are used for such articles. The size varies, depending on the size of the animal. The surface is bright white. Through detailed examinations, we find that the distinctive aspect of the grain structure. The grain structure is such that each grain is formed by a single closed line and the line is wavy. The structure changes according to the portions of the jaw where the teeth under consideration exist. In Fig.1.20, the cross sectional structures of three different teeth of a hippopotamus are presented. In the upper left panel, the cross section of the canine of the upper jaw is illustrated. In the upper right panel, the canine of the lower jaw is illustrated. In the lower panel the structure of an incisor is illustrated.

The cross section of hippo's curved upper canine has a deformed triangular shape. It does not have sharp edges but round ones. In one portion, a sharp dent is made. The interstitial exists but it has an angular shape corresponding to the dent structure. The grain feature is clearly recognized in the dentine. The outermost layer is the cementum. The enamel layer exists, too.

The lower jaw canines are the hippo's largest teeth. They are considerably curved. The lower jaw canine tooth has a triangular cross section. The lower jaw canine does not have the dent shape. The interstitial zone is angular but has

a hollow area with an arch shape in the center. The cross section of the incisor has round shape. Both the lower jaw canine and incisor have two layers of dentine. The outer primary dentine, and the inner, secondary dentine. The innermost layer has a marbled appearance which differs by species. It can even appear to have a greenish cast. The pulp cavities of these teeth are quite small. Unlike elephant ivory, hippo ivory does have a thick enamel coating.
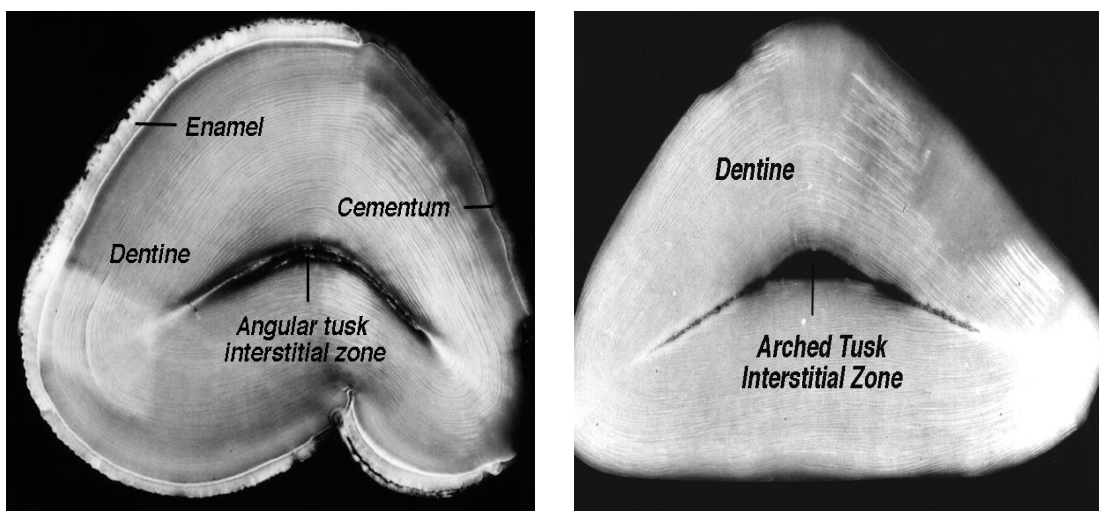
Upper jaw canine   Lower jaw canine
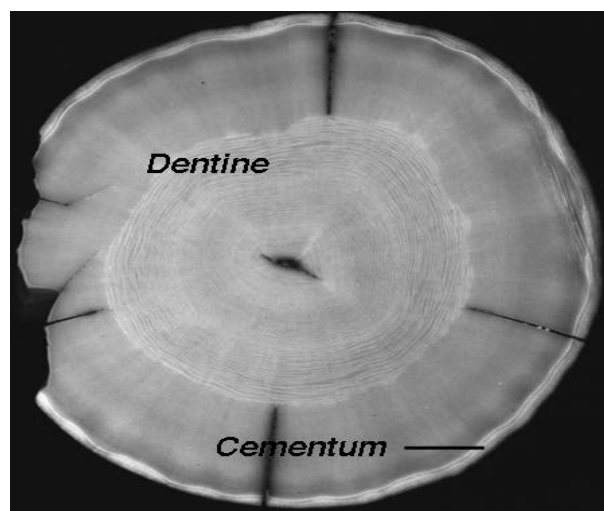
Incisor

Fig. 1.20 Visual cross sectional views of hippo's canines and incisor. The upper part, the lower part and the incisor part are shown.

Hippo ivory is denser than elephant ivory, harder to carve, and has a finer grain. There is none of the "engine turned" effect in cross section. Rather, hippo ivory has concentric rings in the cross section.

-        **Sperm Whale Tooth:** Thirty teeth of the sperm whale can be used for ivory. The teeth are very large. Sperm whale ivory is easily confused with walrus ivory, as both have two distinct layers. The inner layer of sperm whale ivory, however, is much larger. Similarly, in a longitudinal section, sperm whale dentin has yellow "globules" included in the marbilization.
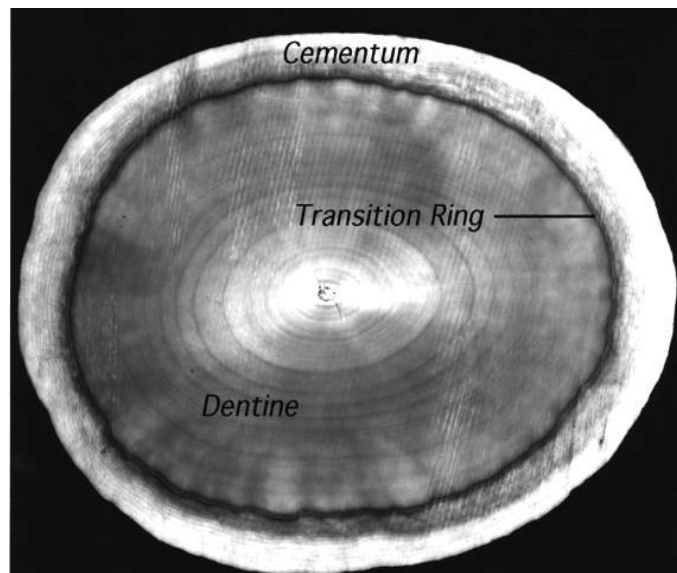
Fig. 1.21   Visual cross section of a sperm whale tooth.

The cross section of the tooth of sperm whale is shown in Fig.1.21. Basically, it is similar to that of the incisor of hippopotamus. The cementum thickness appears to be larger in the case of sperm whale. The interstitial zone does not exist in case of sperm whale. The grains are not so dense. A closer inspection of the figure indicates that slightly inclined lines exist in the tooth of sperm whale.

1.3.4 Walrus Tooth and Tusk

The ivory of walrus comes from the upper jaw canines. It is oval in cross section and can be over 2 feet in length. The cross sectional views of a tooth and a tusk of walrus are shown in Fig.1.22. In the left panel, the cross section of tooth is shown. In the right panel, the cross section of tusk is shown. In the figure on the right panel, C represents cementum, PD the primary dentine, and SD the secondary dentine.

<div align="center">

tooth   tusk

</div>
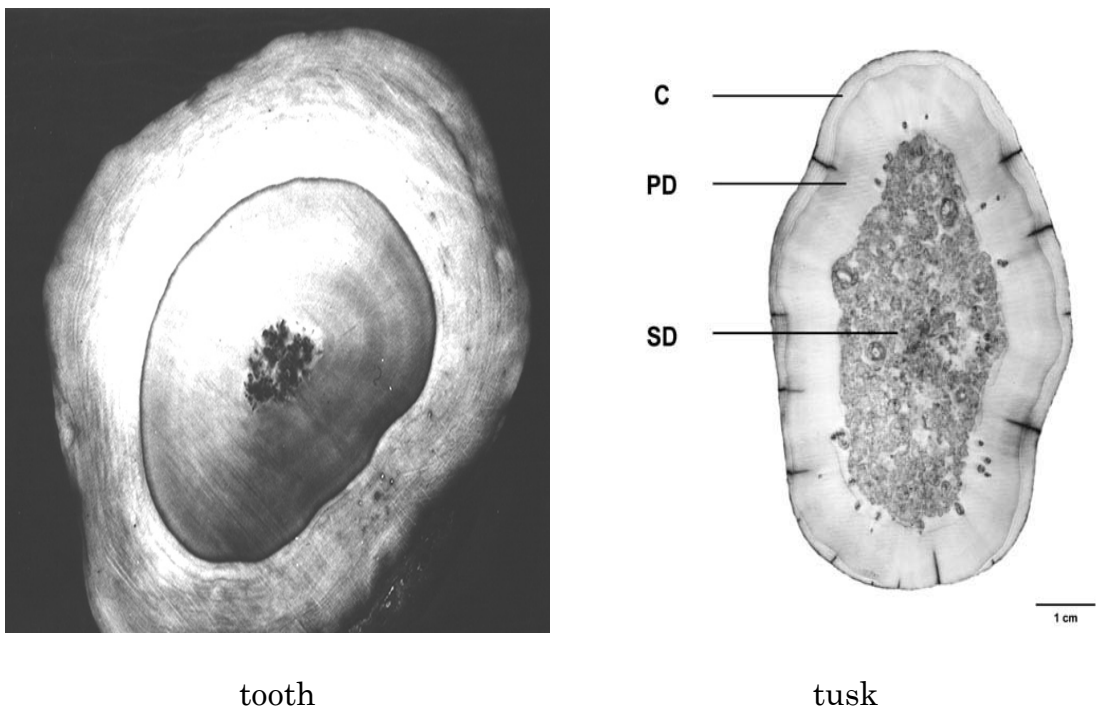
Fig. 1.22 Visual cross section of a walrus tooth and tusk.

In both tooth and tusk, the dentine has the two layer structure. The outer dentine layer is called the primary dentine and the inner dentine layer is called the secondary dentine. The inner dentine layer has a high mineral content. It is formed as the tusk grows and leaves a marbled look on finished objects. The cementum layer is dense and smooth.

Walrus ivory is used primarily for small objects. Items carved from walrus tusks exhibit a mottled appearance caused by the interior of the tusk which is harder than the exterior. These are usually used in netsukes and dagger handles.

The dentine in the walrus tooth means the mainly primary dentine. The center of the tooth contains a small core of the apparent secondary dentine. The dentine is completely surrounded by the cementum layer. A cross section of the tooth will show very thick cementum with prominent cementum rings.

1.3.5   Antler

The tooth of an antler is hollow in the central part. The outer surface of the tooth is harder than a bone. The teeth have been used for knives and dagger handles. Their shades are from a deep brown to a light yellow.

1.3.6   Plastic

Since the invention of celluloid, several different plastic materials have been made to resemble ivory. In particular, ivorine is composed of alternating dark and light layers of plastic so as to make the grain pattern of ivory. This pattern is too regular for real ivory. All plastics do not have the weight or density of real ivory. Plastics are a poor conductor of heat and will feel warm to the touch.

1.3.7   Vegetable Ivory

The source of a vegetable ivory or an ivory nut is the inner seed of the South American ivory Tagua palm tree. A vegetable ivory is thus completely made of cellulose but not of collagen. These seeds have sizes and shapes of small hen's eggs. They are very

hard and solid all the way through. Vegetable ivory has a smooth surface which can be polished well and easily absorbs dyes. The vegetable ivory is relatively inexpensive. It is used for small items only, such as dice and buttons. Now vegetable ivory has been largely replaced by plastics.

Figure 1.23 shows the cross sectional view of vegetable ivory. Regularly spaced center lines are similar to lines in the hippopotamus.
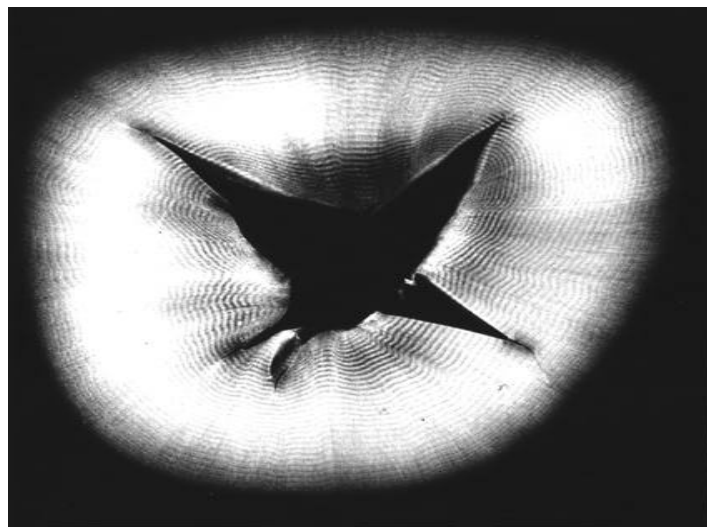
Fig. 1.23   Visual cross section of a tagua nut or a vegetable ivory.

1.3.8   Method of Distinguishing Ivories

The cross-sectional patterns and Schreger patterns provide us with the way how to distinguish many kind of ivory. In the following table, the ways to examine the samples to be distinguished are listed. All of ivory, tusk and others that were used in the experiments made here have a size of 20 mm diameter and 6 cm long.

Substance	Red Hot Pin (Touch to Surface)	Use of Knife (Draw Across Surface)	Acetone (Drop to Surface)	Sulphuric Acid (Drop to Surface)
Antler	No effect	Light scratching	No effect	No effect
Bone	No effect	Light scratching	No effect	No effect
Elephant Ivory	No effect	Light scratching	No effect	No effect
Plastic	Smoke or visible hole	Deep cut	Begin to dissolve	Unknown
Teeth	No effect	Light scratching	No effect	No effect
Tusks	No effect	Light scratching	No effect	No effect
Vegetable	Unknown	Unknown	Unknown	Brown stain

1.3.9 Breast Cancer

Cancer is a word meaning a crab in Latin. Since the disease we call cancer has the affected part resembling the shell of a crab, the name of disease came out. Thus, the cancer is a term for diseases in which abnormal cells divide without control. Cancer cells can invade nearby tissues and spread through the bloodstream and lymphatic system to other parts of the body.

The structure of breast is shown in Fig.1.24. Each breast has 15 to 20 sections called lobes. There are many smaller lobules in each lobe. Lobules end in dozens of tiny bulbs that can produce milk. Thin tubes called ducts link all the lobes, lobules, and bulbs. These ducts lead to the nipple in the center of a dark area of skin called the areola. Fat surrounds the lobules and ducts. There are no muscles in the breast, but muscles lie under each breast and cover the ribs. Each breast also contains blood vessels and lymph vessels. The lymph vessels carry colorless fluid called lymph and lead to small bean-shaped organs called lymph nodes. Clusters of lymph nodes are found near the breast in the axilla (under the arm), above the collarbone, and in the chest. Lymph nodes are also found in many other parts of the body.
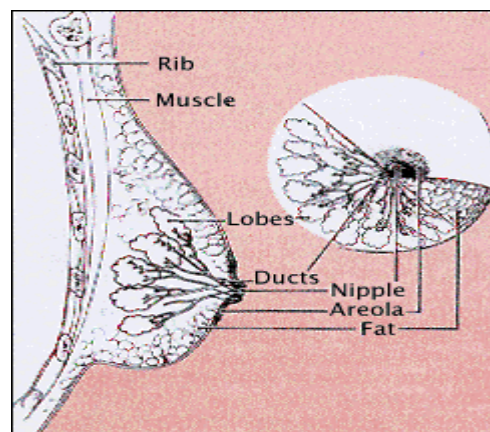
Fig. 1.24 Illustration of breast.

Cancer is a group of many diseases that break out in cells, the body's basic unit of life, and are connected to each other. To understand cancer, it is helpful to know what happens when normal cells become cancerous. The body is made up of many types of cells. Normally, cells grow and divide to produce more cells only when the body needs them. This orderly process helps keep the body healthy. Sometimes, however, cells keep dividing when new cells are not needed. These extra cells form a mass of tissue, called a growth or tumor. Tumors can be benign or malignant.

Benign tumors are not cancer. They can usually be removed and, in most cases, they do not come back. Cells from benign tumors do not spread to other parts of the body. An important fact is that benign breast tumors are not a threat to life.

Malignant tumors are cancer. Cells in these tumors are abnormal. They divide without control or order. They can invade and damage nearby tissues and organs. Also, cancer cells can break away from a malignant tumor and enter the bloodstream or the lymphatic system. That is how cancer spreads from the original (primary) cancer site to form new tumors in other organs. The spread of cancer is called metastasis.

They are many techniques for breast cancer examination. First is self examination. Patients could find it by themselves by touching their breasts. Second is biopsy. A physician will cut tissue and sent it to parasitologist in order to prove that tissue is cancer or not. Third is ultrasound or ultrasonolophy. Using high-frequency sound waves, the existence of a lump can be shown in case of fluid-filled cyst (not cancer) or solid mass (may or may not be cancer). This examination may be used along with mammography. Ultrasound can show significant freedom for obtaining images of the breast in any orientations. Ultrasound is excellent for imaging cysts such as round ones, fluid-filled ones and pockets inside the breast. In Figs.1.24-1.26, the ultrasound images of breasts are shown. Figure 1.24 shows the image of the healthy normal breast tissue. In the upper part of the figure which is surrounded by a square, the image of nipple is recognized. The image of such a normal breast tissue is compared with these having defects. In Fig.1.25, the ultrasound image of breast cysts is shown. The breast cysts are made of accumulated tiny pieces of fluid. They are the most common causes of benign breast lumps in women of ages between 30 and 50. The benign breast lumps are not cancer. In Fig.1.25, dark parts are images of cysts. In

Fig.1.26, the ultrasound image of breast abscess is shown. The breast is brought about by suppuration. The dark image in the figure is that of closed pocket tissue containing pus which is creamy, thick, pale yellow or yellow-green fluid. Abscesses are most commonly caused by bacterial infection.
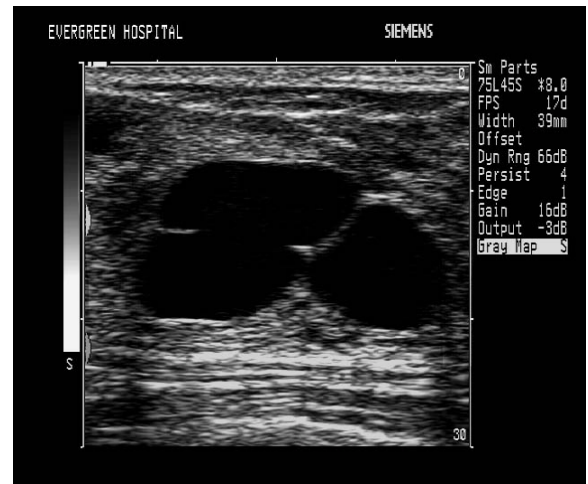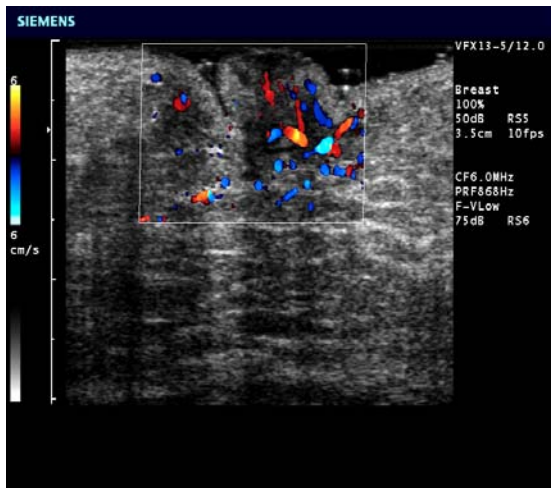
Fig. 1.25 Ultrasound image of the normal breast tissue and the nipple part is shown at the top.

Fig.1.26 Ultrasound image of breast cysts, which are tiny accumulations of fluid.
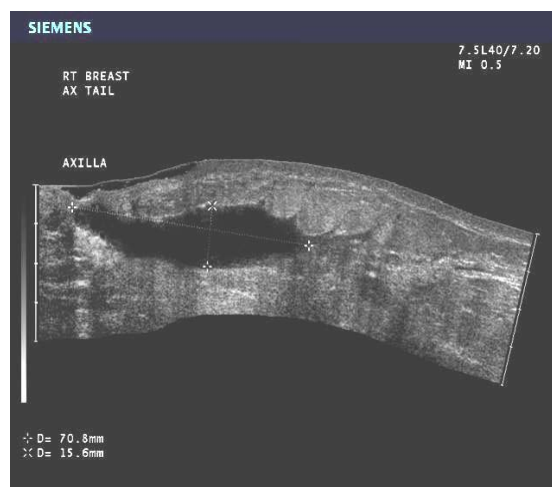
Fig. 1.27 Ultrasound image of a breast abscess.
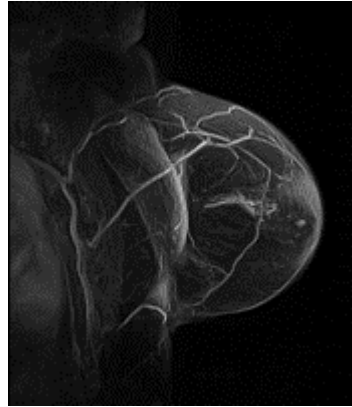
Fig. 1.28   Side view of the breast image by MRI with contrast enhancement showing

chest and blood vessels.
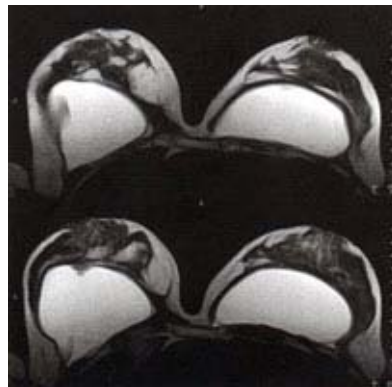
Fig. 1.29   Transverse high-resolution MRI scan of breast and implants.

Fourth is magnetic resonance breast imaging (MRI, MR) being used as a supplemental tool for helping mammography to detect breast cancer. The MRI imaging method is applicable to both the breast implant and the breast tissue surrounding the implant. Figures 1.27 and 1.28, the images of magnetic resonance of breasts are illustrated. In Fig.1.27, the side view of the breast MRI image is shown. The contrast materials to enhance the contrast of the image is given. The figure clearly shows the chest and blood vessels which are white lines in the image. Figure 1.28 illustrated the transverse high-resolution MRI scan of breast and implants. In the figure, white portions show implants. In the upper left image, it is found that the

implant is twisted. In the lower left image, the implant value is observed. The images on the right, implants sit properly. MRI may be useful for screening of younger women who have high risk of breast cancer predicted from family history or a mutated breast cancer gene (BRCA1 or BRCA2). Such persons therefore need breast imaging inspection before an age of 40 years.

Fifth is mammography that uses low dose x-rays and best techniques. High contrast and high-resolution film are used. X-ray systems designed specifically for imaging the breasts have been developed. In Fig.1.30, a mammogram is shown, where the pectoral muscle, breast, nipple and breast ducts are observed. Using an advanced mammography, it is possible to detect a tumor that cannot be felt just by touching. Once a lump is discovered, mammography can be used for investigating the lump to determine if it is cancer. If a breast abnormality is found or confirmed by mammography, additional breast imaging tests such as ultrasound (sonography) or a breast biopsy may be performed. There are also other techniques but five examinations are quite commonly used for patients.

Fig. 1.30 Medio lateral oblique (MLO) view mammogram showing the pectoral muscle, breast, nipple and breast ducts.

- **Breast Cancer Phantom**

As mentioned above, we have various methods for the detection and treatment of breast cancer. Every treatment, however, needs very high accuracy in finding breast cancer. Mammography remains the best method available today to detect breast cancer. There are several reasons for requirements of developing new screening and diagnostic technologies. However they have some limitations. A mammogram may miss some cancers that are present or may find things that are not a cancer. The former case is referred to as "false negative" and the latter case to "false positive". Even if a tumor is detected in its early stage, it is not necessarily guaranteed that woman's life will be saved. Since everyone wishes early discovery of breast cancer even before an apparent symptom appears, intensive development of detecting breast cancer visually using synchrotron radiation is under way all over the world. Various types of breast phantom specimens are in use. The mammography accreditation phantom RMI 156 has been designed to test performance of a mammography by the company call Gammex Radiation Mesurements Inc., Middleton, WI, U.S.A.
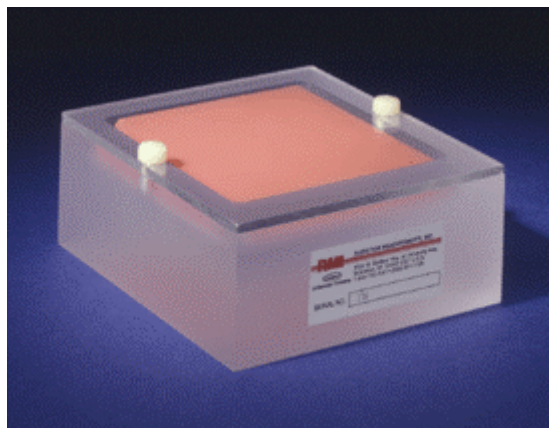
Fig. 1.31   Appearance of the mammographic accredited phantom RMI 156

The Mammographic Accredited Phantom RMI 156 is designed to attenuate the x-ray beam in the same way as a human breast composed of 50% adipose and 50% glandular tissue compressed to a thickness of 4.0 to 4.5 cm. Test objects that represent malignancies or small breast structures are embedded in an insert which is enclosed in an acrylic base. Each piece has a dimension of 20 mm by 20 mm and 6 mm in thickness. All inclusion is embedded in wax.

The system for quantitative evaluation of the images of small structures is similar to those found clinically. Objects within the phantom simulate micro-calcifications, fibrous structure in ducts and tumor-like masses. This RMI 156 has been chosen to determine if our mammography system can detect small structures that are important in the early detection of breast cancer.
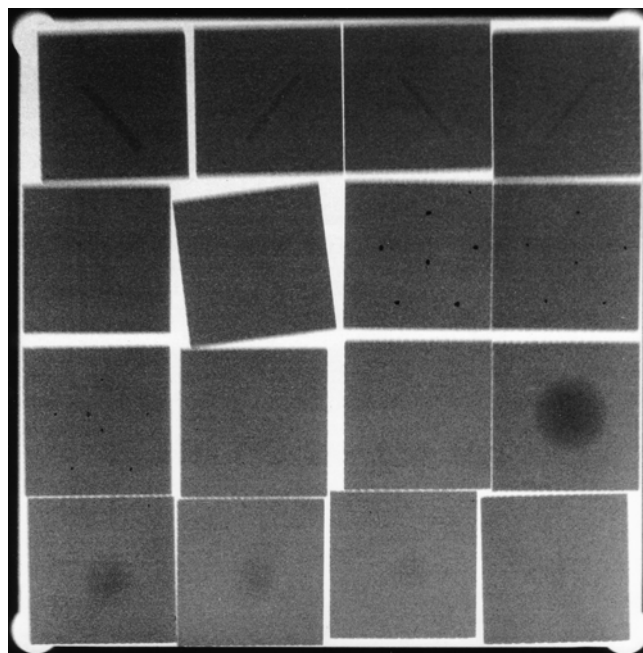
Fig. 1.32   X-ray picture of each piece of RMI 156.

In Fig.1.31, the appearance of mammographic accredited phantom RMI 156 is shown. Sixteen are contained in this square. The components of the phantom specimens are shown in Fig.1.32. In the figure, the x-ray photographic images are illustrated. Each small square indicate the component of RMI 156. What are shown there are as illustrated in the following picture for explanation. Small panel on left hand side illustrates what are contained in each component. The numbers in the figure distinguish small square components in RMI 156. The explanations of the contents of the components are given in the table on the right panel.
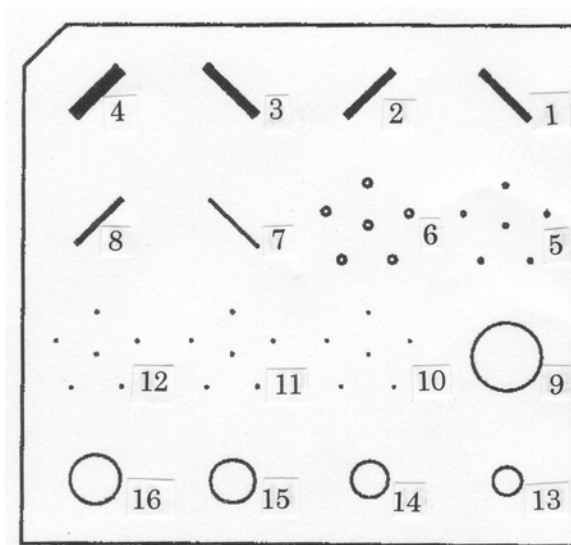
Region Material	
1	0.75 mm nylon fiber
2	0.89 mm nylon fiber
3	1.12 mm nylon fiber
4	1.56 mm nylon fiber
5	0.40 mm simulated micro-calcification
6	0.54 mm simulated micro-calcification
7	0.40 mm nylon fiber
8	0.54 mm nylon fiber
9	2.00 mm thick tumor-like mass
10	0.16 mm simulated micro-calcification
11	0.24 mm simulated micro-calcification
12	0.32 mm simulated micro-calcification
13	0.25 mm thick tumor-like mass
14	0.50 mm thick tumor-like mass
15	0.75 mm thick tumor-like mass
16	1.00 mm thick tumor-like mass

1.4 X-ray Diffraction

The image formation is closely related with the light diffraction. This is particularly so, if we deal with the phase contrast phenomena. In the following section the fundamentals of x-ray diffraction are dealt with as preparatory work.

1.4.1 Geometrical Theory of Diffraction

- Introduction

In this section, let us consider the elementary theory of the diffraction of x-rays by a simple space-lattice. X-rays are scattered by atoms in a crystal as shown below.
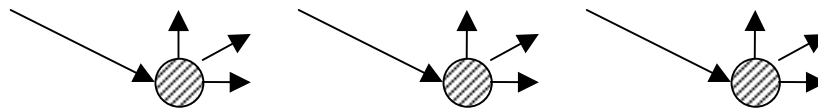
The scattering cross section is small and the intensity of the scattered x-rays is low. Although the intensity is low, we can observe scattered x-rays. The scattering of x-rays by atoms is the origin of the x-ray diffraction. If the scattered x-ray waves have the phase relation that various scattered x-ray waves add constructively, the resulting scattered waves become strong. In case of the reflection of visible light by crystal surface, atoms are considered to be very densely packed forming a continuous medium to react with light, since the wavelength of light is far much longer than the interatomic distance. In case of x-rays their wavelength is shorter than the interatomic spacing. Therefore atoms are taken to be sparsely distributed. Thus, x-rays reflected by one atomic plane is weak. The reflected or scattered x-rays are detectable if those

reflected by many atomic planes are summed up. The summed up x-ray waves interfere with each other. Reflected x-rays are detectable only when the constructive interference occurs. This is the x-ray diffraction by a crystal. The x-ray diffraction phenomenon is treated by the Laue theory. The geometrical consideration of this theory will be given later. First we assume that the primary x-ray beams travel through a crystal with the velocity of light and interaction between the incident and scattered wavelets is neglected. Also the refractive index of the crystal is assumed to be unity. Secondly, we assume that scattered wavelets travel through the crystal without being rescattered at other lattice points. Finally we assume that neither incident nor scattered x-rays are not absorbed by the crystal.
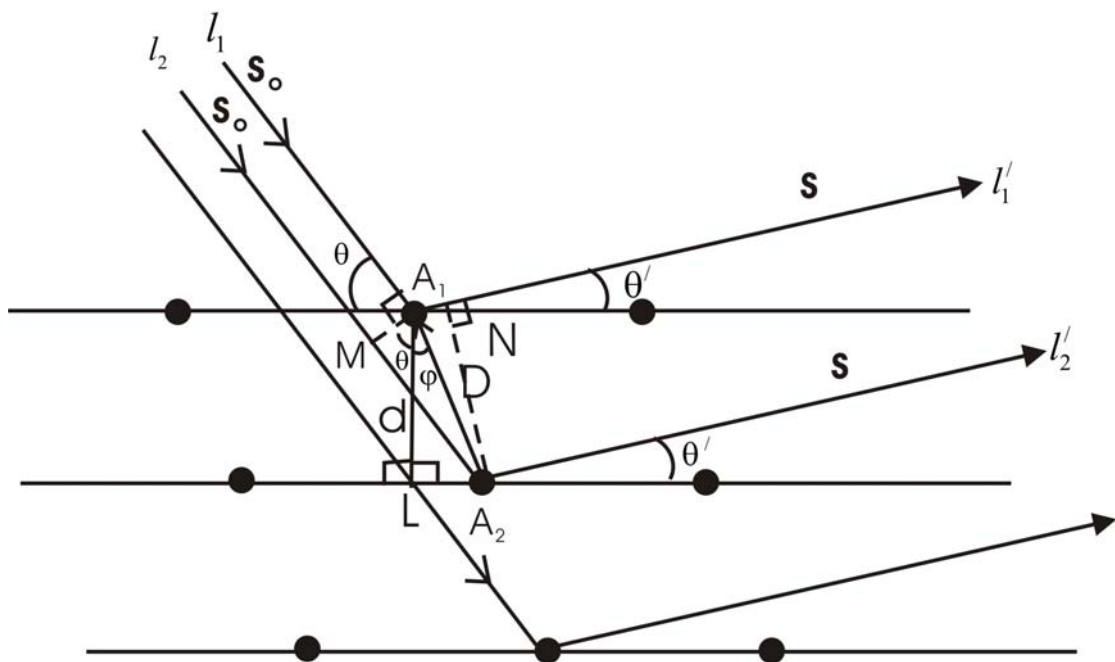
Fig. 1.33   Scattering of x-rays by atoms in a crystal

The relation between the incident x-ray beams and the scattered x-ray beams is illustrated in Fig.1.33. Two x-ray beams, l_1 and l_2, are incident on atoms

located at adjacent lattice points, A_1 and A_2, separated by a distance of D, in a crystal, respectively. Then beams l_1 and l_2 are scattered to beams $l_1^/$ and $l_2^/$, respectively. Let the direction, A_1A_2, makes an angle φ to the normal to the reflection plane. The separation between the adjacent reflection plane is assumed to be equal to d.

The x-ray beams are incident on atoms along the direction, $\mathbf{s_o}$, with an incident glancing angle of θ and scattered toward the direction, $\mathbf{s}$, with a scattered glancing angle of $\theta^/$. Both $\mathbf{s_o}$ and $\mathbf{s}$ are unit vectors. The wavefront of the incident x-rays arriving at A_1 is expressed as A_1M. The wavefront of the scattered x-rays leaving A_2 is expressed as A_2N. Let the lacttice vector $\overrightarrow{A_1A_2}$ be $\mathbf{D}$. The path difference, δ, between two x-ray beams, $l_1l_1^/$ and $l_2l_2^/$ is given as

$$\delta = A_1N - A_2M$$

$$= \mathbf{Ds} - \mathbf{Ds_o}$$

$$= \mathbf{D} (\mathbf{s} - \mathbf{s_o})$$

$$= \mathbf{DS} \qquad (1.27)$$

Here, we put

$$\mathbf{S} = \mathbf{s} - \mathbf{s_o} \qquad (1.28)$$

From Fig.1.33, we obviously see

$$\mathbf{Ds} \quad = \quad A_1N$$

$$= \quad D \cos (\theta^/ + 90° - φ)$$

$$= \quad - D \sin (\theta^/ - φ)$$

$$= \quad -D \sin \theta^/ \cos φ \quad + \quad D \cos \theta^/ \sin φ$$

$$= \quad -d \sin \theta^/ \quad + \quad d \tan φ \cos \theta^/$$

$$\mathbf{Ds_o} \quad = \quad A_2M$$

$$\mathbf{Ds_o} \qquad = \qquad D \sin (\theta + \varphi)$$

$$= \quad D \sin \theta \cos \varphi \quad + \quad D \cos\theta \sin \varphi$$

$$= \quad d \sin \theta \quad + \quad d \tan \varphi \cos \theta$$

Here, we note that D cos φ is equal to d

Therefore, from (1.27) we have

$$\delta \quad = \quad - d (\sin \theta' + \sin \theta) + d \tan \varphi (\cos \theta' - \cos \theta) \qquad (1.29)$$
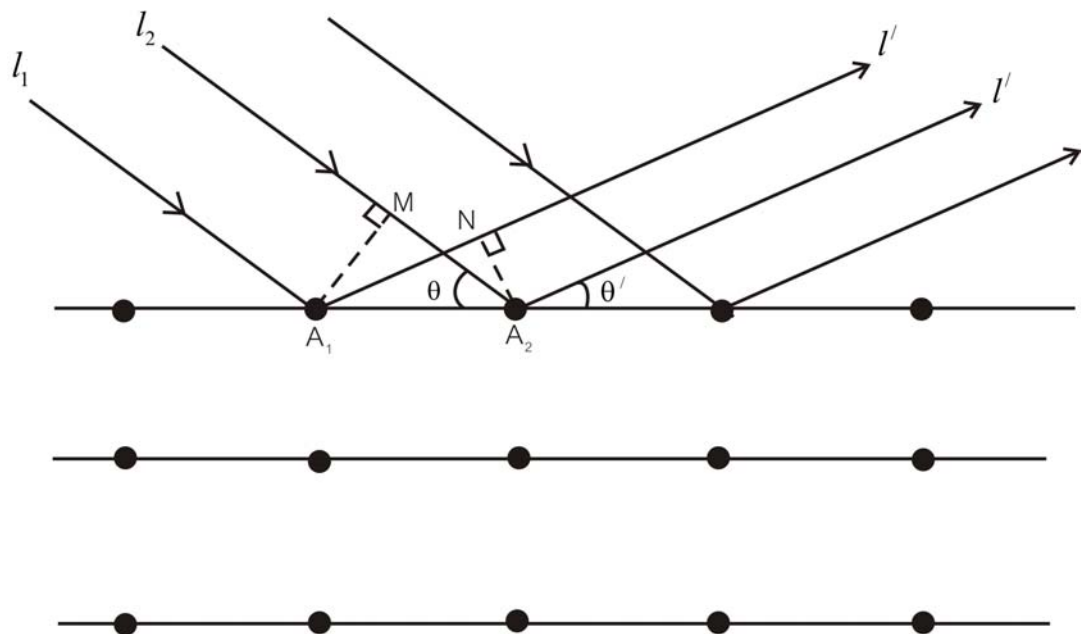
Fig. 1.34   Scattering of x-rays by atoms in a single plane of a crystal.

On the other hand, Fig.1.34 shows that the path difference δ' of two x-ray beams, $l_1 l_1'$ and $l_2 l_2'$, incident on and scattered by atoms, A_1 and A_2, in the reflection plane is given as

$$\delta' \quad = \quad A_1 N - A_2 M$$

$$= \quad D \cos \theta' \quad - \quad D \cos \theta$$

$$\delta' = -D \sin\frac{\theta+\theta'}{2}\sin\frac{\theta-\theta'}{2} \tag{1.30}$$

Here D is the interatomic distance. Obviously $\delta' = 0$ if $\theta' = \theta$. The constructive interference occurs when the path difference equals to an integral multiple of the wavelength. This is the well known equal-angle (speculum) reflection, well known in optics. The rule of speculum reflection of light on a flat plane is referred to as Snell's law. It is analytically proved by solving the electric field strength using the boundary condition at flat plane. On the other hand, if we apply the Huygens principle of the wave propagation to a flat plane, Snell's law is derived. The Huygens principle states that the wavefront is formed by the envelope of the secondary elementary waves whose sources are located on the wavefront. In Fig.1.35, the reflection of a plane wave by a flat plane is shown. In the figure, OO' represents the plane of reflection. P_n (n = 1, …5) represents arbitrarily selected source points of the secondary elementary waves. If there is no plane of reflection, the fronts of the wavelets reach the envelope line made by the fronts of the wavelets, M_n (n = 1, …5). If the plane of the reflection, OO', exists the secondary elementary wavelets travel to points N_n (n = 1, …5). Since the secondary wavelet are spherical waves, the wavefront, OW, formed by N_n is symmetric to wavefront, OW_v, formed by M_n in regard to the OO' plane. Naturally, the glancing angle, θ, of reflected wave is equal to that of the incident wave.

Incident light   Reflected light
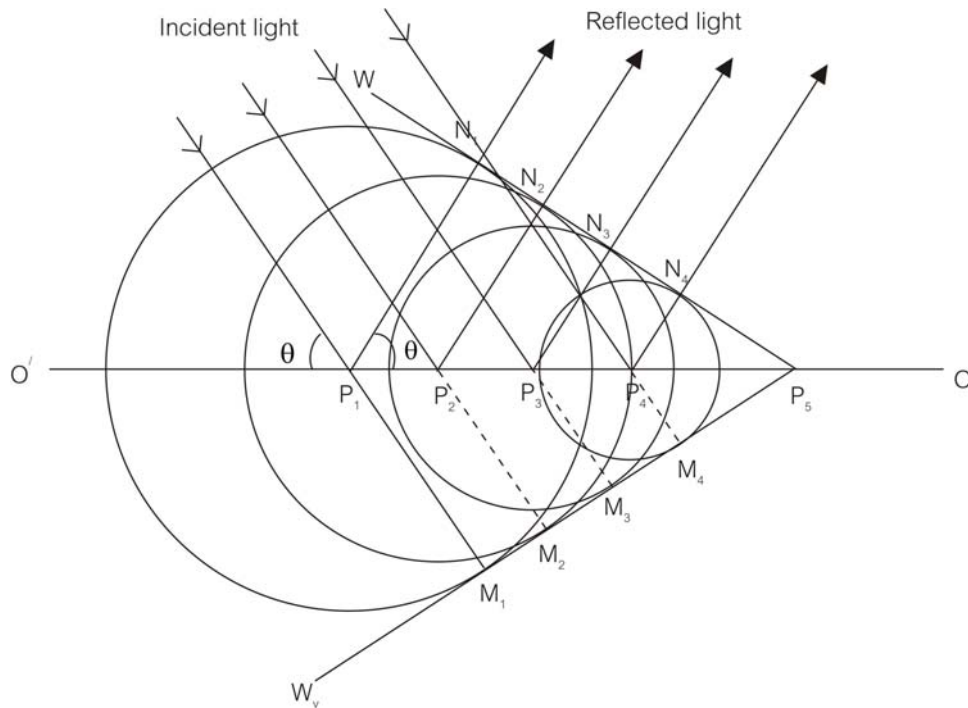
Fig. 1.35 Reflection of light satisfying the Huygens principle. Circles: Wavefronts of secondary wavelets. OO': Plane of reflection. P_n: Sources of the secondary wavelets. N_n: Wavefronts of secondary wavelets. M_n: Supposed wavefronts of secondary wavelets. P_5W: Wavefront of the reflected wave. P_5W_v: Supposed wavefront of the incident wave.

Thus, the constructive interference occurs if the condition $\theta = \theta'$ is fulfilled in (1.30), since δ' in (1.30) is zero in this case. For the case of $\theta = \theta'$ (speculum reflection), we have

$$\delta = -2d \sin \theta \qquad (1.31)$$

The assumption of the continuous reflection plane is not necessarily correct for x-rays whose wavelengths are shorter than the interatomic spacing. However, the electron clouds of adjoining atoms in a crystal overlap each other. Since it is electrons that scatter x-rays, the approximation of continuous reflection plane makes sense in some cases.

This situation is illustrated in Fig.1.36. In the upper panel, the atomic arrangement is shown. In the lower panel, the path difference leading to the relation, (1.31), is illustrated it is quite obvious that the path difference is

$$MP_2 + NP_2$$

and this is equal to the amount given in (1.31).
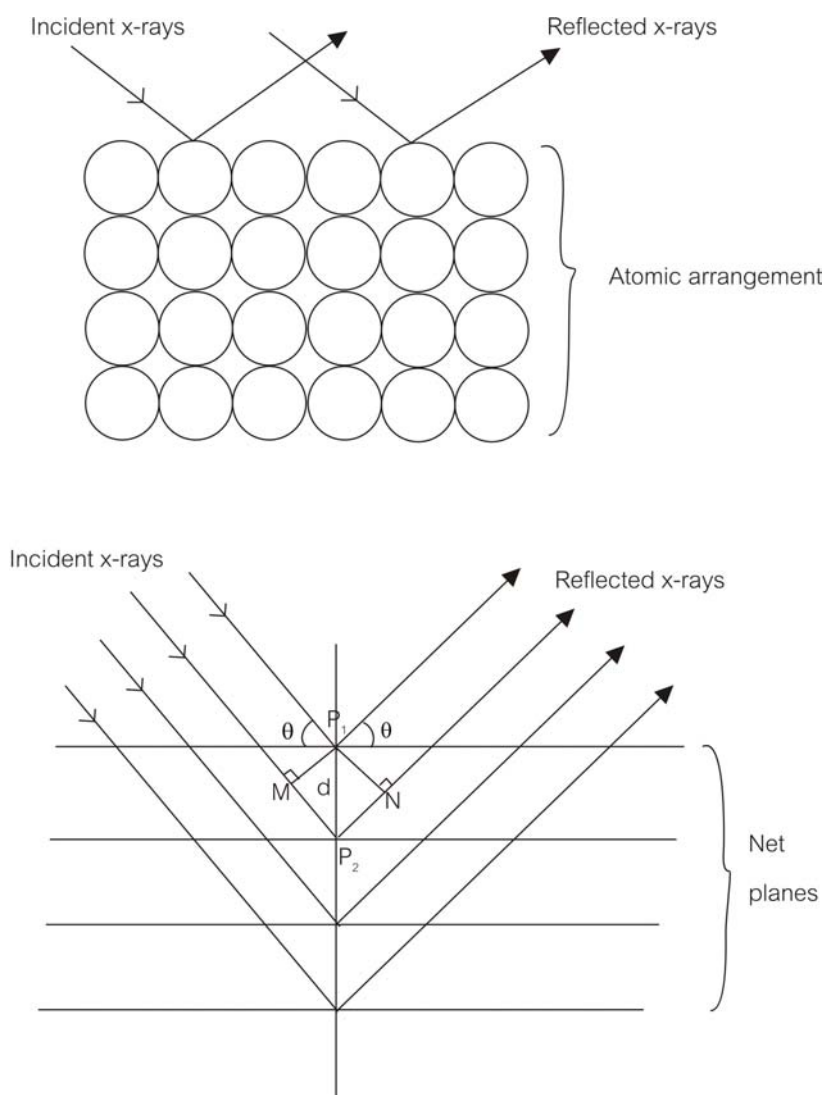
Fig. 1.36   The concept that x-rays are reflected by net planes. Atomic arrangements are taken to be continuous flat planes. P_1, P_2: Points where reflection occurs. P_1M, P_1N: Wavefronts. θ: Glancing angle.

The condition of speculum reflection is the necessary condition for the scatted x-ray enhancement. The intensity of scattered x-rays is still weak because of the law scattering cross section of x-rays. For the real enhancement of the intensity of scattered x-rays to occur, the path difference must be integral multiples of the x-ray wavelength as will be mentioned later. In this case, the constructive interference of x-ray beams occurs in the whole volume of the crystal.
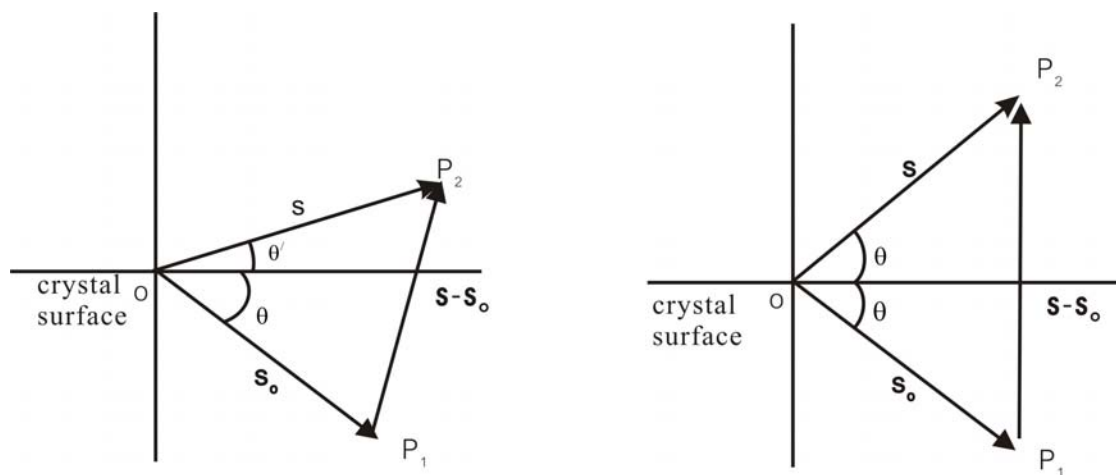
Fig. 1.37   Relation between the directions of incident and scattered x-ray beams.

In Fig.1.37, the relation of the two unit vector $\mathbf{s}$ and $\mathbf{s_0}$ are illustrated. Obviously

$$\mathbf{s} - \mathbf{s_0} \quad = \quad \overrightarrow{OP_2} - \overrightarrow{OP_1} = \overrightarrow{P_2P_1}$$

In case of the speculum reflection, we have

$$|\,\mathbf{s} - \mathbf{s_0}\,| \quad = \quad 2\sin\theta \tag{1.32}$$

As recognized in the drawing on the right panel in Fig.1.37, the condition is fulfilled by the situation described as follows: The crystal surface, i.e. the plane of reflection, is the plane equally dividing the angle made by the incident direction $\mathbf{s_0}$ and the scattered direction $\mathbf{s}$.

Even if the condition of equal angle reflection (speculum reflection) is satisfied, the scattered x-rays are weak as mentioned already. The constructive interference occurs if the phase condition favorable for the constructive interference is satisfied. This is known as the condition that the optical path difference of the adjoining x-ray beams is equal to the integral multiple of the wavelength, as

$$\delta = n\lambda$$

In this case, all adjacent beams is enhanced by the interference. If δ is equal to $n\lambda$, the interference occurs constructively and the diffraction occurs. Here λ is the wavelength of x-rays and n is an integer ($n = 0, \pm 1, \pm 2 \ldots$). From (1.31), the constructive interference occurs if the following condition is satisfied:

$$n\lambda \quad = \quad 2d \sin \theta. \tag{1.33}$$

This is referred to as the Bragg condition. The strong x-ray reflection caused by the fulfillment of the Bragg condition is called the Bragg reflection.

In a crystal, there are many atomic planes. We call these atomic planes the net planes. There are many different net planes oriented in different directions in a crystal. A net plane is specified by a set of integers. Each integer represents the primitive translation numbers. In the orthogonal crystal or the parallelopiped, the set of integers corresponds to the coordinate (x, y, z). Thus the set of the integers represents a vector. The plane normal to this vector is the specified net plane. Let a set of three integers be (k l m). If the spacing between adjacent (k l m) planes is d_{klm}, the Bragg condition given as (1.33) is extended to the three dimensional case.

The examples showing d_{lmn} are illustrated in Fig.1.38. The interatomic distances in the vertical and horizontal directions are assumed to be slightly different. In

the figure, atomic net planes are shown with straight lines connecting lattice points. The spacing between adjoining atomic net planes are indicated as d_{klm} (k, l, m integers). This formula is well-known for the diffraction of x-rays by a crystal lattice and called Bragg's law. Although the rigorous proof of general Bragg's law is complicated, it is understable intuitively using the consideration similar to those made for Figs.1.33 and 1.37. Once the lattice plane is specified, the drawing similar to that given in Figs.1.33 and 1.36 can be drawn immediately. The x-ray diffraction occurs when the Bragg reflection condition is satisfied. Generally, the Bragg condition is written as

$$n\lambda \quad = \quad 2d_{klm} \sin \theta. \qquad (1.34)$$
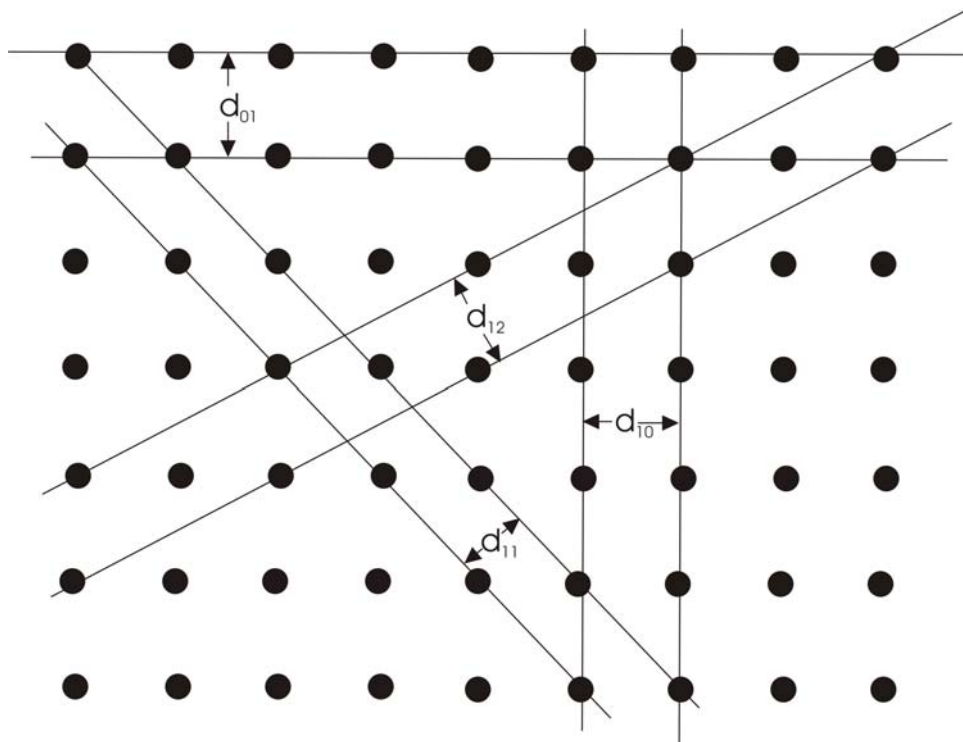
Fig. 1.38 Various atomic net planes in case of a two dimensional fictitious crystal. Dots are lattice points. Lines indicate atomic planes. d_{lm} represents the spacing of the adjacent net planes.

[Debye-Sycherer Powder Diffraction]
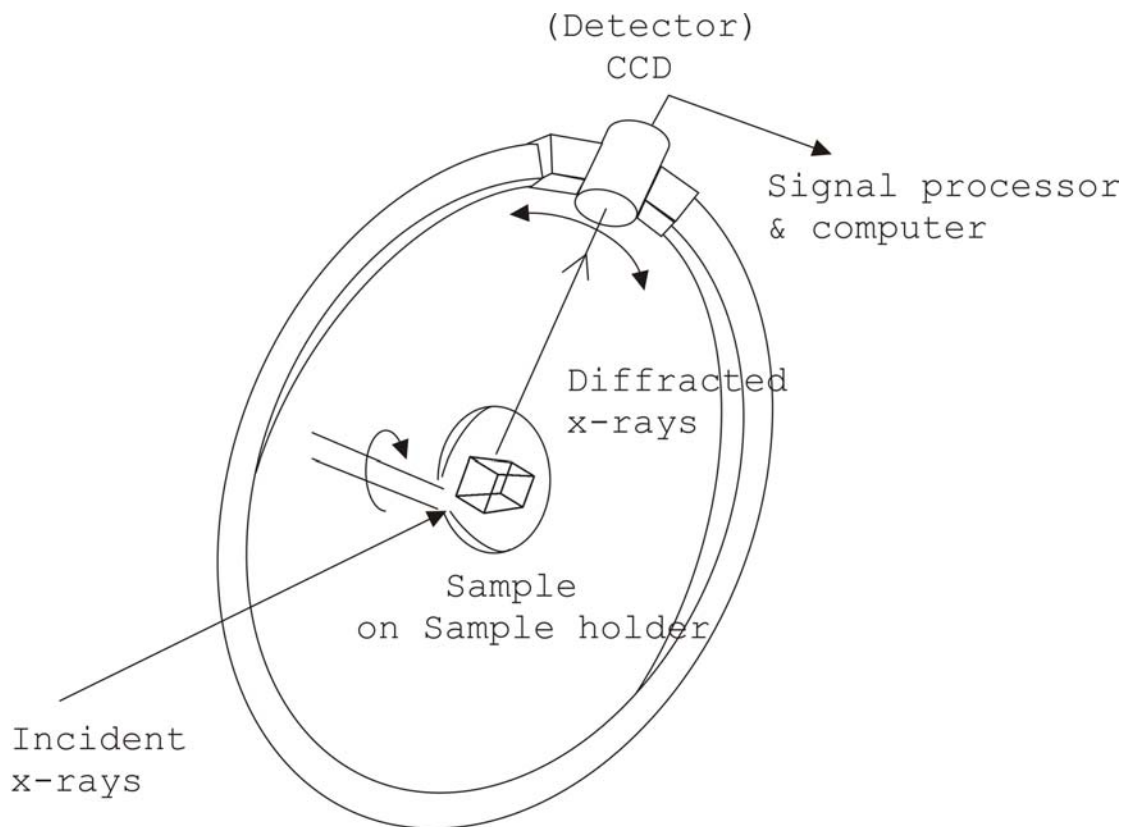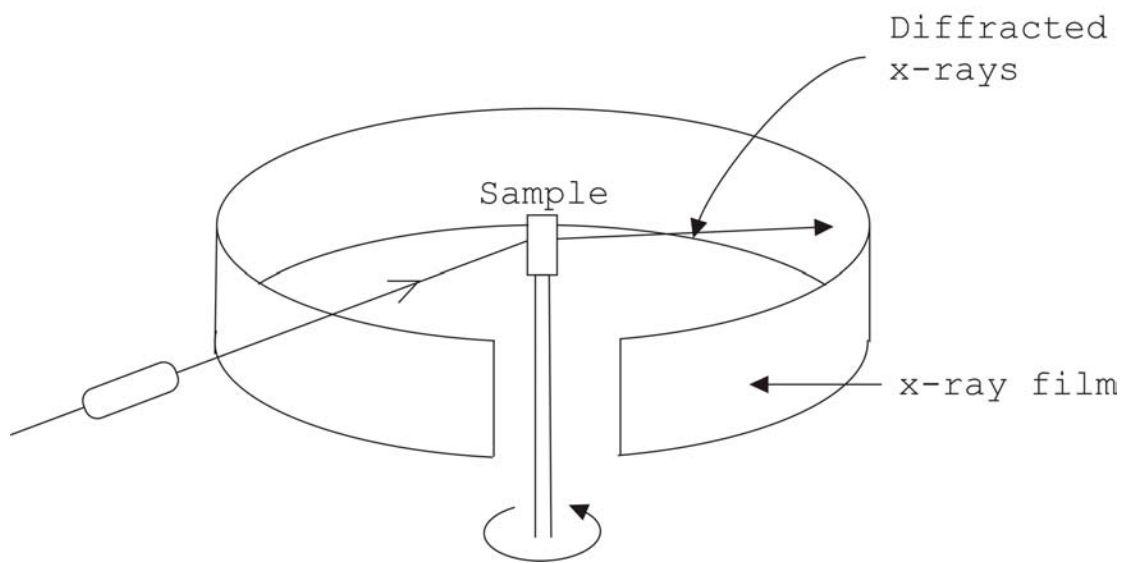
Fig. 1.39 Schematic illustration of x-ray diffractometers. Upper panel: power diffractometer. Lower panel: Crystal diffractometer.

In order to recognize the x-ray diffraction more practically, the concept of the experimental arrangement is illustrated in Fig.1.39. In the lower panel, the concept of the diffractometer for a crystal is shown. In this apparatus, a detector is rotatable around the sample which is also rotatable. Recently, a charge-coupled-device (CCD) is used as a detector. In the diffractometer of this type, the diffraction angle 2θ is changed by rotating the detector, while the intensity of diffracted x-rays is recorded. In the upper panel of Fig.1.39, the principle of the Debye-Scherer diffraction of a power sample is illustrated. The power diffraction is a simple striking example of x-ray diffraction. If a sample is power, small crystal grain composing the power is randomly oriented. For certain values of θ and λ, d_{klm} satisfying the Bragg reflection condition, (1.34), must exist x-rays are diffracted strongly toward this direction. Reflected x-rays satisfying (1.34) proceed along the face of the cone with the axis in the direction of incident x-rays and an apex of 4θ. Thus concentric circle images are procedure on the film.

A sample is made in a form of a rod or powder over a glass rod. The rod is rotated to keep uniformity. The method is referred to the Debye-Scherer method. In this method, the net plane spacing, d_{klm}, are measured. By comparing the measured values with the know values of materials, we can analyze the sample to identify the unknown material contained in the sample.

In case of a crystal diffractometer, the crystal structures are examined. X-ray diffraction from a single crystal occurs to various directions discretely as the Laue theory indicates. Therefore the analyses of the data are complicated. By the use of computer, the data processing can be preformed without taking time. The Laue theory is described later.

[Power diffraction pattern recorded on an x-ray film]
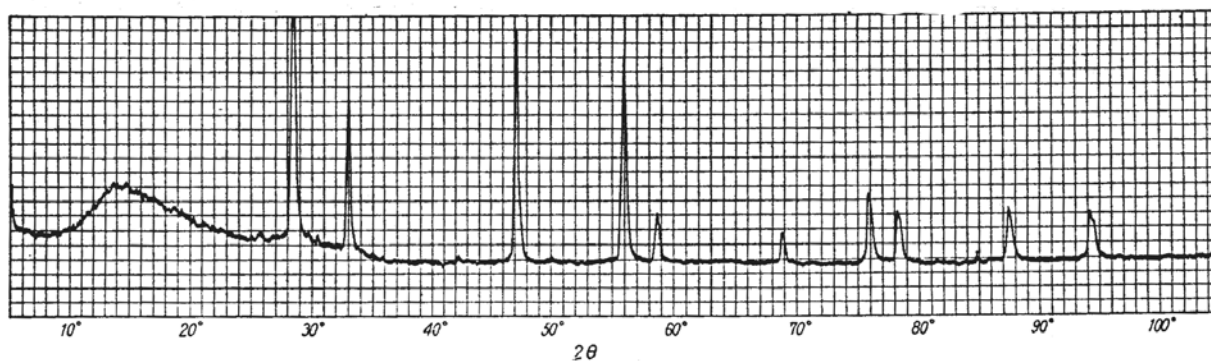
[The intensity distribution of diffracted x-rays from a power sample]

Fig. 1.40 Diffraction patterns of power samples of UO_2. Upper panel: Diffraction pattern recorded on an x-ray film. Lower panel: The intensity distribution of diffracted x-rays detected with a proportional counter. $\lambda = 1.16$ A° (MoKα) is used.

In Figure 1.40, the diffraction patterns of the powder sample of UO_2 are shown. In the upper panel, the Debye-Scherer rings recorded on a film are shown. In the lower panel, the intensity of the diffracted x-rays are shown as a function of 2θ. Each line corresponds to the angle for the spacings between net planes.
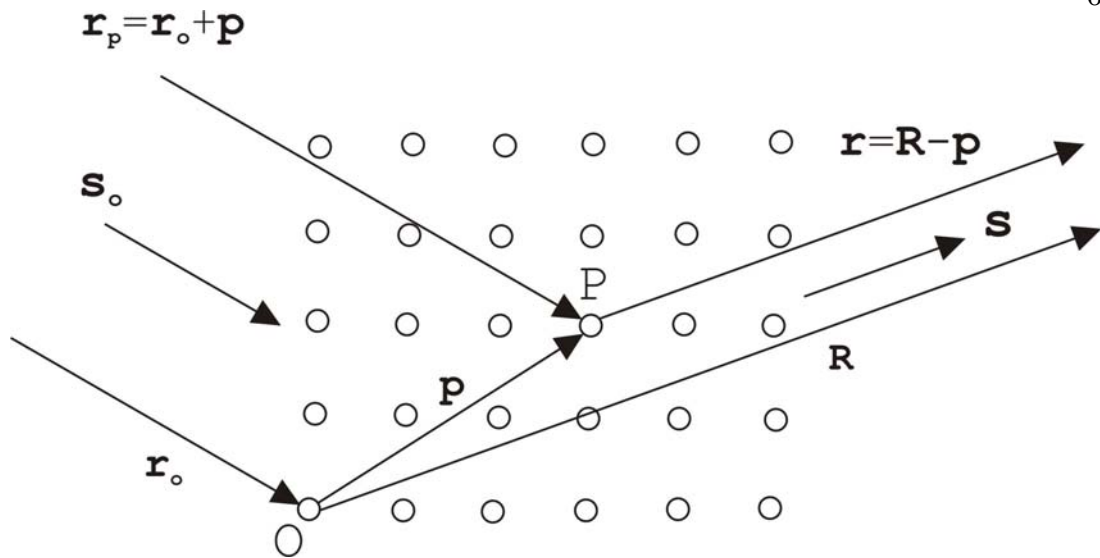
Fig. 1.41 X-ray scattering by atoms in a crystal. X-rays are incident on the crystal toward the $\mathbf{s_o}$ direction and scattered to the $\mathbf{s}$ direction. $|\mathbf{r_o}|$ represents the distance between the source point and an atom, O, in the crystal. $\mathbf{r_o}$ // $\mathbf{s_o}$. Both $\mathbf{s}$ and $\mathbf{s_o}$ are unit vectors. The x-ray detector is located at $\mathbf{r}$ from the scattering atom at P and at $\mathbf{R}$ from the scattering atom at O. $\overrightarrow{OP} = \mathbf{P}$.

In order to understand x-ray diffraction in a more detailed manner, the Laue theory is considered here. The concept of the Laue theory is shown in Fig.1.41. We assume that an x-ray source and a detector are located far away from the crystal. We take the position of an atom at O as the origin of the lattice point. The source point is located at $-\mathbf{r_o}$ from O. Similarly, the detector is located at $\mathbf{R}$ from O. Then we consider the scattering of x-rays by an atom at the lattice site, P. We take the vector, $\overline{OP}$, to be $\mathbf{p}$. We assume that the detector is located at $\mathbf{r}$ from P. Similarly we assume that the source point is located at $\mathbf{r_p}$ from P. Suppose unit vectors indicating the directions of incident and scattered x-rays are $\mathbf{s_o}$ and $\mathbf{s}$, respectively. Obviously we have

$$\left.\begin{array}{l} \mathbf{r_o} \, / \! / \, \mathbf{s_o} \\ \mathbf{R} \, / \! / \, \mathbf{s} \end{array}\right\} \tag{1.35}$$

$$\left.\begin{array}{l} \mathbf{r_p} = \mathbf{r_o} + \mathbf{p} \\ \mathbf{r} \ = \mathbf{R} - \mathbf{p} \end{array}\right\} \tag{1.36}$$

We define the wave vector of x-rays as

$$\left.\begin{array}{l} \mathbf{k} = \dfrac{2\pi}{\lambda}\mathbf{s} \\[2mm] \mathbf{k_o} = \dfrac{2\pi}{\lambda}\mathbf{s_o} \end{array}\right\} \tag{1.37}$$

The field strengths at the detector of x-rays scattered by atoms, O and P, are given respectively as

$$\left.\begin{array}{l} \mathbf{E}(\mathbf{R}) = c\mathbf{E}(O)\dfrac{\exp(i\mathbf{kR})}{R} \\[3mm] \mathbf{E}(\mathbf{r}) = c\mathbf{E}(P)\dfrac{\exp(i\mathbf{kr})}{r} \end{array}\right\} \tag{1.37}$$

Here we use the relation (1.35). C is a constant determined by the scattering cross section. $\mathbf{E}(O)$ and $\mathbf{E}(P)$ are equal to the field strengths of x-rays arriving at O and P, respectively. They are given as

$$\mathbf{E}(O) = \mathbf{E_o}\frac{\exp[i(\mathbf{k_o r_o} - \omega t)}{r_o} \tag{1.38}$$

$$\mathbf{E}(P) = \mathbf{E_o}\frac{\exp[i(\mathbf{k_o r_p} - \omega t)}{\left|\mathbf{r_o} + \mathbf{p}\right|}$$

$$= \frac{\mathbf{E_o}}{r_o}\exp[i\mathbf{k_o}(\mathbf{r_o} + \mathbf{p}) - i\omega t]$$

$$= \mathbf{E}(0)\exp(i\mathbf{k_o p}) \tag{1.39}$$

Here we ignore $\mathbf{p}$ in the denominator. Similarly from (1.37) through (1.39) we have the field strength at $\mathbf{R}$ as

$$\mathbf{E}(\mathbf{R}) = \frac{c\mathbf{E}(0)}{R}\exp(i\mathbf{k}\mathbf{R})$$

$$= \hat{\mathbf{E}}(0)\exp(i\mathbf{k}\mathbf{R}) \tag{1.40}$$

$$\mathbf{E}(\mathbf{r}) = c\mathbf{E}(0)\exp(i\mathbf{k}_\mathbf{o}\mathbf{p})\frac{\exp(i\mathbf{k}_\mathbf{o}\mathbf{r})}{r}$$

$$= \frac{c\mathbf{E}(0)}{R}\exp[i(\mathbf{k}_\mathbf{o}\mathbf{p} + \mathbf{k}(\mathbf{R} - \mathbf{P})]$$

$$= \hat{\mathbf{E}}(0)\exp(i\mathbf{k}\mathbf{R})\cdot\exp[-i(\mathbf{k} - \mathbf{k}_\mathbf{o})\mathbf{p}]$$

$$= \mathbf{E}(\mathbf{R})\exp[-i(\mathbf{k} - \mathbf{k}_\mathbf{o})\mathbf{p}] \qquad (1.41) \quad (\because (1.40))$$

Since there are many lattice points in a crystal, the total field strength of x-rays reaching the detector is the sum of those from all $P^{/}$s. This gives the real strength of the field. We define the lattice points as

$$\mathbf{P}_{lmn} = l\mathbf{a} + m\mathbf{b} + n\mathbf{c} \tag{1.42}$$

Here **a**, **b** and **c** are primitive translation vectors of the lattice and l, m and n are integers. From (1.41), the whole strength is given as

$$\mathbf{E}_{sc} = \sum_{l,m,n}\mathbf{E}(\mathbf{R})\exp[-i(\mathbf{k} - \mathbf{k}_\mathbf{o})\mathbf{P}_{lmn}]$$

$$= \mathbf{E}(\mathbf{R})\sum_{l,m,n}\exp[-i(\mathbf{k} - \mathbf{k}_\mathbf{o})(l\mathbf{a} + m\mathbf{b} + n\mathbf{c})] \tag{1.43}$$

The value of $\mathbf{E}_{sc}$ takes its maximum if the following condition is fulfilled:

$$(\mathbf{k} - \mathbf{k_o})(l\mathbf{a} + m\mathbf{b} + n\mathbf{c}) = 2\pi \times \text{integer} \tag{1.44}$$

We can prove that $\mathbf{E}_{sc} = 0$, if (1.44) is not satisfied. This is understandable, since the value of $\exp(-i(\mathbf{k} - \mathbf{k_o})\,\mathbf{P}_{lmn})$ takes positive and negative values randomly with its absolute value smaller than 1 as l, m and n changes and l, m and n takes values up to very large ones. The condition (1.44) is satisfied if the following conditions are fulfilled:

$$\left.\begin{array}{l} (\mathbf{k} - \mathbf{k_o})\, \mathbf{a} = 2\pi g \\ (\mathbf{k} - \mathbf{k_o})\, \mathbf{b} = 2\pi h \\ (\mathbf{k} - \mathbf{k_o})\, \mathbf{c} = 2\pi j \end{array}\right\}$$

(1.45)

where g, h and j are integers. It is evident that

$$(\mathbf{k} - \mathbf{k_o}) \;=\; \frac{2\pi}{\lambda}(\mathbf{s} - \mathbf{s_o}) = \frac{2\pi}{\lambda}\mathbf{S} \qquad\qquad (1.46)$$

Then (1.45) is written as

$$\left.\begin{array}{l} \mathbf{S}\,\mathbf{a} = g\lambda \\ \mathbf{S}\,\mathbf{b} = h\lambda \\ \mathbf{S}\,\mathbf{c} = j\lambda \end{array}\right\} \qquad\qquad (1.47)$$

The relations, (1.45) and (1.47), are called the Laue equations. Diffraction of x-rays by a crystal toward the directions that satisfy the simultaneous equations (1.45) or (1.47). It is complicated to do this. The solutions give many different directions discretely. Then, we obtain many spots on the film, if it is placed at the position of the detector.

If we use synchrotron x-rays, we can utilize the distinctive nature of synchrotron radiation. We can select various wavelengths at will. Small beam divergence is convenient to produce a narrow parallel beam. The beam intensity is high. Two examples of the diffractometer and the connected optical system for synchrotron radiation is schematically shown in Fig.1.42. The upper panel is the case of small angle scattering and the signal processing system is illustrated. The lower panel shows the mechanical part of the diffractometer. The diffractometer is of the 4 axis type.
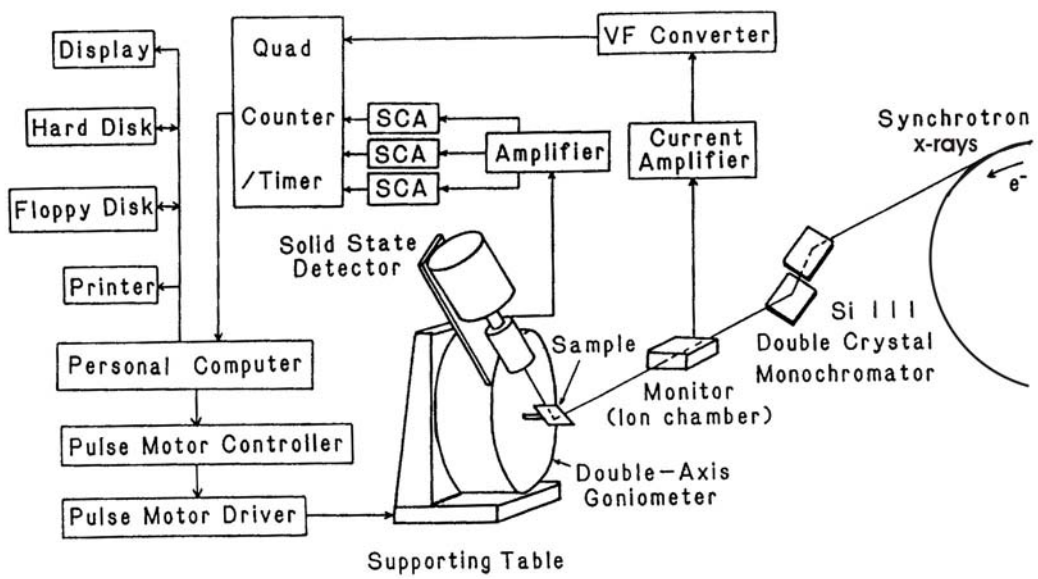
[Synchrotron x-ray diffraction measurement system]
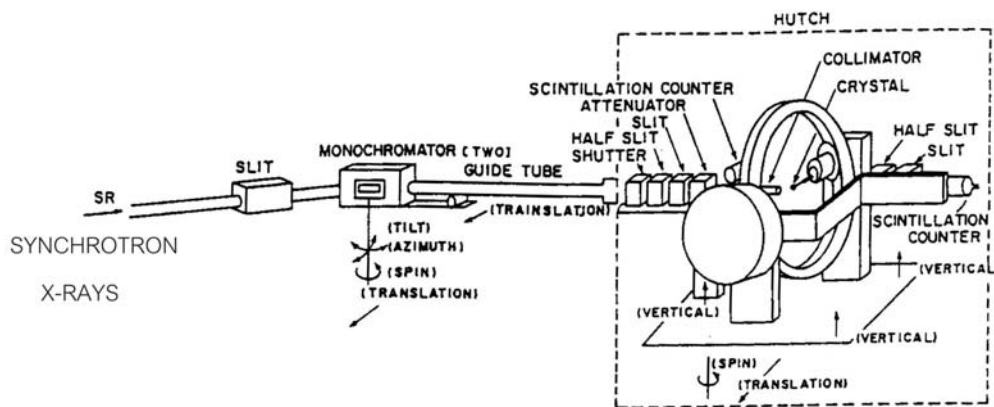
[4 axis diffractometer and the connected optical system in BL-10 of Photon Factory]

Fig. 1.42   Illustration of the concept of x-ray diffractometers for synchrotron x-rays.

- Diffraction Conditions in Terms of Reciprocal Lattice

Diffraction conditions take a very elegant geometrical form when it is expressed in the reciprocal lattice space and not in the real lattice space. Let $\mathbf{a}^*$, $\mathbf{b}^*$, $\mathbf{c}^*$ be the corresponding primitive vectors in the reciprocal lattice. The magnitudes of the primitive vector in the reciprocal lattice in the orthogonal coordinate are

$$|\mathbf{a}^*| = \frac{2\pi}{a}, \ |\mathbf{b}^*| = \frac{2\pi}{b}, \ |\mathbf{c}^*| = \frac{2\pi}{c}, \tag{1.48}$$

In general, the primitive translation vectors in the reciprocal lattice is defined as

$$\left. \begin{array}{l} \mathbf{a}^* = \dfrac{2\pi[\mathbf{b} \times \mathbf{c}]}{\mathbf{a}(\mathbf{b} \times \mathbf{c})} \\[3mm] \mathbf{b}^* = \dfrac{2\pi[\mathbf{c} \times \mathbf{a}]}{\mathbf{b}(\mathbf{c} \times \mathbf{a})} \\[3mm] \mathbf{c}^* = \dfrac{2\pi[\mathbf{a} \times \mathbf{b}]}{\mathbf{c}(\mathbf{a} \times \mathbf{b})} \end{array} \right\} \tag{1.49}$$

The factor, 2π, arises from the mathematical convenience as we have seen in the case of the wave vectors. It is obvious in the orthogonal coordinate that the following relations hold:

$$\left. \begin{array}{l} \mathbf{a} \ // \ \mathbf{b} \times \mathbf{c} \\ \mathbf{b} \ // \ \mathbf{c} \times \mathbf{a} \\ \mathbf{c} \ // \ \mathbf{a} \times \mathbf{b} \end{array} \right\} \tag{1.50}$$

Therefore the following relation holds:

$$\mathbf{a}^*\mathbf{b} = \mathbf{a}^*\mathbf{c} = \mathbf{b}^*\mathbf{a} = \mathbf{b}^*\mathbf{c} = \mathbf{c}^*\mathbf{a} = \mathbf{c}^*\mathbf{b} = 0 \tag{1.51}$$

Also
$$\mathbf{a}^*\mathbf{a} = \mathbf{b}^*\mathbf{b} = \mathbf{c}^*\mathbf{c} = 2\pi \tag{1.52}$$

Then $\mathbf{a}^*$ is perpendicular $\mathbf{b}$ and $\mathbf{c}$, $\mathbf{b}^*$ to both $\mathbf{a}$ and $\mathbf{c}$ and $\mathbf{c}^*$ to both $\mathbf{a}$ and $\mathbf{b}$

The x-ray diffraction problem is to find the direction of diffracted x-rays for a given incident x-ray beam direction. The diffraction is governed by the Laue equations.

This is to find **k** satisfying (1.45) for a given **k₀**. This is equivalent to find

s + **s₀** satisfying equation (1.47). We use the reciprocal latitice to solve (1.45) or

(1.47).

First we see the solutions of (1.45) are given as

$$(\mathbf{k} - \mathbf{k_o}) = 2\pi \left(\frac{g}{a} \cdot \frac{\mathbf{a}}{a} + \frac{h}{b} \cdot \frac{\mathbf{b}}{b} + \frac{j}{c} \cdot \frac{\mathbf{c}}{c} \right) \tag{1.53}$$

if **a**, **b** and **c** are orthogonal to each other. This is evident, for instance, from

$$(\mathbf{k} - \mathbf{k_o})\mathbf{a} = 2\pi \left(\frac{g}{a} \cdot \frac{a^2}{a} \right) = 2\pi g$$

This is the first equation of (1.45)

In order to solve the Laue equations, we put

$$\mathbf{k} - \mathbf{k_o} = g\mathbf{x} + h\mathbf{y} + j\mathbf{z} \tag{1.54}$$

(1.54) is the solution of (1.45), if the following conditions are satisfied:

$$\left. \begin{array}{lll} \mathbf{xa} = 2\pi, & \mathbf{ya} = 0, & \mathbf{za} = 0 \\ \mathbf{xb} = 0, & \mathbf{yb} = 2\pi, & \mathbf{zb} = 0 \\ \mathbf{xc} = 0, & \mathbf{yc} = 0, & \mathbf{zc} = 2\pi \end{array} \right\} \tag{1.55}$$

If we compare (1.55) with (1.51) and (1.52), we find

$$\left. \begin{array}{l} \mathbf{x} = \mathbf{a}^* \\ \mathbf{y} = \mathbf{b}^* \\ \mathbf{z} = \mathbf{c}^* \end{array} \right\} \tag{1.56}$$

Thus we find that the solutions to the Laue equations are given by the use of the

primitive translation vectors in the reciprocal lattice.

Here we define the reciprocal lattice vector, **G**, as

$$\mathbf{G_{ghj}} = g\mathbf{a}^* + h\mathbf{b}^* + j\mathbf{c}^* \tag{1.57}$$

with g, h and j being integers.

Using (1.42), (1.51), (1.52) and (1.57), we see

$$\mathbf{G_{ghj}} \ \mathbf{P_{lmn}} = (g\mathbf{a}^* + h\mathbf{b}^* + j\mathbf{c}^*) \ (l\mathbf{a} + m\mathbf{b} + n\mathbf{c})$$

$$= 2\pi \ (gl + hm + jn)$$

$$= 2\pi \times \text{integer} \qquad (1.58)$$

This is what (1.44) requires, if $\mathbf{k} - \mathbf{k_o} = \mathbf{G}$.

Thus, we have

$$\exp(i \ \mathbf{G_{ghj}} \ \mathbf{P_{lmn}}) = 1 \qquad (1.59)$$

In the discussion made above, we find the solutions of the Laue equations as

$$\mathbf{k} - \mathbf{k_o} = \mathbf{G} \qquad (1.60)$$

It follows that

$$\mathbf{k_o^2} = \mathbf{k^2} - 2\mathbf{kG} + \mathbf{G^2}$$

Since $\mathbf{k^2} = \mathbf{k_o^2} = \left(\dfrac{2\pi}{\lambda}\right)^2$, we have

$$- 2\mathbf{k} \ \mathbf{G} + \mathbf{G^2} \ = \ 0 \qquad (1.61)$$

Then we have

$$+ 2k \ G \cos \varphi \ = \ G^2$$

$$\therefore \ 2k \cos \varphi \ = \ G \qquad (1.62)$$

From Fig.1.37, we find

$$k \cos \varphi \ = \ k \sin \theta$$

Then we have, from (1.62)

$$2k \sin\theta \ = \ G \qquad (1.63)$$

From the definition of $\mathbf{G}$, (1.57), we may put G is equal to $2\pi/d_{ghj}$. Then, from (1.63), we have

$$2 \cdot \frac{2\pi}{\lambda} \sin\theta = \frac{2\pi}{d_{ghj}}$$

$$\therefore 2d_{ghj} \sin\theta = \lambda \qquad\qquad (1.64)$$

This is equivalent to the Bragg condition.
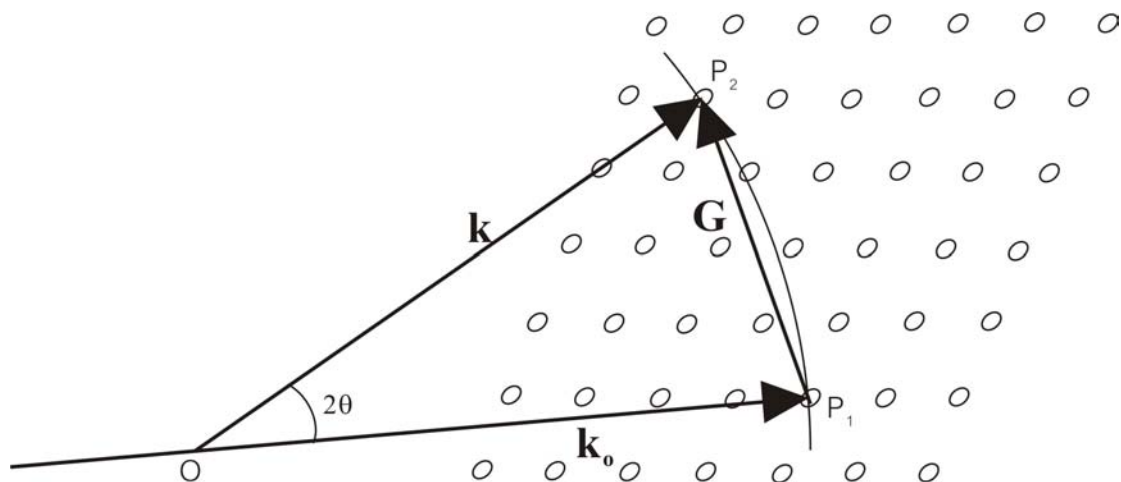
Fig. 1.43 Finding the wave vector of diffracted x-rays by the use of the reciprocal lattice and Ewald's sphere. O: Center of Ewald's sphere. $\mathbf{k_o}$: Wave vector of incident x-rays. $\mathbf{k}$: Wave vector of diffracted x-rays. $\mathbf{G}$: A reciprocal lattice vector. (see text)

Let us try to find the solution of the Laue equations using the reciprocal lattice. This is possible because the solutions, (1.60), contain the reciprocal lattice vector, $\mathbf{G}$. Note that the coordinate system of reciprocal lattice is the same as that of the real space. The primitive translation vectors are defined in the coordinate system in the real space. For instance, $\mathbf{a}$ is given as

$$\mathbf{a} = \alpha\mathbf{x} + \beta\mathbf{y} + \gamma\mathbf{z}$$

Here (x, y, z) is the coordinate in the real space. The corresponding primitive translation

vector, $\mathbf{a}^*$, in the reciprocal lattice space is also defined as

$$\mathbf{a}^* = \alpha^* \mathbf{x} + \beta^* \mathbf{y} + \gamma^* \mathbf{z}$$

That can put this is obvious from (1.60). The wave vectors of x-rays are defined in the coordinate system in the real space. Therefore, the reciprocal lattice vector, $\mathbf{G}$, must be defined in the same coordinate system, so that (1.60) holds.

The method to find $\mathbf{k}$ satisfying (1.60) for a given wave vector, $\mathbf{k_0}$, of incident x-rays is illustrated in Fig.1.41. First, we set up the wave vector, $\mathbf{k_0}$, so that it terminates at a lattice site, P_1, of the reciprocal lattice space. This procedure is equivalent to setting up of the direction of the incident x-ray beam. Then, we draw a sphere of radius equal to $\mathbf{k_0} = \dfrac{2\pi}{\lambda}$ with its center, O, at the origin of vector, $\mathbf{k_0}$. As a next step, find the lattice site that intersects the sphere. Call this site P_2. Obviously $\overrightarrow{P_1 P_2}$ is equal to a reciprocal lattice, $\mathbf{G}$. The vector, $\overrightarrow{OP_2}$, is equal to the wave vector, $\mathbf{k}$, of diffracted x-rays. Thus our goal to find $\mathbf{k}$ is achieved. The angle between $\mathbf{k_0}$ and $\mathbf{k}$ is equal to the diffraction angle, 2θ. The sphere we have drawn is called the Ewald sphere.

1.4.2 Qualitative aspects of the theories of x-ray diffraction

In the present thesis work, the x-ray imaging is treated. Imaging of x-rays is closely related with x-ray diffraction phenomena. In the refraction imaging using synchrotron radiation, the crystal monochromators and analyzer crystals play a crucial role. Thus the understanding of the x-ray diffraction is essential. In the proceeding section, x-ray diffraction phenomena are considered on the basis of Bragg diffraction condition. In the derivation of the Bragg condition, the assumption is made that x-rays are diffracted strongly toward the direction in which x-ray beams scattered by atoms in a solid

interfere constructively with each other. However the scattering and interference process should be treated more rigorously. This includes the problem of x-ray generation at an atomic site must be described by the electromagnetic field theory and quantum mechanics.

There are two kinds of theories: One is called the kinematic theory and the other is called the dynamical theory.

- Kinematic Theory

X-ray diffraction phenomena are used practically to clarify the atomic structure of condensed matter. If we limit our discussion only to a crystal, we have two types of the atomic structure. One is the structure inside the unit cell. The other is the arrangement the unit cells. The analysis of the structure inside the unit cell is nothing but the crystal structure analysis. The analysis of the unit cell arrangement is the estimation of the decided crystal structure. In the analysis of the structure inside the unit cell, the Bragg reflection condition plays an important role. In the estimation of the unit cell arrangement, the diffuse scattering and the small angle scattering are taken into account in addition to the Bragg reflection. The theory to treat the analyses mentioned above is the kinematical theory.

First, we deal with the elastic scattering. In principle, we can obtain the scattered x-ray waves by solving the Maxwell equations. However, the secondary light wave coming out of the secondary sources such as scatterers is more conveniently expressed as

$$\mathbf{D}(\mathbf{r}) = \mathbf{D}_o(\mathbf{r}) - \frac{1}{4\pi} \int G(\mathbf{r} - \mathbf{r}^/) curl\,curl\,\chi(\mathbf{r}^/)\mathbf{D}(\mathbf{r}^/)dV \qquad (1.65)$$

$$G(\mathbf{r} - \mathbf{r}^/) = [\exp(i\mathbf{k}|\mathbf{r} - \mathbf{r}^/|]/|\mathbf{r} - \mathbf{r}^/| \qquad (1.66)$$

Here **D(r)** is the electric displacement vector of the scattered wave, **D₀(r)** is the electric displacement vector of the incident wave, and $\chi(\mathbf{r})$ is the polarizability of the crystal. $G(\mathbf{r}-\mathbf{r}')$ is referred to as the Green function. Equation (1.65) is well-known formula of the amplitude of scattered wave or the intensity of the scattered particle. Usually, we assume that the incident wave is a plane wave as

$$\mathbf{D}(\mathbf{r}) = \hat{\mathbf{D}}_o(\mathbf{r})\exp i(\mathbf{kr} - \omega t) \tag{1.67}$$

or
$$\mathbf{E}(\mathbf{r}) = \hat{\mathbf{E}}_o(\mathbf{r})\exp i(\mathbf{kr} - \omega t) \tag{1.68}$$

The second term of (1.65) presents the scattered wave part. In the kinematic theory of x-ray diffraction, we adopt the Born approximation, where we replace **D(r′)** in the integrand of (1.65) with **D₀(r′)**. At the point, **R**, far away from the scattering center, equation (1.65) and (1.66) give the electromagnetic fields as

$$
\left.
\begin{aligned}
\mathbf{E}_s(\mathbf{R}) &= r_c[\mathbf{R}\times(\mathbf{R}\times\mathbf{E}_o)]F(\hat{\mathbf{k}})\frac{\exp(ik\mathbf{R})}{R} \\
\mathbf{H}_s(\mathbf{R}) &= r_c[\mathbf{E}_o\times\mathbf{R}]F(\hat{\mathbf{k}})\frac{\exp(ik\mathbf{R})}{R}
\end{aligned}
\right\} \tag{1.69}
$$

Here, r_c is the classical electron radius. $F(\hat{\mathbf{k}})$ is given by

$$F(\hat{\mathbf{k}}) = \int G(\mathbf{r},\omega)\exp(-i\hat{\mathbf{k}}\mathbf{r})dV \tag{1.70}$$

$$\hat{\mathbf{k}} = \mathbf{k}_s - \mathbf{k}_o \tag{1.71}$$

$\mathbf{k}_s$ is the wave vector toward the direction of **R**. $G(\mathbf{r},\omega)$ is the distribution of electrons given by

$$G(\mathbf{r},\omega) = \sum_l N_l(\mathbf{r})g_l(\mathbf{r}) \tag{1.72}$$

N_l is the number of electrons in l^{th} atom and g_l is equal to the resonance factor. Equation (1.70) indicates that F(**k**) is the Fourier transform of G(**r**,ω). Equation (1.69) indicates

that the field strength at a point far way from the scatterer is determined by the amplitude F(**k**), and that F(**k**) is given by (1.70) arising from the electron distribution, (1.72). This is the most important conclusion of the kinematic theory.

In what follows, some important items are described. One is the scattering cross section. The differential cross section, $\sigma(\Omega)$, presents the probability of x-rays to be scattered into the solid angle, Ω, in the direction with the polar angle θ from the direction of incident. The differencial cross section is given by

$$\left.\begin{aligned}\sigma(\Omega) &= C\left|F^2\right| \\ C &= \frac{1}{2}(1+\cos 2\theta)\end{aligned}\right\} \tag{1.73}$$

C is referred to as the polarization factor.

(1) Thomson scattering

When high energy radiation is incident on atoms, electrons are forced to oscillate with the same frequency as that of the incident radiation. By this electronic oscillation, radiation with the same frequency as that of the incident radiation is emitted. This is ordinary x-ray scattering. This type of scattering is referred to the Thomson scattering, which is contrasted to the Compton scattering. This Compton scattering is the inelastic scattering in which a small fraction of x-ray photon energy is given to an electron and frequency of scattered x-rays is slightly different from that of incident x-rays. In the case of Thomson scattering

$$G(\mathbf{r},\omega) = \delta(\mathbf{r})$$

$$\left.\begin{aligned}\sigma(\Omega) &= C\left|r_c^2\right| \\ \sigma &= \frac{8}{3}\pi r_c^2\end{aligned}\right\} \tag{1.74}$$

$$r_c = \frac{e^2}{mc^2} = 2.8178 \times 10^{-13}\, cm \quad \text{(classical radius of electron)}$$

(1.75)

(2) Atomic scattering factor

The atomic scattering factor is given by

$$\left.\begin{array}{l} f(\mathbf{k}) = f_o + f' + if'' \\ f_o(\mathbf{k}) = \int \rho(\mathbf{r})\exp(-i\mathbf{kr})dV \end{array}\right\}$$

(1.76)

Here, $\rho(\mathbf{r})$ is the distribution of the electron cloud of an atom. The terms, f' and f'' are those of the anomalous scattering. f_o can be found in a published table.

(3) Crystal structure factor

The crystal structure factor is given by

$$F(\mathbf{k}) = \sum_i f_i(\mathbf{k})\exp(-i\mathbf{kr})$$

(1.77)

Here $f_i(\mathbf{k})$ is the scattering factor of the i-th atom in the unit cell. If we deal with the Bragg reflection, $\mathbf{k}$ can be replaced by a reciprocal lattice vector $\mathbf{G}(l, m, n)$.

(4) Perfect crystal with a finite size

Suppose an atom on a lattice site at $\mathbf{r}_n$ in a real crystal lattice scatters x-rays with an amplitude of $\exp(-i\mathbf{kr})$, the amplitude of x-rays from the whole crystal is given by

$$S(\mathbf{k}) = \sum_n \exp(-i\mathbf{kr}_n)$$

(1.78)

This is called the form factor. It is given as the lattice sum as (1.78). $S(\mathbf{k})$ has the translational symmetry in the reciprocal lattice, as

$$S(\mathbf{k}) = S(\mathbf{k} + \mathbf{G})$$

If the vector $\mathbf{q}$ defined as

$$\mathbf{q} = \mathbf{k} - \mathbf{G}$$

is very small, S(**k**) is given by

$$S(\mathbf{k}) = \frac{1}{V} \int \exp(-i\mathbf{q}\mathbf{r}) dV$$

V is the crystal volume. The sharp Bragg reflection is expected to occur at **q** ~0. The divergence of diffracted x-rays is determined by the shape of the crystal.

- Dynamical Theory

The dynamical theory deals with the diffraction with multiple scattering being taken into account. Mathematically, the purpose of this theoretical treatment is to solve (1.65). Since we take the multiple scattering into account, the mathematical treatment is quite complicated as compared to the kinematical theory. The dynamical theory is used for the estimation of the unit cell structure. We do not treat the dynamical theory in this thesis.   We only use the results of the dynamical theory in the next chapter. There, we use the theory in the treatment of the dark filed imaging.

1.5 Purpose of the Study

The purposes of this thesis work are summarized as follows:

1.)   X-ray optics which is suitable to make imaging experiments at synchrotron radiation beamlines are designed and built.

2.)   X-ray images are obtained using novel dark filed imaging technique.

3.)   Visual identification of ivory, tusk, horn and tooth is made.

4.)   Visual test of breast cancer phantom specimens is carried out.

5.)   The results are compared with those obtained by other technique.

Chapter II

Experimental

2.1 Experimental Apparatus

Experiments were carried out at the beam line, BL14B, of the Photon Factory of the High Energy Accelerator Research Organization (KEK) and the beam line BL20B at SPring-8. Synchrotron radiation available in those two beam lines was used for experiments. In what follows, the optical structures of the two beam lines are described.

2.1.1 BL 14B of Photon Factory (PF)

Figure 2.1 shows the schematic illustration of the layout of the optical system of beam line, BL14 of the Photon Factory storage ring. In the upper panel, the part extending downstream of the source point is shown. The area located within about 20 m from the source point is illustrated there. The light source is a vertical wiggler. The wiggler is located upstream along the electron beam and is shown in the figure on the left end. The locations of two monochromators for BL14A and BL14B are also illustrated in the upper panel. The distance toward downstream from the source point is indicated at lower panel of the figure. As is obvious in the figure, the drawings shown in Fig. 2.1 are only qualitative and incorrect quantitatively. Also, detailed components which are really necessary to compose the beam line are omitted for the sake of the simplicity of the explanation.

Synchrotron radiation generated in the wiggler proceeds downstream along the electron orbit in the straight section of the storage ring. This radiation proceeds straight and comes out of the storage ring at the bending section, B14. The electron orbit is bent there and proceeds toward the following bending section, B15. In the straight sections between adjacent bending sections quadrupole magnets for focusing the electron beam is installed. Sextupole magnets and octupole magnets to correct the electron trajectory are also located. The locations of quadrupole magnets are indicated by small rectangles in the upper panel of Fig. 2.1. The wiggler is installed in the long straight section between the bending sections B13 and B14.
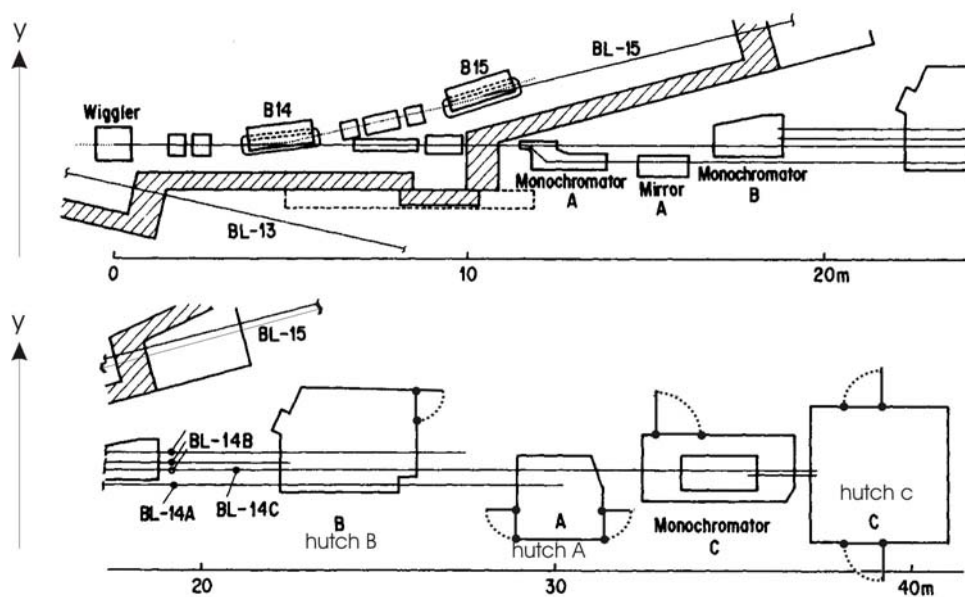
Fig. 2.1 The schematic illustration of the layout of hutches of BL14 of the PF ring.

The beam line outside of the radiation shield wall of the storage ring is shown in both upper and lower panel. In the upper panel, a simplified feature of the front end part is also shown. The figure is just qualitative. It is also for showing the layout of monochromators. More realistic example of the front end part is presented in

Fig. 2.2. This part is mostly devoted for the control of the beam size and pressure in the vacuum chamber.

Usually x-rays are split into a few beams and the slit beam travel toward almost the same direction until a beam terminates at a hutch where an experimental station is located. In the lower panel, the locations of hutches in BL14 are shown. In using synchrotron radiation x-rays, they pass through air in many cases. This is particularly so in the experimental station. Therefore it is dangerous for a person carrying out experiments if the person exposes its body or hands to the x-ray beam. Thus, the experimental instruments are installed in a hutch and the person cannot approach the instruments while x-ray beam is there. If the person opens the door without closing the beam shutter, the storage ring stops operation automatically. In this way, the layout of the hutches indicates the layout of the experimental stations. The drawing in Fig. 2.1 is more expanded toward the y direction.
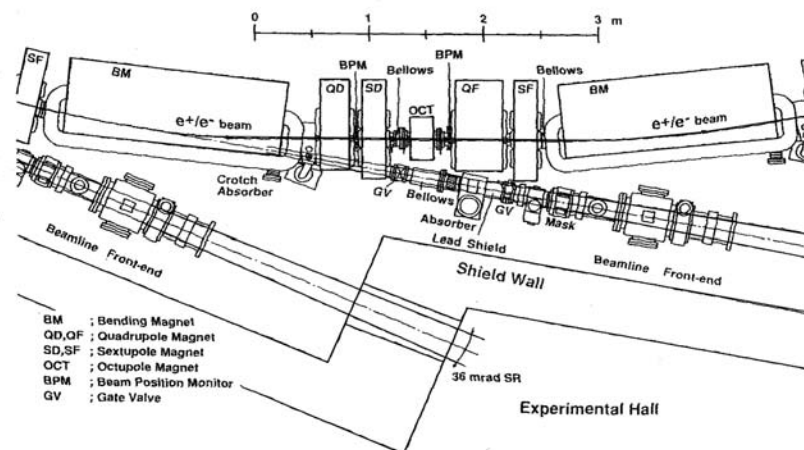
Fig. 2.2 The front end part of a beam line and the accelerator component located nearby.

More detailed drawings of monochromators are presented in Figs. 2.3 and 2.4. They are used in BL14A and BL14B. Synchrotron radiation is monochromatized with two parallel crystals. By the Bragg reflection on the first mirror monochromatic x-rays are taken out. By the Bragg reflection by the second crystal, the monochromatized beam is reflected parallel to the incident white light beam. Monochromatization in this layout of crystals is possible owing to the facts that synchrotron radiation has beam with very low divergence and the reflecting crystals are quite near to a perfect crystal.
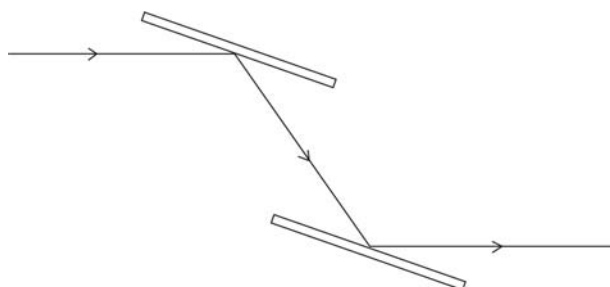
In the monochromator shown in Fig. 2.3, the first crystal is rotated around the fixed rotation center. Rotation is made by a sine bar whose end portion is movable along the y direction. The second mirror can be moved along the x direction. As it moves along the x direction, it rotates so that monochromatized x-rays are reflected toward the x direction (the A direction). A part of the incident beam does not touch the first mirror and proceeds straight toward the B/C monochromator direction.

In the monochromator shown in Fig. 2.4, the first mirror moves along the x direction. The crystal can be rotated to the arbitrary angle at any translational positions. The second crystal can be moved along the y direction. It can be rotated. By the combination of the motions of the first and second crystals, two monochromatized x-ray beams are sent to two different experimental stages in the B hutch. In the figure, beams parts are designated as B, and B_2. A part of the incident white x-rays do not touch the crystals and proceeds straight toward the C monochromator.
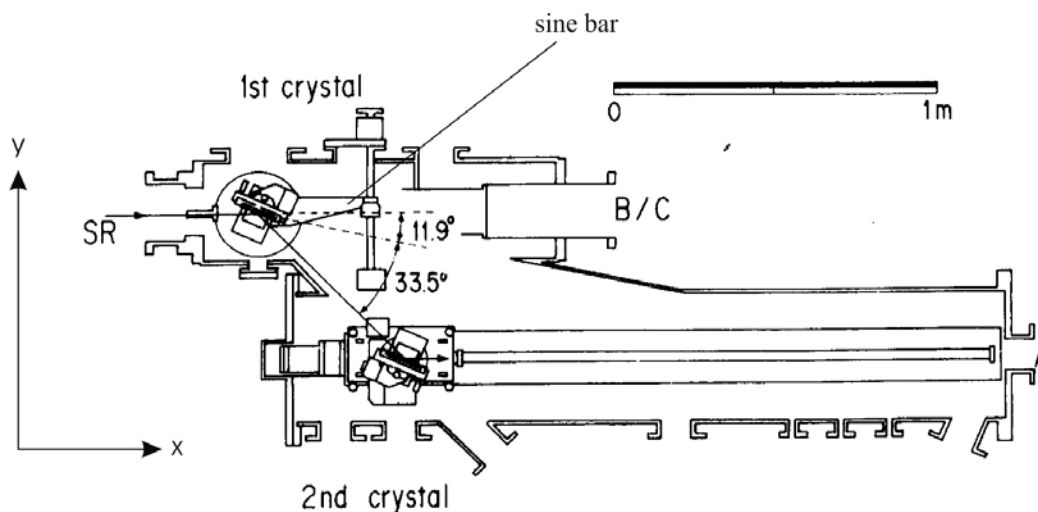
Fig. 2.3 Top view of monochromator BL14A. B/C represents the outlet for Beamlines 14B and 14C which pass through this chamber by insertion of a vacuum pipe above the first crystal.
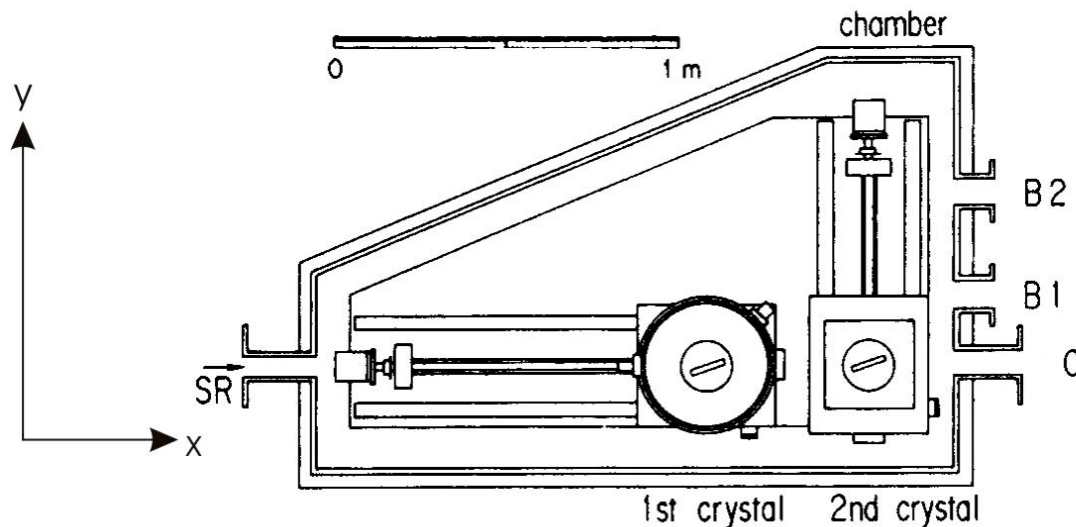
Fig. 2.4 Monochromator of BL14 B. B1 and B2 are separated from the beam B/C by 200mm and 500mm, respectively. B/C stands for the outlet of white synchrotron radiation for BL14B and BL14C.

The superconducting vertical wiggler beamline is dedicated to BL14. The beam duct of BL14 extracting synchrotron radiation from wiggler is 2050 mm. long. Its aperture at the SR outlet is 53 mm. The monochromator in 14B slightly is inclined upward to select the required x-ray photon energy. BL14B is designed and built for providing the system for hyper precision x-ray optics and x-ray diffraction.

- **Characteristics of the Beam**

The characteristic features of the optical system of BL14 are summarized in the table shown below. The spectra of synchrotron radiation in the beam lines in the PF ring are shown in Fig. 2.5. The curve marked as VW#14 illustrates the spectrum of synchrotron radiation in BL14.

Horizontal acceptance	2.2 mrad (vertical)
Type of monochromator	Double Crystal Si (111)
Mirror	None
Photon energy	10 – 57 keV
Beam size	5mm (H) x 14mm (V)
Energy Resolution ($\Delta E/E$)x10^{-4}	2
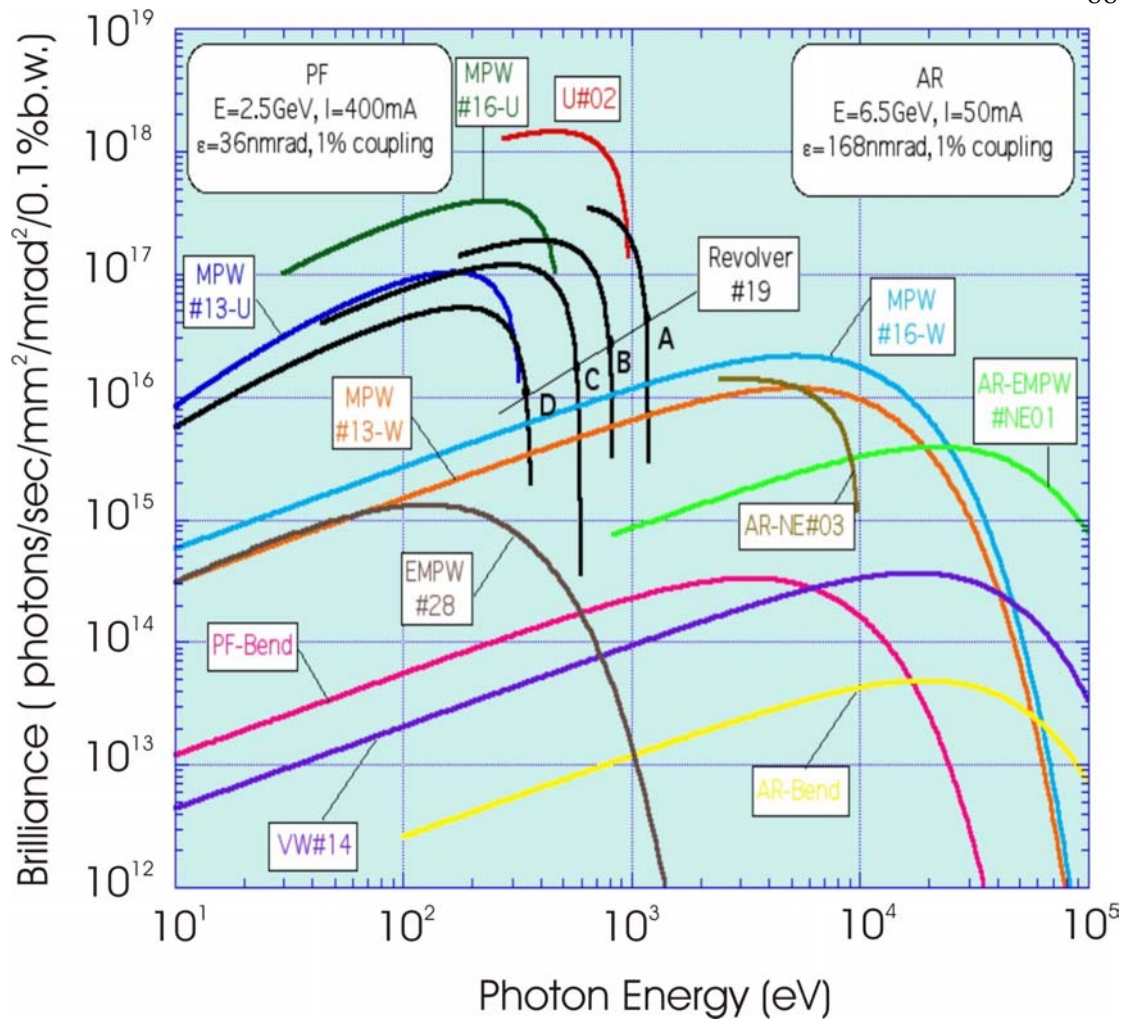
Fig. 2.5 The spectrum at Photon Factory (PF)

- Experimental Station

BL14 in PF ring consists of three beam lines: BL14A for protein crystallography, BL14B for a precision x-ray crystal analyzer system and BL14C for miscellaneous purposes such as x-ray topography, Compton scattering and angiography. Then beamlines are so designed that BL14A is located at the left end of the three beam lines, BL14B has two beams lines and located at the right end and the BL14C is located in the middle. One beam is for x-ray topography and the other is for other two experiments. This concept seen in Fig. 2.1. As is found in Fig. 2.3, one incoming beam is reflected by

two crystals to the direction of BL14A. The remaining beam travels toward the monochromator B. BL14B monochromater in Fig. 2.4 has two separated beams. The goniometer size is 400mm in diameter. The shutter behind the shield for BL14 is designed to be 180mm thick for radiation safety. For BL14B, a 6 mm thick lead cap is added to the first goniometer. This reduces γ–ray and SR background.

The electronics system to control measurements in BL 14B are shown in Figs. 2.6A and B. They are installed outside the hutch. The system is used to control the monochromator drive. The data acquisition system is also included in this control system.

Fig. 2.6A Control panel for the BL14B.

Fig. 2.6B   Control panel for BL14B.

2.1.2   BL 20B at SPring-8

- **Overview:** BL 20B2 for medical science and imaging research.

Experiments were also carried out at BL20B at SPring-8. The bending-magnet beam line is allocated to medical applications and various imaging techniques in the photon energy range of 5 ~ 100 keV. The main optical system is the same as that the standard SPring-8 bending magnet beam line system, which contains a fixed-exit double crystal monochromator. The X-ray beam produced by the bending magnet passes out of the experimental hall surrounding the storage ring and enters the building of the Biomedical Imaging Center. The experiments have been performed at the experimental station in and the Biomedical Imaging Center. Since the x-ray beam is used in the experimental station in the experimental hall for other kind of

experiments by other users, our experiments and their experiments. The x-ray beam cannot be used at the same time at two different experimental stations.

The outside appearance of the Biomedical Imaging Center is shown in Fig. 2.7. We see the main experimental hall area around the storage ring on the left side of the picture. In the middle, the beam line coming out of the main hall and going into the Biomedical Imaging Center is seen on right side of the picture. From this picture, we recognize how far from the main hall the experimental area of the Biomedical Imaging Center is located.
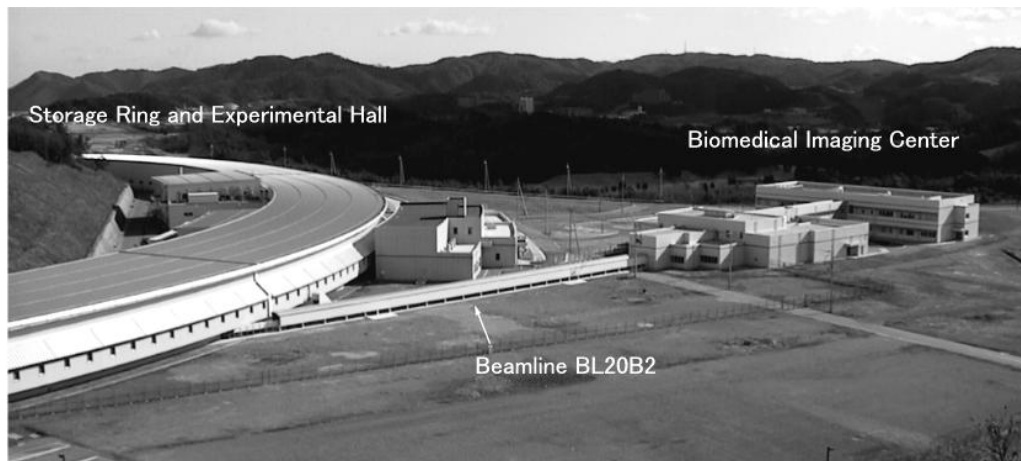
Fig. 2.7 Overview of beamline.

Figure 2.8 shows the photograph of the experimental hall in the main building around the storage ring. The figure is self explaining. In the area near the storage ring the beam optic components are installed. They are in a hutch. Following this hutch, a hutch for experiments is installed. Further downstream, the beam line going straight toward the building wall is seen.
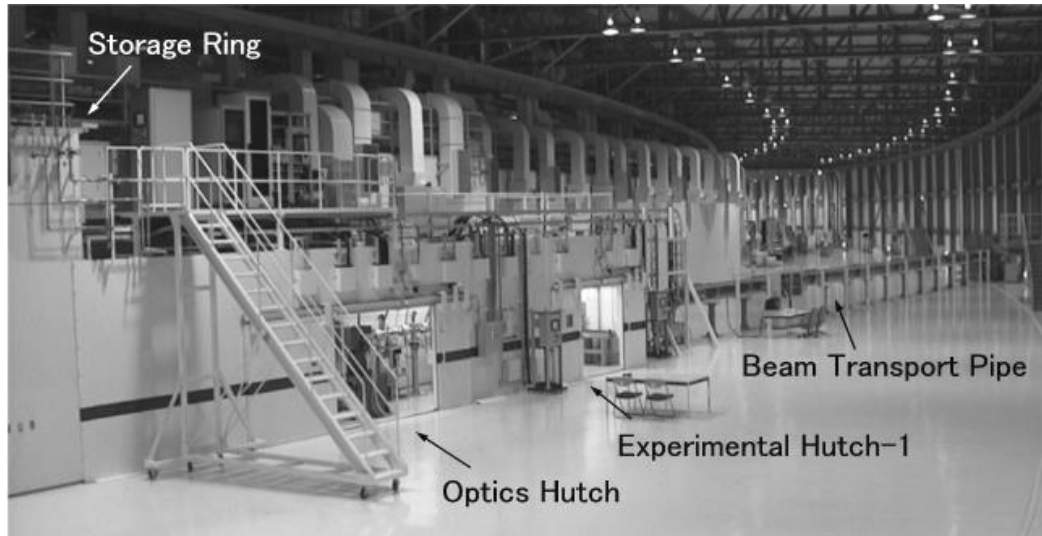
Fig. 2.8 Beamline at experimental hall
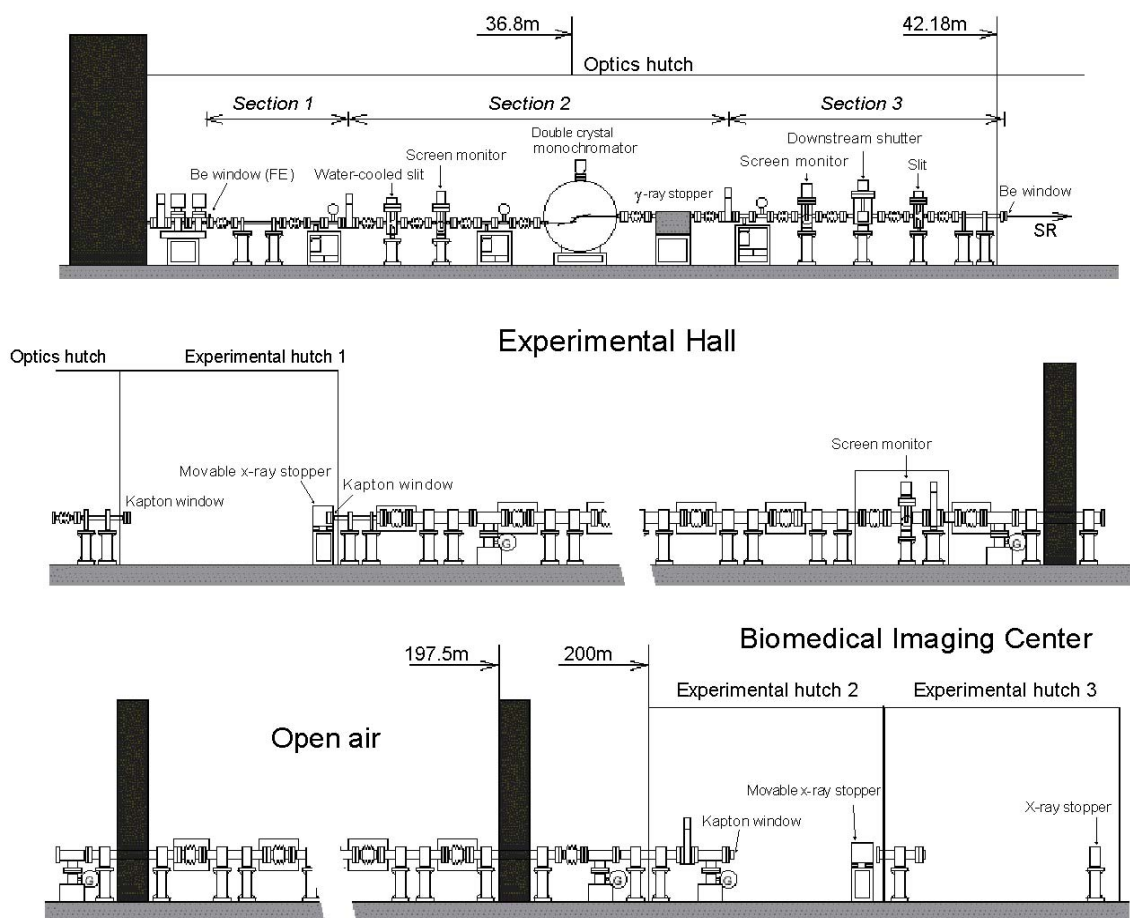
Fig. 2.9 Transport channel of beamline.

The beam line structure is shown in more detail in Fig. 2.9. The SPring-8 storage ring has an electron beam energy of 8 GeV. Therefore stray x-rays and x-rays generated by stray x-rays and γ-rays in the optical elements in the beam line come out of the beam line while the electron beam is stored in the storage ring. The amount of such stray x-rays reaches an indispensable amount. Therefore, the portion of the beam line where various components such as a monochromator, a γ-ray stopper, a screen monitor, a downstream shutter, a slit and Be windows are installed is placed in a hutch. This hutch is called optics hutch. The portion of the compartment for such components is composed of three parts illustrated as Section 1, Section 2 and Section 3 in Fig. 2.9. X-rays coming out of each section are guided to different experimental stations.

Fig. 2.10   Experimental hutches in Biomedical Imaging Center

A screen monitor is for observing the x-ray beam cross section by fluorescent visible light from a fluorescent material placed in the vacuum chamber. If x-rays hit the fluorescent screen, fluorescent light is recognized and the light spot gives the rough size of the x-ray beam cross section.

In Fig. 2.10, experimental hutches inside the laboratory of Biomedical Imaging Center are shown. In this photograph, we recognize that the door of the Hutch No.3 is open and a part of an optical instrument can be seen. Since the hutches are installed very near to each other, racks for wires are placed just above the entrances and running straight through one hutch to another.

- **Experimental Hall**

Two hutches are installed in the experimental hall in the Biomedical Imaging Center as is shown in Fig. 2.10. One hutch, hutch #2, is not used at present. Hutch #3 contains the experimental stations for imaging experiments. In other words, the research fields currently being promoted in the biomedical area is the work on imaging technology. This is the origin of the name, "Biochemical Imaging Center". The experiments on micro-radiography and micro-tomography are carried out in hutch #1. It is in the main experimental hall. The experiments being carried out in hutch #3 is on refraction-contrast imaging on biological specimens and small animals. The present work was performed in the hutch #3.

Imaging techniques involve the evaluation and development of various kinds of optical elements for novel imaging techniques. The hutch #3, the refraction-contrast imaging, the main part of which we call the dark field imaging, is implemented. The details will be described later. Here we summarize the characteristics of the x-ray beam coming to this experimental station in the table given below.

- Characteristics of the Beam

Type	Bending magnet
Critical energy	28.9 keV
Beam divergence	1.5 mrad (Horizontal) 0.06 mrad (Vertical)
Energy range	8.4 ~ 71.9 keV
Beam size	about 300 mm (H) × 20 mm (V),

300-mm-wide beam profile.
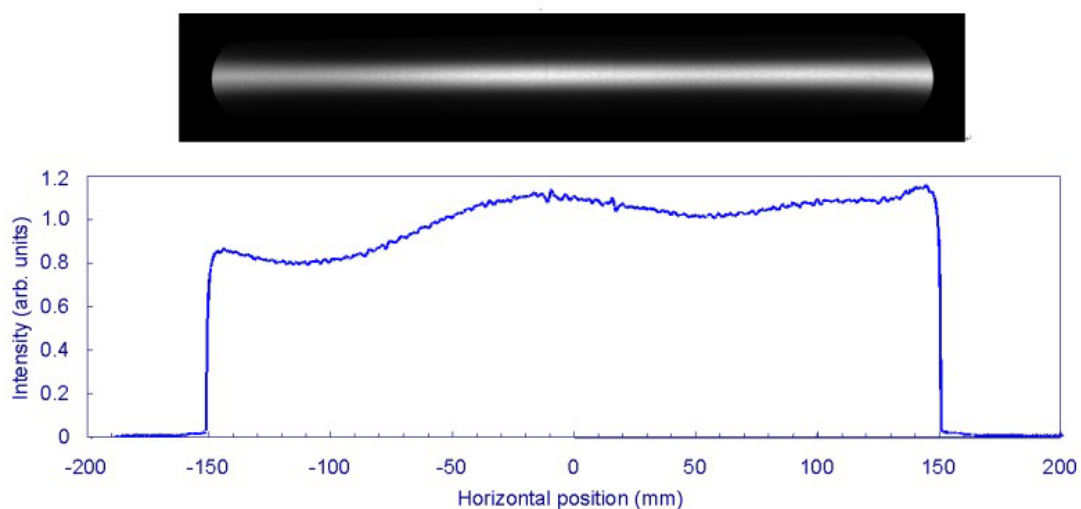
Fig. 2.11   Beam size

The size and the profile of the x-ray beam coming to this experimental station are shown in Fig. 2.11. The beam profile coming out of the storage ring has a cross section of the elliptic shape. The profile shown in Fig. 2.11 is quite different from the elliptic shape. This strange shape is brought about by the optical elements inserted in the beam line, such as slits, mirrors, and a shutter.
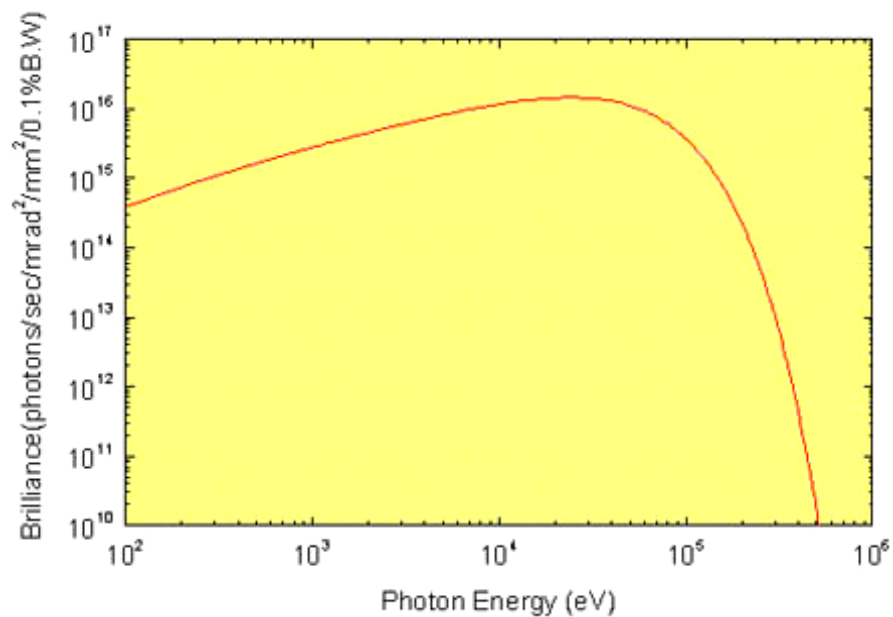
Fig. 2.12 The white spectrum was given by bending magnet at SPring-8.

In Fig. 2.12, the original spectrum of the x-rays to be sent to the experimental station is shown. This is the spectrum of synchrotron radiation emitted from the portion of the bending magnet, #20, in the SPring-8 storage ring. The spectrum of x-rays getting to the experimental station is deformed by reflecting elements in the beam line. In other words, it is deformed by the reflectance spectra of mirrors in the beam line.

- Experimental Station

As shown in Fig. 2.9, the beam line, BL20 consists of an optics hutch and three experimental hutches. Among three experimental hutches, the hutch #1 is located in the main experimental hall as mention already. Just upstream hutch #1, the optics hutch is installed. As is depicted in Fig. 2.9, the optics hutch is connected directly to the radiation shield wall. A double crystal monochromator is located in the optics hutch.

Experimental hutch #1 (4 m long and 2.8 m wide) is located 42 meters away from the source point in the Main Experimental Hall. Figure 2.10 shows the second and third experimental hutches, which are located 200 and 206 meters away from the source point, respectively, in the Biomedical Imaging Center.

The second and third hutches are 3 meters wide and 6 and 9 meters long, respectively. In the third hutch, a large space is reserved for multipurpose use including refraction-contrast imaging experiments with a long object-to-detector distance.

In Fig. 2.13, the inside view of hutch #3 is shown. In the central part of the photograph, a large flange is located. This is the end portion of the monochromator. On the frame, two instruments are seen. Both provide rotary motion at the bottom of the axes, where samples and crystals for monochromatization are mounted. The rotational motion is generated by step motors. Something like a white box is installed on the table downstream the two rotary mechanics is the detector, a CCD camera. More practical explanation is given in the following section.
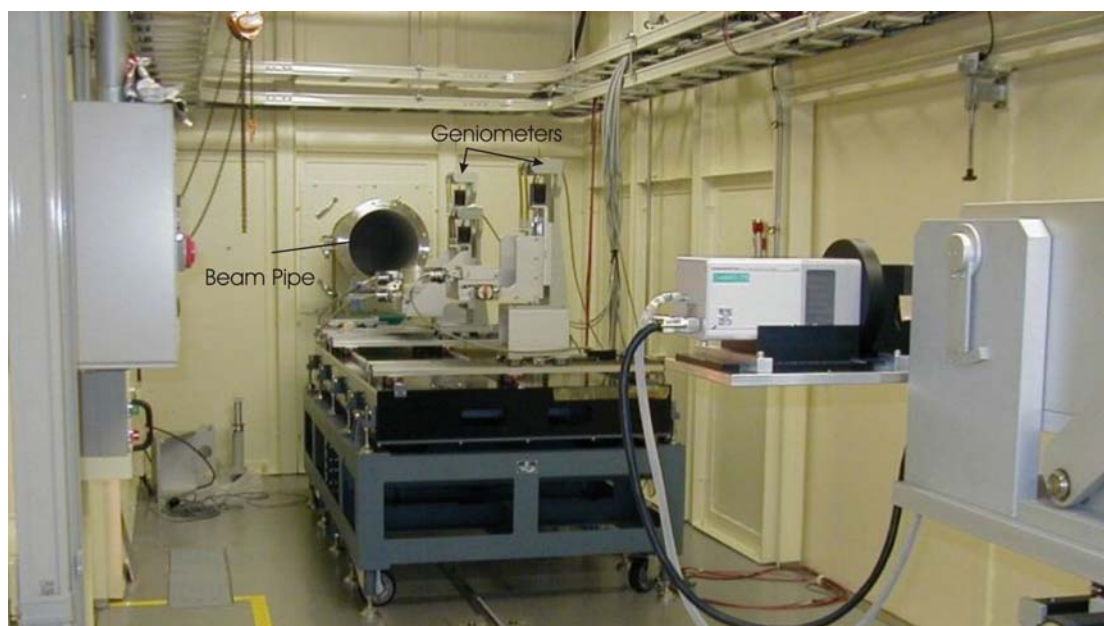
Fig. 2.13   Experimental Hutch 3

2.2 Design and Fabrication of DFI

In the imaging of x-rays, x-rays passing through an object reduce their intensities owing to the absorption of x-rays by the object. There are many grains or equivalents with different absorption coefficient in the object, the image of the object is obtained as dark and bright parts. However, this method is not effective for materials in which the absorption constant is not high. Therefore we can not employ this method for almost transparent.

Instead there are methods to use the phase change or the propagation direction change in a target material from place to place. A simple way to use this nature is to utilize refraction. In a sample almost transparent, in which the absolute value of the absorption coefficient is small, the distribution of the refractive index is finite. Here, we have to be careful, because the refractive index of a material in the x-ray region is nearly equal to unity. However, we are making the image of the material. Thus, relative value of the refractive index is important.

Then a question arises: How do we use the refraction of the material for the imaging? Consider a thin film material.
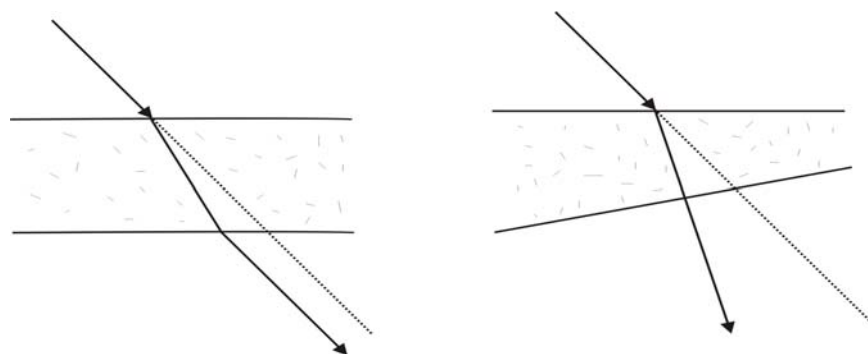
Fig. 2.14 Example of x-ray penetration in a material. Left: Two surfaces of the material are parallel. Right: Two surface of the material are not parallel.
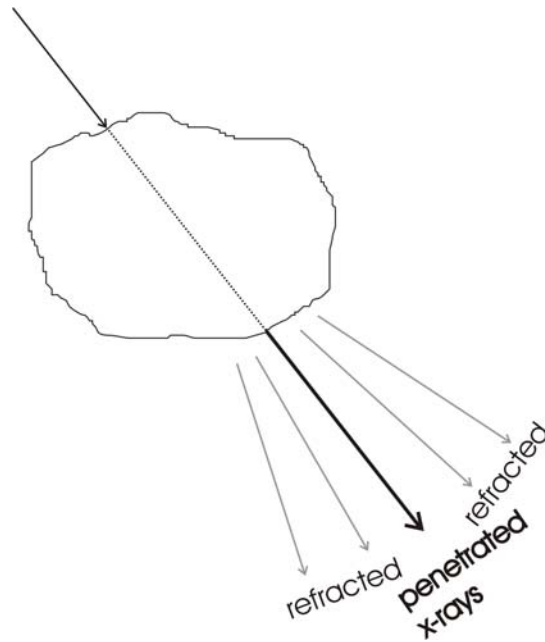
Fig. 2.15 Direction of x-ray beams penetrated through the target material.

Suppose the two surfaces of the film is parallel. In this case the penetrated x-ray beam after refraction is parallel to the incident x-ray beam. If two surfaces of the film is not parallel, the penetrated x-ray beam after refraction is not parallel to the incident x-ray beam. This is illustrated in Fig. 2.14. As far as the light propagation is concerned, the optical effect is similar to scattering. This situation is illustrated in Fig. 2.15. There, we show the straight penetrating x-rays and refracted and penetrating x-rays.

If we place an analyzer crystal so that the Bragg condition is satisfied for straight penetrating x-rays. This x-ray beam is be transmitted through the crystal strongly, since the Bragg condition is satisfied on the reflection in the atomic net planes in the analyzer crystal. Obviously, the beam intensity is strong. However, the original beam is not refracted in the target material. Then, the image of the target material obtained this x-rays reflect the absorption contrast. The intensity, I, we obtain after the x-ray beam is transmitted, is given as

$$I \quad = \quad I_o \qquad\qquad e^{-\mu l}$$

(2.1)

Here, I_o is the intensity of the incident beam, μ is the absorption coefficient of the material and l is the thickness of the target material. If we put $\Delta I \equiv I_o - I$, we obtain form (2.1)

$$\frac{\Delta I}{I_o} = \ln I - \ln I_o \qquad\qquad (2.2)$$

For materials and the wavelength range where the absorption coefficient is small, I is nearly equal to I_o and this makes $\Delta I/I_o$ very small. In other word, we can obtain the images of very low contrast. We refer to this image as bright field image (BFI), since the x-ray intensity reaching the detector is high.

On the other hand, the refracted x-ray beam is transmitted through the analyzer crystal straight, since the Bragg condition is not satisfied. Furthermore, the intensity is weak, since constructive interference does not occur in the analyzer crystal because of the incident angle not satisfying the Bragg condition. The images formed by this beam reflect the refraction of the target material. Since the refracted beam has a wider beam divergence, we can obtain the wider image of the target material. We refer to the image formed by this x-ray beam as the dark field image (DFI). As mentioned before, the contrast is better than that of BFI. The asymmetric cut monochrochromator crystal is used for improve beam divergent and expand beam size. It is put before sample that was shown in Fig. 2.16.
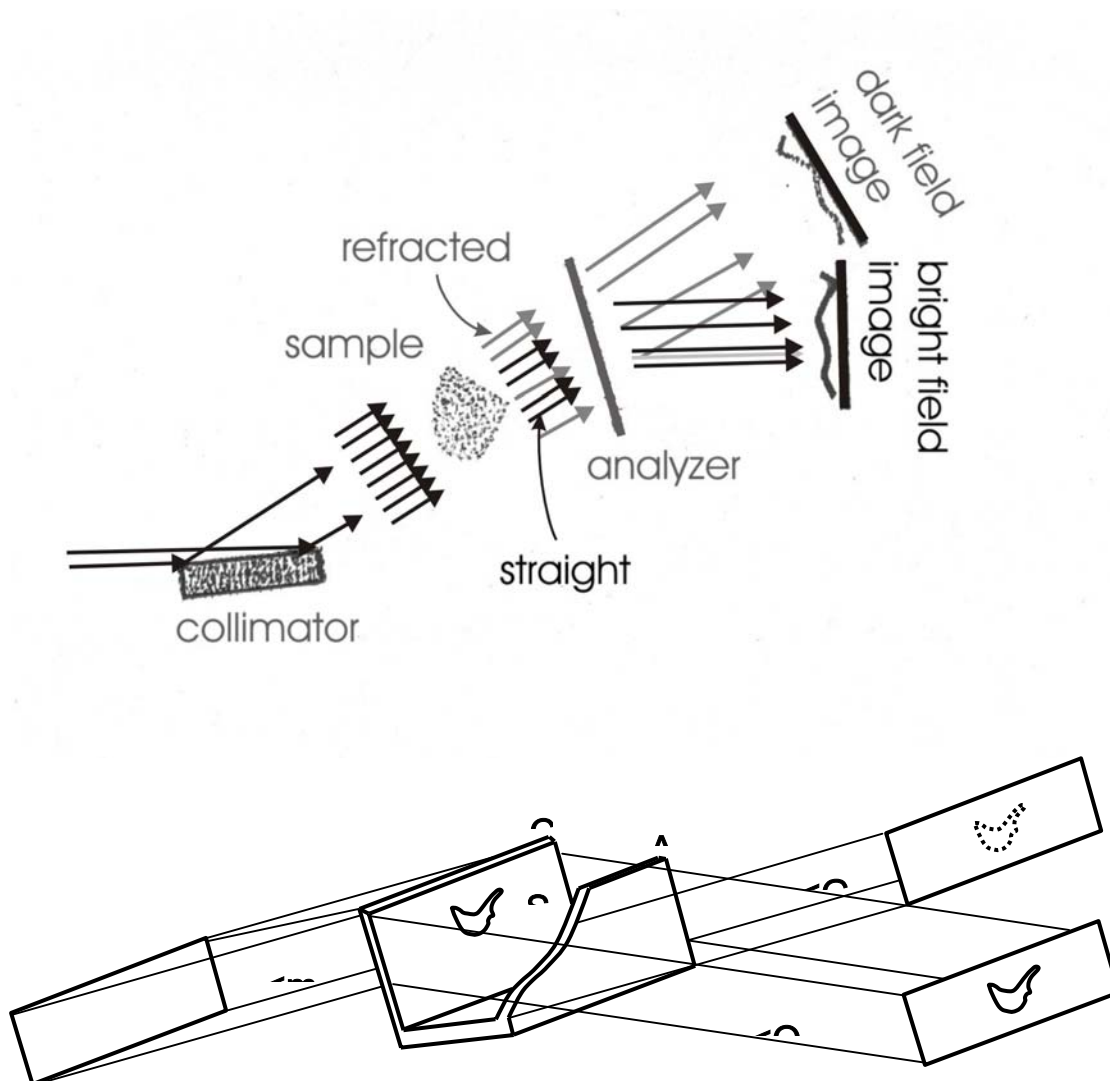
Fig. 2.16 Basic layout of optical elements in the dark filed imaging of x-rays. The upper panel shows the concept of the optics in two dimensional display and the lower panel shows the same concept in more like the three dimensional display.

2.2.1   Theory and Design of Dark-field Imaging

The deflection angle $\psi(x, y : k)$ which leads to the refraction contrast can be described as follows:

$$\psi(x, y : k) \;=\; -a\int_{z_0}^{z_1} \partial\delta(x, y, z : k)/\partial x \, dz \tag{2.3}$$

where $\delta(x, y, z : k)$ is a part of the refractive index given as $n = 1 - \delta(x, y, z : k)$. z is the direction of x-ray beam propagation and z_0 and z_1 are z coordinates at which the x-ray beams enter and leave a sample, respectively. x is the coordinate perpendicular to the plane of incidence. Thus, x is perpendicular to z. The derivation of equation (2.3) is not difficult. Physically, the equation is understood to express the following:

Consider a small volume in a material and x-rays pass through it. For simplicity the plane on which x-rays fall is assumed to be parallel to the plane from which x-rays come out of this small volume. If the reflective index is uniform and does not change from space to space, x-rays are not deflected by the small volume. If the refractive index varies from space to space, x-rays are deflected by this small volume. A simple calculation shows that the amount of the deflection angle is proportional to the product of the negative of the gradient of the refractive index toward the direction transversal to the direction of the x-ray propagation and the distance that x-rays propagate. We have to make an assumption, however, that refractive index is almost uniform in the z direction. Thus, if we integrate the deflection caused by the small volume along the direction of the x-ray propagation, we obtain (2.3).

The Laue geometry of diffraction is a key technology for dark-field imaging. We consider the case described above. For a specific thickness of the angular filter virtually, any x-ray beams with a certain photon energy are diffracted

toward the diffraction direction at the center of the Bragg condition. This is not

the case, however, if an illuminated sample through which x-rays penetrate with

divergence is present. Thus, the concept leading to (2.3) results.

Let us define I_O and I_G in the Laue case as the beam intensity in the

direction of forward diffraction and that in the diffraction direction, respectively, in

case of almost no absorption. As a simple model, they are given as follows:

$$I_O = \sin^2(\pi W\sqrt{1+\varphi^2}/\Lambda)/(1+\varphi^2) \tag{2.4}$$

$$I_G = [\varphi^2 + \cos^2(\pi W\sqrt{1+\varphi^2}/\Lambda)]/(1+\varphi^2) \tag{2.5}$$

$$I_O + I_G = 1 \tag{2.6}$$

$$\Lambda = \lambda\cos\theta_B/|P\chi_G| \tag{2.7}$$

where W is the thickness of an analyzer A, and φ is the normalized angular deviation

from the center of the Bragg peak. The condition $|\varphi| \leq 1$ corresponds to the reflection

range and Λ the extinction distance defined in (2.7). λ is the x-ray wavelength, θ_B

the Bragg angle, P the polarization factor and χ_G the polarizability. One can

recognize that the relation $I_O + I_G = 1$ holds for all φ's. Figure 2.17 shows I_O (broken

line) and I_G (solid line) in the angular range between ± 1 μrad for various thicknesses

between 1.10 and 1.15 mm. The thickness change of only approximately 50 μm of the

analyzer crystal, A, may significantly change the reflection rate, perhaps from a

maximum to next minimum of zero or vice versa. This means that the fabrication of

the analyzer crystal A requires approximately 5 μm precision of its thickness

fluctuation. The profile outside $|\varphi| = 1$, I_O maintains a constant high reflectivity while

I_G shows a rapid decrease. One can easily find that the profile I_O in the angular range

$|\varphi| > 1$ may have high reflectivity for refracted x-rays from a sample, while the

profile I_G in the angular range $|\varphi| > 1$ shows low
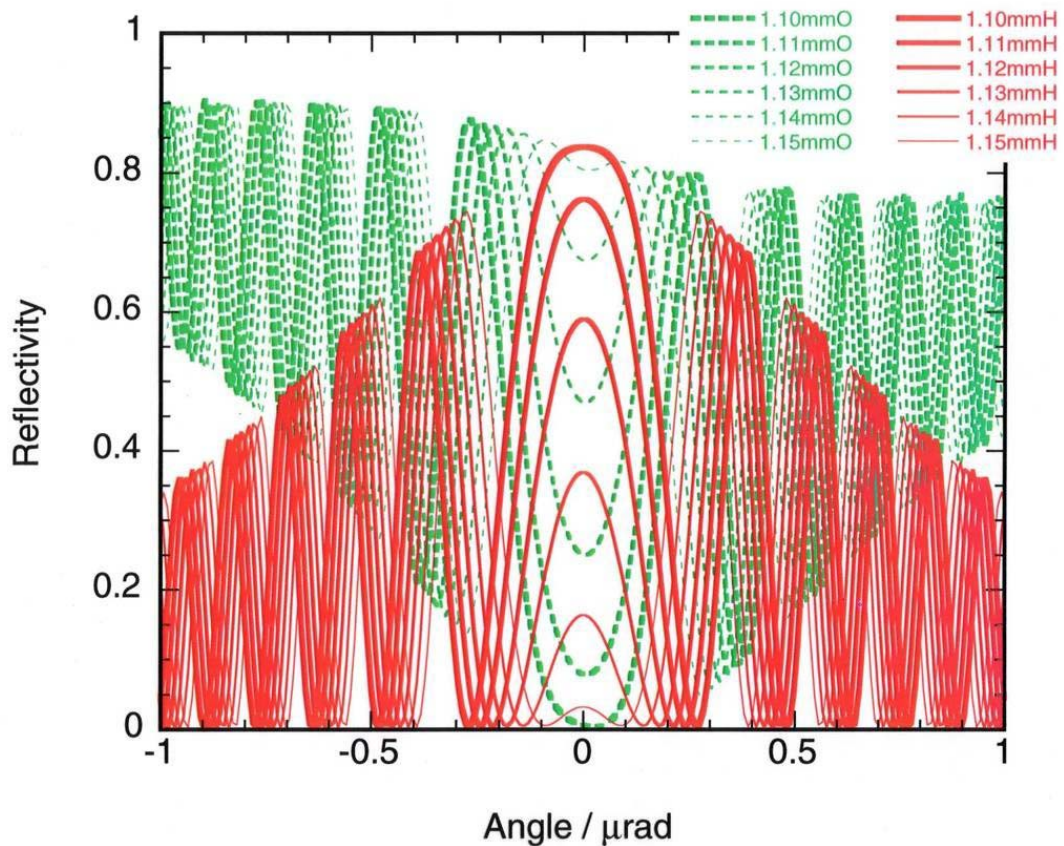
Fig. 2.17 Reflectivity I_O for O-beam, in the forward diffraction direction, and I_G for

G-beam, in the diffraction direction, versus angular position within 1 μrad

for the range of crystal thicknesses between 1.10 mm and 1.15 mm. The

angular range in the x axis is approximately of the order of ±1.0 arc sec.

One can recognize that every change by approximately 10 μm may lead to

a 20% reflection both in I_O and I_G. Thus, only a 50 μm thickness change

may lead to the full change of function of I_O and I_G.

reflectivity for refracted x-rays from a sample. Thus, the signal level at I_O will be relatively high compared to I_G. Based on this consideration, I_O may yield dark-field imaging with a relatively low level of illumination, and I_G, conventional bright-field imaging with a high level of illumination. It is clearly seen that profiles in Fig. 2.17 hold for the relation $I_O + I_G \sim 0.9$ if not 1.0 due to some absorption for all thicknesses and angular positions.

The pioneering system of Ingal and Beliaevskaya (Ingal and Beliavskaya, 1995), Chapman et al. (Chapman et al., 1996) and Thomlinson et al. (Thomlinson, Chapman, Zhong, Johnston and Sayers, 1998) have shown that in principle, one can achieve near-dark-field imaging by adjusting the reflection angle of the analyzer crystal. This means that one may need more than one exposure for collecting all refracted images.

If the beam with the narrowest angular width, produced by asymmetric reflection, is incident onto an object and is used under achromatic conditions, one would not need analyzer rotation. Our new system, named 'Owl', shown in Fig.2.16 can provide all information inherent in an image by a single shot without rotating an analyzer crystal. Collimator C and analyzer A are parts of a monolithic block which keeps their angular relationship quite stable. S indicates a sample. The incident beam <m> with 0.3 μrad beam divergence from an asymmetric monochromator produces a beam via C that passes through a sample S. The bright field image <G>, which is formed by a beam with a beam divergence of 0.3 μrad is incident on analyzer A. The analyzer exhibits reflectivity acceptances in the angular range only outside ± 0.15 μrad so that <O> containing refraction information is forward diffracted to realize dark-field imaging.

Fig. 2.18 X-ray optics setup for simultaneously producing dark-field image and bright-field images. The incident beam I (φ) is incident onto an asymmetric monochromator M that reduces outgoing beam divergence by a factor of 0.2. The beam divergence of P (φ), which is incident onto object Q (φ), has 0.3μrad. The modulated beam R (φ) contains information on Q (φ); R (φ) splits into D (φ) and B (φ) due to I_O (φ) and I_G (φ), respectively. D (φ) and B (φ) lead to production of a dark-field image and a bright-field image using an imaging device, respectively.

In order to understand the situation described above more simply and schematically, we consider the change in the beam in Fig. 2.18. Note that the crystal used as monochromator has the orientation of the plane that reflects beam incident in the grazing incidence made symmetry to the direction making a much larger take-off angle. This expands the x-ray beam width. Reflection by the crystal M makes the x-ray beam more parallel.

Figure 2.19 shows a schematic explanation how dark- and bright-field images are produced: Panel (a) shows the angular divergence of an incident beam that has as narrow an angular divergence as possible. Its horizontal axis corresponds to the angular scale. A horizontal axis in other figures also has the same angular scale. Panel (b) shows a mapping of a potential refraction object that comprises four refraction boundaries with four kinds of refraction indices. Panel (c) shows a profile of the beam from an object. It has the form of the convolution of the beam profiles in (a) and (b). Panel (d) shows the calculated curve I_O. It gives almost zero intensity at $|\varphi| \leq 1$. Panel (e) shows the intensity of x-rays given in (c) transferred by A, the analyzer, in the forward diffraction beam direction. This can be called dark-field imaging because it has almost no background illumination. Panel (f) shows a theoretical diffraction profile I_G. Panel (g) shows the intensity x-rays given in (c) transferred by analyzer A in the direction of the diffraction beam. This can be called bright-field imaging because it contains illumination light to some extent.
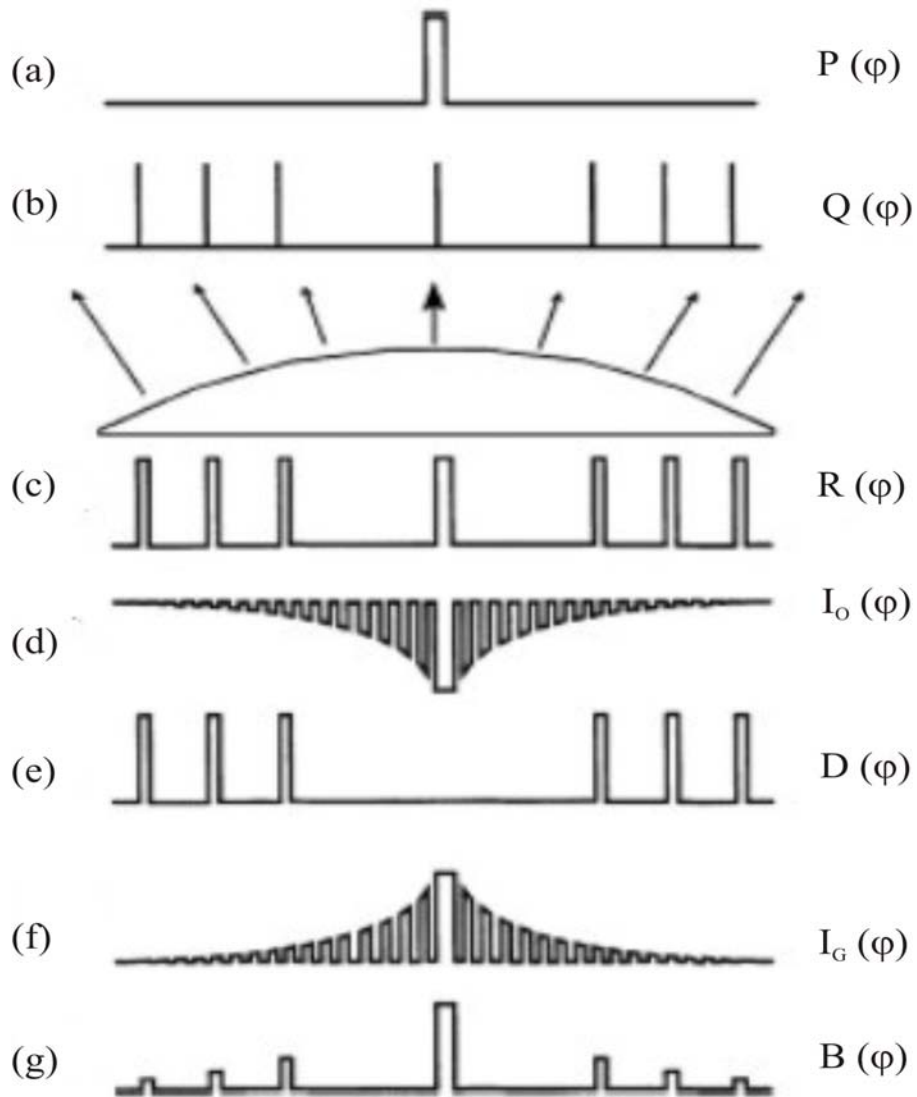
Fig. 2.19 Diagram showing how DFI and BFI can be formed. The horizontal axis represents the angular scale represented by φ, while the vertical axis represents the power of X-rays. Panel (a) shows the profile, $P(\varphi)$ of an incident. $P(\varphi)$ is equal to 1 for $|\varphi| < 1$ and 0 for $|\varphi| \geq 1$, where $\varphi = \pm 1$ corresponds to a rocking curve width for asymmetric 4, 4, 0 diffraction that has the order of $0.15 \mu rad$; Panel (b) represents a schematic angular distribution of object $Q(\varphi)$ as shown in the inset between Panels (b) and (c). This shows a model with an 8-face polygon whose refractive index is equal to the value for vacuum or larger than that for its surrounding

atmosphere; Panel (c) represents the angular distribution $R(\varphi)$ that is defined $R(\varphi) = P(\varphi)*Q(\varphi)$, where asterisk represents the convolution of the two functions; Panel (d) represents a transmission function $I_O(\varphi)$ of an analyzer crystal A along the forward diffraction direction; Panel (e) shows $D(\varphi) = I_O(\varphi)R(\varphi)$, the intensity profile of the beam after passing through A along the forward diffraction direction. This corresponds to DFI because no apparent illumination light remains; Panel (f) shows the transmission function $I_G(\varphi)$ along the diffraction direction of A, Panel (g) shows $B(\varphi) = I_G(\varphi)R(\varphi)$ that can be BFI because an image due to refraction contains the illumination light as well.

Furthermore, since I_O in (2.4) and I_G in (2.5) can be simplified at $\varphi = 0$ as

$$I_O = \sin^2(\pi W / \Lambda) \tag{2.8}$$

$$I_G = \cos^2(\pi W / \Lambda) \tag{2.9}$$

both I_O and I_G oscillate between zero and 1. The I_O oscillation and I_G oscillation are $\pi/2$ out of phase.

$$W = n\Lambda / 2 \tag{2.10}$$

Maximum and minimum values for I_O and I_G are given when W is equal to $n\Lambda / 2$ and n is an integer. If one needs the condition of $I_O = 0$ and $I_G = 1$ or vice versa for the fixed x-ray wavelength, a certain precision of thickness W in the fabrication of the analyzer crystal A is needed. The relation between x-ray wavelength and W is decided by the equations (2.7) and (2.10). Note that $I_O + I_G = 1$.

Figure 2.20 shows the relationship among I_O (or I_G), crystal thickness and x-ray photon energy. If the crystal thickness control is difficult in its fabrication, one can alternatively tune the x-ray photon energy so that I_O can achieve the minimum value. We can learn from (2.10) that the x-ray photon energy corresponding to a thickness change of 62.5 μm is approximately 1.05 keV.

One shot in the dark-field imaging that enables clear visualization of the entire image seems very advantageous over other methods. The entire image obtained by one shot contains almost all information on the structure inside the object at a fixed angle position $\varphi = 0$ of the analyzer crystal. In other method it is necessary to take many pictures by detuning the analyzer crystal under the exact Bragg condition of $|\varphi| = 0$. This is so both in the Laue and the Bragg cases.
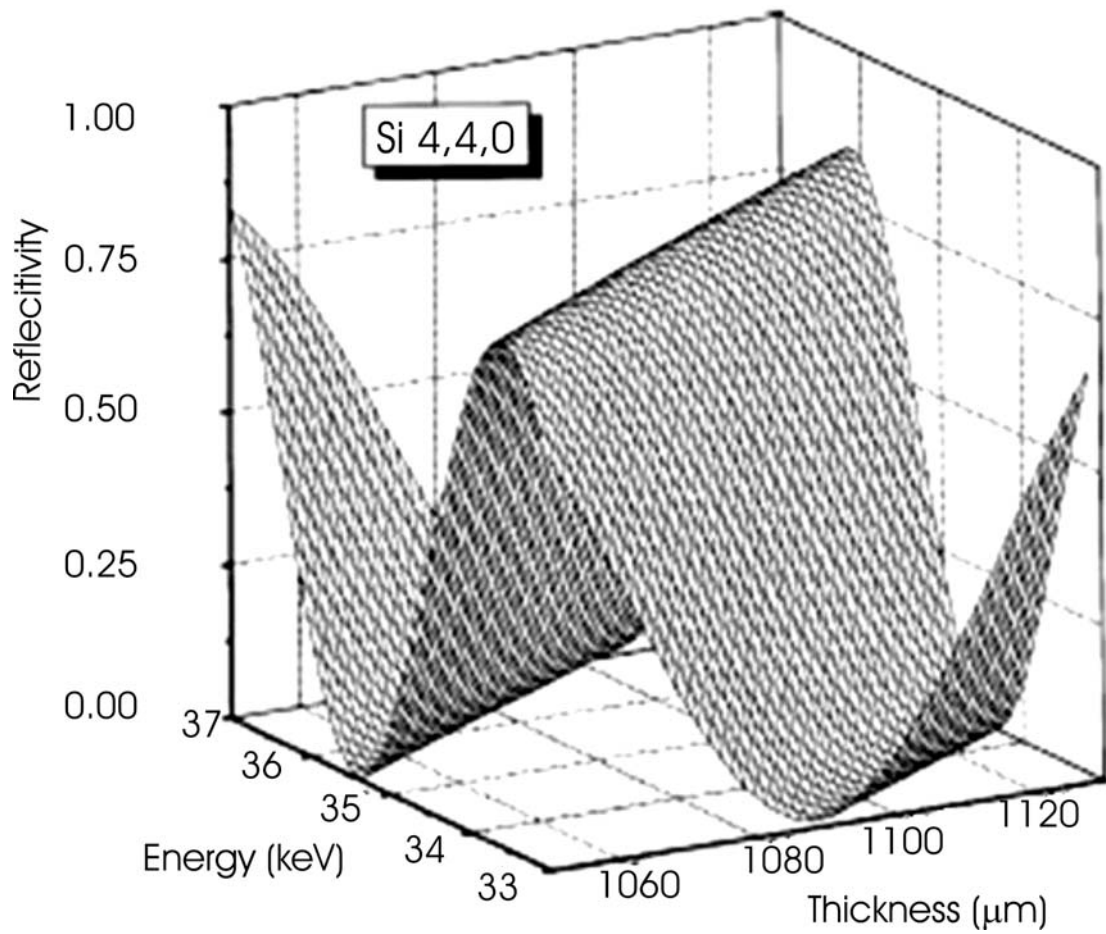
Fig. 2.20 The relationship among reflectivity I_O or I_G, crystal thickness and the x-ray photon energy. One period that gives minimum or maximum I_O or I_G corresponds to a crystal thickness of approximately 62.5μm and an x-ray photon energy of 4keV. When control of the crystal thickness is difficult, one can alternatively control the x-ray photon energy by 1.05 keV.

In an experiment, asymmetric reflection was used as a key technique to expand the beam size as well as to narrow the beam divergence at experimental stations BL14B at Photon Factory and BL20B at SPring-8. In the experimental stations, an x-ray optical system 'Owl' and the parallel plate or wedge-shaped crystal analyzer systems, both of which were manufactured on site, are installed. Using this system, we have successfully taken x-ray pictures of a variety of samples. The experiment was carried out under the following conditions: The crystal thickness was 1.08 mm, the x-ray photon energy 35 keV, and the asymmetric parameter b is 0.05 in the scheme as shown in Fig. 2.16. The current in the storage ring was approximately 400mA at Photon Factory and 100mA at SPring-8. A wave packet <m>, shown in Fig. 2.16, with a divergence of 0.3 μrad from a monochromator with asymmetrically cut crystal is incident onto a sample S in the way that the beam from S is incident onto A and split into two wave packets <O> and <G>. The beam from S carries the information of the sample.

To demonstrate dark-field imaging, we have used a variety of samples: A mammographic phantom specimens, elephant tusk, and similar mammalian materials. Images were stored on an electron microscopy film, x-ray film, or nuclear plate with spatial resolution of approximately 10 μm or better. The limit of spatial resolution of the system is defined by the beam width at the exit of the Borrmann fan which is formed both in the incident beam direction and the diffracted beam direction after the analyzer A of a finite thickness. The exposure time for each picture was approximately 1–2 min at all stations such as BL14B at the Photon Factory ring where synchrotron radiation from a superconducting magnet wiggler of 5 Tesla at beam energy of 2.5 GeV and a stored current of 400mA is used or at BL20B connected to a bend source at SPring-8.

2.2.2 Owl Optical System.

In Fig. 2.16, which is used to explain the principle of making dark and bright images, two different optical systems are shown. The lower panel there shows the Owl system. The distinctive aspect of the Owl system is that a sample is mounted between two parallel crystals. The first crystal is used as a collimator and the second crystal is the analyzer. The actual size of the parallel crystal system is shown in Fig. 2.21. The reflectivities of the O-wave and the G-wave are shown in Fig. 2.22.
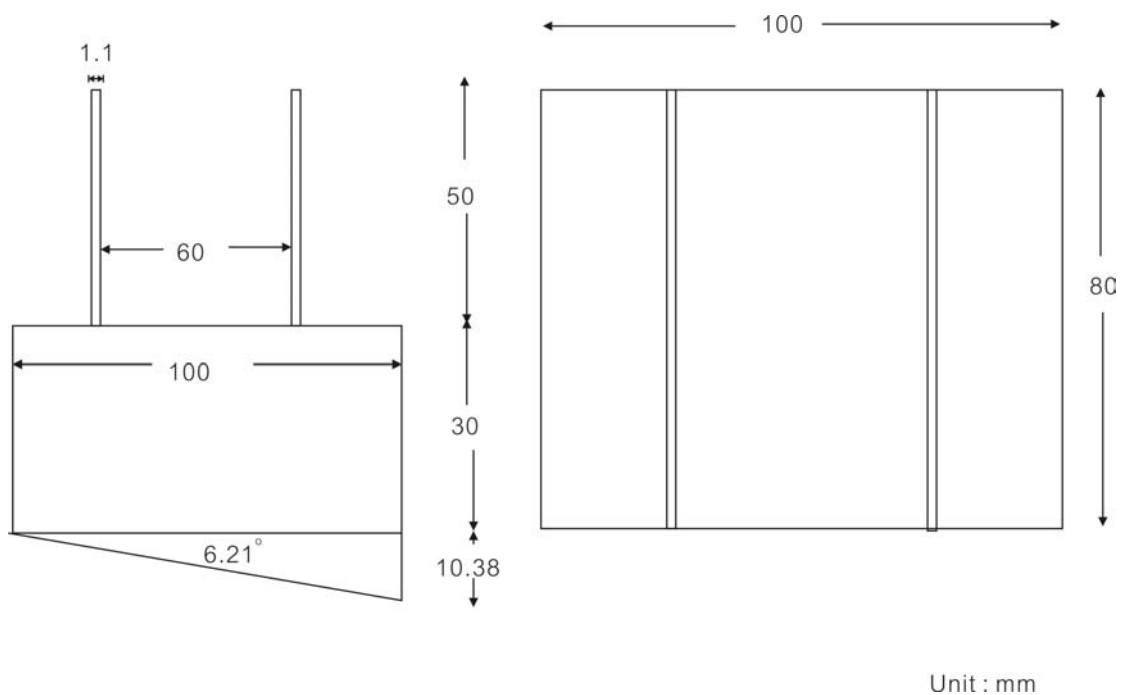
Fig. 2.21 Drawing of 'Owl' optics.
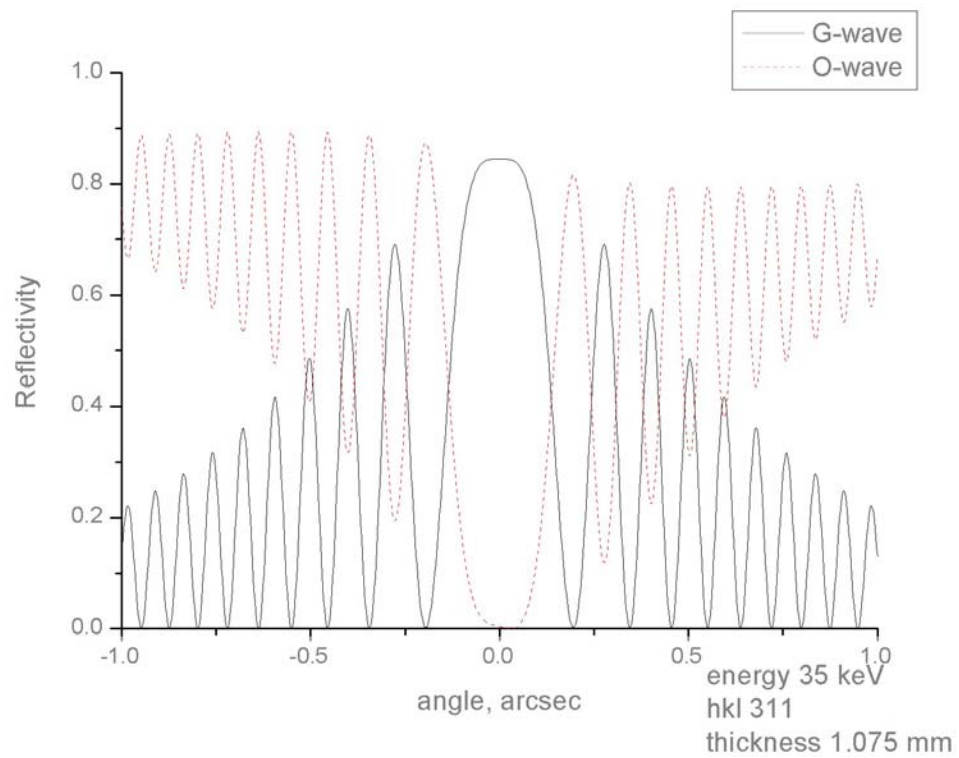
Fig. 2.22 Reflectivity dependence of I_o for O-beam, in the forward diffraction direction, and I_G for G-beam, in the diffraction direction for an x-ray energy of 35 keV. The crystal is 1.075 mm thick. The diffraction index is (311).

2.2.3 The Plane Parallel Analyzer

In the upper panel of Fig. 2.16, an other optical system is shown. In this system, only one analyzer is used. The analyzer crystal has the surfaces parallel to each other. We refer to this crystal as the single parallel blade.
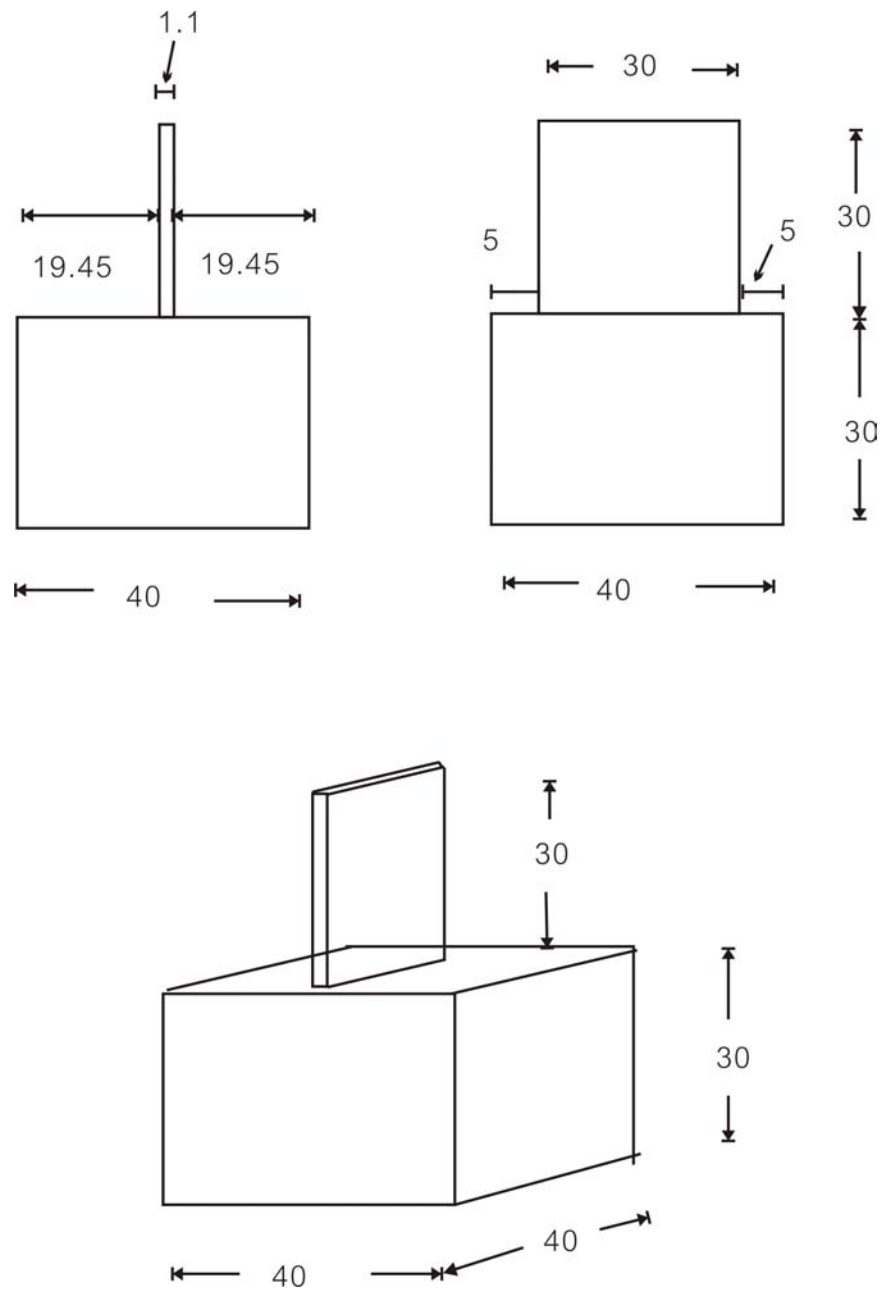
Fig. 2.23   Drawing of Plane parallel analyzer.

In the present case, the reflection from the (440) plane is used. Only one blade is used because only two images, bright and dark field images, are present. This is contrasted to case of the Owl optical system where three images bright field image, dark field image and phase contrast image are present. This is inconvenient. The practical size of the single blade analyzer is shown in Fig. 2.23. The size is not too large because the beam size in beam line 14B is only 1.1 mm in x-axis and 15 mm in y-axis. The reflectivities of G wave and O wave in this system are shown in Fig. 2.24. A thickness of 1.1mm is suitable after calculation using the data of Fig. 2.24.
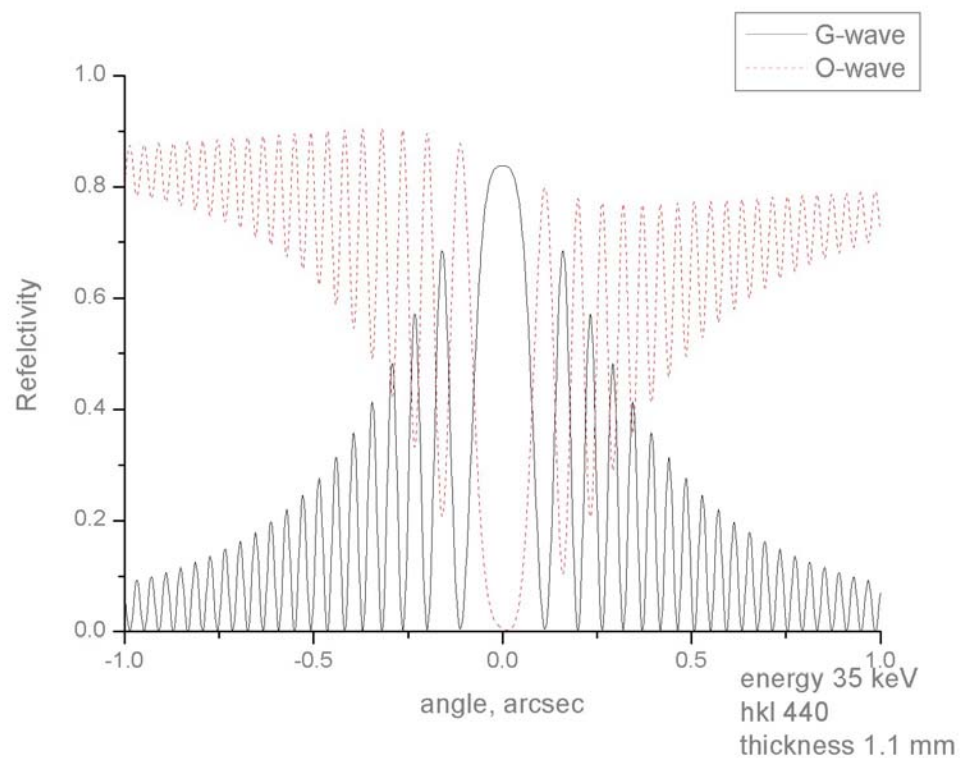
Fig. 2.24 Reflectivity dependence of I_o for O-beam, in the forward diffraction direction, and I_G for G-beam, in the diffraction direction. X-ray photon energy is 35 keV. The crystal is 1.1 mm thick. The diffraction index is (440).

2.2.3   The Wedge Analyzer

In the optical system shown in the upper panel of Fig. 2.16, a wedge shaped crystal can be also used as the analyzer. The analyzer splits the beam into two. In this case, the bright and dark images are present in each picture. The bright field image and the dark field image are separately observed on one film. This means that we can compare the dark field image and the bright field image on a recording film. Because of this convenience the wedge blade is chosen. In Fig. 2.25, the spatial distributions of the G wave and the O wave are shown. Using this data, the dark and bright regions are found to consist of 11 fringes. The practical sizes of the wedge shape and its holder are shown in Fig. 2.26. In this case, too, the sizes are suitable for beam line 14B at photon factory in KEK.
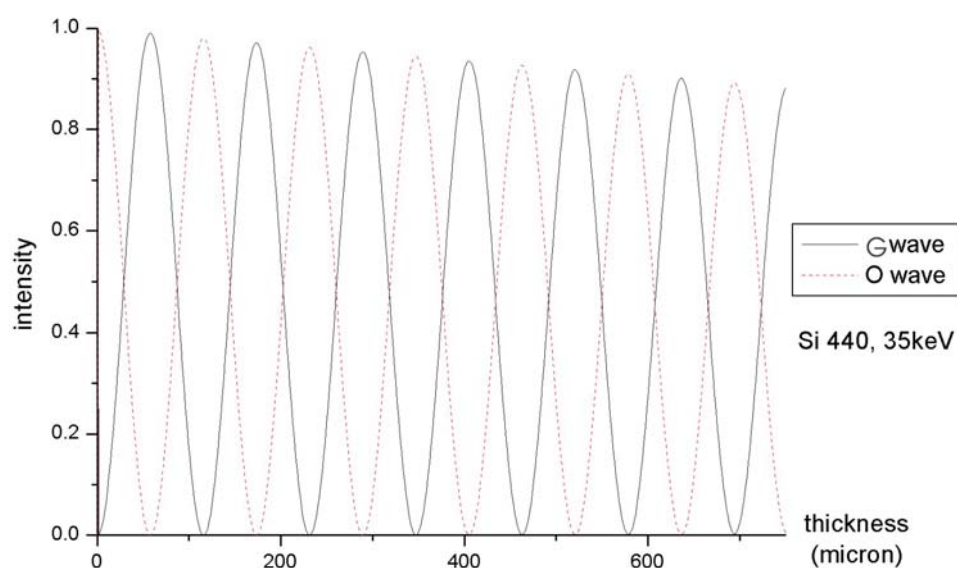
Fig. 2.25   Reflectivity dependence of I_o for O-beam, in the forward diffraction direction, and I_G for G-beam, in the diffraction direction for x-rays with an energy of 35 keV. The crystal is wedge-shaped with a summit angle of 3.35°. The diffraction index is and (440).
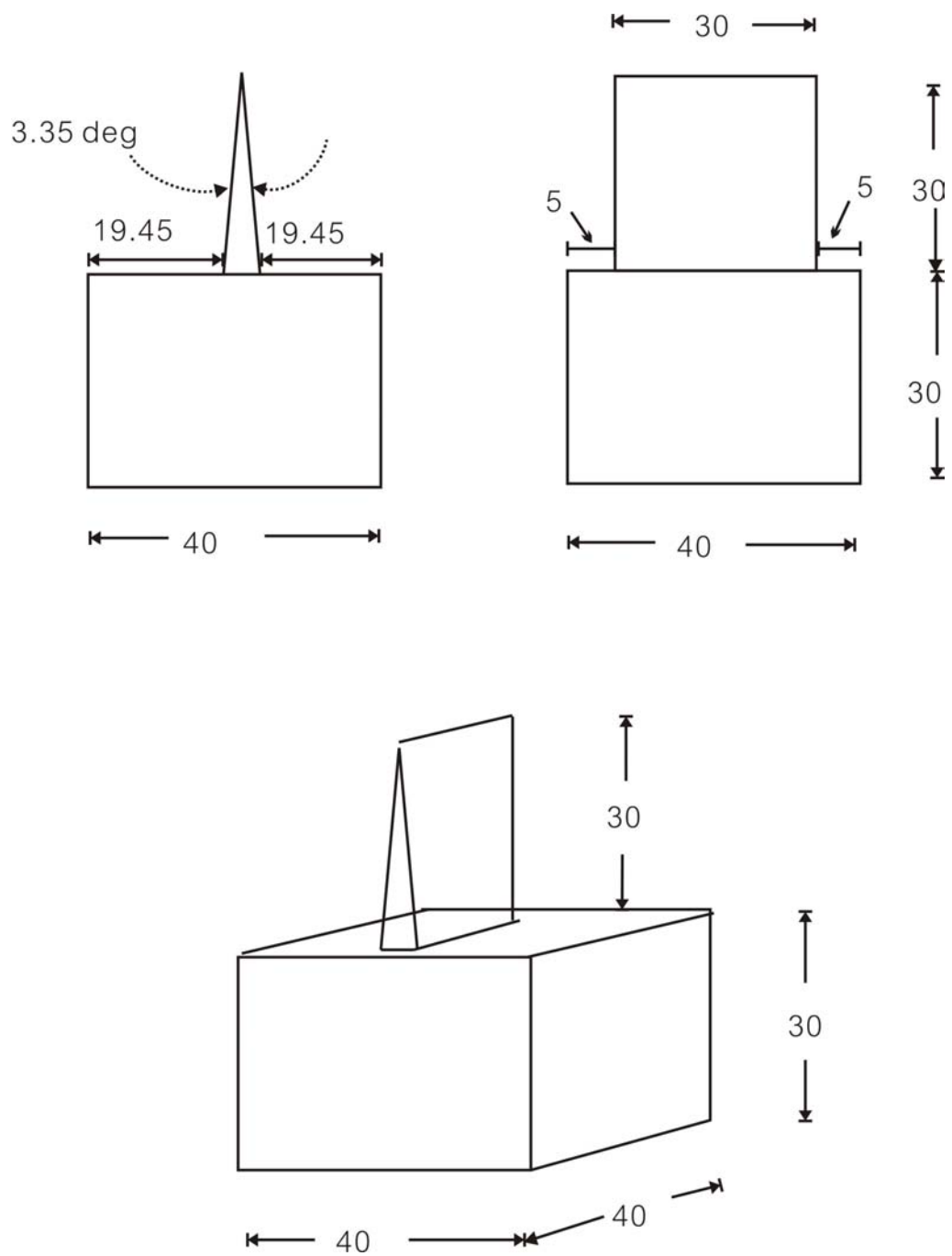
Fig. 2.26 Drawing of wedge shade analyzer.

As the preparation of the experimental station, the necessary work proceeded in the following way: First the setting up of the mechanical parts was carried out. There we started with the design work of the system. After this had been done and the design drawings, we started the work of the preparation of the analyzer crystals. We cut a silicon crystal in a way that the desired surface was obtained. We did not polish the crystal surface but etched it in acid. The crystal was cut with a diamond saw. It took us 1 week to finish cutting. Before etching, the crystal was washed in acetone.

Fig. 2.27   Cutting machine.

Before cutting a crystal, the ingot was mounted on a ceramic holder and glued to the holder. A crystal blade was cut out. The crystal ingot has two surfaces,

(110) and (111), which were cut out accurately from the begging. The (111)

surface was cut along the ingot axis and the (110) surface was at the end of the ingot.

It is known that the (111) surface and the (110) surface is perpendicular to each other.

The two surfaces were used to align the ingot mechanically to the cutting machine.

Figure 2.27 shows the cutting machine. In the upper left, we see two panels which are

transparent plastic windows. The window panels can move along slide rails. The

cutter is installed behind the windows. We can see the crystal and cutter through the

windows. When we first adjust the ingot location, we open the windows and see the

ingot location through a telescope which is seen on the lower right in the Fig. 2.27.

Fine adjustment of the ingot orientation was made first manually with two circular

handle seen in the lower part of the figure. Finer adjustment was made by stepping

motors installed near the handles. A controller also control the diamond saw to cut the

ingot.
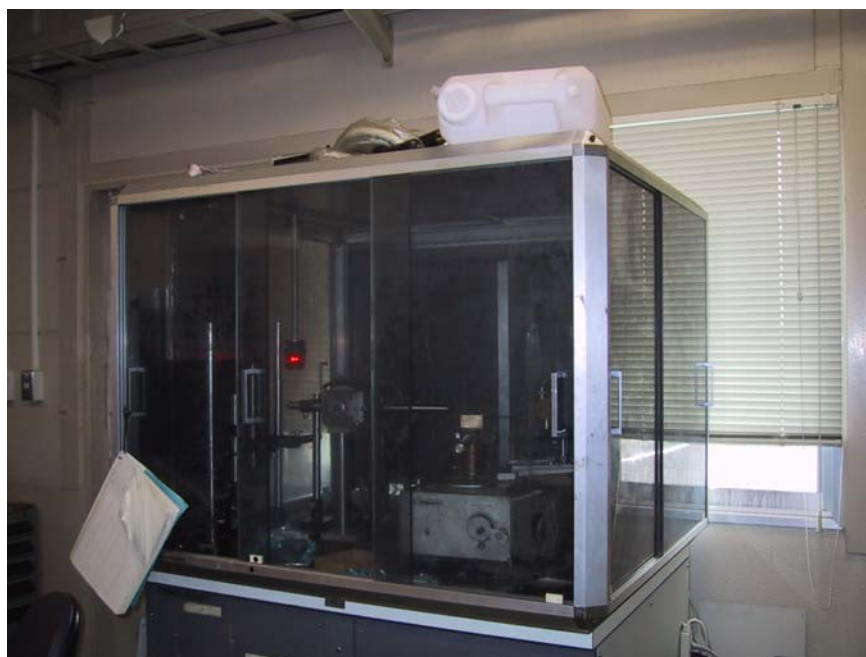
Fig. 2.28 Ordinary x-ray diffractrometer used to examine the crystal blades for the

analyzer.
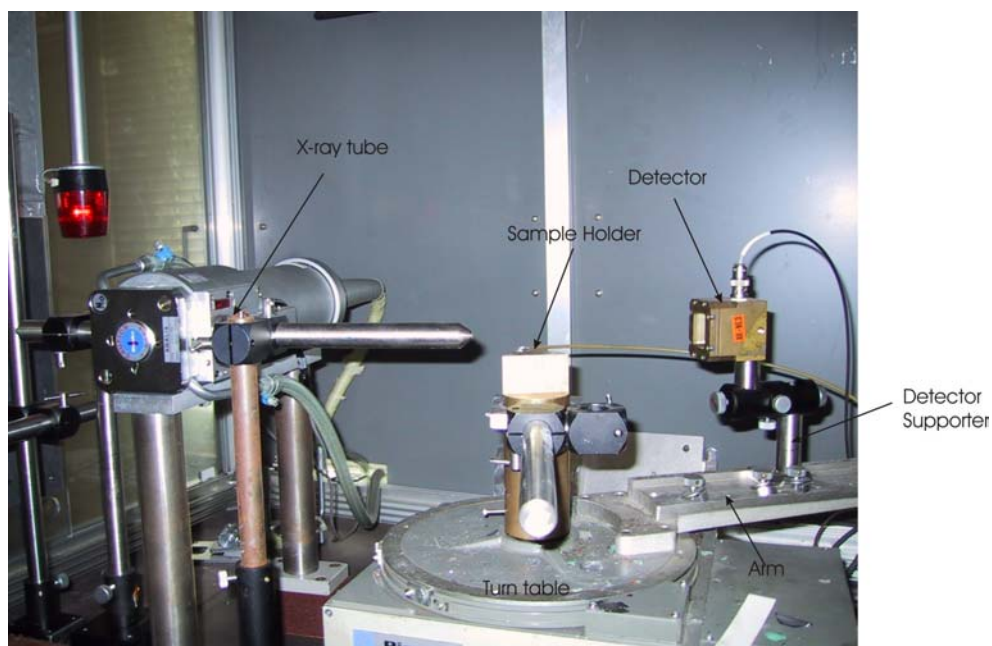
Fig. 2.29 X-ray diffractrometer exhibiting, from left to right, an x-ray tube, a sample holder and an x-ray detector.

The crystal axis of the cut out blades was examined by an x-ray diffractometer with which the direction of the Bragg angle was observed. Figure 2.28 shows the x-ray diffractometer used. The figure illustrates the whole aspect of the diffractometer. It is installed in a large transparent plastic box. In the box, we can recognize an x-ray tube, a sample holder and a detector. In order to see the major part of the picture, we show the elements illustrated in Fig. 2.28. In Fig. 2.29, we show it in more detail. On the left side of the picture, we see the x-ray tube. The power supply to the x-ray tube is placed out side the plastic box. The sample (crystal) holder is located on the top of the column fixed to the center of a turn table. From the turn table, an arm sticks out. On the arm, we find a detector. While the crystal is rotated by the turn-tables the intensity of the signal out of the detector is measured. From the angle position of the turn-table when the output signal from the detector is maximum, we find the Bragg angle.

The crystal cleaning before etching was carried out as follows: The crystal was cleaned in an ultrasonic cleaning machine. We used acetone for 5-10 min cleaning, in new acetone for further 5-10 min cleaning, in ethylalcohol for 5-10 min cleaning and in purified water for a few minutes cleaning. In etching process, 3 acid may used, 1) HNO_3, 2) HF and 3) CH_3COOH. They were mixed in 5:3:3 ratios. This formula is called CP4. The crystal was put in acid and left for 5 min. The thickness 100-200 μm was lost during these processes.

2.3 Experimental Procedure

Using crystals for analyzer prepared in the way described in the proceeding section, we carried out practical measurements. In this section, the experimental set up is described. As mentioned already, three optical arrangements for refraction imaging measurements were used. They are "Owl", the plane parallel analyzer system, and the wedge analyzer system.

2.3.1 'Owl'

Using "Owl", experiments were performed at beamline BL 20B at SPring-8. Figure 2.30 shows schematic diagram of "owl". In this beam line, a double crystal monochromator is installed upstream the experimental station. The x-ray beam from the storage ring is monochromatized there and sent to the "Owl" system. The monochromatized x-ray beam falls first on the asymmetric cut crystal monochromator in order to collimate monochromatic x-rays and expand the beam cross section. A monochromator with an asymmetrically cut crystal with an index of (311) was used. The situation is illustrated in Fig. 2.30. The asymmetrically cut crystal has the surface which is not parallel to the reflection net plane. In the present case, the reflection net

plane is the (311) plane. This plane was selected because it is easy to cut this plane from the ingot. As the x-ray photon energy, we selected 35 keV because this energy can satisfy the Bragg condition for the (311) plane. Further the 'Owl' comprises a monolithic crystal as shown in Fig. 2.30. A specimen has been put into a channel between two crystal wafers. Images have been stored on x-ray films used as detector. The exposure time for each measurement was 1-2 min.
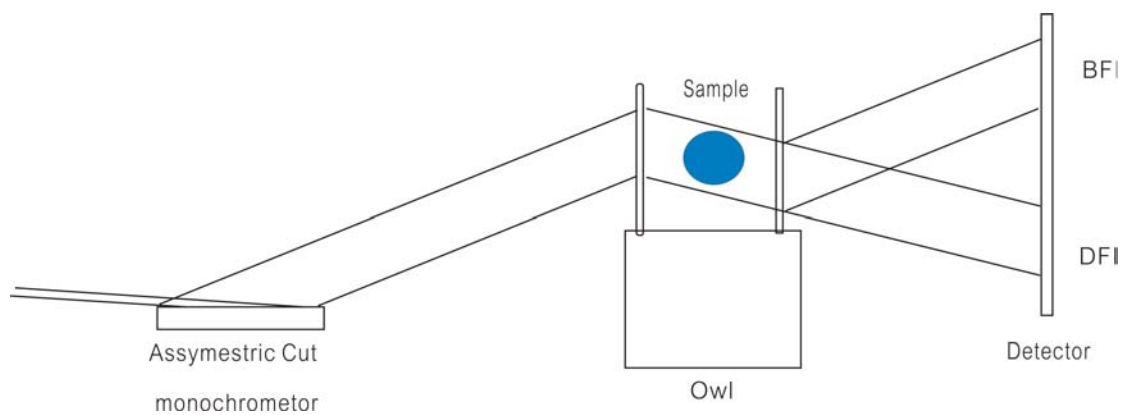
Fig. 2.30 Schematic diagram of experimental setup using "owl".

In practical measurements, 6 kinds of ivory specimens were used. They were placed in cylindrical boxes made of a variety of seal materials with a diameter of approximately 20 mm. Sample had a rod shape. They were a hard ivory available from Central and Western Africa, a soft ivory in East and Southern Africa, a mammoth tusk, a tooth of a Dutch water buffalo, a tooth of a sperm whale and a tooth of hippo. The results of will be presented in the next chapter.
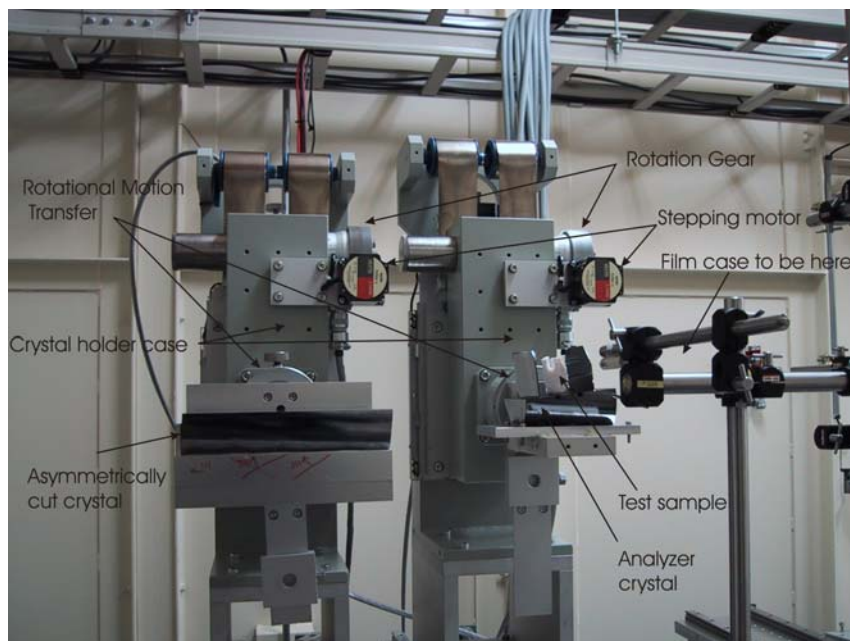
Fig. 2.31 Side view of the experimental setup for "owl" at BL20B, SPring-8.
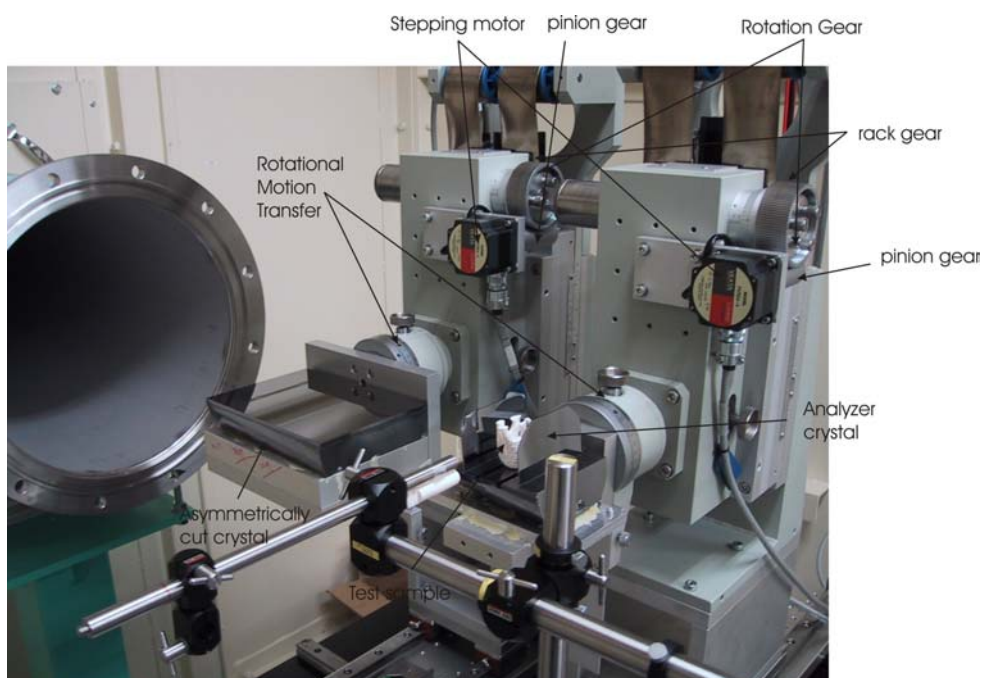
Fig. 2.32 Bird eye view of the experimental setup for "owl" at BL20B, SPring-8.
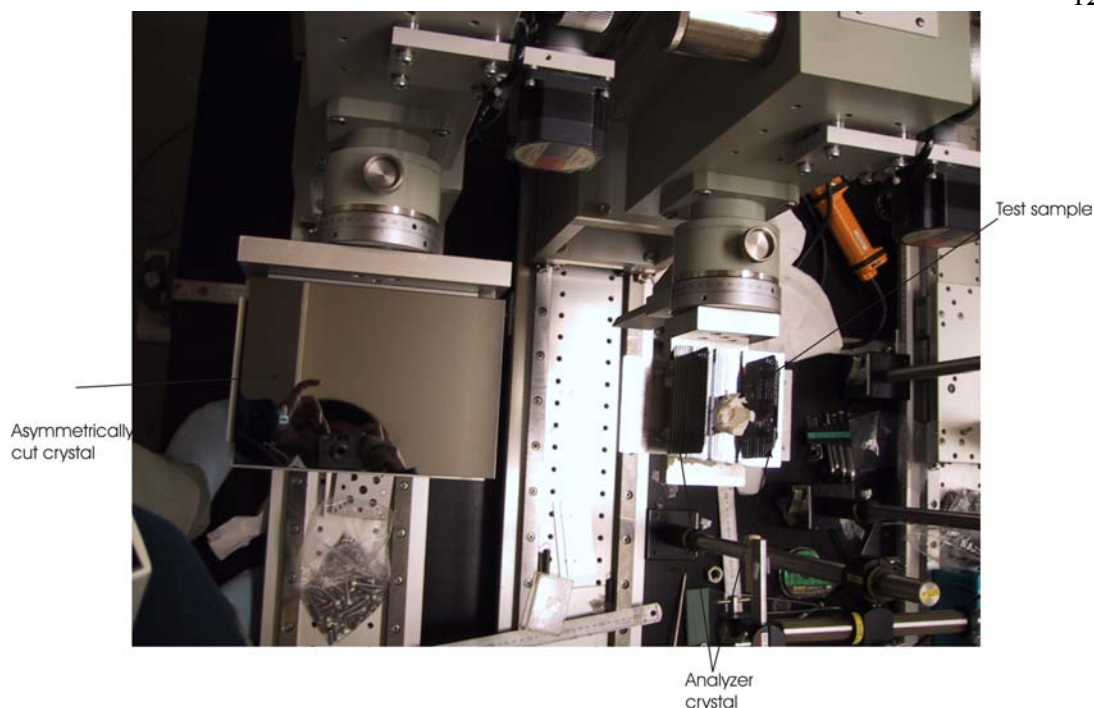
Fig. 2.33 Top-view of the experimental setup using "owl" at BL20B, SPring-8.

The practical settings up of the instrument are shown in Figs. 2.31, 2.32 and 2.33. The pictures included in the figures are those of the same setup viewed from different directions. Figure 2.31 shows the side view that includes all important elements. There are two similar holders of crystals. Both have devices to rotate crystals. Precision rotation is made by stepping motors. Rotational motions of crystals around horizontal axis are made through the mechanism of many gears. First, the rotational motion of a stepping motor is transferred to a rotation gear by means of the pinion-rack mechanism. The rotational motion of the rotation gear is transferred to the crystal holder through the rotational motion transfer. Crystals are rotated precisely around the horizontal axis.

The bird eye view shown in Fig. 2.32 illustrates a nearer view. In the picture, the pinion-rack mechanism and the rotational motion transfer are better viewed. The surface of the asymmetrically cut crystal can be seen clearly. Small

rotation wheels on the rotational motion transfer are connected to the rotational

motion transfer and make coarse adjustment. A test sample is clearly seen in this

picture.

Fig. 2.33 shows the top view. In this figure, not only the elements to

make the rotational motion but also the crystals are clearly seen. Particularly two

analyzer crystal blades and test sample is recognized clearly.

2.3.2   The Plane Parallel Analyzer

We also used another analyzer crystal system. It is the plane parallel

crystal analyzer and the wedge shape crystal analyzer systems. The experiments were

performed at beamline BL 14B at PF, KEK. The layouts of the elements are

schematically shown in Fig.2.34. An asymmetrically cut crystal was used to collimate

monochromatic x-rays and expand the beam cross section from the double crystal

monochromator at an upstream station of the beamline. In this case, the

asymmetrically cut crystal had the net reflection plane of the (440) index. We used

x-rays with a photon energy of 35 keV. First, the parallel plane analyzer was

installed. A specimen was installed between the asymmetrically cut crystal

monochromater and parallel plane analyzer which divides the x-ray beam to dark and

bright field images. Images were stored on x-ray films. The exposure time for each

picture was approximately 40 sec. In this experiment system, breast phantom RMI

156 was used as a specimen. It comprises sixteen types of cancerous fibers, speck and

discs which are embedded in wax. Phantom specimen x-ray pictures were also taken

without acrylic plate as will be shown later in Fig. 2.38.
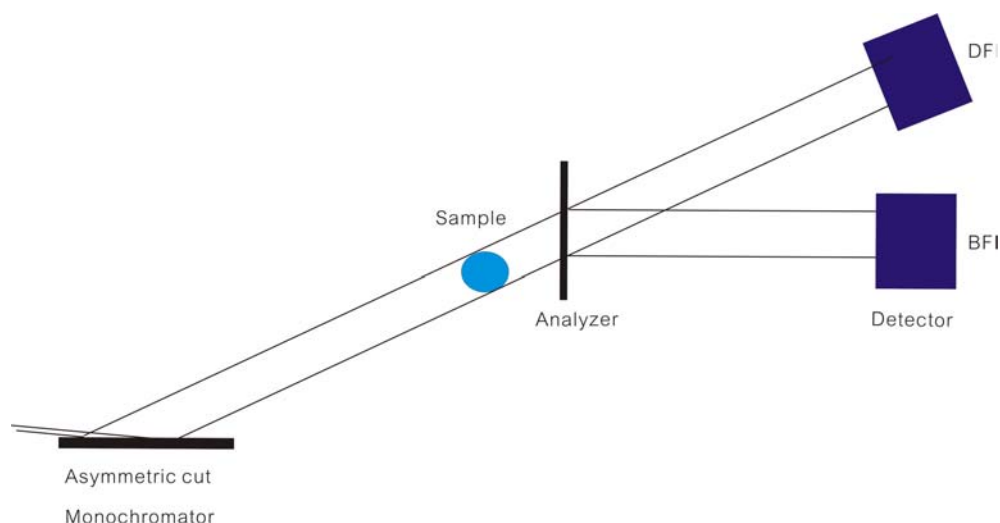
Fig. 2.34 Schematic diagram and picture of experimental setup at BL14B in PF, KEK. Wedge and parallel plane analyzers are used there.

Practical experimental setup is shown in Figs. 2.35, 2.36 and 2.37. The pictures show the inside of Hutch B in BL14. The schematic illustration of BL14 is shown in Fig. 2.1. On the left side of the picture in Fig. 2.35, the beam pipe of BL14C which passes through the Hutch B is seen. In the central part of the picture, two similar chambers are found. They are the chambers containing shutters and apertures. The x-rays from the storage ring is monochromatized with the monochromator B placed upstream outside Hutch B. The two beams coming inside the Hutch, one is not used. Thus, the beam exit of the chamber on the right side is closed. Both of the beams belong to BL14B.

In Fig. 2.36, the experimental setup is shown in more detail. The monochromatized x-rays are coming out of the shutter chamber through a Be window. An intensity monitor is installed just upstream the Be window. Further upstream, a slit chamber is installed. The x-ray beam proceeds in air after coming out of the chamber system through the Be window, it falls on the asymmetrically cut crystal

monochromator. The monochromatic x-ray beam expanded by the crystal then hit

a specimen that is a

white rod and shown on the left side of the picture.

Fig. 2.35   Experimental setup inside Hutch B in BL14B of PF at KEK.

Fig. 2.36 Experimental setup inside Hutch B in BL14B of PF at KEK.
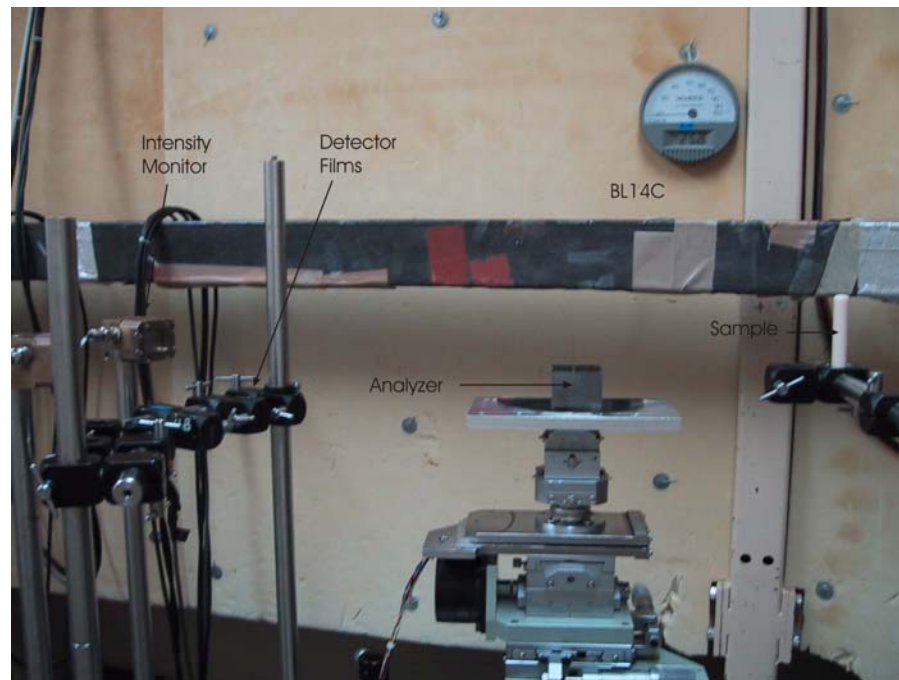
Fig. 2.37 Experimental setup picture at BL14B of PF at KEK.

Figure 2.37 shows the setup of the further downstream part. In the center of the picture, the analyzer crystal is shown. On the right side of the picture, we notice the specimen, a white rod. A detector x-ray film is set in a cassette. The cassette is installed on a holder shown on the left side. Another x-ray intensity monitor is also installed here.
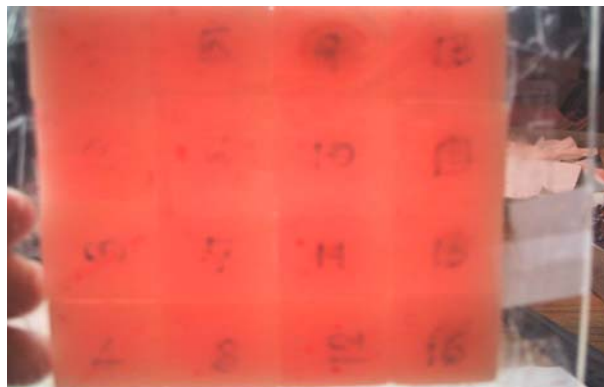
Fig. 2.38 Picture of breast cancer phantoms that are collected on an acrylic plate.

2.3.3 The Wedge Analyzer

The wedge analyzer crystal was also used in this beam line. In the experiments, the experimental setup is almost the same as that in case of the plane parallel analyzer. The analyzer crystal was replaced with the wedge analyzer. Thus, the layouts of the elements are schematically shown in Fig. 2.34. Two specimens were employed. Images have been stored on electron microscopy films with spatial resolution of 5 μm. The exposure time for each picture was approximately 1 min.

First specimen was the accredited phantom RMI 156 comprising sixteen types of cancerous fibers, speck and discs which are embedded in wax. The phantoms were collected and fixed on an acrylic plate. The picture of them is shown in Fig. 3.38. Note the author's fingers holding the acrylic plate found on the left side of the picture. When the image of each phantom is measured, each phantom was taken off from the acrylic plate and fixed on the sample holder. Thus, phantom x-ray pictures were taken without acrylic plate.

Second specimens were a variety of seal which is made of ivory: Hard ivory available from Central and Western Africa, soft ivory in Eastern and Southern Africa, mammoth tusk, teeth of Dutch water buffalo, teeth of sperm whale, teeth of hippo and plastic. The x-ray images of them were measured one by one. All the experiments were carried out with x-rays with an energy of 35 keV.

The use of high energy x-rays with high intensity is quite advantageous since they penetrate the human body more easily than those with energies of 20-25 keV that are used in the contemporary mammography examination system. In the contemporary system available in a clinic, an x-ray source part is pressed on the patient's breast. In many cases, this brings pain to the patient. Thus the use of synchrotron x-rays

with an energy of 35 keV removes the pain coursed by the source pressed on the

patient breast, since the pressing is not necessary in case of synchrotron radiation.

Chapter III

Experimental Results

The very important parts of the present work are described in the preceding chapter, where the work for developing the x-ray imaging camera is presented. The performance of the imaging system developed here is assessed by measuring the images of various specimens. The results of the work for the assessment are described here.

As already mentioned specimens employed here are the following:

- Hard ivory from western Africa

- Soft ivory from middle and eastern Africa

- Mammoth tusk.

- Water buffalo horn

- Tooth of sperm whale

- Tooth of hippopotamus

- Cancer phantom RMI 156

- Insects

- Composite materials

Images were stored on an electron microscopy films, x-ray films or nuclear plate with spatial resolution of approximately 10 μm or better. The exposure time for each picture was approximately 1–2 min. As mentioned already, measurements were carried out at BL14B of the Photon Factory and BL20B of the Spring8. In what follows, the results are described according to the optical systems used.

3.1 'Owl'

Three kinds of samples are employed for the demonstration of the dark field imaging taken with Owl. They are ivories, a composite material and mammographic phantom specimens. The ivory samples comprise a hard ivory obtained from Central and Western Africa, a soft ivory in East and Southern Africa, a mammoth tusk, a tooth of a Dutch water buffalo, a tooth of a sperm whale and a tooth of hippo. The composite material consists of boron fibers of 300 μm diameter embedded in the middle of 1.0 mm thick Al plate. Its absorption coefficient is 1.7 cm^{-1} at 35 keV. The third sample is a 7 mm thick wax block containing a nylon fiber of a 400 μm diameter. This sample is the in mammographic accredited phantom RMI 156 obtained from Gammex in Wisconsin. In these samples, only poor contrast has been achieved in the bright field images if the measured with ordinary x-rays of 35 keV. The images are invisible if they are recoeded by the absorption-contrast method.

Figures 3.1 and 3.2 show dark-field images of ivories. In this case, images with better contrast as expected theoretically are obtained. For obtaining good x-ray dark-field images, we need to control only the thickness of the analyzer and the collimator in the course of fabricating them. This system can accommodate a relatively large size sample in the space between the analyzer and the collimator. By this new technique we are able to observe the internal fine structures of materials used in a variety of research fields such as biology, medicine, materials science and physics.
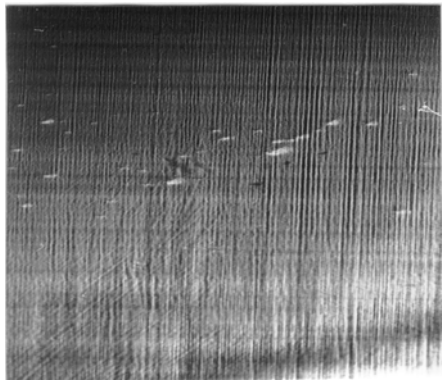
(a) Hard Ivory
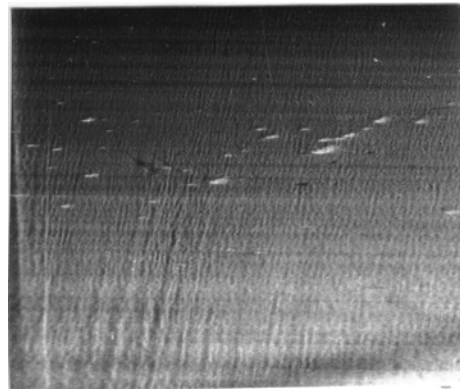
(b) Soft Ivory

(c) Tusk of Mammoth

(d) Horn of Dutch water buffalo
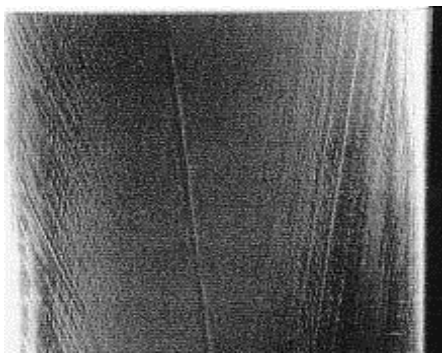
(e) Tooth of Sperm whale

(f) Tooth of Hippo

Fig. 3.1 Fibrous structure of (a) hard ivory, (b) soft ivory, (c) mammoth tusk, (d) tooth of Dutch water buffalo, (e) tooth of sperm whale and (f) tooth of hippo taken by the 'Owl' system with x-rays at energy of 35 keV. These are projection of 20 mm diameter seal materials. One can easily obtain the image of the internal structure each specimen in a nondestructive way.
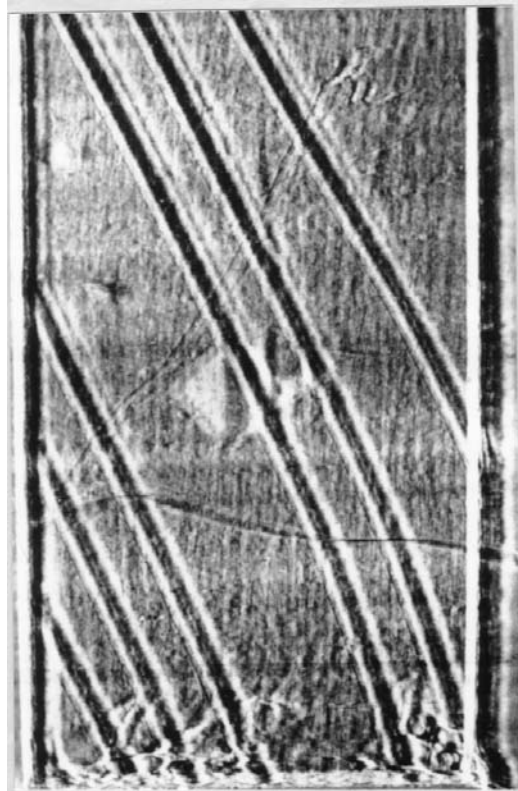
Fig. 3.2 Dark-field image of Al plate of 1.0 mm thickness containing boron fibers with 300 μm diameter taken by the "Owl" system. This structure had been invisible under illumination of only plane-wave x-rays. This dark-field contrast is a collection of all x-rays due to the refraction process excluding the component of the forward x-rays. The field size is approximately 7.0 mm by 12.0 mm.

Figure 3.1(a)-(f) clearly show the inner structure of ivories. The internal structure of an ivory is the character inherent in itself. The images shown in Fig. 3.1 indicate the difference of the details of the pattern so that they offer the data to distinguish different ivories. The internal structure of hard ivory shows very periodic lines, while soft ivory and mammoth tusk show less regular lines compared with hard ivory. The image of the mammoth tusk even shows additional structure with which it is distinguished from others clearly. The image of the horn of the Dutch water buffalo has many tree-like structures in the center as a characteristic feature. The image of the tooth of a sperm whale and that of a hippo show slant lines extending from edge to center. The slant lines in the hippo tooth image are smoother than those of sperm whale. This aspect of the difference in the details of image pattern is quite useful in non-destructive investigation of such materials.

The image of the Al plate with embedded boron fiber shown in Fig. 3.2 is also quite interesting. In the image, the structures brought about by the boron fibers are clearly resolved with good contrast. Al and B belong to the same column in the periodic table. There are in the rows adjacent to each other. Thus their physical and chemical properties are alike in some respects. The x-ray absorption coefficients and the refractive indices are of similar magnitude in both materials. This makes it difficult to observe the structure like are shown in Fig. 3.2. In fact, the image pattern conspicuous in Fig. 3.2 can not be obtained by ordinary absorption image nor by bright field refraction imaging.

Figure 3.3 shows the dark field x-ray image of piece of the mammographic accredited specimen RMI 156. The thickness of the specimen is 7 mm. The cross section is 5 mm x 5 mm. The image of nylon fiber of 400 μm diameter is distinct in the picture. Bubbles accidentally brought in the specimen during the course of the

fabrication process are also clearly resolved. In the ordinary x-ray absorption imaging the structure exhibited

in the image of Fig. 3.3 cannot be seen clearly.
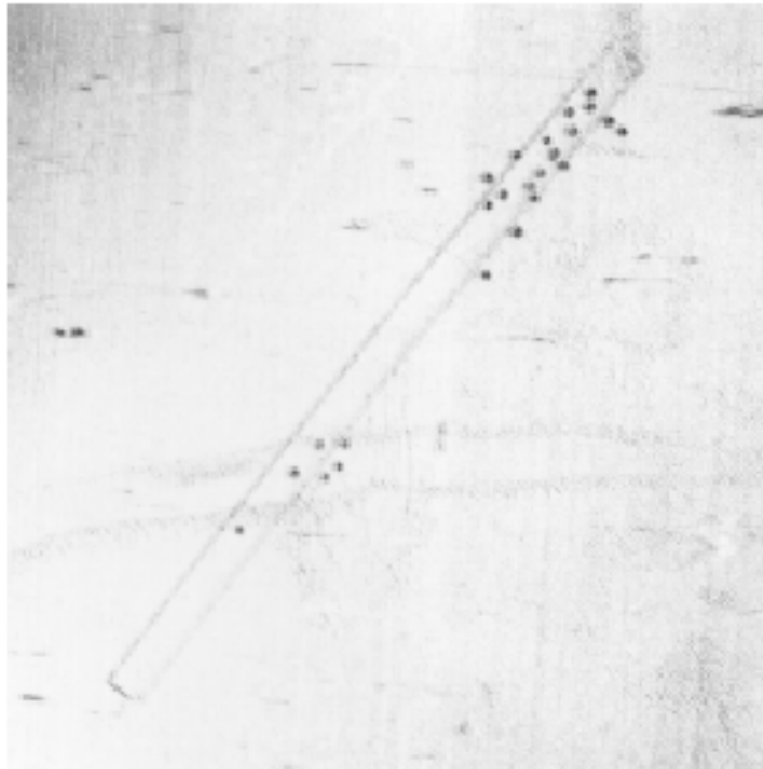
Fig. 3.3 The dark field image of a component piece of the mammographic accredited phantom specimen RMI 156.

3.2 The Plane Parallel Analyzer

Experiments were performed at beamline BL14B of Photon Factory using hard x-rays from a 5T superconducting magnet vertical wiggler. Very good agreement between calculated and experimental values of $I_O(\varphi)$ and $I_G(\varphi)$ given in (2.4) and (2.5) has been confirmed. The beam intensities to measure images were stored on a nuclear plate. The exposure time was approximately 60s. Although the measured spectra are not shown here, the obtained data are in agreement with those shown in Fig. 2.17.

Fig. 3.4 X-ray picture of component pieces of mammographic accredited phantom specimens RMI 156. A monochromatic X-ray beam with a size of 15 mm by 15 mm is used. The edge of its piece is clearly recognized.

X-ray pictures of the mammographic accredited phantom specimens RMI 156 are shown in Fig. 3.4. These are for the estimation of the usefulness of the OWL optic system. The phantom specimens RMI 156 is supplied by Gammex, U.S.A.. It consists of 16 blocks each of which has a dimension of 20 mm 20 mm and a thickness of

7 mm. This cross sectional dimension is the same as that of x-rays used for measurements. The brest cancer phantom specimens contain nylon fibers of a 400 μm diameter. The specimens are 7 mm thick. They are molded in wax blocks. The

existence of fibers is well recognized in the images of some blocks. In two specimens, bubbles are found. Such bubbles may have been introduced during the course of the fabrication of the specimens. The thin horizontal lines seen in all pictures are not real ones. They are produced in the processes of the development of films. Another possibility is that the feature is that it is included in the incoming x-ray beam. This pattern may be caused by carbon atoms contained in the crystal of the upstream monochromator. Such carbon atoms, if any, are located in the periodic manner in the lattice.

The fibers in the specimens simulate the pseudo cancer tissue structure. As mentioned in the preceding chapter, the accurate optical alignment of the optical components and the use of crystal blades with the accurate parallel crystal surfaces of the required index are crucial issue for obtaining good dark field images. Furthermore, there is the situation that analyzer crystal blade is degraded by prolonged irradiation with x-rays. This degradation arises from the radiation damage and the surface deterioration. Thus the crystal blades to replace the degraded one must be prepared on the site. Both the degradation and the optical alignment not very well preformed give rise to the deviation from the condition to produce the dark field images.

The data shown in Fig. 3.4 are taken in optical system of the parallel surfaces crystal blade well aligned. Therefore, the forward diffracted beam to produce the dark field images is mixed with the diffracted beam to produce the bright field image to some extent. The pictures in the third column of Fig. 3.4 correspond to dark field images because of the virtual absence of a background. X-ray pictures of breast cancer phantom showed very clear inner images of three kinds of inclusions such as fibers, speck and discs. The picture shown on the lower row and most left part was not taken. Even some of the discs

(a)   (b)
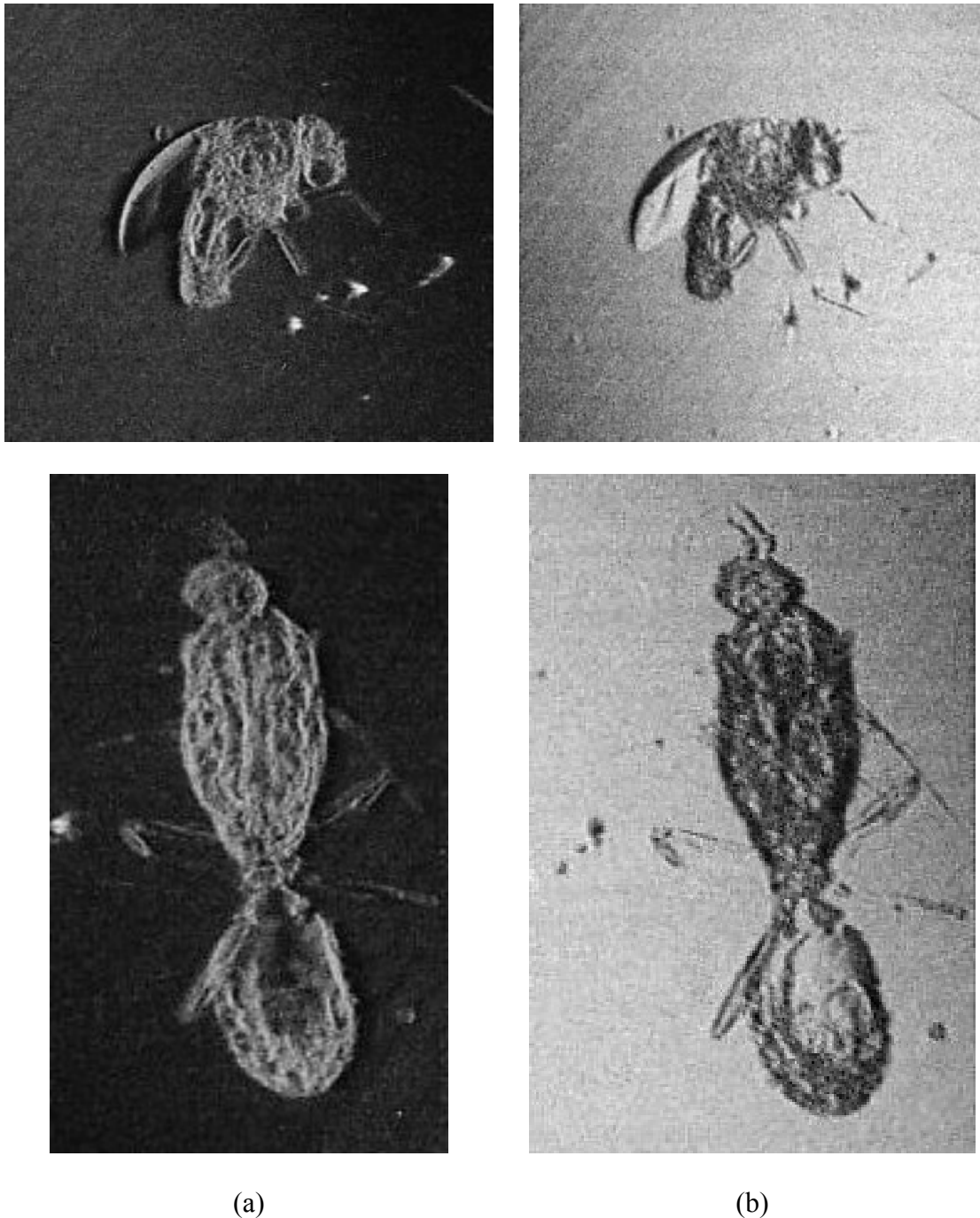
Fig. 3.5 (a) Dark-field images and (b) bright-field images of a fly (upper panel) and a mosquito (lower panel) embedded in polymethymethacrylate. The cross section of the x-ray beam is 5 mm x 5 mm. Exposure time using a nuclear plate was approximately 60s. The dark-field images (a) have almost no background.

show additional contrast which might show how each was formed. If we compare the images shown in Fig. 3.4 with those taken by the absorption contrast method, we find

the latter images have very low contrast. In these measurements the dose rate of exposure is 0.0114 mSv/sec.

Figure 3.5(a) shows a dark field image of insects embedded in polymethylmethacrylate. Figure 3.5(b) shows the image of the same sample measured in the bright field image mode. In both cases, the x-ray beam cross section was 5 mm x 5 mm. The sample was fabricated in a factory in Thailand where these kinds of embedded insects such as various butterflies for souvenirs are produced. The sample whose images are shown in upper row is for a fly and that in the lower row is for a mosquito. Figure 3.5(a) shows apparently almost no background. This increases the practical contrast appreciably.

The images of insects can be obtained with an ordinary x-rays in the absorption contrast mode. However, good contrast of the dark field image in the refraction contrast mode makes it possible to see the inner structure of the body. This is quite obvious in the dark field images shown in Fig. 3.5(a). In the bright field images, only the outside features of the insects are recognized.

As one more example of the images of a small insect, the dark and bright field images of a tick of a dog are shown in Figs. 3.6(a) and (b), respectively. Better contrast for inspecting inside the body is also conspicuous in this case. In addition to these two more similar examples are presented in Figs. 3.7 and 3.8. Figures 3.7(a) and (b) compare the dark field images of a SiC fiber embedded in the titanium with the bright field image of the same sample. Figures 3.8(a) and (b) shows the similar comparison of the dark and bright field images of a tooth a Dutch water buffalo.
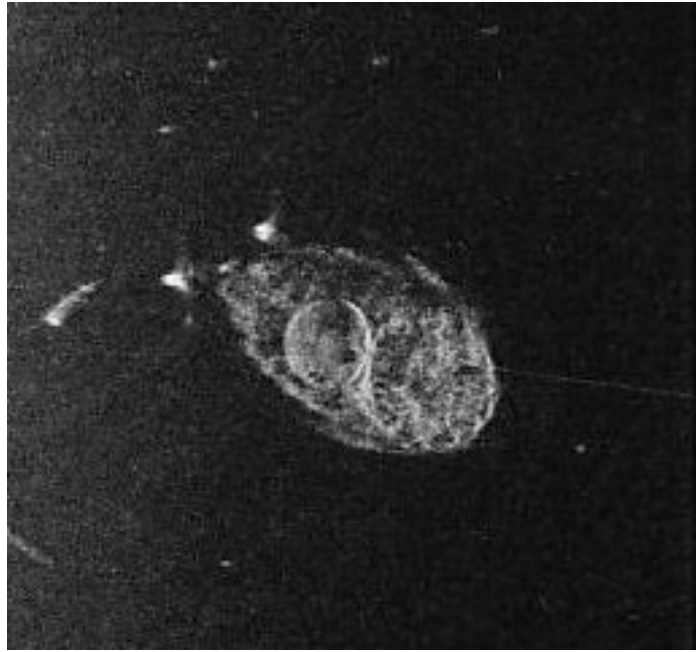
(a)

(b)

Fig. 3.6 (a) Dark-field images and (b) bright-field images of tick of the dog embedded in polymethymethacrylate. The cross section of the x-ray beam is 5 mm x 5 mm. Exposure time using a nuclear plate was approximately 60s. The dark-field images (a) have almost no background.
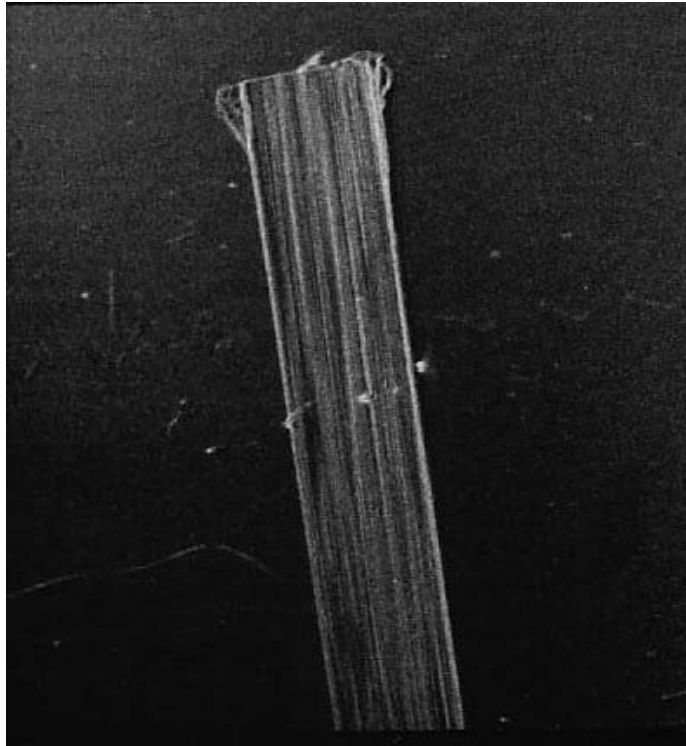
(a)
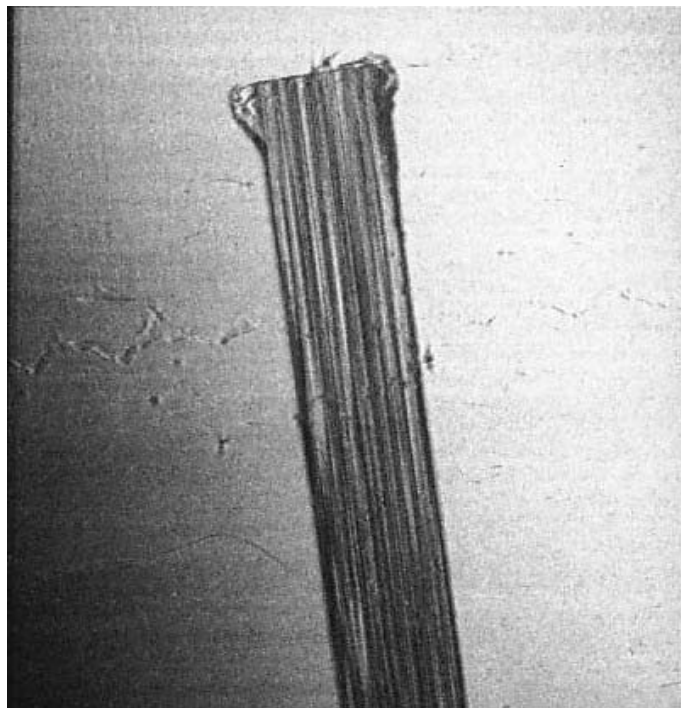
(b)

Fig. 3.7 (a) Dark-field images and (b) bright-field images of a SiC fiber embedded in

the titanium.
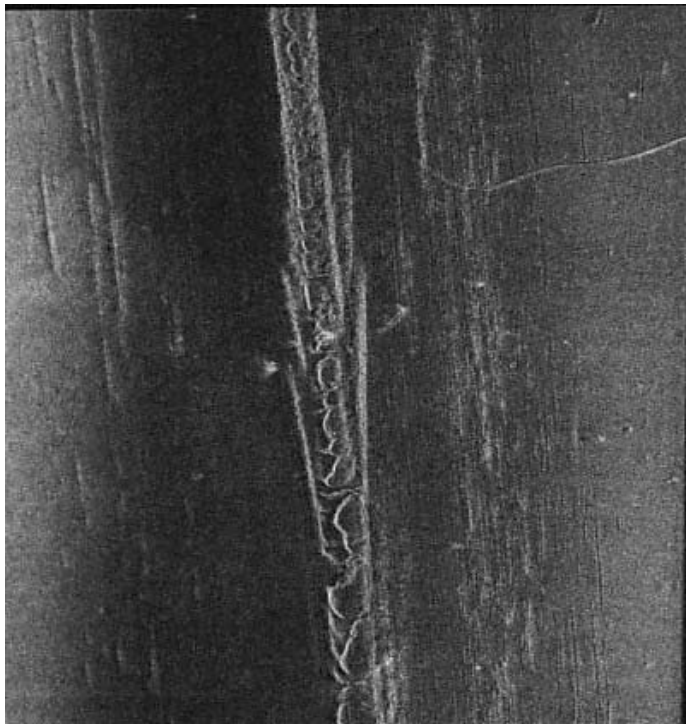
(a)
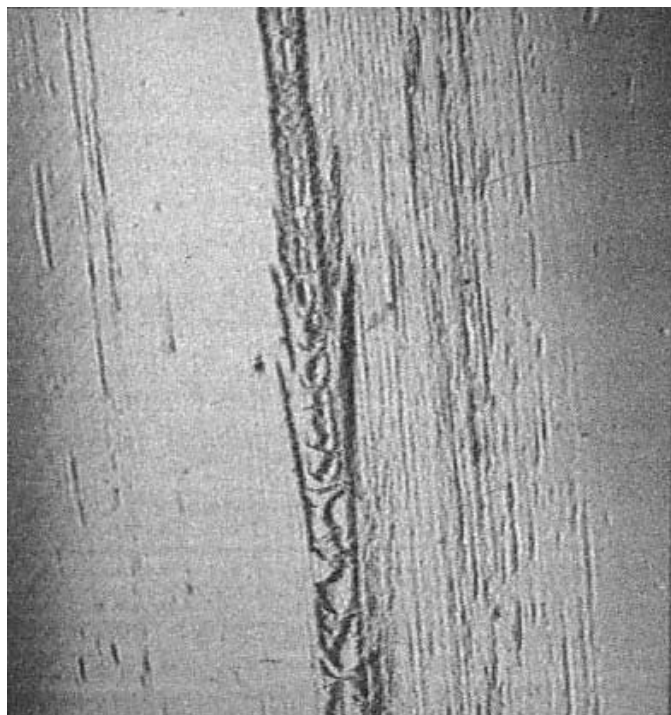
(b)

Fig. 3.8 (a) and (b) shows the similar comparison of the dark and bright field images of a tooth a Dutch water buffalo.

3.3 The Wedge Analyzer

Although the analytical form is shown in Appendix, the resulting beam intensity profile is shown in Fig. 2.25. According to this the images from a wedge-shaped analyzer have the stripe profile. In this pattern, the forward diffraction beam and the diffraction beam show up alternately on the recorder film. This is the objective to investigate first.
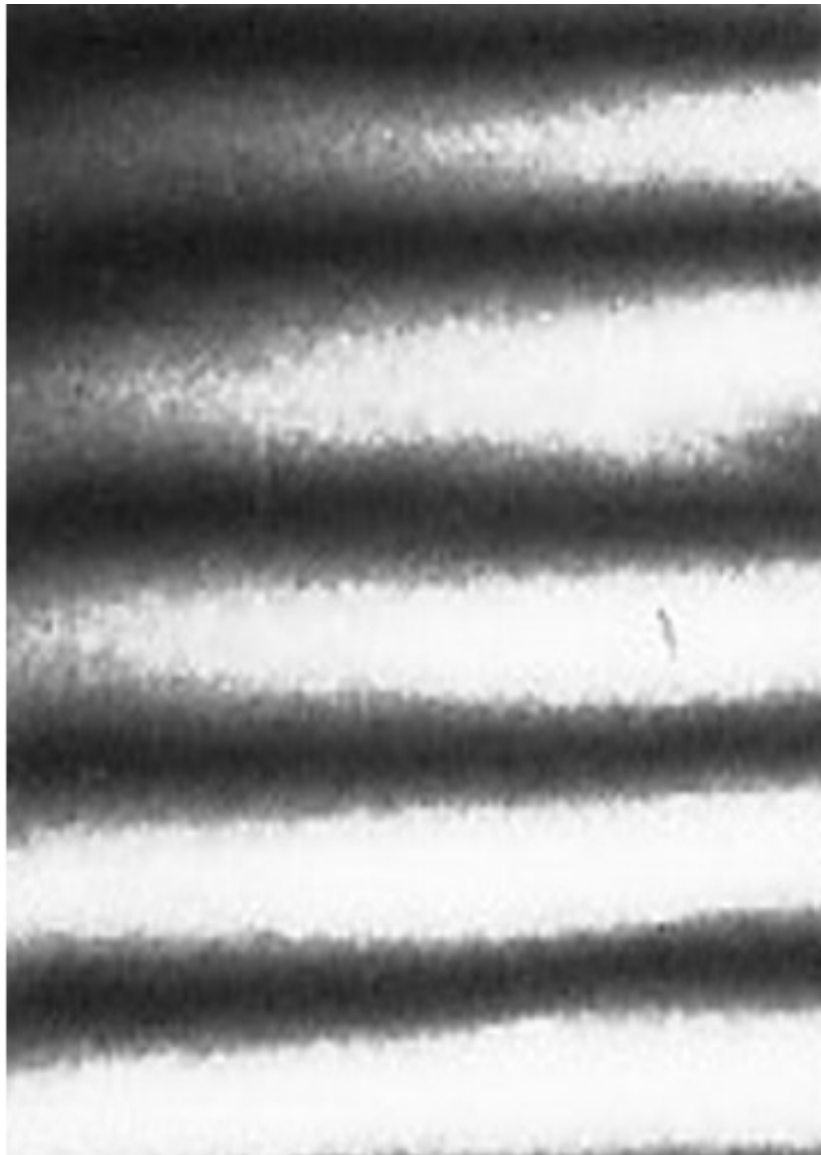
Fig. 3.9 Images of O- and G-wave which are diffracted by a wedge-shaped analyzer crystal.

Experiments were carried out at beamline BL14B using a radiation from a 5T vertical wiggler at Photon Factory. Images were stored on x-ray films. The exposure time was about 60s. Figure 3.9 shows the image of the refracted x-ray beams. Figure 3.9 clearly shows the bright field beam and dark field beam alternately on the same film. This is as expected from the theory illustrated in Fig. 2.25. The situation that the bright field image and the dark field image can be recorded on the same film is capable of increasing the efficiency of the observation and quite convenient, since both bright field and dark field images are obtained at one time.

X-ray pictures of the mammographic accredited phantom RMI 156 are shown in Fig. 3.10. Since the beam size was not sufficiently large to cover the whole part of an 16 individual object. Therefore, the picture only a part of each specimen is shown in Fig. 3.10. In some picture, the images are bent in the edge areas. This is caused by the incomplete optical alignment. Although the dark field images are narrower than the bright field images, they offer important information that a sample has inside. X-ray pictures of breast phantom specimens shows clear images of inner structure. They illustrate two kinds of contents as fibers and speck. Figure 3.10 also show fibers simulating the normal tissues we see. The materials shown here are explained in the table in section 1.3.9 following Fig. 1.29. Fibers simulate the normal tissues, specks cancer and some obscure images tumors. They are clearly resolved.

In case of discs which simulate tumors in Fig. 3.10 is still difficult to see it by our eye. If we compare the images shown in Fig. 3.10 with those taken by the absorption contrast method, we recognize that the latter images have very low contrast. The exposure dose rate is 2.46 Gy. If we compare the dark field image with the bright field image, the edge of the sample in bright field area is sharper. However, the inner structure is better

Fig. 3.10 X-ray picture of component pieces of RMI 156 taken with monochromatic

x-ray beam. The cross section of the view side is 10 mm by 15 mm.

resolved in the dark field image. This point will be shown more in detail in what

follows.

Fig. 3.11 The example illustrating better contrast in the dark field image. The

sample is a piece of the breast cancer phantom specimen no. 2 of RMI 156.

The cross section of the view side is 10 mm by 15 mm.
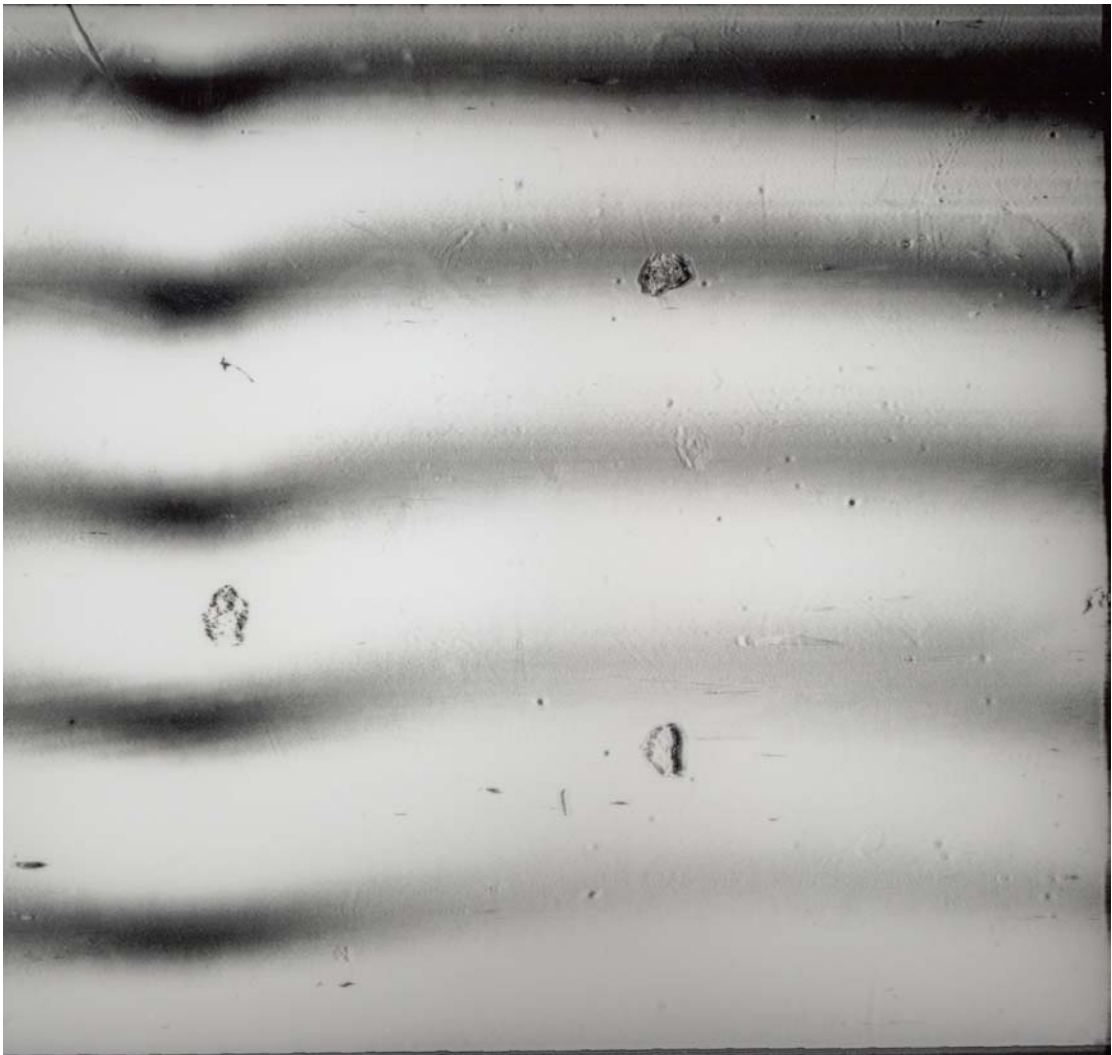
Fig. 3.12   The sample is a piece of the breast cancer phantom specimen no. 6 of RMI

156. The cross section of the view side is 10 mm by 15 mm.

Fig. 3.13   The sample is a piece of the breast cancer phantom specimen no. 13 of

RMI 156. The cross section of the view side is 10 mm by 15 mm.

Figure 3.11 shows the example illustrating better contrast in the dark field image.
The sample is a piece of the breast cancer phantom specimens RMI 156. In this case,
because of the short time for processing printing, the contrast of the bright field image
is too low to illustrate the edge of the fiber.

Figure 3.12 show the similar example. Here images specks are recorded. Only the fringe parts are visible in the bright field images, while the inside structure of a speak is noticeable in the dark field image. The specks simulate cancers.

Fig. 3.13 shows the image that simulates a tumor. It is not easy to obtain the good contrast of the tumor image. In Fig. 3.13 the tumor part can be seen only in the dark field images.

X-ray picture of the Horn of a Dutch water buffalo is shown in Fig. 3.14. As in the case of the data shown for other optical systems, the sample was in the form of a seal. The inner structure of the Horn of Dutch water buffalo is clearly identified. It has many trees like structure in the center. The edges of the seal is recognized as the vertical lines. In order to show the inner structure more distinctly, a part of the seal is made thinner. The surfaces of the seal are parallel in the part where thicker round part is removed. Figure 3.12 show the boarder as a horizontal line. Above it, the dark and bright images are curved. This is caused by the round surface of the seal. If we compare the dark field images with the bright field images, we find the internal structure is better resolved in the dark field image.
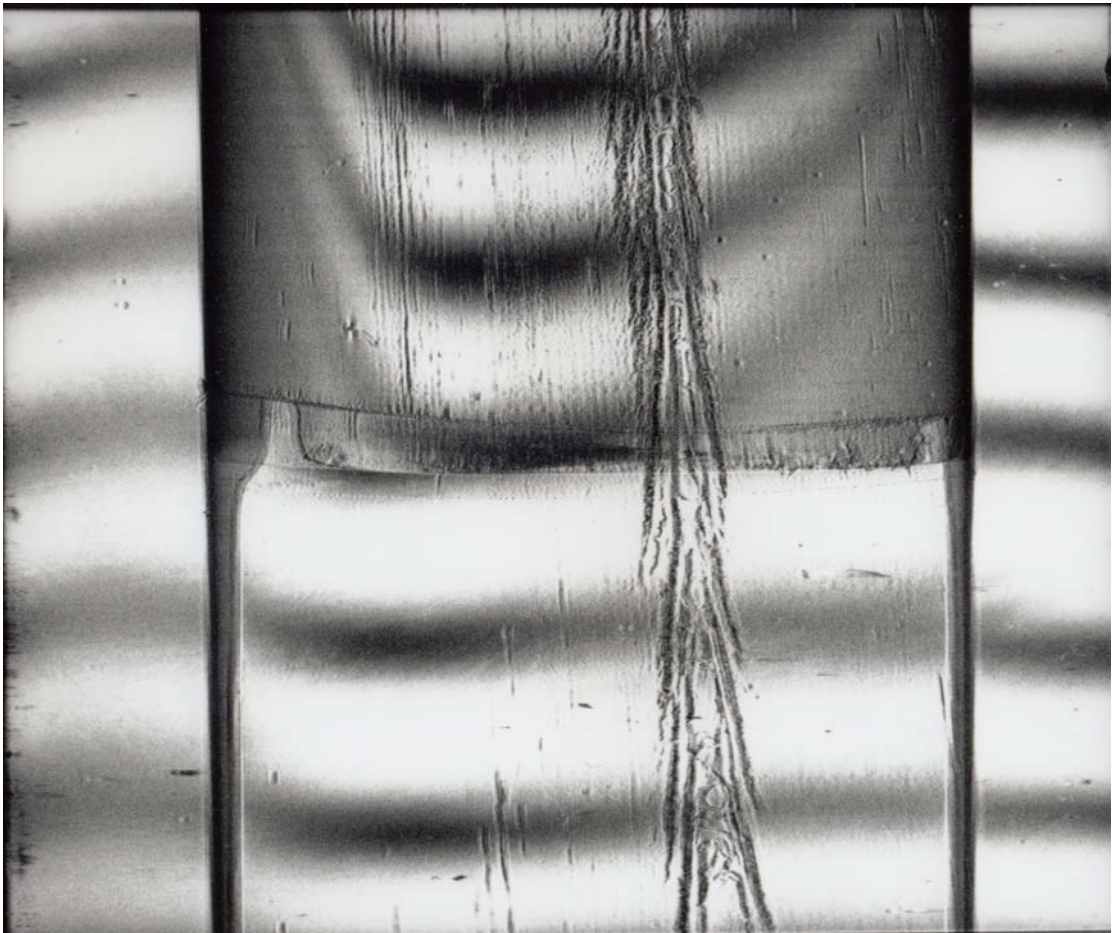
Fig. 3.14 X-ray picture of seal which was made by horn of Dutch water buffalo. The cross section of the view side is 10 mm by 15 mm.

The examples presented so far indicate that the distinctive nature of the dark field image as good contrast is also the case of the optical system with a wedge-shaped analyzer crystal. Two problems are remarked in the optical system with a wedge-shaped analyzer. One is that the dark field image portion is narrower than that of the bright field image. The other is the boarder of the dark field image part to the bright field image is most sharp. Thus the region where the dark field image and the bright field image are mixed together. Both natures are inherent in the principle of operation. In spite of these problems, the examples of the images obtained here appear to show the usefulness of the optical system using the wedge-shaped analyzer crystal.

Chapter IV

Discussion and Conclusion

The research work carried out for the present thesis is summarized as follows:

(1)   The usefulness of the refraction contrast imaging is shown theoretically.

(2)   It is shown that the use of synchrotron radiation is indispensable for realizing the refraction contrast imaging.

(3)   The optical system for realizing the refraction imaging are designed and built.

(4)   Excellent contrast expected in the dark field imaging is experimentally examined and proved.

In spite of the success of the investigations, however, the practical test experiments revealed a few problems to be solve in the future. They are summarized as follows:

(i)   The alignment of the optical system must be carried out very accurately.

(ii)   The analyzer crystal must be cut very accurately.

(iii)   Strong synchrotron radiation degrades the analyzer crystal.

(iv)   Chemical processing of exposed films and the printing affect the image contrast crucially.

The issues described above are discussed more definitely in the following.

One can achieve x-ray dark-field imaging under a certain thickness of an analyzer crystal with an accuracy of 10 μm as exhibited in the lower panel of Fig. 2.16. Some figures such as a part of Fig. 3.3 have been taken as dark-field images. Other images shown there appear to be the mixture of the dark- and bright-field images. This is brought

about by the imperfect optical system. The major cause of this may be inaccurate crystal thickness because the accurate thickness control is not easy to realize. If thickness control fails, photon energy tuning cannot meet the condition for realizing x-ray dark-field imaging. This new technique is capable of visualizing the internal fine structure of any materials in a wide range of disciplines, such as medicine, biology, material science and possibly physics. Probably the images shown in Fig. 3.1 were not obtained in the system satisfying the condition of dark-field imaging accurately owing to optical imperfections. The images are also dependent on the film and printing procedures. This was not carefully controlled. The third line of the figure shows almost no background. Some of the image pictures show the features like striations that are not inherent in the specimens used but emergent in the incident x-rays coming from the upstream optical system as a monochromator, as mentioned in the preceding chapter. This unwanted background could be suppressed by introducing a high-quality crystal or by data processing. It should be pointed out that one can simultaneously take three images, phase-interference contrast, refraction contrast and absorption contrast.

A technique to reconstruct three dimensional images using the images that are of two dimensional in practical has been reported (Defrise, Townsend and Clack, 1989, Defrise, Clack and Townsend, 1995). In this technique, images are obtained using absorption-based contrast. This is equivalent to CT scanning. Since the absorption imaging has the limitation of the application of application in that various specimens, particularly those excised human bodies, have low absorption contrast as the intrinsic nature. Thus, it is very much desirable for us to extend this technology to the refraction contrast imaging.

A pioneering work to apply the image reconstruction technique of the two dimensional case to the refraction contrast imaging has been carried out by Dilmanian (Dilmanian, 2000) using a simple cancer phantom specimen. For realizing this, the first step for us to do is that the optical system must be established so as to supply the sufficiently good image with good contrast. For establishing it, the photographic recording of images is the initial stage of the investigation. This is what we implemented in present work. This trial has been successful. The samples of breast cancer phantom similar to ones used here were measured by an Italian group (Arfelli, Bonvicini, Bravin, Cantatore, Castelli, Palma, Michiel, Fabrizioli, Longo, Menk, Olivo, Pani, Pontoni, Poropat, Prest, Rashevsky, Patti, Rigon, Tromba, Vacchi, Vallazza and Zanconati, 1998) and French group (Fiedler, Bravin, Thomlinson, Keyrilainen and Suortti, 2001). Our data give resolution and contrast than those they obtained.

When the major part of these basic technique is achieved, the technique to record the image by electronic methods as one with CCD cameras much be established. Then the computer software for the three dimensional reconstruction of the images is required.

The radiation dose will also be carefully taken into account before applying the method clinically. The intravenous coronary angiography (Hyodo, Nishimura, Ando, 1991) has now been established technique of an application of synchrotron radiation to medical diagnosis. In several synchrotron radiation laboratories over the world, clinics for this are attached. In these clinics a special care is taken not to give patients too much dose. In the future use of synchrotron radiation for CT scan using refraction contrast imaging similar caution must be paid.

We have been successful to distinguish ivories and other similar materials by a new technique, the dark field imaging. Each piece of 16 breast cancer phantom specimens showed very clear element. Every detailed structure such as fiber structure, disc type and speck shape has been successfully revealed. Because of the mechanism of refraction contrast available in this x-ray optics system, the images of edges of any inclusions are emphasized too much. Nevertheless this has been taken only without additional acryl so that as a next step the phantom together with the acryl which simulates a real breast thickness of 45 mm has to be imaged. A whole phantom can be taken by a single shot if using the fairly large size monochromatic x-rays available at BL 20B at SPring-8. That each element in a phantom piece showed so clear edge encourages us to try to see realistic cancer in excised tissue. In other words unless applied to excised human tissue we can not draw out a decisive conclusion whether or not our system works properly.

A lot of fringes seen in the background may bother quality of images a lot. This is probably due to growth striations which may correspond to a rotation and pulling speed of a grown crystal. Basically one can subtract this by a computational technique but it appears to be much better that the quality control of the crystal itself is possible.

The use of the wedge-shaped crystal analyzer is a new technique to let the bright and dark image be taken on one picture. The work implemented in the present thesis is a sort of preliminary one. In this sense, the work has been successful.

If we compare the present results with those in Shimoyama et al. (Shimoyama, Maeda, Sato, Ninomiya and Ozaki, 1997 and Shimoyama, Nakanishi, Hamanaga, Ninomiya and Ozaki, 1998), Van der Merwe et al. (Van der Merwe, Lee-Throp, Thackeray, Hall-Martin, Kruger, Coetzee, Bell and Lindeque, 1990) and Vogel et al.

(Vogel, Eglington and Auret, 1990), we find that they tired to distinguish ivory. However, they used technique of spectroscopy, isotopic analysis of C, N and Sr. Their results are shown in graphic display and this is a destructive method. The present technique of dark field image is much better because it is non-destructive method and the inner structure can easily be distinguished.

The refraction imaging of the present research is to develop methods to visualize the images of materials internal structures that can not be seen by means of the absorption contrast method. As mentioned already, we employed the photographic recording method because we have been interested in establishing the optical system. We have been successful to realize this purpose.

As the future prospects of the work, we point out the importance of the expansion of images. In case of the dark field imaging, the principle operation tells us that the expansion of the image is quite useful to separate the bright field images. This is particularly so in case of the optical system using the wedge-shaped crystal analyzer.

In addition to settle a very accurate optical system, the improvement in the data processing technique is also very importance. This indirectly enhances the resolution and contrast of images. The transfer to the electronic recording is also indispensable. This is crucial for realizing x-ray microscopy in materials imaging.

References

References

Ando, M., and Hosoya, S., (1972). An Attempt at X-ray phase contrast microscopy. In
G. Shinoda, K. Kohra and T. Ichinokawa (eds). **Proc. 6th Int. Conf on X-Ray Optics & Microanalysis** (pp.63-68). Tokyo: Univ. of Tokyo Press.

Ando, M., et al. (2001, March). An X-ray trichrome imaging 'Trinity': absorption, phase-interference and angle-resolved contrast. **Jpn. J. Appl. Phys.** 40: L298-L301.

Ando, M., et al. (2001, August). A new optics for dark-field imaging in X-ray region 'Owl'. **Jpn. J. Appl. Phys.** 40: L844-L846.

Ando, M., et al. (2002, July). X-Ray Optics 'Owl' and 'Trinity'. **Jpn. J. Appl. Phys.** 41: 4742-4749.

Ando, M., et al. (2002, September). Simple X-Ray Dark- and Bright-Field Imaging Using Achromatic Laue Optics. **Jpn. J. Appl. Phys.** 41: L1016-L1018.

Ando, M., et al. (2001, August). Possible Detection of Bony Trabeculae, Vascular Channels in Auditory Ossicles and Breast Cancer by Means of X-Ray Dark Field Imaging. **Proc. Joint Symp. Bio-Sensing and Bio-Imaging.** ed. Akatsuka, T. (Biology Radical Institute and the Japan Society for Analytical Chemistry, 2002): 95-100.

Arfelli, F., et al. (1998, September). Mammography of a phantom and breast tissue with synchrotron radiation and linear-array silicon detector. **Radiology.** 208: 709-715.

Arfelli, F., et al. (1995, February). Digital mammography with synchrotron radiation. **Rev. Sci. Instrum.** 66: 1325-1328.

Arfelli, F., et al. (2000, April). Mammography with synchrotron radiation: phase-detection techniques. **Radiology.** 215: 286-298.

Bonse, U. and Hart, M. (1965, April). An x-ray interferometer. **Appl. Phys. Lett.** 6: 155-156.

Bonse, U. and Hart, M. (1965, August). An x-ray interferometer with long separated interfering beam paths. **Appl. Phys. Lett.** 7: 99-100.

Chapman, D. et al. (1996, September). Mammography imaging studies using a Laue crystal analyzer. **Rev. Sci. Instr.** 67: 3360.

Clotens, P., Barrett, R., Guigay, J. R., and Shlenker, M. (1996, January). Phase objects in synchrotron radiation hard X-ray imaging. **J. Phys. D** 29: 133-146.

Cosslet, V.E. and Nixon,W.C. (1953, May). The X-Ray Shadow Microscope. **J. Appl. Phys.** 24: 616-623.

Dance, D.R. (1990, September). Monte Carlo calculation of conversion factors for the estimation of mean glandular breast dose. **Phys. Med. Biol**. 35: 1211-1219.

Defrise, M., Clack R., and Townsend, D. W. (1995). Image reconstruction from truncated, two-dimensional, parallel projections. **Inverse Problems.** 11: 287-313.

Defrise, M., Townsend, D. W., Clack, R. (1989). Three-dimensional image reconstruction from complete projections. **Phys. Med. Biol.** 34(5): 573-587.

Dilmanian, A. (2000). Computed tomography of x-ray index of refraction using the diffraction enhanced imaging method. **Phys. Med. Biol.** 45: 933-946.

Fiedler, S., Bravin, A., Thomlinson, W., Keyrilainen, J., and Suortti, P. (2001). Prospects for Diffraction Enhanced Imaging Mammography. **Proc. of Joint Symposium on Bio-sensing and Bio-imaging.** 1(B)-4: 111.

Gao, D., Gureyev, T. E., Pogany, A., Stevenson, A. W., and Wilkins, S.W. (1998). New methods of X-ray imaging based on phase contrast. In M. Ando and C. Uyama (eds). **Medical Applications of Synchrotron Radiation.** (pp. 63-71). Tokyo: Springer-Verlag.

Ingal, V. N., and Beliavskaya, E. A. (1995, November). X-ray plane-wave topography observation of the Phase contrast from a non-crystalline object. **J. Phys. D** 28: 2314-2317.

James, R. W. (1962). **The optical principles of the diffraction of X-rays.** Connecticut: OX Bow press.

Kato, N. and Lang, A. R. (1959). A study of Pendellosung Fringes in X-ray Diffraction. **Acta Cryst** 12: 784-794.

Kato, N. (1961). A Theoretical Study of Pendellosung Fringes. Part I. General Consideration. **Acta Cryst** 14: 526 – 533.

Kato, N. (1968, April). Spherical-Wave Theory of Dynamical X-Ray Diffraction for Absorbing Perfect Crystals. **J. Appl. Phys.** 39: 2225 – 2230.

Krol, A., et al. (1997, May). Laser-based microfocused X-ray source for mammography feasibility. **Med. Phys.** 24: 725-732.

Law, J. (1991, February). A new phantom for mammography. **Br. J. Radiol.** 64: 116-120.

Momose, A., Takeda, T., Itai, Y., and Hirano, K. (1996, February). Phase-contrast X-ray computed tomography for observating biological soft tissues. **Nature Medicine.** 2: 473-475.

Momose, A., Takeda, T., Itai, Y., Yoneyama, A., and Hirano, K. (1998). Perspective for medical applications of phase-contrast X-ray imaging. In M. Ando and C. Uyama (eds). **Medical Applications of Synchrotron Radiation.** (pp.54-61). Tokyo: Springer-Verlag.

Momose, A., Takeda, T., Itai, Y., Yoneyama, A., and Hirano, K. (1998, May). Phase-contrast tomographic imaging using an X-ray interferometer. **J. Synchrotron Rad.** 5: 309-314.

Pattanasiriwisawa, W., et al. (2001). Visualization of Biomedical Specimens by X-Ray Dark Field Imaging. **Proc.of Joint Symposium on Bio-sensing and Bio-imaging.** 1(B): 105-110.

Pinsker, Z. G. (1978). **Dynamical scattering of X-rays in crystals.** New York: Springer-Verlag.

Podurets, K. M., Somenkov, V. A., and Shil'stein, S. (1989, June). Refraction-contrast radiology. **Sov. Phys. Thech. Phys.** 34(6): 654-657.

Shimoyama, M., Maeda, H., Sato, H., Ninomiya, T., and Ozaki, Y. (1997, August). Nondestructive discrimination of biological materials by near-infrared fourier transform Raman spectroscopy and chemometrics: discrimination and mammoth tusks and prediction of specific gravity of the ivories. **Applied Spectroscopy.** 51: 1154-1158.

Shimoyama, M., Nakanishi, T., Hamanaga, Y., Ninomiya, T., and Ozaki, Y. (1998, February). Non-destructive discrimination between elephant ivory products and mammoth tusk products by glancing incidence X-ray fluorescence spectroscopy. **J. Trace and Microprobe Techniques.** 16 (2): 175-182.

Thomlinson, W., Chapman, D., Zhong, Z., Johnston, R. E., and Sayers, D. (1998). Diffraction enhanced X-ray imaging. In M. Ando and C. Uyama (eds). **Medical Applications of Synchrotron Radiation.** (pp. 72-77). Tokyo: Springer-Verlag.

Van der Merwe, N.J., et al. (1990, August). Source-area determination of elephant ivory by isotopic analysis. **Nature.** 346: 744-746.

Vogel, J.C., Eglington, B., and Auret, J.M. (1990, August). Isotope fingerprints in elephant bone and ivory. **Nature.** 346: 747-749.

Warren, B. E. (1969). **X-ray diffraction.** Massachusetts: Addison-Wesley Publishing Company.

Wilkins, S. W., Gureyev, T. E., Gao, D., Pogany, A., and Stevenson, A. W. (1996, November). Phase-contrast imaging using polychromatic hard X-rays. **Nature.** 384: 335-338.

Appendices

<div align="center">

Appendix I

Mathematical Background of the X-Ray Intensity

Expression.

</div>

A.1 The Fundamental Equation of Wave-Field

The filed vector must be followed Maxwell's equation for an electromagnetic field in an insulation medium:

$$d\mathbf{D}/dt = c \text{ curl } \mathbf{H}, \quad d\mathbf{H}/dt = -c \text{ curl } \mathbf{E} = -c \text{ curl } (\mathbf{D}/\eta) \tag{A.1}$$

The wave-field is consisted of large number of plane wave and it should be in term of reciprocal lattice.

Then
$$\mathbf{D} = e^{j\nu t} \sum_m \mathbf{D_m}\, e^{-j\,(\mathbf{Km}\bullet\,\mathbf{r})} \tag{A.2}$$

$$\mathbf{H} = e^{j\nu t} \sum_m \mathbf{H_m}\, e^{-j\,(\mathbf{Km}\bullet\,\mathbf{r})} \tag{A.3}$$

Where
$$\mathbf{K_m} = \mathbf{K_o} + \mathbf{r_m}^* \tag{A.4}$$

$\mathbf{K_o}$ is wave vector which is satisfied Maxell's equation.

From equation (A.3)

$$\text{curl } \mathbf{H} = j e^{j\nu t} \sum_m (\mathbf{H_m} \times \mathbf{K_m})\, e^{-j\,(\mathbf{Km}\bullet\,\mathbf{r})} \tag{A.5}$$

And equation (A.2)

$$\frac{1}{c}\frac{dD}{dt} = j\frac{\nu}{c} e^{j\nu t} \sum_m \mathbf{D_m}\, e^{-j\,(\mathbf{Km}\bullet\,\mathbf{r})} \tag{A.6}$$

From equation (A.1) right hand can rearrange in

$$k\mathbf{D_m} = \mathbf{H_m} \times \mathbf{K_m} \tag{A.7}$$

Which $k = 1/\lambda = v/c$. This equation is mean that the electronic induction in each constituent wave is perpendicular to the corresponding of wave-normal and magnetic filed.

Also equation (A.2) can rearrange in term of three-dimensional of co-ordinates.

$$\mathbf{D}/\eta = - e^{jvt} \sum_p \sum_q \phi'_p \mathbf{D}_q \, e^{-j\,(\mathbf{K}p+q \,\bullet\, \mathbf{r})} \tag{A.8}$$

Suppose $m = p + q$. Then

$$\mathbf{D}/\eta = - e^{jvt} \sum_m \sum_q \phi'_{m-q} \mathbf{D}_q \, e^{-j\,(\mathbf{K}m \,\bullet\, \mathbf{r})} \tag{A.9}$$

And
$$\text{curl} \,(\mathbf{D}/\eta) = je^{jvt} \sum_m \{\mathbf{K}_m \times \sum_q \phi'_{m-q} \mathbf{D}_q\} \, e^{-j\,(\mathbf{K}m \,\bullet\, \mathbf{r})} \tag{A.10}$$

From (A.3)

$$-\frac{1}{c}\frac{dH}{dt} = -\frac{vj}{c} \sum_m \mathbf{H}_m \, e^{-j\,(\mathbf{K}m \bullet \, \mathbf{r})} \tag{A.11}$$

Using Maxell's equation (A.1) and compare with (A.10) and (A.11). We get

$$k\mathbf{H}_m = - \sum_q \phi'_{m-q}(\mathbf{K}_m \times \mathbf{D}_q) \tag{A.12}$$

and put in (A.7). So

$$k^2\mathbf{D}_m = - \sum_q \phi'_{m-q} \{\mathbf{K}_m \times (\mathbf{K}_m \times \mathbf{D}_q)\} \tag{A.13}$$

Equation (A.13) can rearrange by the rule of vector product.

$$k^2\mathbf{D}_m = - \mathbf{K}^2_m \sum_q \phi'_{m-q} \mathbf{D}_{q[m]}$$

$$= - \mathbf{K}^2_m \phi'_0 \mathbf{D}_{m[m]} - \mathbf{K}^2_m \sum_{q \neq m} \phi'_{m-q} \mathbf{D}_{q[m]} \tag{A.14}$$

Suppose $\mathbf{D}_{q[m]} = \mathbf{D}_m$ so finally we get

$$\frac{K^2_m - k^2}{K^2_m} \mathbf{D}_m = \sum_q \phi_{m-q} \, \mathbf{D}_{q[m]} \tag{A.15}$$

This is fundamental equation of wave-field in the crystal which has amplitude m.

Then put $|\mathbf{K}_m| = k\,(1+\varepsilon_m)$ so (A.15) become

$$2\varepsilon_m\,\mathbf{D}_m = \sum_q \phi_{m-q}\,\mathbf{D}_{q[m]} \qquad\qquad (A.16)$$

By (A.2), (A.3), (A.4) and (A.16), the induction of whole wave-field at ant point is

$$\mathbf{D} = e^{j\nu t}\sum_m\left(\frac{1}{2\varepsilon_m}\sum_q \phi_{m-q}\mathbf{D}_{q[m]}\right)e^{-j\,(\mathbf{K}m\,\bullet\,\mathbf{r})}$$

$$= e^{j(\nu t - \mathbf{Ko}\,\bullet\,\mathbf{r})}\sum_m\left(\frac{1}{2\varepsilon_m}\sum_q \phi_{m-q}\mathbf{D}_{q[m]}\right)e^{-j\,(\mathbf{r}^{*}_{m}\,\bullet\,\mathbf{r})} \qquad (A.17)$$

Equation (A.17) represent plane wave of wave vector $\mathbf{K}_o$ traveling through crystal.
The amplitude is given by summation and bracket of (A.17) can calculate coefficient
and phase of the wave (m).

Equation (A.17) can rearrange to new form, if we put $\phi_{m-q} = \phi_0$ and $e^{-j\,(\mathbf{K}m\,\bullet\,\mathbf{r})}$ are all
equal. Then

$$\mathbf{D} = e^{j\nu t}\phi_o.\sum_m \frac{1}{2\varepsilon_m}\sum_q \mathbf{D}_{q[m]}\,e^{-j\,(\mathbf{K}q\,\bullet\,\mathbf{r})}$$

$$= \phi_o.\sum_m \frac{1}{2\varepsilon_m}\mathbf{D}_{[m]} \qquad\qquad (A.18)$$

Where $\mathbf{D}_{[m]}$ is perpendicular with $\mathbf{K}_m$ of $\mathbf{D}$ so (A.18) become

$$\mathbf{b} = \frac{1}{\Omega}\sum \frac{1}{\varepsilon_m}\,\mathbf{b}_{[m]} \qquad\qquad (A.19)$$

$\mathbf{b}$ is moment of dipole. This equation is same result of Ewald's equation.

A.2 Two-Wave Approximation of Dispersion Surface

From equation (A.19) is sum of right-hand side on n terms and $\mathbf{b}_{[m]}$ is contain
component of $\mathbf{b}$ which perpendicular to wave vector $\mathbf{K}_m$ from the wave point A to the
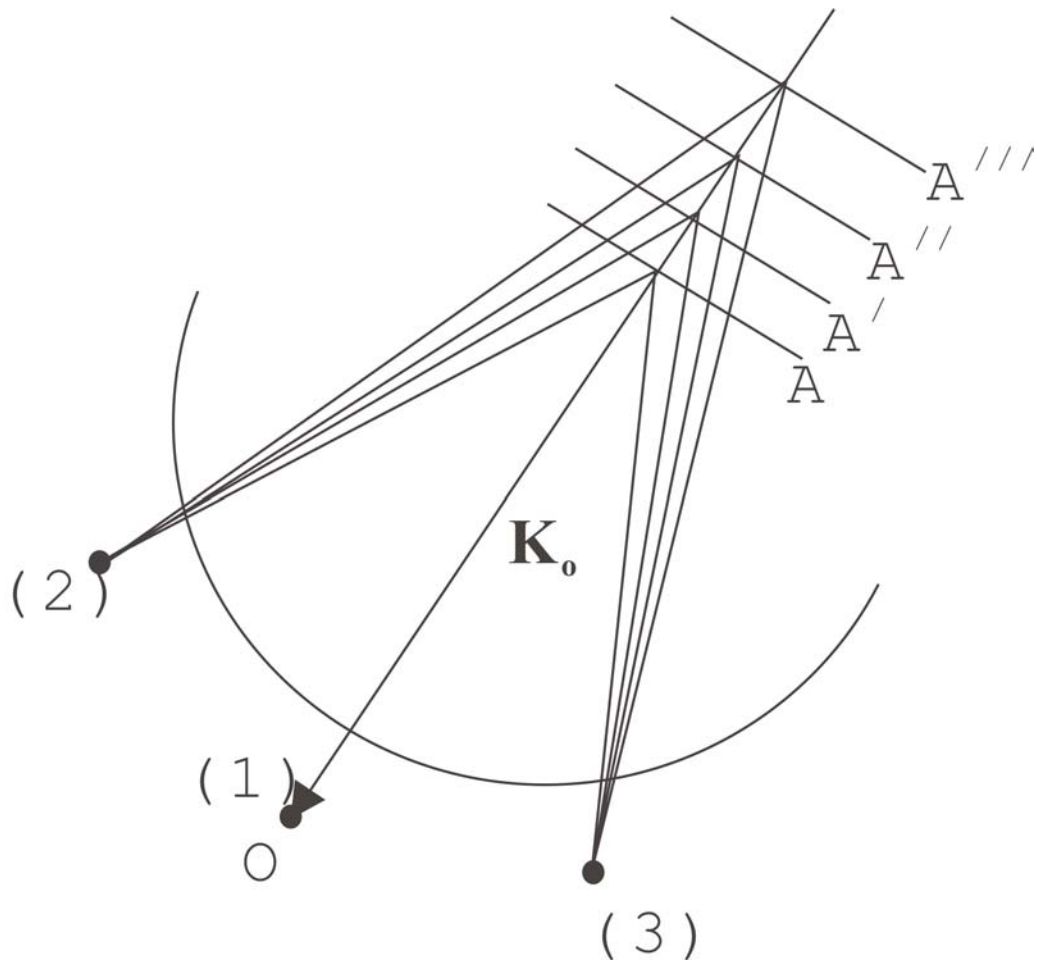
Fig. A.1   The wave-points and dispersion surface

reciprocal lattice (m). For a given position of A, $2n$ components are required for sum of right-hand side of (A.19). Therefore it is $2n$ linear equation contain ε_o only for $2n$ components. Then equation degree of $2n$ contain ε_o has $2n$ solution which call dispersion equation. Let A, A′ … (Fig. A.1) be the $2n$ possible positions of the wave-point which satisfied dispersion equation. Suppose that $\mathbf{K}_o$ is small range enough to the wave-sphere to produce interference wave. Then the dispersion surface which is the locus of all position of wave-point, give dynamically self-contained sets of interference waves so that the dispersion equation is need to describe dispersion surface.

Let two point of reciprocal lattice lie near sphere of reflection, is (o) and (m) which corresponding with wave vector $\mathbf{K}_o$ and $\mathbf{K}_m$. Suppose that dipole vibrations is perpendicular to plane containing with wave-vectors so that $\mathbf{b} = \mathbf{b}_{[m]}$. Then equation (A.19) is given to

$$\frac{1}{\varepsilon_o} + \frac{1}{\varepsilon_m} = \Omega \qquad (A.20)$$

Equation (A.20) show that wave point must be lie on hyperbolic sphere.

Consider 2 cases, (a) induction vector is perpendicular to $\mathbf{K}_o$ and $\mathbf{K}_m$, (b) induction is incline of plane.

In case (a) by equation (A.16),

$$(\phi_o - 2\varepsilon_o)\mathbf{D}_o + \phi_{-m}\mathbf{D}_m = 0$$

$$\phi_m\mathbf{D}_o + (\phi_o - 2\varepsilon_m)\,\mathbf{D}_m = 0 \qquad (A.21)$$

And also in case (b),

$$(\phi_o - 2\varepsilon_o)\mathbf{D}_o + \phi_{-m}\cos 2\theta\,\mathbf{D}_m = 0$$

$$\phi_m\cos 2\theta\,\mathbf{D}_o + (\phi_o - 2\varepsilon_m)\mathbf{D}_m = 0 \qquad (A.22)$$
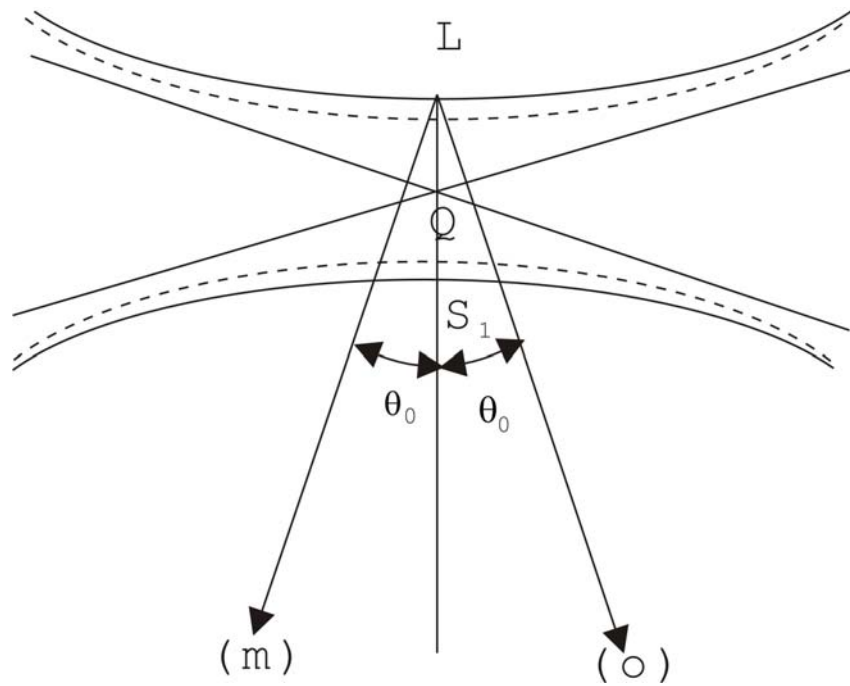
Fig. A.2   The dispersion hyperbolic of two waves.
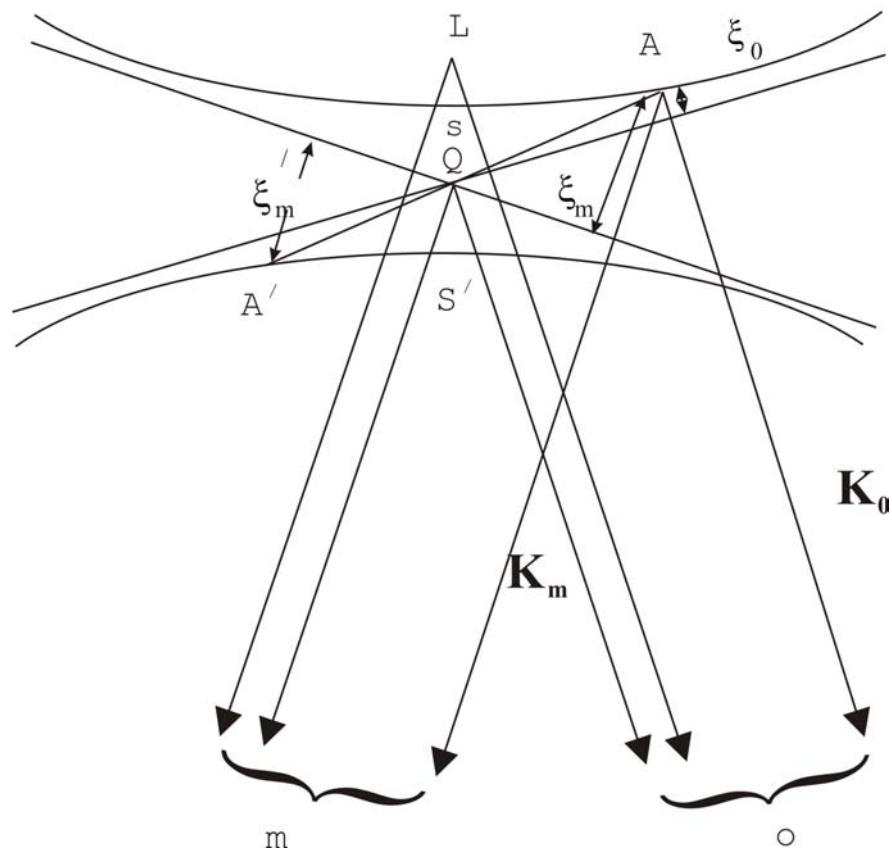
Fig. A.3   Trace of the dispersion surface for two waves.

Where 2θ is angle between $\mathbf{K}_m$ and $\mathbf{K}_o$ that it shown in Fig. A.2 which is equal $2\theta_o$ (θ_o is Bragg angle).

From Fig. A.3 $\mathbf{A_o}$ and $\mathbf{A_m}$ is wave vector $\mathbf{K}_o$ and $\mathbf{K}_m$ that is satisfied fundamental equation. If $\mathbf{K}_o$ and $\mathbf{K}_m$ are superposition, it produce a dynamically self-consistent wave-field in the crystal.

There are certain relationship between the amplitudes and phases of wave-fields corresponding to different wave-point. For case (a) and equation (A.21)

$$\frac{D_o}{D_m} = \frac{2\varepsilon_m - \phi_o}{\phi_m} = \frac{\phi_{-m}}{2\varepsilon_o - \phi_o}$$

or

$$\frac{D_o}{D_m} = \frac{2\xi_m}{k\phi_m} = \frac{k\phi_{-m}}{2\xi_o} \tag{A.23}$$

Assume that ξ_m is always same sign as long as $\mathbf{A}$ remains on the branch of hyperbolic, ϕ_m and ϕ_{-m} are constant. The phase different between $\mathbf{D}_o$ and $\mathbf{D}_m$ is constant all of wave-point on the same branch of hyperbolic.

A.3 Determination of the Wave-Point when the Crystal is Bounded by Plane Surface and a Primary Wave Enter It from Outside

A.3.1 Transmission and Reflection Coefficient by Plane Parallel Plate

In this case, $\mathbf{k}_m$ leave the lower surface, $\theta_o < \phi$, γ_m is positive and γ_o / γ_m is also positive quantity. The boundary conditions on the entrance surface is

$$\mathbf{D}_0^{(1)} + \mathbf{D}_0^{(2)} = \mathbf{D}_0^{(a)} \tag{A.24}$$

$$\chi_1 \mathbf{D}_0^{(1)} + \chi_2 \mathbf{D}_0^{(2)} = 0 \tag{A.25}$$

Where

$$\chi = \left(-\eta \pm \sqrt{\eta^2 + 4\frac{\gamma_m}{\gamma_0}\phi_m\phi_{-m}} \right) \Bigg/ 2\frac{\gamma_m}{\gamma_0}\phi_{-m} \tag{A.26}$$
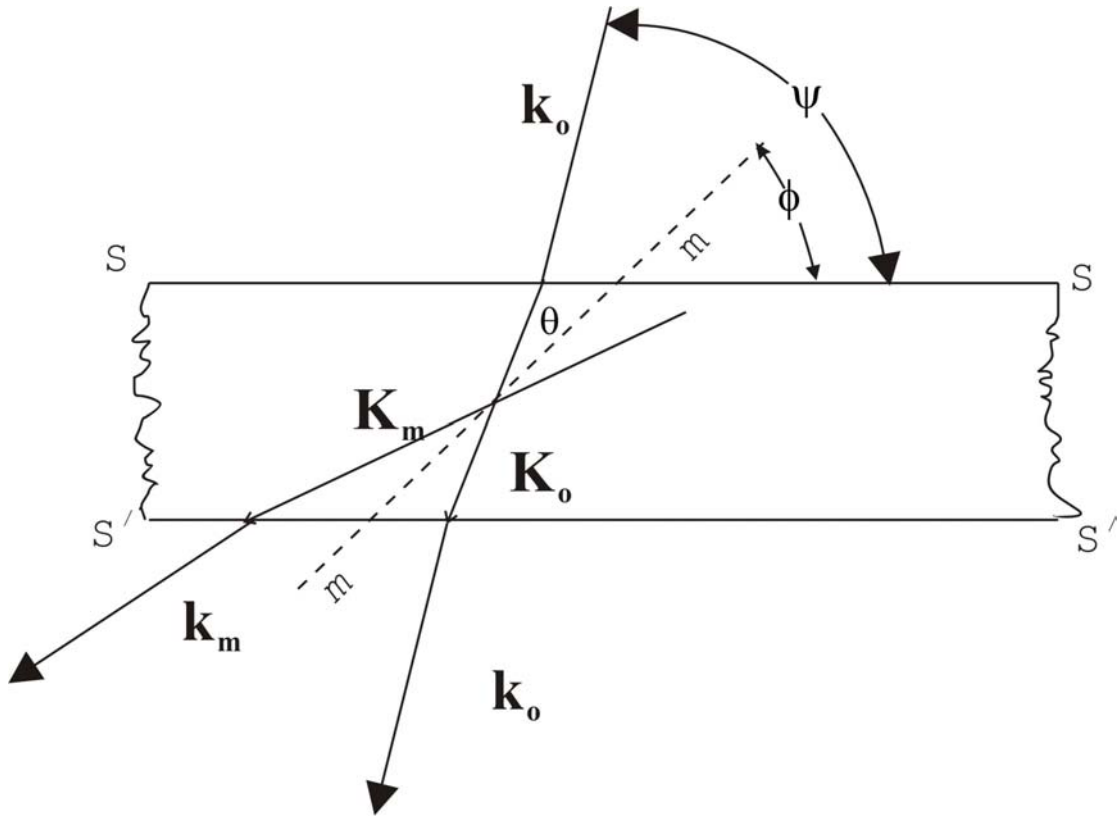
Fig. A.4   Transmission of x-rays by Laue reflection.

(A.26) and the exit surface should include phase factor and thickness t

$$\mathbf{D}_0^{(1)} \exp(-2\pi it\mathbf{k}_0^{(1)}) + \mathbf{D}_0^{(2)} \exp(-2\pi it\mathbf{k}_0^{(2)}) = \mathbf{D}_0^{(m)} \exp(-2\pi it\mathbf{k}_0^{(m)}) \qquad (A.27)$$

$$\chi_1 \mathbf{D}_0^{(1)} \exp(-2\pi it\mathbf{k}_0^{(1)}) + \chi_2 \mathbf{D}_0^{(2)} \exp(-2\pi it\mathbf{k}_0^{(2)}) = \mathbf{D}_h^{(m)} \exp(-2\pi it\mathbf{k}_h^{(m)}) \quad (A.28)$$

From equations (A.24) and (A.25)

$$\mathbf{D}_0^{(1)} = \frac{\chi_2}{\chi_2 - \chi_1} \mathbf{D}_0^{(a)}, \quad \mathbf{D}_0^{(2)} = -\frac{\chi_1}{\chi_2 - \chi_1} \mathbf{D}_0^{(a)} \qquad (A.29)$$

Then (A.27) and (A.28) become

$$\mathbf{D}_0^{(m)} \exp(-2\pi it\mathbf{k}_0^{(m)}) = \frac{\chi_2}{\chi_2 - \chi_1} \mathbf{D}_0^{(a)} \exp(-2\pi it\mathbf{k}_0^{(1)}) +$$

$$-\frac{\chi_1}{\chi_2 - \chi_1} \mathbf{D}_0^{(a)} \exp(-2\pi it\mathbf{k}_0^{(2)}) \qquad (A.30)$$

$$\mathbf{D}_h^{(m)} \exp(-2\pi it\mathbf{k}_h^{(m)}) = \chi_1 \frac{\chi_2}{\chi_2 - \chi_1} \mathbf{D}_0^{(a)} \exp(-2\pi it\mathbf{k}_0^{(1)}) +$$

$$- \chi_2 \frac{\chi_1}{\chi_2 - \chi_1} \mathbf{D}_0^{(a)} \exp(-2\pi it\mathbf{k}_0^{(2)}) \qquad (A.31)$$

From $\mathbf{k}_0^{(i)} = \mathbf{K}_0^{(a)} - \mathbf{K}\,\delta^{(i)}$ and $\mathbf{K}_0^{(a)} = \mathbf{K}_0^{(m)}$ in case plane parallel plate so it can be

rewrite (A.30)

$$\mathbf{D}_0^{(m)} = \mathbf{D}_0^{(a)} \frac{1}{\chi_2 - \chi_1} \exp(\pi it\mathbf{K}(\delta^{(1)} + \delta^{(2)}))$$

$$\bullet (\chi_2 \exp(\pi it\mathbf{K}(\delta^{(1)} - \delta^{(2)})) - \chi_1 \exp(-\pi it\mathbf{K}(\delta^{(1)} - \delta^{(2)})) \qquad (A.32)$$

For transmission coefficient

$$\mathbf{T} = \left| \frac{D_0^{(m)}}{D_0^{(a)}} \right|^2$$

$$= \frac{1}{|\chi_1 - \chi_2|^2} \left[|\chi_1|^2 + |\chi_2|^2 - 2\chi_1\chi_2^* \cos 2\alpha \right] \qquad (A.33)$$

Where
$$\alpha = \pi it\mathbf{K}(\delta^{(1)} - \delta^{(2)}) \tag{A.34}$$

And reflection coefficient is

$$R = \frac{\gamma_m}{\gamma_0}\left|\frac{D_h^{(m)}}{D_0^{(a)}}\right|$$

$$= \frac{\gamma_m}{\gamma_0}\frac{|\chi_1|^2|\chi_2|^2}{|\chi_2 - \chi_2|^2}(2 - 2\cos 2\alpha) \tag{A.35}$$

Rewrite (A.33) and (A.35) in function of W which W is normalized angular deviation from the center of the Bragg peak

$$W = \frac{\eta}{2(\phi_m\phi_{-m})^{1/2}(\gamma_m/\gamma_0)^{1/2}} \tag{A.36}$$

Suppose
$$\Lambda = \frac{1}{K(\phi_m\phi_{-m})^{1/2}}\sqrt{\gamma_0\gamma_m} \tag{A.37}$$

Then
$$T(W) = \frac{1}{1+W^2}(W^2 + \cos^2\pi t\sqrt{1+W^2}/\Lambda) \tag{A.38}$$

$$R(W) = \frac{\sin^2\pi t\sqrt{1+W^2}/\Lambda}{1+W^2} \tag{A.39}$$
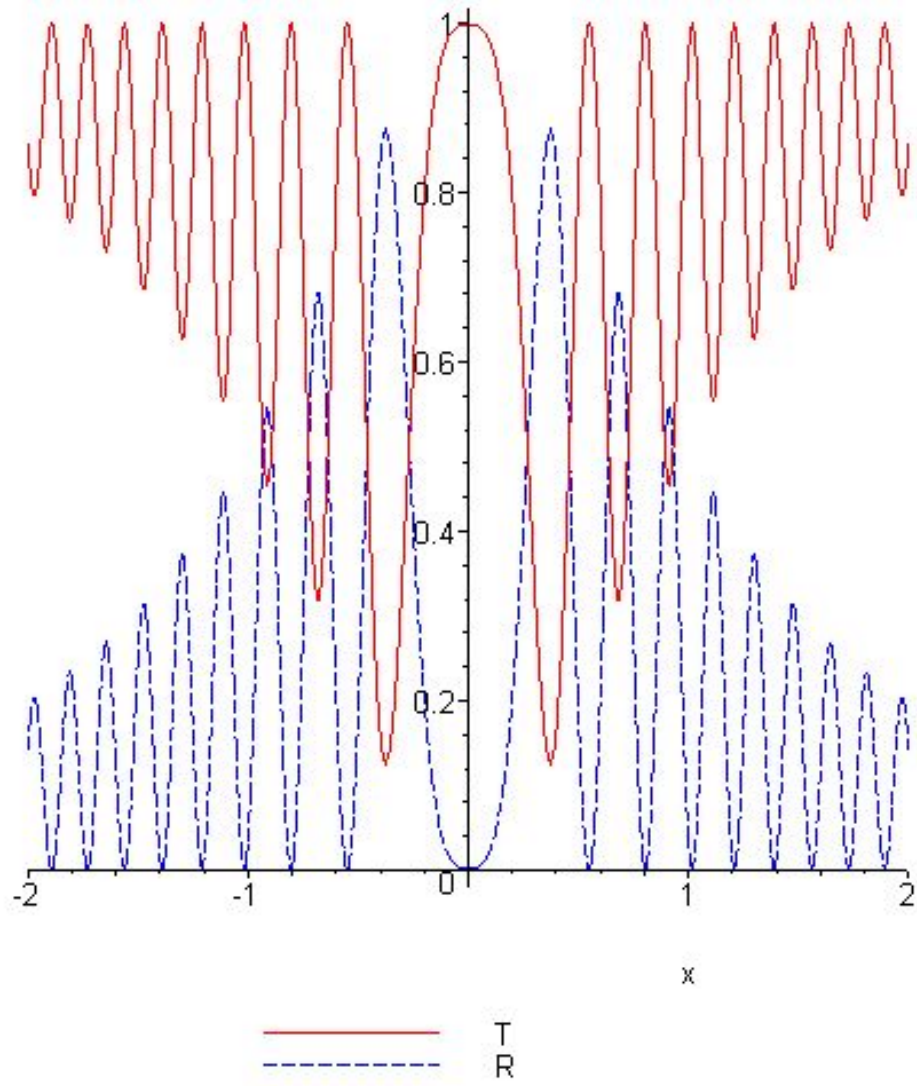
Fig. A.5   R and T curves.
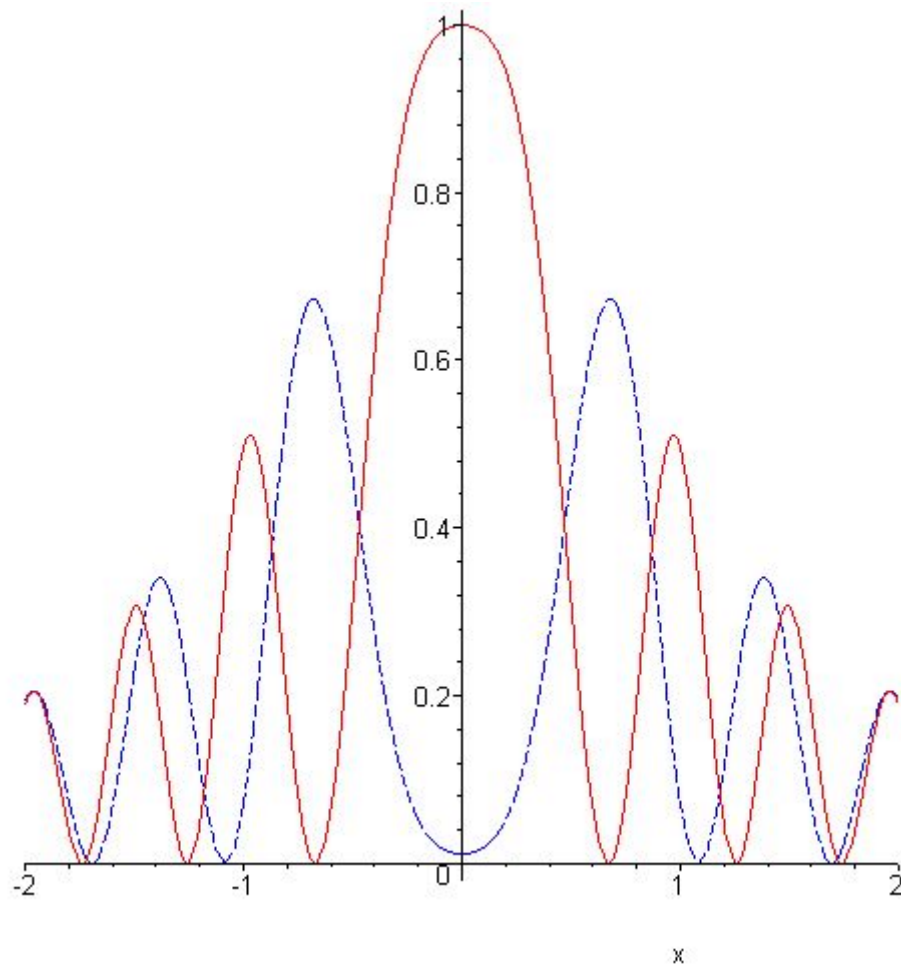
Fig. A.6   R curve with various value of thickness (*t*).

A.3.2 Transmission by Wedge-Shaped Plate

In This case assume that the wave-field entering surface must divert.

Consider boundary condition from entrance and exit surface is

$$\mathbf{k}_h^{(i)} = \mathbf{K}_o^{(a)} + \mathbf{h} - \mathbf{K}\delta^{(i)}\mathbf{n}_o \tag{A.40}$$

By

$$\mathbf{K}\delta^{(i)}\mathbf{n}_o = \mp \frac{\mathbf{n}_o}{\gamma_m}\frac{1}{2}|\phi_m|\sqrt{\frac{\gamma_m}{\gamma_o}} \bullet (\sqrt{1+W^2}+W \quad \mp \frac{\mathbf{n}_o}{\gamma_m}\frac{\phi_o}{2}\frac{\gamma_m}{\gamma_o} - P \tag{A.41}$$

The boundary condition at exit surface (Fig. A.7) is

$$\mathbf{K}_h^{m(i)} = \mathbf{k}_h^{(i)} + K\overline{\mathbf{P}^{(i)}\mathbf{A}^{(i)}}\mathbf{n}_m \tag{A.42}$$

Which

$$K\overline{\mathbf{P}^{(i)}\mathbf{A}^{(i)}}\mathbf{n}_d = (-\xi_m^{(i)} - \frac{1}{2}K\phi_o + K\alpha^{(i)}), \quad \mathbf{K}\alpha^{(i)} = \overline{\mathbf{P}^{(i)}\mathbf{Q}^{(i)}} \tag{A.43}$$

By

$$\xi_m^{(i)} = \frac{|\phi_m|}{2}\sqrt{\frac{\gamma_o}{\gamma_m}} \tag{A.44}$$

From equations (A.40), (A.41), (A.42), (A.43) and (A.44) so $\mathbf{K}_h^{(m_i)}$ became

$$\mathbf{K}_h^{m(1)} = K_o^{(a)} + \mathbf{h} - m\frac{\gamma_m}{\gamma_o}\left[\frac{\mathbf{n}_o}{\gamma_m}(\sqrt{1+W^2}+W - \frac{\mathbf{n}_m}{\gamma_m^{(1)}}(\sqrt{1+W^2}+W\right]$$
$$+\frac{K\phi_o}{2}\left(\frac{\mathbf{n}_o}{\gamma_m} - \frac{\mathbf{n}_m}{\gamma_m^{(1)}}\right)\frac{\gamma_m}{\gamma_o} - (\mathbf{P}\text{-}\mathbf{P}_l) \tag{A.45}$$

$$\mathbf{K}_h^{m(2)} = K_o^{(a)} + \mathbf{h} - m\frac{\gamma_m}{\gamma_o}\left[\frac{\mathbf{n}_o}{\gamma_m}(\sqrt{1+W^2}+W - \frac{\mathbf{n}_m}{\gamma_m^{(2)}}(\sqrt{1+W^2}+W\right]$$
$$+\frac{K\phi_o}{2}\left(\frac{\mathbf{n}_o}{\gamma_m} - \frac{\mathbf{n}_m}{\gamma_m^{(2)}}\right)\frac{\gamma_m}{\gamma_o} - (\mathbf{P}\text{-}\mathbf{P}_2) \tag{A.46}$$

$$\mathbf{P} = \frac{\mathbf{n}_o}{\gamma_m}K\alpha, \quad \mathbf{P_i} = \frac{\mathbf{n}_o}{\gamma_m^{(i)}}K\alpha_i$$

Equations (A.45) and (A.46) can be rewrite in wedge angle term at (A.47) and (A.48)

Fig. A.7 Dispersion surface in reciprocal lattice for wedge-shaped plate

$$\mathbf{K}_h^{m(1)} = K_o^{(a)} + \mathbf{h} - A_o \left[(W - \sqrt{1+W^2}) \frac{v_e}{\cos\theta_h} + (W + \sqrt{1+W^2}) \frac{v_a}{\varphi_h} \right] \qquad \text{(A.47)}$$

$$\mathbf{K}_h^{m(2)} = K_o^{(a)} + \mathbf{h} - A_o \left[(W + \sqrt{1+W^2}) \frac{v_e}{\cos\theta_h} + (W - \sqrt{1+W^2}) \frac{v_a}{\varphi_h} \right] \qquad \text{(A.48)}$$

Where
$$A_o = k_o \mathbf{K} \left| \varphi_H^/ \right| \sqrt{\frac{\cos\theta_h}{\cos\theta_o}} \qquad \text{(A.49)}$$

$\varphi_H^/$ is proportional to a structure factor. v_e and v_e are unit vectors normal to the incident and exit surfaces, θ_h is the angle between v_e and the diffracted beam and φ_h is the angle between v_e and the diffracted beam. Then fringe spacing is given by;

$$\Lambda = (\Delta \mathbf{K}_h^{(m)})^{-1}$$

$$= \lambda \left\{ K \left| \varphi_H^/ \right| \sqrt{\frac{(1+W^2)\cos\theta_h}{\cos\theta_o}} \; \Phi \right\}^{-1} \qquad \text{(A.50)}$$

By Φ is geometric factor which can be written as

$$\Phi = \left| \frac{v_e}{\cos\theta_h} - \frac{v_a}{\cos\varphi_h} \right|$$
$$= \sqrt{\frac{1}{\cos^2\theta_h} + \frac{1}{\cos^2\varphi_h} - \frac{2\cos(v_e v_a)}{\cos\theta_h \cos\varphi_h}} \qquad \text{(A.51)}$$

Where $(v_e v_a)$ is the wedge angle.
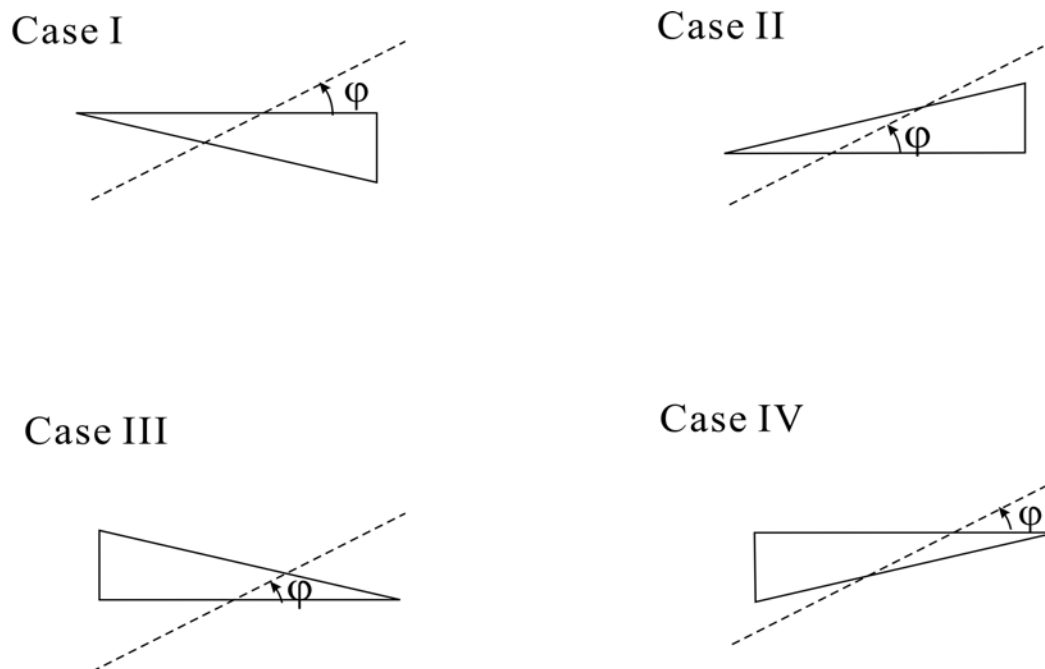
Fig. A.8   Four different configuration of wedge-shape plate.

Case I: $\theta_o = \pi/2 - \varphi - \theta_B$, $\theta_h = \theta_o + 2\theta_B$, $\varphi_h = \theta_h - (v_e v_e)$;

Case II: $\varphi_h = \pi/2 - \varphi + \theta_B$, $\theta_h = \varphi_h + (v_e v_e)$, $\theta_o = \theta_h - 2\theta_B$;

Case III: $\varphi_h = \pi/2 - \varphi + \theta_B$, $\theta_h = \varphi_h - (v_e v_e)$, $\theta_o = \theta_h - 2\theta_B$;

Case IV: $\theta_o = \pi/2 - \varphi - \theta_B$, $\theta_h = \theta_o + 2\theta_B$, $\varphi_h = \theta_h + (v_e v_e)$;

After the wedge fringe is calculated, the fringe's figure is shown in Fig. A.9.

Fig. A.9   The interference pattern in pendellÖsung fringe solution form plane

incident wave.

Appendix II

Literature for References

An X-Ray Trichrome Imaging 'Trinity':
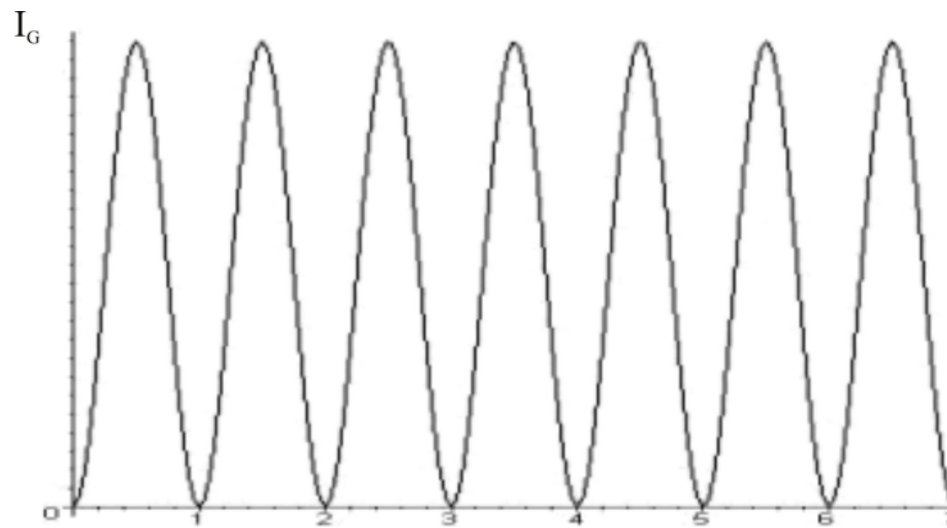# Absorption, Phase-Interference and Angle-Resolved Contrast

Masami ANDO[1,2], Hiroshi SUGIYAMA[1,2], Xiaowei ZHANG[1,3], Kazuyuki HYODO[1,3],
Anton MAKSIMENKO[2] and Wanwisa PATTANASIRIWISAWA[2]

[1]*Photon Factory, Institute of Materials Structure Science, High Energy Accelerator Research Organization,
1-1 Oho, Tsukuba, Ibaraki 305-0801, Japan*

[2]*Department of Photo-Science, School of Advanced Studies, Graduate University for Advanced Studies,
Shonan International Village, Hayama, Miura, Kanagawa 240-0193, Japan*

[3]*Department of Materials Structure Science, School of Mathematical Physical Sciences, Graduate University for Advanced Studies,
1-1 Oho, Tsukuba, Ibaraki 305-0801, Japan*

A newly designed 100-mm-long X-ray trichrome optics for imaging has been proposed. Its working X-ray photon energy is 35 keV. Since this optics has two alternate mirrors, it can simultaneously supply three types of images: absorption, phase-interference and angle-resolved contrast for a sample space of 7 mm width. Examples of imaging by this novel X-ray interferometer in medicine, biology and material science are presented.

Recently we have proposed a new concept of imaging[1] using a conventional X-ray interferometer[2,3] in which we emphasize that X-ray interferometry in imaging can provide not only phase-interference contrast[4–6] but also angle-resolved contrast[7] by utilizing its analyzer wafer. This angle-resolved contrast is actually the refraction contrast based on an early work by Cosslett and Nixon[8] in 1953 which many studies[9–14] followed.

It is well known that an X-ray interferometer can provide imaging with phase-interference contrast. Assuming the phase advance of X-rays $\phi(x, y: k)$ while passing through a sample ranging z_0 and z_1 along the direction of optical path z is

$$\phi(x, y: k) = 2e\lambda/mc^2 \int_{z_0}^{z_1} \rho(x, y, z)dz, \quad (1)$$

where $\rho(x, y, z)$ is a local density of electron at coordinate (x, y, z), e is electron charge, λ is the X-ray wavelength, m is electron mass and c is the light velocity. $\rho(x, y, z)$ and the refractive index $n = 1 - \delta(x, y, z)$ has a following relation.

$$\delta(x, y, z) = e\rho(x, y, z)/m\pi v^2, \quad (2)$$

Using (1) the phase-interference contrast $I(x, y: k)$ can be described as follows:

$$I(x, y: k) \propto 1 + \langle\cos\phi(x, y: k)\rangle, \quad (3)$$

The deflection angle $\Delta(x, y: k)$ at z along the direction of x perpendicular to z in the plane of incidence is

$$\Delta(x, y: k) \propto -\int_{z_0}^{z_1} \partial\delta(x, y: k)/\partial x dz \quad (4)$$

This associates with angle-resolved contrast. The absorption contrast $-\log\{I(x, y: k)/I_0(x, y: k)\}$ is

$$-\log\{I(x, y: k)/I_0(x, y: k)\} \propto \int_{z_0}^{z_1} \sum_m N_m(x, y, z)\mu_m dz, \quad (5)$$

where $I(x, y: k)$ and $I_0(x, y: k)$ is the X-ray intensity after and before sample, respectively and $N_m(x, y, z)$ and μ_m is density of atom m and atomic absorption coefficient of atom m, respectively.

In this work in order to visualize the internal structure of a material, we propose a newly designed X-ray trichrome optics that can provide these three types of contrast simultaneously in addition to a larger sample space.

The distance D between S (splitter) and M (mirror), and M (analyzer) and A in a conventional L-L-L X-ray interferometer[2–4] comprising S, M and A must be the same. The diameter R of the cylindrical shaped sample inscribed in a triangle, which has been formed by diffracted and forward-diffracted beams, can be deduced as $R = D\sin\theta/(1 + \sin\theta)$, where θ is the Bragg angle. Since the beam width W is expressed as $W = 2D\sin\theta$ the ratio 2R/W is $1/(1 + \sin\theta)$. The size of the X-ray interferometer is 2D by 4D $\tan\theta$.

In a newly designed X-ray trichrome optics, M has been divided into two pieces, MI and MII, as shown in the Fig. 1. One half of the monochromatic beam available from an asymmetrically cut monochromator penetrates through a sample to project the sample's internal structure due to its absorption contrast onto a film, while the other half, after passing through S, is incident on this sample so that two types of images, namely, phase-interference contrast and angle-resolved contrast are available. Considering application of the X-ray trichrome optics to computer tomography (CT), the shape of a zone for rotating a sample is either cylindrical and/or spherical when choosing the rotation axis vertical to the plane of incidence or spherical when choosing the horizontal one. 2R/W is 1 since both 2R and W are 2D $\sin\theta$. The size of the X-ray trichrome optics becomes 3D by 5D $\tan\theta$. The ratio of a sample diameter to the X-ray trichrome optics size is 2 $\sin\theta$ which means that the ratio is always larger compared to that of the ordinary design by a factor between 4/3 and 8/3, depending on θ.

This X-ray trichrome optics was cut out from a 50-mm-thick boule with the orientation of ⟨100⟩ of a floating-zone silicon crystal. The thickness of each wafer was 1.1 mm in design for the (440) diffracting planes. This size of 70 mm for 3D can provide a sample with a beam of 7 mm in size. The entire X-ray trichrome optics including an additional guard space is 100 mm long and 42 mm wide. The X-ray photon energy of 35 keV has been chosen so that one can use metals as sample such as Al with thickness of 5 mm
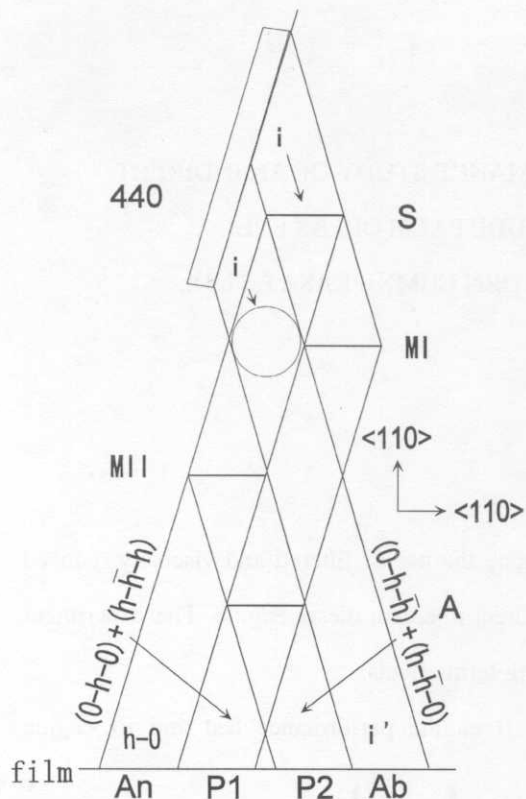
Fig. 1. New X-ray trichrome optics, simultaneously providing three types of image contrast comprising a splitter S, two mirrors MI and MII and analyzer A. An corresponds to angle-resolved contrast due to (h-o), P1 corresponds to phase-interference contrast due to (o-h-o) + (h-h̄-h), and P2 also corresponds to phase-interference contrast due to (o-h-h̄) + (h-h̄-o) and an Ab image due to absorption contrast corresponding to an image receiving I'. The X-ray trichrome optics used in this paper is approximately 100 mm by 42 mm in size. The thickness of each wafer is approximately 1.1 mm. The inset shows the crystallographic orientation. To conserve space, the figure is not to scale.

Fig. 2. Composite material of SiC in titanium showing each fiber whose internal structure is invisible in a conventional X-ray technique. Very clear internal structure images are available in angle-resolved contrast (a), phase-interference contrast (b and c) as well as in absorption contrast (d). Each fiber is 140 μm in diameter and in the center a single carbon core of 30 μm diameter is located. The field size is 7 mm in width by 14 mm in height for each.

and X-ray attenuation of 35%. An experiment was carried out at BL14B where the vertical polarization of synchrotron radiation is produced by a horizontal 5T magnetic field that provides the critical photon energy of approximately 20 keV. The horizontal beam size of 2 mm available in the hutch was increased by the asymmetrically cut monochromator on the experimental stage in the hutch and its angular divergence from the outgoing beam is 0.06 arcsec due to the asymmetry factor.[15] The exposure time was on the order of 2–4 min using a Polaroid film, and 10–20 min using an electron microscopy film. Their spatial resolution was 25 μm and 2 μm, respectively. The sample-to-film distance was approximately 150 mm. Commissioning was carried out using a wedge-shaped phase plate to observe equal thickness fringes and a hypodermic syringe containing a 10% iodine contrast agent whose absorption edge is 33.17 keV to observe the three types of contrast. This test was successfully performed.

Figure 2 shows the three kinds of contrast available in reinforced SiC fibers[16] in a Ti-15-3 matrix. In the center of SiC with the diameter of approximately 140 μm, a 30-μm-diameter carbon has been built in as cores. All images with different contrast are very clearly shown. All details appear clearly distinguished in both angle-resolved (a) and phase-interference contrast (b and c) of SiC fibers that

are spaced approximately 200–300 μm apart horizontally and another 200–300 μm apart vertically to the picture with six layers,[17] whilst in the absorption contrast (d) the number of stripes appears to be approximately 30 based on the result of superimposition of SiC fibers.

The visual and nondestructive inspection of hard ivory from Africa[18] and their mock materials such as the horn of Dutch water buffalo has long been desired. Alternative techniques to identify them have been developed such as infrared spectroscopy[19] and fluorescent spectroscopy.[20] By the present technique, a very clear and distinct difference in the arrangement of fibers, which is probably due to collagen and hydroxyapatite between species has been shown. The ivory structure is very periodic, while that of the Dutch water buffalo looks like branches and leaves of a tree, as shown in Figs. 3(a) and 3(b), respectively. This is a first visual, suc-
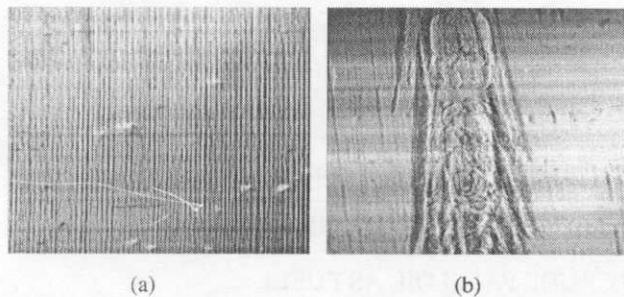
Fig. 3. Details and the difference in the internal structure of ivory and a horn from a Dutch water buffalo is shown at An in Fig. 1. Their contrast must be due to the refraction effect of fine fibers inside their tissue. The image Ab is not shown because there is almost no contrast. Since phase-interference contrast images P1 and P2 show overlap with equally thick fringes due to their round outer shape, they are not shown here. Each field is 5 mm by 4 mm in size.
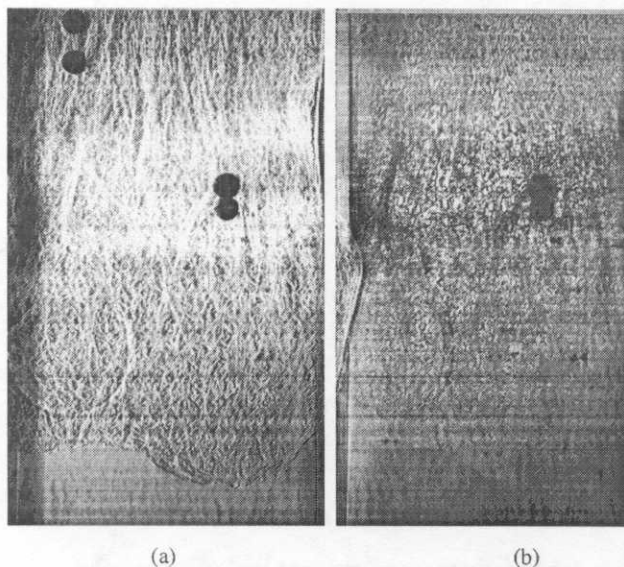
Fig. 4. Trabeculate bone of human dried proximal phalanx. Each field is 7 mm by 14 mm in size. (a) shows the angle-resolved contrast and (b) shows the phase-interference contrast.

cessful and clear identification that will be an indispensible technique for forensic study.[21]

A very clear image of trabeculate bone in a human dried proximal phalanx, which is invisible by a conventional X-ray technique. Even plane wave could not have revealed inside structure[22] in angle-resolved contrast and (b) in phase-interference contrast. This technique will be applicable to diagnosis of bone diseases such as osteoporosis.[23]

The ratio of the sample diameter to the length of a conventional X-ray interferometer is $\sin\theta/(1+\sin\theta)$, while $2\sin\theta/3$ for the new X-ray trichrome optics. The ratio between R/W of the new X-ray trichrome optics and that of the conventional one is $(1+\sin\theta)/$, indicating that its value ranges between 1 and 2. In order to reconstruct a CT image based on an angle-resolved contrast, development of appropriate software will also definitely be needed so that the internal structure can be precisely imaged based on these three types of images: image based on absorption contrast, based on phase shift and based on angle resolution. In other words, a complete mapping of electron distribution, and integrated interpretation over the

atomic and electron distribution will be possible, which is of great importance in understanding the internal electronic structure of matter.

In order to observe a larger sample, a larger X-ray trichrome optics is required. For that purpose, the following technical developments will be required: (1) the growth of a large high-quality floating-zone (FZ) silicon crystal with no striations due to the inhomogeneous distribution of impurities, (2) a novel method of cutting out a larger functional X-ray trichrome optics, (3) means for better spatial resolution, and (4) an alternative technique to improve spatial resolution. It should be noted that there is another approach to make the view field larger. Momose *et al.*[24] attempts to use a two-crystal X-ray interferometer that requires very fine tuning but can significantly economize the material and they also attempted to thin the analyzer A.

1) M. Ando, J. Chen, K. Hyodo, K. Mori, H. Sugiyama, D. Xian and X. Zhang: Jpn. J. Appl. Phys. **39** (2000) L1009.
2) U. Bonse and M. Hart: Appl. Phys. Lett. **6** (1965) 155.
3) U. Bonse and M. Hart: Appl. Phys. Lett. **7** (1965) 99.
4) M. Ando and S. Hosoya: *Proc. 6th Int. Conf. X-Ray Optics & Micro-analysis, Osaka, 1971*, eds. G. Shinoda, K. Kohra and T. Ichinokawa (Univ. of Tokyo Press, Tokyo, 1972) p. 63.
5) A. Momose, T. Takeda, Y. Itai and K. Hirano: Nat. Med. **2** (1996) 473.
6) A. Momose, T. Takeda, Y. Itai, A. Yoneyama and K. Hirano: *Medical Applications of Synchrotron Radiation*, eds. M. Ando and C. Uyama (Springer-Verlag, Tokyo, 1998) p. 54.
7) D. Chapman, W. Thomlinson, F. Arfelli, N. Gmuer, Z. Zhong, R. Menk, R. E. Johnson, D. Washburn, E. Pisano and D. Sayers: Rev. Sci. Instrum. **67** (1996) 3360.
8) V. E. Cosslett and W. C. Nixon: J. Appl. Phys. **24** (1953) 616.
9) K. M. Podurets, V. A. Somenkov and S. Sh. Shilstein: Sov. Phys. Tech. Phys. **34** (1989) 654.
10) V. N. Ingal and E. A. Beliaevskaya: J. Phys. D **28** (1995) 2314.
11) S. W. Wilkins, T. E. Gureyev, D. Gao, A. Pogany and A. W. Stevenson: Nature **384–28** (1996) 335.
12) P. Clotens, R. Barrett, J. Bruchel, J.-P. Guigay and M. Shlenker: J. Phys. D **29** (1996) 133.
13) W. Thomlinson, D. Chapman, Z. Zhong, R. E. Johnston and D. Sayers: *Medical Applications of Synchrotron Radiation*, eds. M. Ando and C. Uyama (Springer-Verlag, Tokyo, 1998) p. 72.
14) D. Gao, T. E. Gureyev, A. Pogany, A. W. Stevenson and S. W. Wilkins: *Medical Applications of Synchrotron Radiation*, eds. M. Ando and C. Uyama (Springer-Verlag, Tokyo, 1998) p. 63.
15) K. Kohra: J. Phys. Soc. Jpn. **17** (1962) 589.
16) Y. Tanaka, Y. Kagawa, C. Masuda, Y.-F. Liu and S. Q. Guo: Metall. & Mater. Trans. **30A** (1999) 221.
17) Y. Tanaka, C. Masuda, H. Sugiyama, A. Maksimenko, W. Pattansiriwisawa and M. Ando: in preparation for publication.
18) A. MacGregor and C. Helm: *Bone, Antler, Ivory & Horn, the Technology of Skeletal Materials Since the Roman Period* (London and Sydney, Barnes and Noble Books, Totowa, New Jersey, 1985) p. 14.
19) M. Shimoyama, H. Maeyama, H. Sato, T. Ninomiya and Y. Ozaki: Appl.

Jpn. J. Appl. Phys. Vol. 40 (2001) Pt. 2, No. 3B

M. ANDO *et al.*   L 301

Spectrosc. **51** (1997) 1154.

20) M. Shimoyama, T. Nakanishi, Y. Hamanaga, T. Ninomiya and Y. Ozaki: J. Trace & Microprobe Tech. **16(2)** (1998) 1154.

21) S. Muratsu, T. Ninomiya, H. Sugiyama, A. Maksimenko, W. Pattansiriwisawa and M. Ando: in preparation for publication.

22) K. Mori, K. Hyodo, N. Shikano and M. Ando: Jpn. J. Appl. Phys. **38** (1999) L1339.

23) V. Nedorezov: private communication.

24) A. Momose, T. Takeda, Y. Itai, A. Yoneyama and K. Hirano: J. Synchrotron Rad. **5** (1998) 309.

A New Optics for Dark-Field Imaging in X-Ray Region 'Owl'

Masami ANDO[1,2,3,*], Hiroshi SUGIYAMA[1,2], Anton MAKSIMENKO[2], Wanwisa PATTANASIRIWISAWA[2],
Kazuyuki HYODO[1,3] and ZHANG Xiaowei[1,3]

[1] *Photon Factory, Institute of Materials Structure Science, High Energy Accelerator Research Organization,*
1-1 Oho, Tsukuba, Ibaraki 305-0801, Japan
[2] *Department of Photo-Science, School of Advanced Studies, Graduate University for Advanced Studies,*
Shonan International Village, Hayama, Miura, Kanagawa 240-0193, Japan
[3] *Department of Materials Structure Science, School of Mathematical Physical Sciences, Graduate University for Advanced Studies,*
1-1 Oho, Tsukuba, Ibaraki 305-0801, Japan

An X-ray optics for X-ray dark-field imaging named 'Owl' is proposed. It involves an asymmetric monochromator and a monolithic X-ray optics comprising a collimator C and an analyzer A. The C and A have 4,4,0 diffraction and thickness of 1.08 mm ± 10 μm. The X-ray energy used was 35 keV. These diffractions have an angular width of approximately 0.3 μrad. The analyzer A accepts only the refracted component from a sample S which is located between C and A, while eliminating the straight component without reacting with it. Two samples, one Al matrix containing boron fibers of 300 μm diameter and the other a wax block containing a nylon fiber simulating breast cancer, show very clear fiber imaging usually not visible by the conventional X-ray technique.

KEYWORDS: X-ray dark-field imaging, monolithic X-ray optics, refraction contrast, synchrotron radiation, vertical wiggler, asymmetrically cut monochromator, composite material, fibers, mammographic phantom

Recently, we have proposed a new X-ray trichromator 'Trinity'[1] as was an extension of a novel application[2] of the X-ray interferometer by Bonse and Hart.[3] The trichromator 'Trinity' is capable of supplying three types of contrast simultaneously: absorption, phase[4-7] and refraction contrast.[8-21] Much prior to these, another technique called shadow micrography was discovered by Cosslett and Nixon[22,23] in 1951 and this corresponds to a dark-ground method of observation or schlieren imaging reported in the literature by Born and Wolf.[24]

The deflection angle $\Delta(x, y : k)$[1,17] which leads to refraction contrast can be described as follows:

$$\Delta(x, y : k) \propto - \int_{z_0}^{z_1} \partial \delta(x, y : k)/\partial x dz \qquad (1)$$

where $\delta(x, y : k)$ has a relation to the refractive index of $n = 1 - \delta(x, y : k.)$, z is the direction of X-ray beam propagation, z_0 and z_1 correspond to z the coordinates at which the X-ray beams enter and exit a sample, respectively, and x corresponds to the coordinate perpendicular to z in the incidence plane.

We would like to propose the principle of X-ray dark-field imaging. C, S and A in Fig. 1 correspond to a collimator, a sample and an analyzer, respectively. Rocking curves R_h with a solid line for the H-beam and R_o with a broken line for the O-beam at C or at A are shown in Fig. 2, respectively under the condition of thickness of C and A of 1.08 mm at 35 keV. The factor that when R_h has a maximum reflectivity R_o has a minimum value of zero is a characteristic feature of this system and hence one can surely obtain zero intensity for the forward direction. This may lead to X-ray dark-field imaging. This thickness was selected by calculation of peak reflectivity dependence on wafer thickness. This was performed for thickness between 0.2 mm and 1.2 mm of C or A. This results in Fig. 3 which shows the change of peak reflectivity R_h by the solid line for the H-beam and R_o by the broken line for the O-beam approximately every 62.5 μm versus the thick-

ness change of C or A, respectively. For thickness at 1.08 mm R_o can give practically zero intensity. This graph reveals the precise thickness values of C and A required. In both profiles in Fig. 3, the slope of reflectivity versus thickness change 16%/10 μm so that a thickness control better than 10 μm is required. The thickness of C and A was chosen as 1.08 mm because it retains mechanical strength while still suffering less X-ray absorption for 35 keV.

When a wave packet $\langle \varphi_E \rangle$ with divergence of 0.3 μrad from an asymmetrically cut monochromator[25] is incident on C, wave packets $\langle \varphi_{ChE} \rangle$ and $\langle \varphi_{CoE} \rangle$ shown in Fig. 1, will be produced. Each reflectivity profile is shown below its corresponding wave packet $\langle \varphi \rangle$. The profile $\langle \varphi_{ChE} \rangle$ is a result of multiplication of $\langle \varphi_E \rangle$ and the profile of R_h for the H-beam shown in Fig. 2. It has a reflectivity width of approximately 0.3 μrad. A sample S which contains light element fibers, as a model, has a reflectivity profile as shown in the inset when receiving a wave $\langle \varphi_{ChE} \rangle$. Its center corresponds to the wave $\langle \varphi_{ChE} \rangle$. Since the profile for the O-beam with the broken line shown in Fig. 2 has no intensity in the straight forward direction, the wave packet $\langle \varphi_{AoSChE} \rangle$ will remain to form the image by collecting only all the X-ray refraction components from the S, while the components with no deflection are completely suppressed. The component $\langle \varphi_{AhSChE} \rangle$ should correspond to a bright-field image because it contains the illumination component as well.

Almost all images obtained by the methods described in the refs. 8–21 can be classified as bright-field imaging because the light illuminated onto a specimen remains, while some differences exist in the height of illumination. A pioneering X-ray optics technique reported by Ingal and Beliaevskaya in ref. 13 could have achieved the complete X-ray dark-field imaging if they had adopted the appropriate wafer thickness in a parallel setting.

An experiment was performed at Beamline BL14B[26] at the Photon Factory and at BL20B[27] at SPring-8. Images were stored on electron microscopy films with spatial resolution of 2 μm. The exposure time for each picture was approximately

---

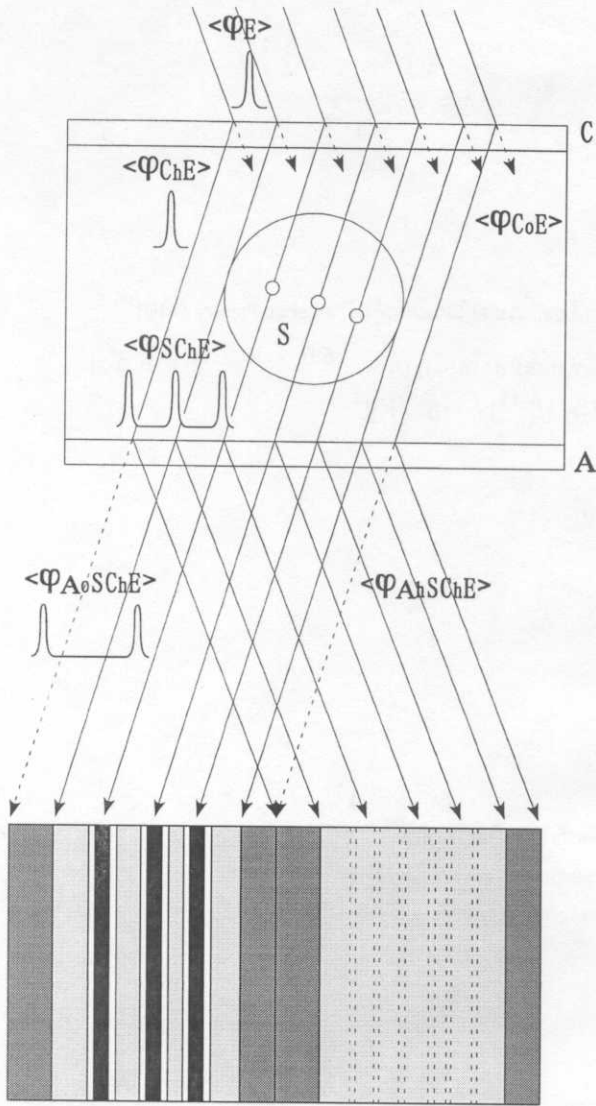*To whom all correspondence should be addressed.

Fig. 1. Geometry of X-ray dark-field imaging named 'Owl'. Collimator C and analyzer A are a part of a monolithic block which keeps their angular relationship stable in between C and A. S means a sample. The incident beam $\langle\varphi_E\rangle$ with 0.3 μrad beam divergence from an asymmetric monochromator excites $\langle\varphi_{ChE}\rangle$ that passes through a sample S. The bright-field image $\langle\varphi_{SChE}\rangle$, which is formed by a beam with beam divergence of 0.3 μrad, is incident on analyzer A. This A holds acceptance in the angular range only outside ±0.15 μrad so that $\langle\varphi_{AoSChE}\rangle$ containing refraction information is forward diffracted to bring about dark-field imaging. See schematic diffraction profiles shown in inset. The diffraction index and X-ray energy were 4,4,0 and 35 keV. Also a sample containing lighter element in a plate with heavier element and the expected image are shown schematically. This 'Owl' has been designed so that the field size of 7 mm by 14 mm is available.

Fig. 2. A rocking curve R_h is shown by a solid line which corresponds to the H-beam and the other rocking curve R_o is represented by a broken line which corresponds to the O-beam. Both were calculated under the assumption of 4,4,0 diffraction for 1.08 mm-thick silicon slabs C or A using 35 keV X-rays. Their central peak range is ±0.15 μrad which coincides with that of the incident beam $\langle\varphi_E\rangle$. At the center of the profiles, R_h has a maximum reflectivity and R_o has a minimum value. As shown in the inset of Fig. 1, the beam profile $\langle\varphi_{ChE}\rangle$, multiplication of $\langle\varphi_E\rangle$ and R_h, does not have X-ray intensity practically outside the angular range of ±0.15 μrad, while R_o has high reflectivity outside ±0.15 μrad so that only information due to refraction from S can be visualized in $\langle\varphi_{AoSChE}\rangle$. Thus, this can be called 'X-ray dark-field imaging'.
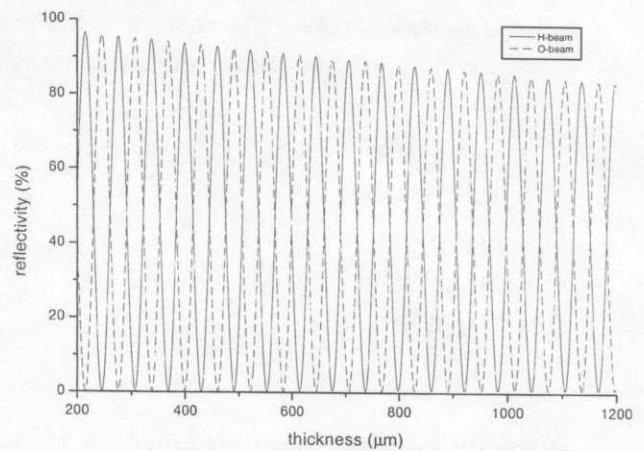
Fig. 3. Dependence of reflectivity R_h for H-beam and R_o for O-beam on wafer thickness with 4,4,0 reflection at 35 keV. At the thickness where the maximum R_h is obtained, R_o has the minimum value and vice versa. This relationship oscillates approximately every 62.5 μm in the range shown between 0.2 mm and 1.2 mm.

10 min.

As demonstration of the dark field imaging, two samples were prepared, one a composite material and the other a mammographic phantom. The composite material comprises boron fibers of 300 μm diameter embedded in the middle of an Al plate of 1.0 mm thickness. Its absorption coefficient is 1.7 cm^{-1} at 35 keV X-rays. The other sample is a wax block of 7 mm thickness containing a nylon fiber of 400 μm diameter which is from the mammographic accreditation phantom RMI 156 from Gammex in Wisconsin. From these samples, only poor contrast has been achieved by irradiating plane

wave X-rays of 35 keV energy. Figures 4 and 5 show thus taken dark-field images with expected contrast from a preliminary consideration.

The X-ray dark-field imaging requires only thickness control of A and C in the fabrication process and can accommodate a relatively large size sample in the space between A and C. This new technique will be able to visualize the internal fine structure of materials in a variety of fields such as biology, medicine, material science, palaeontology, archaeology and probably physics. The fact that this imaging setup can be positioned at the separation of two images $\langle\varphi_{AoSChE}\rangle$ and $\langle\varphi_{AhSChE}\rangle$, as shown in Fig. 1, can lead to a compact size sys-
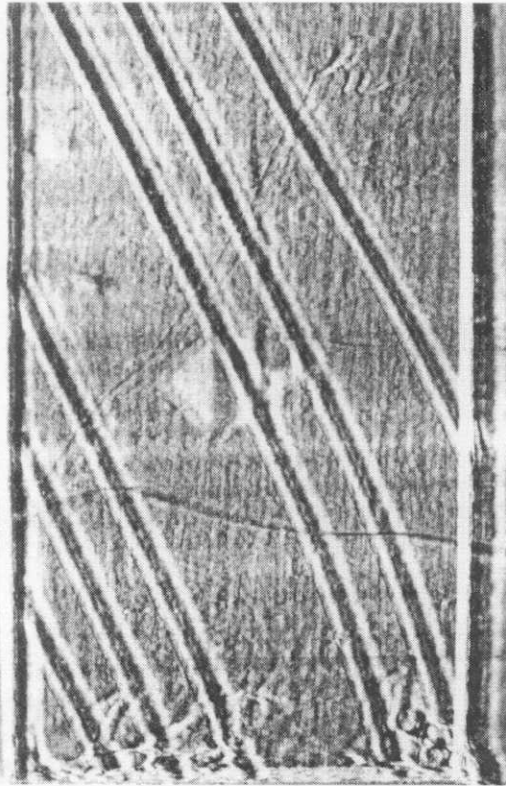
Fig. 4.   Dark-field image taken by the method described in Fig. 1 of an Al plate of 1.0 mm thickness containing boron fibers with 300 μm diameter. This structure had been invisible under illumination of only plane-wave X-rays. This dark-field contrast is a collection of all X-rays due to the refraction process excluding the component of the forward X-rays. The field size is approximately 7.0 mm by 12.0 mm.
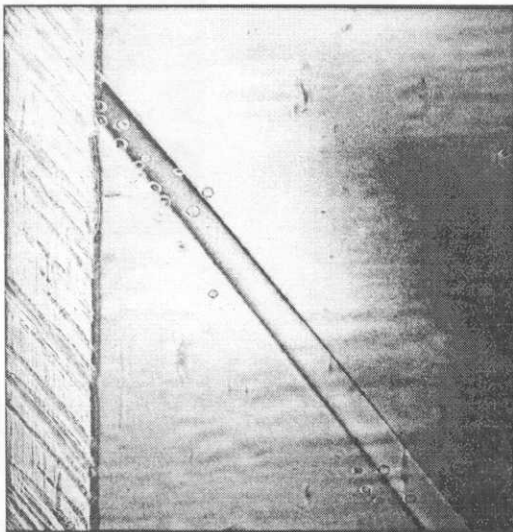
Fig. 5.   Dark-field image taken by the method described in Fig. 1 of a phantom piece #7 containing a nylon fiber of 400 μm diameter molded in a wax block. This is a commercially available mammographic phantom called "the mammographic accreditation phantom RMI 156" from Gammex. Its thickness is 7 mm. Not only the nylon fiber, but also bubbles which might have been introduced during the fabrication process, are very clearly shown. This object can be seen with only poor contrast by a normal projection of plane wave X-rays. The field size is approximately 5 mm by 5 mm.

1) M. Ando, H. Sugiyama, Zhang X., K. Hyodo, A. Maksimenko and W. Pattansiriwisawa: Jpn. J. Appl. Phys. **40** (2001) L298.
2) M. Ando, J. Chen, K. Hyodo, K. Mori, H. Sugiyama, D. Xian and X. Zhang: Jpn. J. Appl. Phys. **39** (2000) L1009.
3) U. Bonse and M. Hart: Appl. Phys. Lett. **7** (1965) 99.
4) M. Ando and S. Hosoya: *Proc. 6th Int. Conf. X-Ray Optics & Microanalysis, Osaka, 1971*, eds. G. Shinoda, K. Kohra and T. Ichinokawa (Univ. of Tokyo Press, Tokyo, 1972) p. 63.
5) A. Momose, T. Takeda, Y. Itai and K. Hirano: Nat. Med. **2** (1996) 473.
6) A. Momose, T. Takeda, Y. Itai, A. Yoneyama and K. Hirano: *Medical Applications of Synchrotron Radiation*, eds. M. Ando and C. Uyama (Springer-Verlag, Tokyo, 1998) p. 54.
7) A. Momose, T. Takeda, Y. Itai, A. Yoneyama and K. Hirano: J. Synchrotron Rad. **5** (1998) 309.
8) K. M. Podurets, V. A. Somenkov and S. Sh. Shil'shtein: Zh. Tekh. Fiz. **59** (1989) 115.
9) K. M. Podurets, V. A. Somenkov and S. Sh. Shil'shtein: Physica B **156/157** (1989) 691.
10) K. M. Podurets, V. A. Somenkov, R. R. Chistyakov and S. Sh. Shil'shtein: Physica B **156/157** (1989) 694.
11) V. A. Somenkov, A. K. Tkalich and S. Sh. Shil'shtein: Zh. Tekh. Fiz. **61** (1991) 197.
12) A. Snigirev, I. Snigireva, V. Kohn, S. Kuznetsov and I. Schelokov: Rev. Sci. Instrum. **66** (1992) 5486.
13) V. N. Ingal and E. A. Beliaevskaya: J. Phys. D **28** (1995) 2314.
14) T. J. Davis, T. E. Gureyev, D. Gao, A. W. Stevenson and S. W. Wilkins: Phys. Rev. Lett. **74** (1995) 3173.
15) T. J. Davis, D. Gao, T. E. Gureyev, A. W. Stevenson and S. W. Wilkins: Nature **373** (1995) 595.
16) K. A. Nugent, T. E. Gureyev, D. F. Cookson, D. Paganin and Z. Barnea: Phys. Rev. Lett. **77** (1996) 2961.
17) S. W. Wilkins, T. E. Gureyev, D. Gao, A. Pogany and A. W. Stevenson: Nature **384** (1996) 335.
18) D. Gao, T. E. Gureyev, A. Pogany, A. W. Stevenson and S. W. Wilkins: *Medical Applications of Synchrotron Radiation*, eds. M. Ando and C. Uyama (Springer-Verlag, Tokyo, 1998) p. 63.
19) D. Chapman, W. Thomlinson, F. Arfelli, N. Gmuer, Z. Zhong, R. Menk, R. E. Johnson, D. Washburn, E. Pisano and D. Sayers: Rev. Sci. Instrum. **67** (1996) 3360.
20) W. Thomlinson, D. Chapman, Z. Zhong, R. E. Johnston and D. Sayers: *Medical Applications of Synchrotron Radiation*, eds. M. Ando and C. Uyama (Springer-Verlag, Tokyo, 1998) p. 72.
21) P. Clotens, R. Barrett, J. Bruchel, J.-P. Guigay and M. Shlenker: J. Phys. D **29** (1996) 133.
22) V. E. Cosslett and W. C. Nixon: Nature **168** (1951) 24.
23) V. E. Cosslett and W. C. Nixon: J. Appl. Phys. **24** (1953) 616.
24) M. Born and E. Wolf: *Principles of Optics* (Pergamon Press, Oxford, New York, Toronto, Sydney, Braunschweig, 1975) 5th ed.
25) K. Kohra: J. Phys. Soc. Jpn. **17** (1962) 589.
26) M. Ando, Y. Satow, H. Kawata, T. Ishikawa, P. Spieker and S. Suzuki: Nucl. Instrum. & Methods A**264** (1986) 144.
27) K. Umetani, Y. Suzuki and N. Yagi: SPring-8 Information **4** (1999) 50 [in Japanese].

X-Ray Optics 'Owl' and 'Trinity'

Masami ANDO[1,2*], Kazuyuki HYODO[1,2], Hiroshi SUGIYAMA[1,2], Anton MAKSIMENKO[2],
Wanwisa PATTANASIRIWISAWA[2], Koichi MORI[3], Joseph ROBERSON[4], Edward RUBENSTEIN[5],
Yoshihisa TANAKA[6], Junyuan CHEN[7], Dingchang XIAN[8] and ZHANG Xiaowei[1,2]

[1]*Photon Factory (PF), Institute of Materials Structure Science, High Energy Accelerator Research Organization (KEK),
Oho 1-1, Tsukuba, Ibaraki 305-0801, Japan*
[2]*Department of Photo-Science, School of Advanced Studies, Graduate University for Advanced Studies (GUAS),
Shonan International Village, Hayama, Miura, Kanagawa 240-0193, Japan*
[3]*Department of Radiological Sciences, Ibaraki Prefectural University of Health Sciences, Ami 4669-2, Inashiki, Ibaraki 300-0394, Japan*
[4]*California Ear Institute at Stanford, Stanford, CA 94304, U.S.A.*
[5]*Department of Medicine, Stanford University School of Medicine, Stanford, CA 94305, U.S.A.*
[6]*National Institute for Materials Science (NIMS), Sengen 1-2-1, Tsukuba, Ibaraki 305-0047, Japan*
[7]*Nanjing Institute of Paleontology and Geology, 39 East Beijing Rd., Nanjing 210008, China*
[8]*Beijing Synchrotron Radiation Laboratory, Institute of High Energy Physics, Academia Sinica, P. O. Box 918, Beijing 100039, China*

We report an X-ray optical system 'Owl', capable of dark-field imaging. It comprises a Bragg case asymmetric monochromator and a monolithic X-ray optics housing a collimator C and an analyzer A that can select only the refracted light by 4,4,0 diffraction and crystals C and A of 1.08 mm thickness. The angular width of diffraction is 0.3 μrad at an X-ray energy of 35 keV. It has been proven that one can obtain the dark-field image corresponding to a forward diffraction beam as well as the bright-field image corresponding to a diffraction beam or vice versa depending on the specified thickness of the analyzer. Images due to refraction contrast in the dark-field imaging are clearly shown. In this paper, design and test of this X-ray optics and its preliminary applications are described in detail. Also another X-ray optics 'Trinity', which is capable of viewing three types of contrast, namely, refraction, phase interference and absorption, has been implemented.
[DOI: 10.1143/JJAP.41.4742]

1. Introduction

Recently, we have proposed an X-ray optics for dark-field imaging called 'Owl',[1] which is based on refraction contrast. Shadow micrography that enhances edge contrast was devised in 1951[2,3] by Cosslett and Nixon. It may correspond to a dark-ground method of observation or schlieren imaging in the visible light region as reported by Born and Wolf.[4] Since 1995, a great number of approaches[5–23] to refraction-based contrast have been developed. Some of them utilize a neutron Bragg diffraction analyzer,[5–10] projection with monochromatized X-rays,[11,15,17,22,23] high coherence white X-ray beam,[16] Laue X-ray transmission analyzer,[12] and Bragg X-ray diffraction analyzer.[13,14,18–20] Those that use an analyzer crystal after the object can provide a near-dark-field image[12–14,18–20] where significant illumination reduction is achieved by adjusting the angle of the analyzer crystal at the flank of the Bragg peak. Nevertheless, these methods (refer to refs. 12–14 and 18–20) cannot readily suppress illumination regardless of how the offset angle position of the analyzer crystal is controlled. In this paper, we describe a new X-ray optics[1] which enables complete dark-field imaging if a suitable analyzer crystal thickness is chosen. This imaging method that can in principle collect almost all of the refracted rays into a single picture in the plane of incidence from a sample is advantageous over other imaging methods. Image information within the peak may be difficult to discern from background fluctuations. Furthermore, one does not have to rotate an analyzer crystal as is required in the case of other methods. Another X-ray optical system called 'Trinity'[24] involving all three kinds of imaging techniques, dark-field imaging, phase-interference, and absorption, has been successfully tested. This will be useful for choosing the optimal image among those obtained by these three types of imaging techniques for an unidentified object.

2. Theory and Design of Dark-field Imaging

The deflection angle $\Delta(x, y : k)$[1] which leads to refraction contrast can be described as follows:

$$\Delta(x, y : k) \propto - \int_{z_0}^{z_1} \partial\delta(x, y, z : k)/\partial x \, dz, \qquad (1)$$

where $\delta(x, y, z : k)$ is related to the refractive index of $n = 1 - \delta(x, y, z : k)$. z is the direction of X-ray beam propagation and z_0 and z_1 are z coordinates at which the X-ray beams enter and exit a sample, respectively. x is the coordinate perpendicular to z in the plane of incidence.

The Laue geometry of diffraction is a key technology for dark-field imaging. For specific thickness of the angular filter, virtually all signals will be diffracted in the diffraction direction at the center of the Bragg condition under a certain X-ray photon energy, except in the presence of an illuminated sample which may permit radiation to be transmitted with divergence.

Let us define I_O and I_G in the Laue case as a beam in the direction of forward diffraction and that in the diffraction direction, respectively in case of almost no absorption, as a simple model, as follows:

$$I_O = \sin^2(\pi H \sqrt{1 + W^2}/\Lambda)/(1 + W^2) \qquad (2)$$

$$I_G = (W^2 + \cos^2(\pi H \sqrt{1 + W^2}/\Lambda))/(1 + W^2) \qquad (3)$$

*E-mail address: masami.ando@kek.jp

$$I_O + I_G = 1 \qquad (4)$$

$$\Lambda = \lambda \cos \theta_B / |P| |\chi_G|, \qquad (5)$$

where H is the thickness of an analyzer A, and W is the normalized angular deviation from the center of the Bragg peak. The condition $|W| \leq 1$ corresponds to the reflection range and Λ the extinction distance defined, as shown in eq. (5), where λ is the X-ray wavelength, θ_B the Bragg angle, P the polarization factor and χ_G the polarizability. One can recognize that the relation $I_O + I_G = 1$ holds for all W's. Figure 1 shows I_O (broken line) and I_G (solid line) in the angular range between $\pm 1 \mu$rad for various thicknesses between 1.10 and 1.15 mm. The thickness change of only approximately 50μm of the analyzer crystal A may significantly change the reflection percent, perhaps from a maximum to next minimum of zero or vice versa. This means fabrication of the analyzer crystal A requires approximately 5μm precision of its thickness fluctuation. The profile outside $|W| = 1$ I_O maintains a constant high reflection percent while I_G shows a rapid decrease. One can easily observe that the profile I_O in the angular range $|W| > 1$ may have high reflectivity for refracted X-rays from a sample, while the profile I_G in the angular range $|W| > 1$ shows low reflectivity for refracted X-rays from a sample. Thus, the signal level at I_O will be relatively high compared to I_G. Based on this consideration, I_O may yield dark-field imaging with a relatively low level of illumination, and I_G, conventional bright-field imaging with a high level of illumination. It is clearly seen that profiles in Fig. 1 hold for the relation $I_O + I_G \sim 0.9$ if not 1.0 due to some absorption for all thicknesses and angular positions.

The pioneering system of Ingal and Beliaevskaya,[12] Davis and coworkers,[13,14] Chapman *et al.*[18] and Thomlinson *et al.*[20] has shown that in principle, one can achieve

Fig. 2. Geometry of X-ray dark field imaging 'Owl'. Collimator C and analyzer A are parts of a monolithic block which keeps their angular relationship quite stable. S refers to the sample. The incident beam ⟨m⟩ from an asymmetric monochromator excites C so that a monochromatic illumination passes through a sample S. The bright field image and the dark field image are formed in the forward diffracted beam ⟨g⟩ and in the diffracted beam ⟨o⟩, respectively.

near-dark-field imaging by adjusting the reflection angle of the analyzer crystal. This means that one may need more than one exposure for collecting all refracted images.

If the beam with the narrowest angular width, produced by asymmetric reflection,[25] is incident onto an object and is utilized under achromatic conditions, one would not need analyzer rotation. Our new system, 'Owl', shown in Fig. 2 can provide all information inherent in an image by a single shot without rotating an analyzer crystal. Collimator C and analyzer A are parts of a monolithic block which keeps their angular relationship quite stable. S indicates a sample. The incident beam ⟨m⟩ with 0.3μrad beam divergence from an asymmetric monochromator produces a beam via C that passes through a sample S. The bright field image ⟨G⟩, which is formed by a beam with a beam divergence of 0.3μrad is incident on analyzer A. The analyzer exhibits reflectivity acceptance in the angular range only outside $\pm 0.15 \mu$rad so that ⟨O⟩ containing refraction information is forward diffracted to realize dark-field imaging.

Figure 3 shows a schematic explaining how dark- and bright-field images are produced: (a) shows an incident beam that has as narrow an angular divergence as possible. Its horizontal axis corresponds to the angular scale. A horizontal axis in other figures also has the same angular scale. (b) shows a mapping of a potential refraction object that comprises four refraction boundaries with four kinds of refraction indices. (c) shows a profile of a beam from an object. A convolution is observed between (a) and (b). The calculated curve (d) I_O gives almost zero intensity at $|W| \leq 1$. (e) shows a result of (c) produced by A in the forward diffraction beam direction. This can be called dark-field imaging because it has almost no background illumination. (f) corresponds to a theoretical diffraction profile I_G. (g) shows a result of (c) produced by A in the direction of the diffraction beam. This can be called bright-field imaging because it contains illumination light to some extent.

Furthermore, since I_O in eq. (2) and I_G in eq. (3) can be simplified at $W = 0$ as

$$I_O = \sin^2(\pi H / \Lambda) \qquad (6)$$

$$I_G = \cos^2(\pi H / \Lambda), \qquad (7)$$

both I_O and I_G oscillate at zero and 1, respectively, or *vice versa* in the case of no absorption.

Maximum and minimum values for I_O and I_G are given

Fig. 1. Reflectivity dependence of I_O for O-beam, in the forward diffraction direction, and I_G for G-beam, in the diffraction direction, versus angular position within 1μrad for the range of crystal thicknesses between 1.10 mm and 1.15 mm. The angular range in the x axis is approximately the order of ± 1.0 arc sec. One can recognize that every change by approximately 10μm may lead to a 20% reflection both in I_O and I_G so that only a 50μm thickness change may lead to the change of function of I_O and I_G.

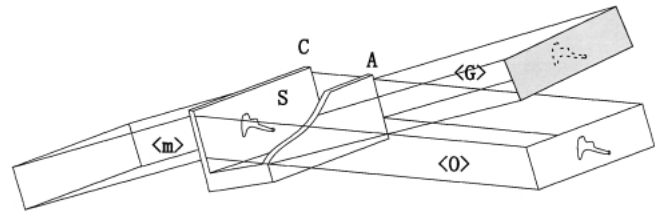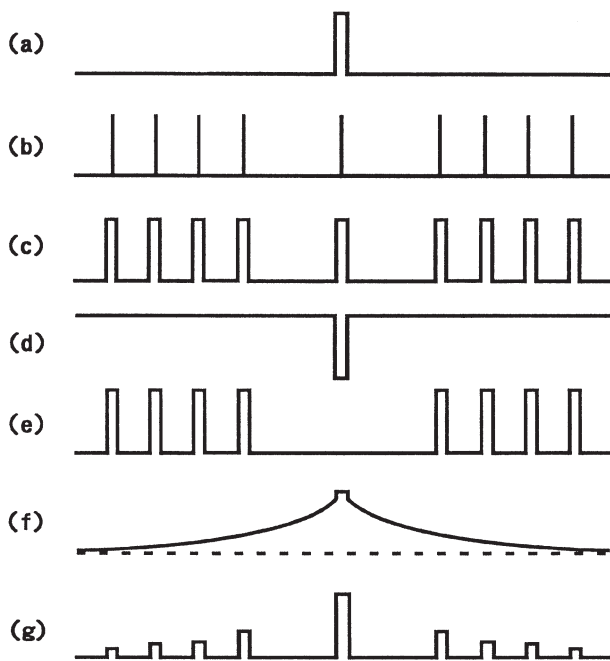Fig. 3. Schematic diagram for producing dark field and bright-field imaging. The symbol (a) corresponds to the incident beam available from an asymmetrically cut crystal that produces narrow divergence. The *x*-axis represents the angular coordinate; (b) expresses the angular distribution of the object due to refraction. This model comprises four boundaries of refraction. (c) is the calculated profile of the beam from a sample. It is the convolution between (a) and (b). The calculated acceptance given by A is shown in (d). In this case, the beam can be reflected for almost all divergence except for $|W| < 1$. The result of the analysis of the beam by A is shown in (e), in other words a dark field imaging. The profile of acceptance by A toward the diffraction beam direction is shown in (f). (g) is a result of the analysis of the beam by A. This should correspond to bright field imaging.

Fig. 4. This shows the relationship between reflectivity I_O or I_G, crystal thickness and the X-ray photon energy. One period that gives minimum or maximum I_O or I_G is approximately $62.5 \mu m$, in crystal thickness and $4 keV$ in X-ray photon energy such that when control of the crystal thickness is difficult, one can alternatively control the X-ray photon energy by $1.05 keV$.

when $H = p\Lambda/2$ here p is an integer. If one needs the condition of $I_O = 0$ and $I_G = \max$ or vice versa for the fixed X-ray wavelength, a certain precision of thickness H in the fabrication of the analyzer crystal A will be needed.

Figure 4 shows the relationship between I_O and crystal thickness and X-ray photon energy. This can indicate if the crystal thickness control is difficult in its fabrication; one can alternatively tune the X-ray photon energy so that I_O can achieve the minimum value. We can learn from eq. (6) that the X-ray photon energy corresponding to a thickness change of $62.5 \mu m$ is approximately $1.05 keV$.

One shot in the dark-field imaging that enables clear visualization of the entire image containing almost all information on the structure inside the object at a fixed angle position $W = 0$ of the analyzer crystal seems very advantageous over other methods that require numerous pictures by detuning the analyzer crystal under the exact Bragg condition of $|W| = 0$ either in the Laue case[12] or in the Bragg case.[13,14,18,20]

3. Experimental

In an experiment, asymmetric reflection[25] was used as a key technique to expand the beam size as well as to narrow the beam divergence at experimental stations BL14B[26] at Photon Factory and BL20B[27,28] and BL24XU[29] at SPring-8. X-ray optics 'Owl'[1] and 'Trinity',[24] both of which were manufactured on site have been successfully installed to take

X-ray pictures of a variety of samples.

The experiment was carried out under the following conditions: the crystal thickness was 1.08 mm, the X-ray photon energy 35 keV and the asymmetric parameter b[25] 0.05 in the scheme as shown in Fig. 2. The current in the storage ring was approximately 400 mA at Photon Factory and 100 mA at SPring-8. A wave packet $\langle m \rangle$ with a divergence of $0.3 \mu rad$ from an asymmetrically cut monochromator is incident onto a sample S so that the beam from S involving the sample condition is incident onto A that splits into two wave packets $\langle O \rangle$ and $\langle G \rangle$.

To demonstrate dark-field imaging, the use of a variety of samples has been attempted: a dried phalanx (Fig. 5), human auditory ossicles (Fig. 6), a mammographic phantom (Fig. 7), elephant tusk, and similar mammalian materials (Fig. 8). Images were stored on an electron microscopy film or X-ray film or nuclear plate with spatial resolution of approximately $10 \mu m$ or better. The limit of spatial resolution of the system is defined by the beam width at the exit of the Borrmann fan which is formed both in the incident beam direction and the diffracted beam direction after a finite thickness of the analyzer A. The exposure time for each picture was approximately 1–2 min at all stations such as at BL14B[26] which utilizes synchrotron radiation from a superconducting wiggler of 5 Tesla at the Photon Factory ring in operation with an acceleration energy of 2.5 GeV and stored current of 400 mA or at BL20B from a bend source at SPring-8 or at BL24XU from an undulator at SPring-8.

Figure 5 shows the fine details of bone trabeculae were not revealed by a conventional X-ray imaging technique. A method of illuminating bone with plane wave X-rays by Mori *et al.*[30] or with a spherical wave from an extremely small X-ray source by Gureyev *et al.*[30] showed slight contrast of bone trabeculae adjacent to a joint. Adoption of an analyzer crystal can reveal a very clear internal structure in spite of the remaining background due to unsatisfactory

Jpn. J. Appl. Phys. Vol. 41 (2002) Pt. 1, No. 7A

M. ANDO et al.   4745
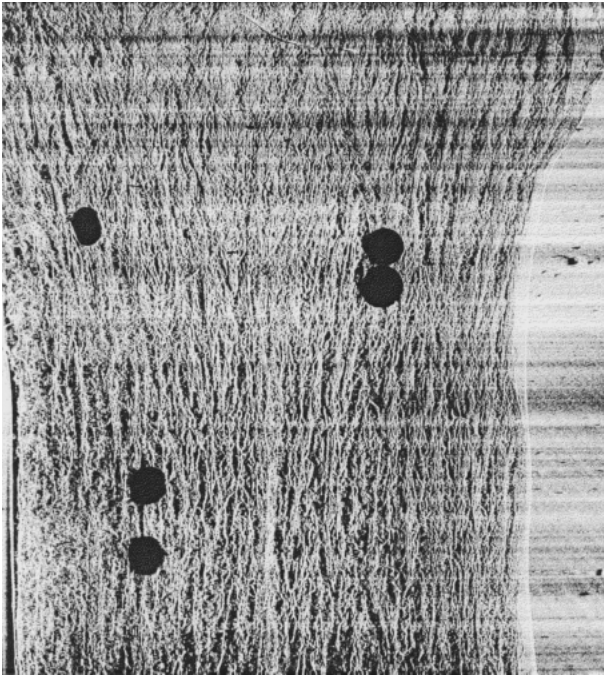
Fig. 5. A human dried proximal phalanx showing vertical bone trabeculae taken by the method shown in Fig. 2. Its size is 7 mm × 14 mm. Several black solid circles on the picture denote radiation arise from marks with Pb for markers. Horizontal lines seen over the picture are crystallographic defects replicated.

Fig. 6. This is a human incus containing multiple intra-osseous channels, parallel to its long axis, which have the appearance of vascular structures.

thickness control of the analyzer crystal. This method will be of great help in understanding the growth mechanism of bone and certain bone diseases such as osteoporosis. Some crystallographic defects, probably striations of a crystal of the X-ray optics used, are also visible in the background.

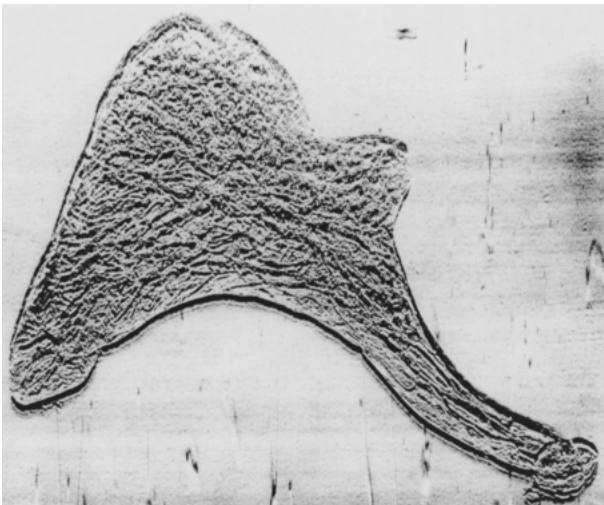The incus of human auditory ossicles[32] is shown in Fig. 6. The optimal X-ray energy was selected with the result that almost no background illumination was achieved. This picture shows some vascular channels. For a more detailed discussion see a paper by Ando et al.[32,33] The vascular structure suggests that the blood flow arises in a body of the incus and proceeds toward the lenticular process.

X-ray pictures of the mammographic accreditation

phantom RMI 156 were taken, as shown in Fig. 7, to evaluate the system 'Owl' because the early discovery of breast cancer is a compelling public health issue. The phantom supplied by Gammex, U.S.A., consists of 16 blocks each with a dimension of 20 mm × 20 mm and a thickness of 7 mm. Each contains a pseudo cancer tissue structure. Since the beam size was not sufficiently large to cover the entire object, Fig. 7 consists of 16 exposures. Some bubbles are visible. The third column corresponds to dark field images because of the virtual absence of a background. All others correspond to images between dark and bright. For more details see the paper by Pattanasiriwisawa et al.[34] A high precision mammographic accreditation phantom RMI 160 was studied by an Italian group.[35] Another study using the same phantom RMI 156 used by us is underway at Grenoble.[36,37] Excised tissue has been imaged by a group in Italy,[38] a group in Russia[39] and a group in Japan.[40]

Some important applications relate to the preservation of endangered species by natural preservation. They include a nondestructive visual examination of ivory and similar materials used in illegal commerce. In Japan, seal impressions have been traditionally used in official documents together with hand-written signatures. African elephant ivory is a prized material used for seals and artifacts. The Japanese appreciate its high quality and prestige. The trade of elephant ivory and objects made from it is prohibited under the control of the Convention on International Trade in Endangered Species (CITES), well known as the 'Washington Convention'. So far, visual inspection, isotope spectrum anlysis[41,42] and X-ray fluorescence analysis[43,44] have been used to identify ivory and other materials. In spite of the above internationally established convention on the comprehensive ban of export and import of ivory their smuggling is still rampant. Alternative reliable, nondestructive and low-cost methods are needed. In Figs. 8(a)–8(d), pictures of hard ivory which is available in western Africa, soft ivory, available in middle and eastern Africa, mammoth tusk and water buffalo horn were taken by the dark-field imaging optics are shown.

4. X-Ray Optics 'Trinity'

In addition to the above X-ray optics 'Owl', with which one can take dark-field images based on the principle of refraction contrast, two other contrasts may exist, absorption and interference[45–47] using an X-ray interferometer which was devised by Bonse and Hart.[48] In order to accommodate these three contrasts another X-ray optics, 'Trinity'[24] has been proposed as shown in Fig. 9. It consists of an asymmetric diffraction monochromator and novel monolithic X-ray optics. The sphere in the drawing represents a sample. Images seen from behind the screen from right to left are from absorption, two phase-interference and refraction contrast. In Fig. 10, these three contrasts are seen in a composite material consisting of boron fibers of $100\,\mu$m diameter embedded in a Ti plate of 1 mm thickness. The symbols (a) correspond to refraction contrast, (b) phase-interference, (c) phase-contrast and (d) absorption contrast. The order of arrangement of the pictures is the same as that in Fig. 9. One sees almost no contrast in image (d) due to absorption, whereas the two others show details of the internal structure. These were taken with an X-ray energy of
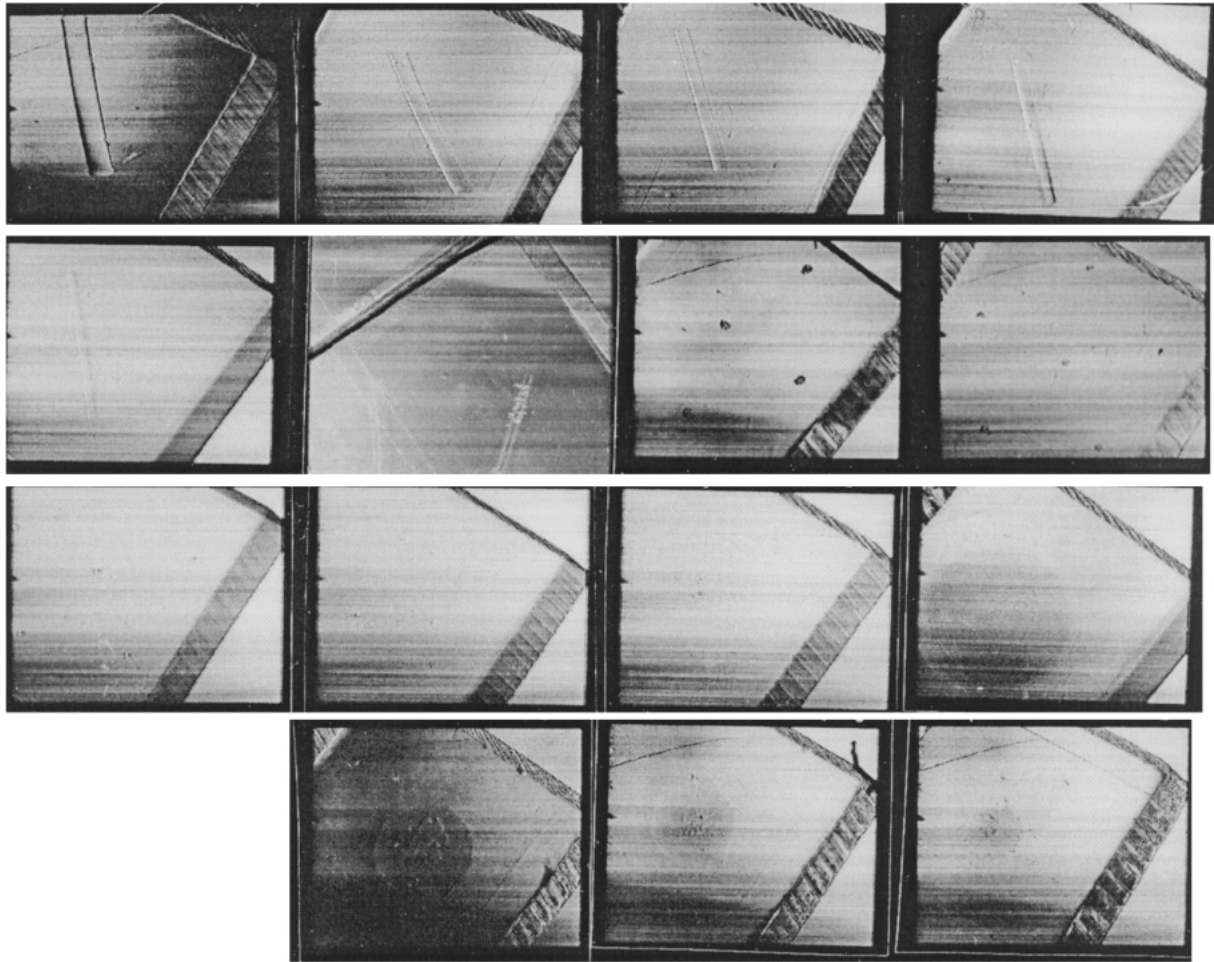
Fig. 7.   The mammographic accreditation phantom RMI 156 that comprises three elements, nylon fibers, specks of Al_2O_3 and nylon disc. The phantom is supplied by Gammex, U.S.A. Images were taken by the 'Owl'. A breast cancer phantom contains a nylon fiber with diameter of $400\,\mu m$ molded in a wax block. Its thickness is $7\,mm$. Both the nylon fiber and bubbles, which might have been introduced during the fabrication process, are clearly shown. Since the beam size was $2\,cm \times 2\,cm$, the same dimensions of the element as those of the object, each picture represents the entire phantom.

$35\,keV$. Surveying the interior of an unknown material with use of 'Trinity' may provide three kinds of contrasts simultaneously. One can readily identify which contrast is most suitable.

5.   Discussion and Conclusion

One can achieve X-ray dark-field imaging under a certain thickness of an analyzer crystal A with the precision of $10\,\mu m$ in Fig. 2. Some figures such as Fig. 6 and a part of Fig. 7 have been taken as dark-field images, while almost all others were taken between dark- and bright-field images because of the difficulty of controlling the analyzer thickness. If thickness control fails, energy tuning can meet the condition of X-ray dark-field imaging. This new technique is capable of visualizing the internal fine structure of any material in a wide range of disciplines, such as medicine, biology, palaeontology,[49] material science and possibly physics.

In Fig. 5 is shown the background due to a crystal imperfection (transverse lines) that may occur in imaging. Figure 6 is a dark-field image without any background. Figure 7 shows a mixture of dark and bright field images. The third line of the figure shows almost no background. The images in Fig. 8 do not satisfy the condition of dark-field

imaging due to optical imperfections.

Almost all images in Figs. 5–8 and Fig. 10 contain horizontal lines that may replicate the features of the beam from an upstream monochromator. This pattern may correspond to striations due to periodical inclusion of carbon atoms in the crystals. This unwanted background could be suppressed by introducing a high-quality crystal or by data processing.

A 3-D reconstruction technique applicable to medicine, using an absorption-based contrast, has been developed. A system for the phase-interference contrast is under construction.[46,47] A pioneering trial of 2-D reconstruction using refraction contrast has been initiated by Dilmanian for a simple phantom.[50] As the progress in 3-D reconstruction and its medical application is likely to result in major imaging advances, we have initiated a computer program for 3-D reconstruction.[51]

The radiation dose will be carefully taken into account before applying the method clinically, in the same manner as we have proceeded with in intravenous coronary angiography.[52–54]

It should be pointed out that one can simultaneously take three images, phase-interference contrast,[45–47] refraction contrast and absorption contrast.

(a)

(b)

(c)

(d)
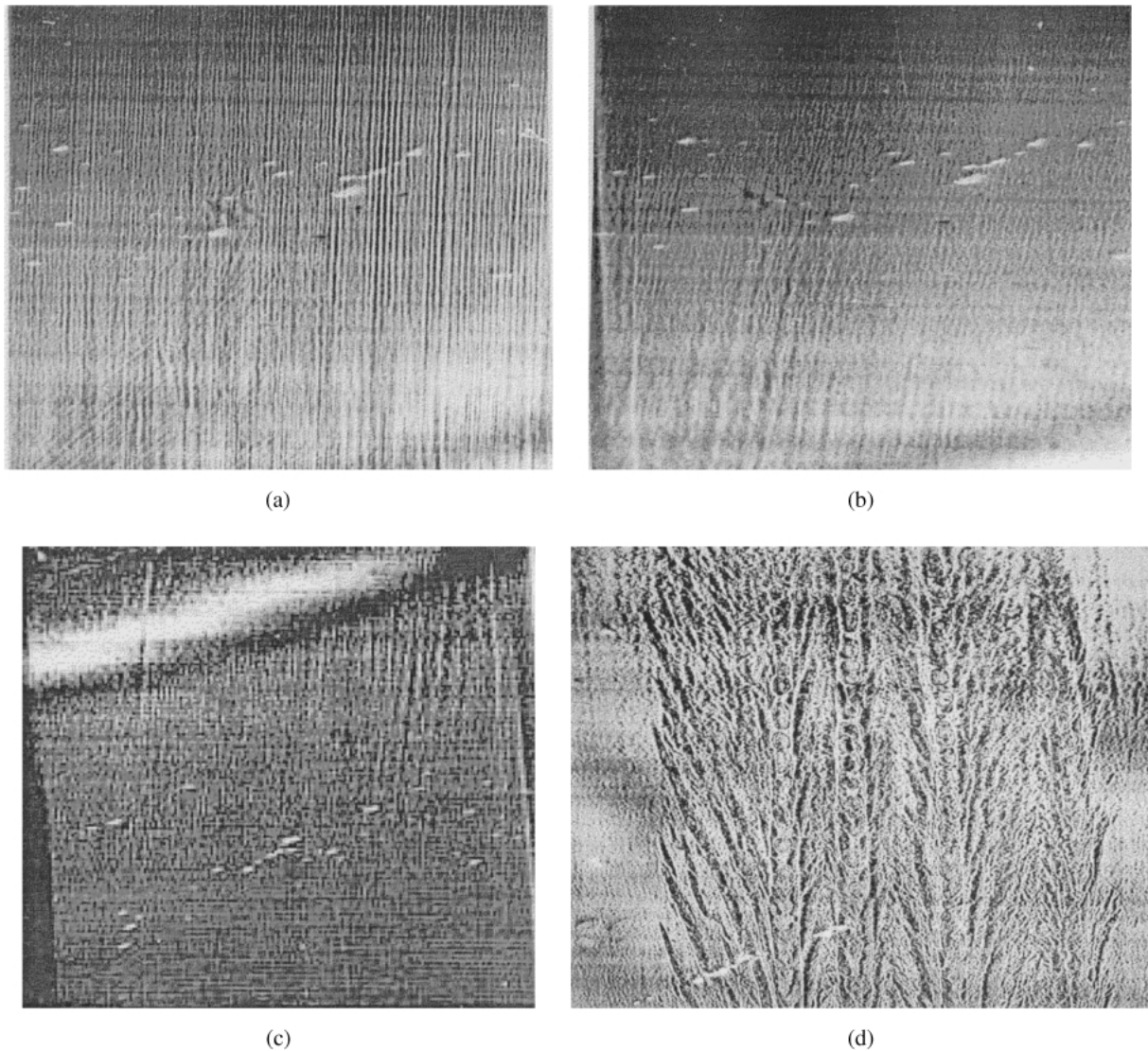
Fig. 8.   Internal structure is visible for (a) hard ivory tusk, (b) soft ivory tusk, (c) mammoth tusk and (d) water buffalo horn. The hard ivory (a) shows mostly periodic vertical lines; (b) and (c) show a less clear vertical structure compared with (a). It is almost impossible to distinguish between (b) and (c) because both show a similar local structure. In (d), the water buffalo displays a distinctive tree-like structure.
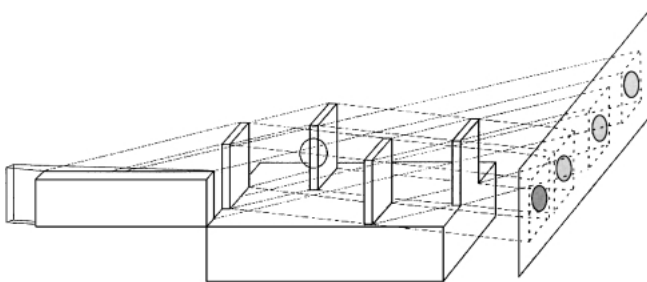
Fig. 9.   This is a drawing of another new X-ray optics capable of taking three kinds of images simultaneously: (a) represents refraction contrast, (b) phase-interference, (c) phase-contrast and (d) absorption contrast. The absorption contrast image (d) shows almost no image, whereas the other three clearly do.

1) M. Ando, H. Sugiyama, A. Maksimenko, W. Pattansiriwisawa, K. Hyodo and X. Zhang: Jpn. J. Appl. Phys. **40** (2001) L844.
2) V. E. Cosslett and W. C. Nixon: Nature **168** (1951) 24.
3) V. E. Cosslett and W. C. Nixon: J. Appl. Phys. **24** (1951) 616.
4) M. Born and E. Wolf: *Principles of Optics* (Pergamon Press, Oxford, 1975) 5th ed.
5) K. M. Podurets, V. A. Somenkov and S. Sh. Shil'stein: Zh. Tekh. Fiz. **59** (1989) 115.

(a)   (b)   (c)   (d)
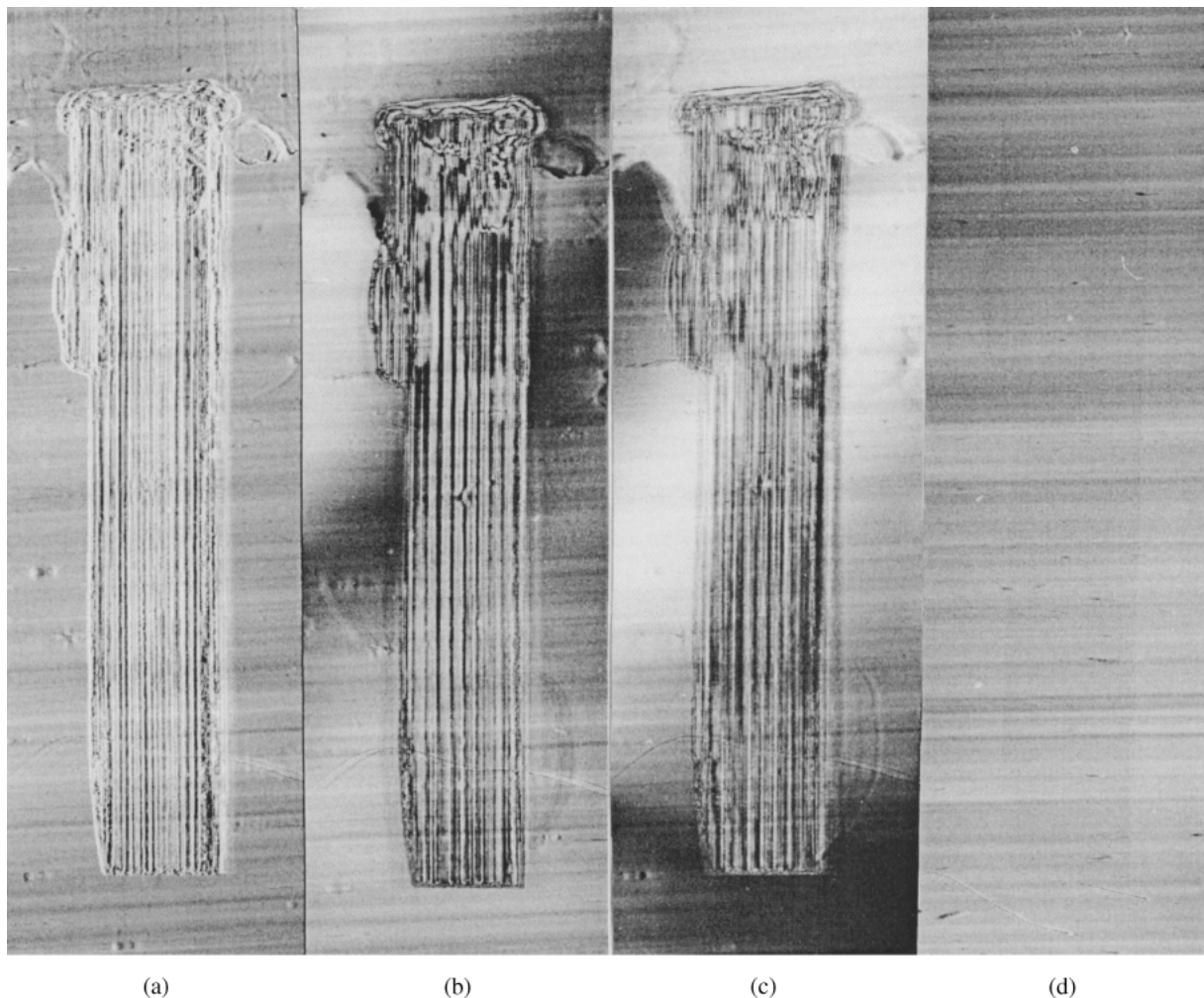
Fig. 10.   This is view of a composite material (B/Ti) showing contrasts depicted in Fig. 9. The material is comprised of boron fibers embedded in a Ti plate. The view size is 4.5 mm × 14 mm. From left to right the refraction, two phase-interference and the absorption contrast are seen. The refraction image shows the sharpest features. The phase-interference image also shows a very sharp contrast. The absorption image shows the least contrast at 35 keV.

6) K. M. Podurets, V. A. Somenkov and S. Sh. Shil'stein: Sov. Phys. Tech. Phys. **34** (1989) 654.

7) K. M. Podurets, V. A. Somenkov and S. Sh. Shil'stein: Physica B **156/157** (1989) 691.

8) K. M. Podurets, V. A. Somenkov, R. R. Chistyakov and S. Sh. Shil'stein: Physica B **156/157** (1989) 694.

9) V. A. Somenkov, A. K. Tkalich and S. Sh. Shil'stein: Zh. Tech. Fiz. **61** (1991) 197.

10) V. A. Somenkov, A. K. Tkalich and S. Sh. Shil'stein: Sov. Phys. Tech. Phys. **36** (1991) 1309.

11) A. Snigirev, I. Snigireva, V. Kohn, S. Kuznetsov and I. Schelokov: Sci. Instrum. **66** (1995) 5486.

12) V. N. Ingal and E. A. Beliaevskaya: J. Phys. D **28** (1995) 2314.

13) T. J. Davis, D. Gao, T. E. Gureyev, A. W. Stevenson and S. W. Wilkins: Nature **373** (1995) 595.

14) T. J. Davis, T. E. Gureyev, D. Gao, A. W. Stevenson and S. W. Wilkins: Phys. Rev. Lett. **74** (1995) 3173.

15) K. A. Nugent, T. E. Gureyev, D. F. Cookson, D. Paganin and Z. Barnea: Phys. Rev. Lett. **77** (1996) 2961.

16) S. W. Wilkins, T. E. Gureyev, D. Gao, A. Pogany and A. W. Stevenson: Nature **384** (1996) 335.

17) P. Clotens, R. Barrett, J. Bruchel, J.-P. Guigay and M. Shlenker: J. Phys. D **29** (1996) 133.

18) D. Chapman, W. Thomlinson, F. Arfelli, N. Gmuer, Z. Zhong, R. Menk, R. E. Johnson, Washburn, D. Pisano and D. Sayers: Rev. Sci. Instrum. **67** (1996) 3360.

19) S. Sh. Shil'stein, K. M. Podurets, V. A. Somenkov and A. A. Manushkin: Surf. Invest. **12** (1997) 451.

20) W. Thomlinson, D. Chapman, Z. Zhong, R. E. Johnston and D. Sayers: *Medical Applications of Synchrotron Radiation*, eds. M. Ando and C. Uyama (Springer-Verlag, Tokyo, 1998) p. 72.

21) D. Gao, T. E. Gureyev, A. Pogany, A. W. Stevenson and S. W. Wilkins: *Medical Applications of Synchrotron Radiation*, eds. M. Ando and C. Uyama (Springer-Verlag, Tokyo, 1998) p. 63.

22) N. Yagi, Y. Suzuki, K. Umetani, Y. Kohmura and K. Yamasaki: Med. Phys. **26** (1999) 2190.

23) T. E. Gureyev, C. Raven, A. Snigirev, I. Snigireva and S. W. Wilkins: J. Digital Imag. **13** (1999) 563.

24) M. Ando, H. Sugiyama, X. Zhang, K. Hyodo, A. Maksimenko and W. Pattansiriwisawa: Jpn. J. Appl. Phys. **40** (2001) L298.

25) K. Kohra: J. Phys. Soc. Jpn. **17** (1962) 589.

26) M. Ando, Y. Satow, H. Kawata, T. Ishikawa, P. Spieker and S. Suzuki: Nucl. Instrum. Methods A **264** (1986) 144.

27) K. Umetani, Y. Suzuki and N. Yagi: Spring-8 Inf. **4** (1999) 50 [in Japanese].

28) S. Goto, K. Takeshita, Y. Suzuki, H. Ohashi, Y. Asano, T. Kimura, N. Matsushita, M. Yagi, H. Isshiki, H. Yamazaki, Y. Yoneda, K. Umetani and T. Ishikawa: Nucl. Instrum. Methods Phys. Res. A **467/468** (2001) 682.

29) Y. Tsusaka, Y. Matsui, S. Takeda, K. Takai, Y. Kagoshima and J. Matsui: Nucl. Instrum. Methods Phys. Res. A **467/468** (2001) 670.

30) K. Mori, K. Hyodo, N. Shikano and M. Ando: Jpn. J. Appl. Phys. **38** (1999) L1339.

31) T. E. Gureyev, A. W. Stevenson, D. Paganin, S. C. Mayo, A. Pogany, D. Gao and S. W. Wilkins: J. Digital Imag. **13** (2000) 121.

32) M. Ando, J. Roberson, E. Rubenstein, W. Pattanasiriwisawa, A.

Maksimenko, H. Sugiyama, K. Hyodo and C. Uyama: *Proc. Joint Symp. Bio-Sensing and Bio-Imaging, 2001*, ed. T. Akatsuka (Biology Radical Institute and the Japan Society for Analytical Chemistry, 2002) p. 95.

33) M. Ando, J. Roberson and E. Rubenstein: in preparation.

34) W. Pattanasiriwisawa, A. Maksimenko, H. Sugiyama, K. Hyodo and M. Ando: *Proc. Joint Symp. Bio-Sensing and Bio-Imaging, 2001*, ed. T. Akatsuka (Biology Radical Institute and the Japan Society for Analytical Chemistry, Tokyo, 2002) p. 105.

35) F. Arfelli, F. Bonvicini, A. Bravin, G. Cantatore, E. Castelli, L. D. Palma, M. Di Michiel, M. Fabrizioli, R. Longo, R. H. Menk, A. Olivo, S. Pani, D. Pontoni, P. Poropat, M. Prest, A. Rashevsky, M. Patti, L. Rigon, G. Tromba, A. Vacchi, E. Vallazza and F. Zanconati: Radiology **215** (2000) 286.

36) S. Fiedler, A. Bravin, W. Thomlinson, J. Keyrilainen and P. Suortti: to be published in Proc. Joint Symp. Bio-Sensing and Bio-Imaging at Yamagata TERRSA 2001, Yamagata.

37) S. Fiedler, A. Bravin, W. Thomlinson, Keyrilainen and P. Suortti: Collected Abstr. Workshop on Medical Imaging at Grenoble 2001.

38) M. Di Michiel, A. Olivo, G. Tromba, F. Arfelli, V. Bonvicini, A. Bravin, G. Cantatore, E. Castelli, L. D. Palma, R. Longo, S. Pani, D. Pontoni, D. Poropat, M. Prest, A. Rashevsky, A. Vacchi and E. Vallazza: *Medical Applications of Synchrotron Radiation*, eds. M. Ando and C. Uyama (Springer-Verlag, Tokyo, 1998) p. 78.

39) V. N. Ingal, E. A. Beliaevskaya, A. P. Brianskaya and R. D. Merkurieva: Phys. Med. Biol. **43** (1998) 2555.

40) Q. Yu, T. Takeda, K. Umetani, E. Ueno, Y. Itai, Y. Hiranaka and T. Akatsuka: J. Synchrotron Radiat. **6** (1999) 1148.

41) Van der Merwe, J. A. Lee-Throp, J. F. Thackeray, A. Hall-Martin, F. J. Kruger, H. Coetzee, R. H. V. Bell and M. Lindeque: Nature **346** (1990) 744.

42) J. C. Vogel, B. Eglington and J. M. Auret: Nature **346** (1990) 747.

43) M. Shimoyama, H. Maeda, H. Sato, T. Ninomiya and Y. Ozaki: Appl. Spectrosc. **51** (1997) 1154.

44) M. Shimoyama, T. Nakanishi, Y. Hamanaga, T. Ninomiya and Y. Ozaki: J. Trace & Microprobe Tech. **16** (1998) 75.

45) M. Ando and S. Hosoya: *Proc. 6th Int. Conf. X-Ray Optics and Microanalysis, Osaka, 1971*, eds. G. Shinoda, K. Kohra and T. Ichinokawa (Univ. of Tokyo Press, Tokyo, 1972) p. 63.

46) A. Momose, T. Takeda, Y. Itai and K. Hirano: Nature Med. **2** (1996) 54.

47) A. Momose, T. Takeda, Y. Itai, A. Yoneyama and K. Hirano: *Medical Applications of Synchrotron Radiation*, eds. M. Ando and C. Uyama (Springer-Verlag, Tokyo, 1998) p. 72.

48) U. Bonse and M. Hart: Appl. Phys. Lett. **7** (1965) 99.

49) M. Ando, J. Chen, K. Hyodo, K. Mori, H. Sugiyama, D. Xian and X. Zhang: Jpn. J. Appl. Phys. **39** (2000) L1009.

50) A. Dilmanian: Phys. Med. Biol. **45** (2000) 933.

51) A. Maksimenko, M. Ando and T. Yuasa: *Proc. Joint Symp. Bio-Sensing and Bio-Imaging, 2001*, ed. T. Akatsuka (Biology Radical Institute and the Japan Society for Analytical Chemistry, Tokyo, 2002) p. 123.

52) S. Ohtsuka, Y. Sugishita, T. Takeda, Y. Itai, K. Hyodo and M. Ando: Jpn. Circ. J. **61** (1997) 432.

53) Y. Sugishita, S. Otsuka, T. Takeda, Y. Itai, K. Hyodo and M. Ando: *Medical Applications of Synchrotron Radiation*, eds. M. Ando and C. Uyama (Springer-Verlag, Tokyo, 1998) p. 15.

54) K. Hyodo, M. Ando, S. Yamamoto, S. Ohtsuka, I. Yamaguchi, T. Takeda and Y. Itai: Collected Abstr. Workshop on Medical Applications of Synchrotron Radiation at Grenoble on March 1–2, 2001, p. 37.

Simple X-Ray Dark- and Bright-Field Imaging Using Achromatic Laue Optics

Masami ANDO[1,2,*], Anton MAKSIMENKO[2], Hiroshi SUGIYAMA[1,2], Wanwisa PATTANASIRIWISAWA[2],
Kazuyuki HYODO[1,3] and Chikao UYAMA[4]

[1]*Photon Factory, Institute of Materials Structure Science, High Energy Accelerator Research Organization (KEK),*
1-1 Oho, Tsukuba, Ibaraki 305-0801, Japan

[2]*Department of Photo-Science, School of Advanced Studies, Graduate University for Advanced Studies (GUAS),*
Shonan International Village, Hayama, Miura, Kanagawa 240-0193, Japan

[3]*Department of Material Structure Science, School of Physical Mathematics, Graduate University for Advanced Studies (GUAS),*
1-1 Oho, Tsukuba, Ibaraki 305-0801, Japan

[4]*Department of Clinical Engineering, Faculty of Health Sciences, Hiroshima International University,*
Kurose-chou, Kamo-gun, Hiroshima 724-0695, Japan

X-ray dark-field and bright-field imaging in the Laue geometry has been successfully demonstrated. Using a Bragg-case asymmetric monochromator that produces an X-ray beam with a 0.3 μrad divergence incident onto an object and a Laue geometry analyzer that can simultaneously provide dark-field imaging (DFI) and bright-field imaging (BFI). The DFI has only an X-ray refraction component on the object without illumination, while the BFI has reasonable illumination. This was achieved by a 1.075 mm thick silicon analyzer with 4, 4, 0 diffraction at 35 keV X-ray photon energy. An image of an insect embedded in polymethylmethacrylate, which can not be visualized by absorption, has been obtained.   [DOI: 10.1143/JJAP.41.L1016]

A new idea concerning very simple X-ray dark-field and bright-field imaging in Laue geometry that has never been proposed before is presented here. Since 1989, various refraction-based imaging[1-15] techniques have been proposed. All of these have originated from X-ray shadow micrography pioneered by Cosslett and Nixon in 1951.[16,17] This may correspond to imaging in the visible-light region, as described in the literature by Born and Wolf.[18] These techniques involve a neutron imaging system using a Bragg diffraction analyzer,[1-4] and X-ray imaging systems without an analyzer,[5,15] with Laue analyzer,[6] with a Bragg analyzer[7,8,12-14] and with no optics.[9-11] All of these, in principle, might be categorized as bright-field imaging under a special analyzer condition.[6-8,12-14] We have recently developed dark-field imaging using new X-ray Laue[19,20] and Bragg[21] optics. The dark-field imaging in Laue geometry[19,20] proposed is very advantageous over the previous imaging developed by others[1-4,6-8,12-14] because one does not have to take a series of pictures while changing the angle of the analyzer crystal; One can simply obtain clear dark- and bright-field image of an object in a single shot.

The deflection angle, $\Delta(x, y: k)$,[19-21] associated with a refraction contrast can be described as follows:

$$\Delta(x, y: k) \propto -\int_{z_0}^{z_1} \partial\delta(x, y, z: k)/\partial x dz, \qquad (1)$$

where $\delta(x, y, z: k)$ is related to the refractive index, $n = 1 - \delta(x, y, z: k)$, z is the direction of the X-ray beam, z_0 and z_1 denote the coordinates where the X-rays go into and out of the object, respectively, and let refraction take place in the (z, x) plane.

In our X-ray dark-field and bright-field imaging arrangement shown in Fig. 1, the Laue geometry of diffraction in an achromatic arrangement, where two diffracting planes involving a monochromator M and an analyzer crystal A are in a $(+, -)$ parallel arrangement, is essential so that imaging receives no effect of wavelength spread that may otherwise blur
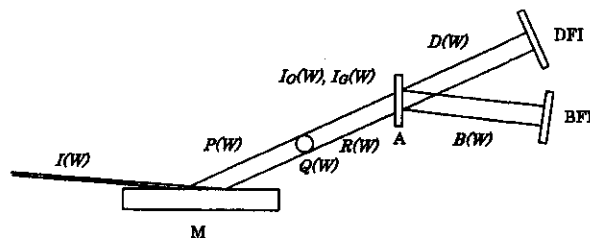
Fig. 1. X-ray optics setup for simultaneously producing dark-field image and bright-field images. The incident beam $I(W)$ is incident onto an asymmetric monochromator M that reduces outgoing beam divergence by a factor of 0.2. The beam divergence of $P(W)$, which is incident onto object $Q(W)$, has 0.3 μrad. The modulated beam $R(W)$ contains information on $Q(W)$; $R(W)$ splits into $D(W)$ and $B(W)$ due to $I_0(W)$ and $I_G(W)$, respectively. $D(W)$ and $B(W)$ lead to production of a dark-field image and a bright-field images using an imaging device, respectively.

the image contrast. We have chosen the asymmetric factor b (refer to ref. 22) to be 0.05 at M so that one can provide the beam $P(W)$ with divergence of 0.3 μrad incident onto the object $Q(W)$ located between M and A. Thus $P(W)$ has been modulated into $R(W)$ due to $Q(W)$. The refraction angles for almost all boundaries of ordinary materials should be on the order of 1 μrad or greater than the angular spread of $P(W)$. This $R(W)$ will be analyzed by A that has a function of $I_0(W)$ along the direction of forward diffraction and $I_G(W)$ along the diffraction direction. $I_0(W)$ has the potential to suppress $R(W)$ completely at $|W| < 1$. Thus $D(W) = I_0(W)R(W)$ after A along the forward diffraction direction corresponds to dark-field imaging (DFI) because there is no apparent X-ray background intensity existing at $|W| < 1$ due to the structure of $I_0(W)$, while $B(W) = I_G(W)R(W)$ corresponds to bright-field imaging (BFI) along the diffraction direction because of the nature of $I_G(W)$. The beams $D(W)$ and $B(W)$ will be stored as a dark-field image and a bright-field image, respectively.

Two reflectivity functions $I_0(W)$ and $I_G(W)$ at A can be

---

*E-mail address: masami.ando@kek.jp
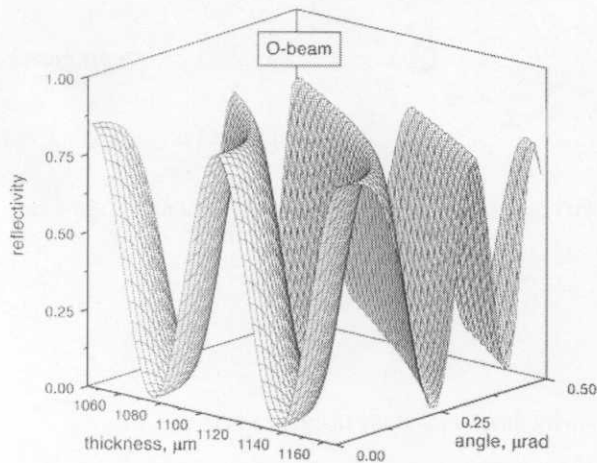
Fig. 2.   Reflectivity $I_O(W)$ versus the analyzer thickness t under the experimental condition of 1.075 mm, the angular coordinate W for 4, 4, 0 reflection and the X-ray energy of 35 keV. At $|W| = 0$, $I_O(W)$ is almost zero in the case of no absorption.

expressed if the X-rays undergo no absorption as follows:

$$I_O(W) = \sin^2(t\pi\sqrt{1 + W^2}/\Lambda)/(1 + W^2), \qquad (2)$$

$$I_G(W) = (\cos^2(t\pi\sqrt{1 + W^2}/\Lambda) + W^2)/(1 + W^2), \qquad (3)$$

$$I_O(W) + I_G(W) = 1, \qquad (4)$$

where t, W, Λ are thickness of A, deviation of the angle from the Bragg condition and the extinction distance, respectively. W can be expressed as $W = 2\Lambda \sin\theta_B(\theta - \theta_B - \Delta\theta_0)/\lambda$, where $\Lambda = \lambda \cos\theta_B/|P\|\chi_G|$ is the extinction distance, P the polarization factor, λ the X-ray wavelength, $\chi_G = -r_e\lambda^2 F_G/\pi V_C$ the polarizability, where r_e is the classical radius of electron, F_G the crystal structure form factor, V_C the volume of unit cell, θ the angle that deviated from the Bragg angle θ_B and $\Delta\theta_0$ correction of the Bragg angle due to refraction expressed as $\Delta\theta_0 = 2(1 - n)/\sin^2\theta_B$. Equations (2) and (3) can be simplified as $I_O(W)|_{w=0} = \sin^2(t\pi/\Lambda)$ and $I_G(W)|_{w=0} = \cos^2(t\pi/\Lambda)$, respectively, at $W = 0$ so that $I_O(0)$ becomes 0%, while $I_G(0)$ 100% with periodicity of $t = p\Lambda$ where p is integer. Figure 2 shows $I_O(W)$ as a function of t and W under an experimental condition of $t = 1.075$ mm and the X-ray energy of 35 keV. The angular range in terms of W is shown only from 0.0 μrad to 0.50 μrad.

An explanation for dark-field and bright-field imaging is given as follows: first prepare an extremely straight forward beam $P(W)$ as shown in Fig. 3(a) using asymmetric diffraction[22] at M in Fig. 1. The horizontal axis should correspond to the angle, and the vertical axis to the power of the X-rays. Second, $P(W)$ that enters the object $Q(W)$ shown in Fig. 3(b) that has, for instance, an octahedral shaped polygon as shown in the inset between (b) and (c), may receive the refraction effect, either from the left or right or both directions, against the incident beam direction. As a result, the X-rays $R(W)$ which exit from $Q(W)$ may possess information on the object as shown in Fig. 3(c). Mathematically, $R(W)$ should be the convolution of $P(W)$ and $Q(W)$. Figure 3(d) shows the reflection profile $I_O(W)$ at A along the direction of forward diffraction. Due to this function of an angular filter apparently the central part of $R(W)$ has been suppressed as shown in Fig. 3(e) due to $I_O(W)$. This is called dark-field imaging $D(W)$. On the other
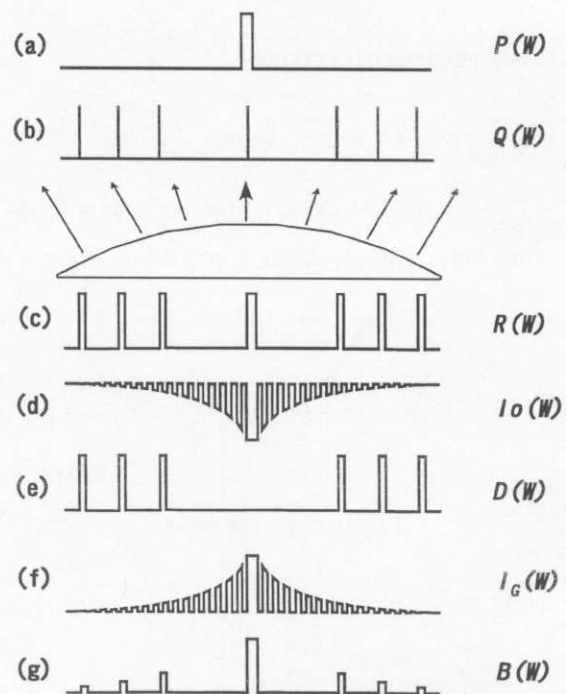
Fig. 3.   Diagram showing how DFI and BFI can be formed. The horizontal axis represents the angular scale represented by W, while the vertical axis represents the power of X-rays. (a) shows an incident beam profile $P(W)$. $P(W) = 1$ for $|W| < 1$, 0 for $|W| \geq 1$, where $W = \pm 1$ corresponds to a rocking curve width for asymmetric 4, 4, 0 diffraction that has the order of 0.15 μrad; (b) represents a schematic angular distribution of object $Q(W)$ as shown in the inset between (b) and (c). This shows a model with an 8-face polygon whose refractive index is for vacuum or larger than that of its surrounding atmosphere; (c) represents the angular distribution $R(W)$ that has information on $Q(W)$ as shown in $R(W) = P(W) * Q(W)$, where $*$ represents convolution of the two functions; (d) represents a transmission function $I_O(W)$ of an analyzer crystal A along the forward diffraction direction; (e) $D(W) = I_O(W)R(W)$ the intensity profile of the beam after A along the forward diffraction direction. This corresponds to DFI because no apparent illumination light remains; (f) The transmission function $I_G(W)$ along the diffraction direction of A, (g) $B(W) = I_G(W)R(W)$ that can be BFI because an image due to refraction involves the illumination light as well.

hand, due to the other function $I_G(W)$, as shown in Fig. 3(f) bright-field imaging $B(W)$ is available, as shown in Fig. 3(g).

The advantages of our method over the previous methods are as follows: first, our system is very simple. It only needs a parallel setting of two diffracting planes at M and A that should satisfy the thickness condition in eq. (1) for $I_O(W) = 0$ at $W = 0$. This can provide complete dark-field and bright-field imaging simultaneously in a single shot at $W = 0$. Also only a small distance between A and DFI or BFI is required. The contrast of all previous imaging techniques such as those by Ingal and Beliaevskaya,[6] Wilkins' group[7,8,10,12] and Chapman's group[13,14] should locate inbetween dark-field imaging and bright-field imaging. Their background could not be suppressed 100% if the Bragg angle at $|W| \gg 0$ is taken.

An experiment was performed at beamline BL14B[23] using a radiation source from a 5 T vertical wiggler at the Photon Factory and at BL20B[24,25] at the 8 GeV SPring-8 storage ring. Very good agreement between calculated and experimental values of $I_O(W)$ and $I_G(W)$ has been confirmed. Images were stored on a nuclear plate which has an exposure

(a)   (b)

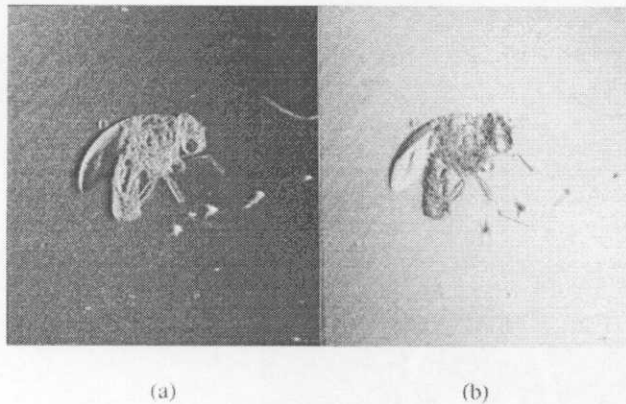Fig. 4.   (a) Dark-field image and (b) bright-field images of an insect embedded in polymethylmethacrylate. The field size is 5 mm × 5 mm. Exposure time using a nuclear plate was approximately 60 s. The dark-field image (a) has an almost completely dark background.

time of approximately 60 s.

Figure 4(a) shows an image of the DFI mode of an insect embedded in polymethylmethacrylate and (b) the BFI mode. Figure 4(a) shows apparently almost no background. The field is 5 mm × 5 mm.

1) K. M. Podurets, V. A. Somenkov and S. Sh. Shil'shtein: Zh. Tekh. Fiz. **59** (1989) 115. Translation: Sov. Phys. Tech. Phys. **34-6** (1989) 654.
2) K. M. Podurets, V. A. Somenkov and S. Sh. Shil'shtein: Physica B **156/157** (1989) 691.
3) K. M. Podurets, V. A. Somenkov, R. R. Chistyakov and S. Sh. Shil'shtein: Physica B **156/157** (1989) 694.
4) V. A. Somenkov, A. K. Tkalich and S. Sh. Shil'stein: Zh. Tech. Fiz. **61** (1991) 197. Translation: Sov. Phys. Tech. Phys. **36-11** (1991) 1309.
5) A. Snigirev, I. Snigireva, V. Kohn, S. Kuznetsov and I. Schelokov: Rev. Sci. Instrum. & Methods **66** (1995) 5486.
6) V. N. Ingal and E. A. Beliaevskaya: J. Phys. D **28** (1995) 2314.
7) T. J. Davis, D. Gao, T. E. Gureyev, A. W. Stevenson and S. W. Wilkins: Nature **373** (1995) 595.
8) T. J. Davis, T. E. Gureyev, D. Gao, A. W. Stevenson and S. W. Wilkins: Phys. Rev. Lett. **74** (1995) 3173.
9) K. A. Nugent, T. E. Gureyev, D. F. Cookson, D. Paganin and Z. Barnea: Phys. Rev. Lett. **77** (1996) 2961.
10) S. W. Wilkins, T. E. Gureyev, D. Gao, A. Pogany and A. W. Stevenson: Nature **384** (1996) 335.
11) P. Clotens, R. Barrett, J. Bruchel, J.-P. Guigay and M. Shlenker: J. Phys. D **29** (1996) 133.
12) D. Gao, T. E. Gureyev, A. Pogany, A. W. Stevenson and S. W. Wilkins: *Medical Applications of Synchrotron Radiation*, eds. M. Ando and C. Uyama (Springer-Verlag, Tokyo, 1998) p. 63.
13) D. Chapman, W. Thomlinson, F. Arfelli, N. Gmuer, Z. Zhong, R. Menk, R. E. Johnson, D. Washburn, E. Pisano and D. Sayers: Rev. Sci. Instrum. Methods **67** (1996) 3360.
14) W. Thomlinson, D. Chapman, Z. Zhong, R. E. Johnston and D. Sayers: *Medical Applications of Synchrotron Radiation*, eds. M. Ando and C. Uyama (Springer-Verlag, Tokyo, 1998) p. 72.
15) N. Yagi, Y. Suzuki, K. Umetani, Y. Kohmura and K. Yamasaki: Med. Phys. **26** (1999) 2190.
16) V. E. Cosslett and W. C. Nixon: Nature **168** (1951) 24.
17) V. E. Cosslett and W. C. Nixon: J. Appl. Phys. **24** (1953) 616.
18) M. Born and E. Wolf: *Principles of Optics* (Pergamon Press, Oxford, New York, Toronto, Sydney, Braunschweig, 1975) 5th ed.
19) M. Ando, H. Sugiyama, A. Maksimenko, W. Pattansiriwisawa, K. Hyodo and X. Zhang: Jpn. J. Appl. Phys. **40** (2001) L844.
20) M. Ando, K. Hyodo, H. Sugiyama, A. Maksimenko, W. Pattanasiriwisawa, K. Mori, J. Roberson, E. Rubenstein and Y. Tanaka: Jpn. J. Appl. Phys. **41** (2002) 4742.
21) K. Hirano, A. Maksimenko, H. Sugiyama and M. Ando: Jpn. J. Appl. Phys. **41** (2002) L595.
22) K. Kohra: J. Phys. Soc. Jpn. **17** (1962) 589.
23) M. Ando, Y. Satow, H. Kawata, T. Ishikawa, P. Spieker and S. Suzuki: Nucl. Instrum. & Methods A **264** (1986) 144.
24) K. Umetani, Y. Suzuki and N. Yagi: SPring-8 Information **4** (1999) 50 [in Japanese].
25) S. Goto, K. Takeshita, Y. Suzuki, H. Ohashi, Y. Asano, T. Kimura, N. Matsushita, M. Yagi, H. Isshiki, H. Yamazaki, Y. Yoneda, K. Umetani and T. Ishikawa: Nucl. Instrum. & Methods in Phys. Res. A **467/468** (2001) 682.

Possible Detection of Bony Trabeculae, Vascular Channels in Auditory Ossicles and Breast Cancer by Means of X-Ray Dark Field Imaging

Masami ANDO,[†,1,2,3]　**Joseph ROBERSON,**[4]　**Edward RUBENSTEIN,**[5]　**Wanwisa PATTANASIRIWISAWA,**[2] **Anton MAKSIMENKO,**[2] **Hiroshi SUGIYAMA,**[1,2] **Kazuyuki HYODO,**[1,3] **Chikao UYAMA**[6]

1[†]　*Photon Factory, Institute of Materials Structure Science, High Energy Accelerator Research Organization, Oho 1-1, Tsukuba, Ibaraki 305-0801, Japan (e-mail: masami.ando@kek.jp)*
2　*Department of Photon Science, School of Advanced Studies, Graduate University for Advanced Studies, Shonan International Village, Hayama, Miura, Kanagawa 240-0193, Japan*
3　*Department of of Materials Structure Science, Institute of Materials Structure Science, High Energy Accelerator Research Organization, Oho 1-1, Tsukuba, Ibaraki 305-0801, Japan*
4　*California Ear Institute at Stanford, Stanford, CA 94304, USA.*
5　*Department of Medicine, Stanford University School of Medicine, Stanford, CA 94305, USA*
6　*Department of Clinical Engineering, Faculty of Health Sciences, Hiroshima International University, Kurose, Kamo, Hiroshima 724-0695 Japan*

A novel X-ray optics for dark field imaging 'Owl' was successfully tested for medical application. The 'Owl' comprises a Bragg case asymmetric monochromator M, a collimator C and an analyzer A that can select only the refracted light under the diffraction with 4,4,0 and thickness at A of 1.08 mm. The angular widths of M and A used were 0.3 μrad at 36 keV of X-ray energy. It has been proven that A produces two beams, one forward diffracted beam which corresponds to the dark field imaging and the other diffracted one to the bright field one or vice versa in case of another specified thickness. Especially images due to refraction contrast in the dark field imaging from medical samples are clearly shown. In this paper an X-ray optics and its some applications to medical samples are described.

Introduction

Recently we have proposed an X-ray optics for a dark field imaging[1]. Physical principle involved is refraction. The refraction based imaging is basically shadow micrography as devised by Cosslett and Nixon in 1951[2,3]. This may correspond to a dark-ground method of observation or schlieren imaging in the visible light region described in an article by Born and Wolf[4]. What we describe here is a new concept in the X-ray region. Since 1995 a large number of approaches[5-18] to refraction-based contrast have appeared. They have been a number of methods based on: a neutron Bragg diffraction analyzer[5-8], monochromatized X-rays from a monochromator[9,12], a Laue X-ray transmission analyzer[10], only X-radiation as illuminating light for a sample without an analyzer[11,16], and an X-ray Bragg diffraction analyzer[13,14,15,17,18]. All of these that use an analyzer crystal behind the object can record dark field images when the analyzer crystal is tuned at a flank away off the main Bragg peak. This reduces X-rays that may cause unnecessary background. The new X-ray optics described in this manuscript can simultaneously provide two images, one a complete dark field imaging and the other bright field image.

Theory

The deflection angle $\Delta(x,y: k)$[1,21] which leads to refraction contrast can be described as follows:

$$\Delta(x,y:k) \propto -\int_{z0}^{z1} \partial\, \delta(x,y:k)\,/\partial\, x\, dz \qquad (1)$$

where $\delta(x,y: k)$ has a relation to the refractive index of $n = 1 - \delta(x,y: k.)$. z is the direction of X-ray beam propagation and z_0 and z_1 correspond to z the coordinates at which the X-ray beams enter and exit a sample, respectively. x corresponds to the coordinate perpendicular to z in the plane of incidence.

The Laue geometry of diffraction is indispensable for the acquisition of dark field imaging (Fig. 1). That can work as a filter that may stop the power towards the forward diffracted direction while the power towards the diffracted direction is most likely transparent. The two beams with the above nature are produced at a certain thickness of a silicon plate with a certain X-ray photon energy.

Let's define I_o as a beam toward the direction of forward diffraction and I_G toward the diffracted direction, respectively in case of no absorption as follows:

$$I_o = \sin^2(\pi H \sqrt{1 + W^2}\,/\,\Lambda)\,/(1 + W^2) \qquad (2)$$

$$I_G = (W^2 + \cos^2(\pi H \sqrt{1 + W^2}\,/\,\Lambda))\,/(1 + W^2) \qquad (3)$$

, where H is the crystal thickness, W the deviation of angle from the Bragg condition where $|W| = 1$ corresponds to the

reflection range and Λ the extinction distance defined as

$$\Lambda = \lambda \cos\theta_B / |P| |\chi_G| \qquad (4)$$

λ is the X-ray wavelength, θ_B the Bragg angle, P the polarization factor and χ_G the polarizability . The equations (2) and (3), if one considers only at W = 0, can be simplified as follows:

$$I_o = \sin^2 (\pi H/\Lambda) \qquad (5)$$
$$I_G = \cos^2 (\pi H/\Lambda) \qquad (6)$$

Analytically

$$I_o + I_G = 1 \qquad (7)$$

and I_o and I_G becomes zero and max, respectively when $H = \Lambda$. H that may lead to $I_o = 0$ and I_G = max needs its precision in fabrication better than with the order of 10 microns. Once H has been fixed one may tune the X-ray photon energy λ so that one can find out H that satisfies the condition $I_o = 0$ and I_G = max.

Typical reflection curves of I_o and I_G of the crystal plate are shown in Fig.2 under the condition of a crystal thickness of 1.08 mm, diffraction of 4,4,0, X-ray photon energy of 36 keV and the X-ray reflection at W = 0. It clearly shows that I_G and I_0 periodically oscillates approximately with period of 67.5 μm between 100 % and 0 %, respectively while keeping the relations of (5) and (6).

Bright field imaging and dark field imaging

Most of the previous works can be classified as the bright field imaging. Some can be dark field imaging in case of tuning the angular position of the analyzer at |W| >> 1. The condition of W = 1 gives the angle of the order of 0.3 arc sec in our case. For instance, both pioneering work of Ingal and Beliaevskaya[10] and Chapman et al[17,18] in principle can provide the dark field imaging. However, this may need a relatively long exposure time when it is taken at the flank of the diffraction peak by tuning the Bragg position of the analyzer crystal away from the main rocking curve and may introduce complicated data acquisition because since this method has angular dependence of imaging contrast one has to rotate the analyzer crystal to obtain a complete set of imaging. The system by Ingal and Beliaevskaya[10] is in a non-parallel setting and the other by Chapman et al[17] a parallel setting. The former may not be free from a wavelength spread while the latter does not present this problem.

On the other hand our new system still under development provides all information inherent in an image by a single shot without rotating the analyzer crystal. This may save the time of data acquisition. The dark field imaging, in principle, provides only internal structures of a material without illumination light that may cause lowering the signal to noise ratio. Nevertheless the conventional bright field imaging may contain a lot of information so that some data process of both imaging such as image subtraction from one to the other could provide informative image such as an edge enhancement.

Experimental

An experiment using the X-ray optics involving the asymmetric reflection[19] shown in Fig. 1 was performed at beamline BL14B[20] at Photon Factory, at BL20B[21] at Spring-8 and at BL24XU[22] at Spring-8. The experiment was performed under the following conditions: crystal thickness of 1.08 mm, the X-ray photon energy of 36 keV and the asymmetric parameter b[19] of 0.05 in the scheme shown in Fig. 1. This is for X-ray dark field imaging. First a wave packet $< \varphi_E >$ with divergence of 0.3 μrad from an asymmetric cut monochromator is prepared. This is incident onto the sample S so that the beam $< \varphi_{SCGE} >$ from S involving the sample condition is incident onto A that analyzes into two wave packets $< \varphi_{AOSCGE} >$ and $< \varphi_{AHSCGE} >$.

For demonstration of the dark field imaging three samples were prepared: a dried phalanx, human auditory ossicles and a mammographic phantom. Visual observation was performed to store images on electron microscopy films or X-ray film with spatial resolution of approximately 2 μm. Exposure time for each picture was approximately 1–2 min.

The dried proximal phalanx (see Fig. 3) shows the fine details of bony trabeculae, structures that had never been revealed by the conventional X-ray imaging technique. The technique of illuminating a bone with plane wave X-rays that was developed by Mori et al[23] or illuminating with an extremely coherent radiation from a microfocus X-ray source by Gureyev et al[24] showed also bony trabeculae especially adjacent to a joint. Nevertheless only adoption of the analyzer crystal can uniquely reveal very precision internal structure clearly. This method will be of great help to understand growth mechanism of bone and some bony diseases such as osteoporosis as the methods referred to 23 and 24.

The malleus as an example of the human auditory ossicles is shown in Fig. 4. As is the previous case[25] this picture shows some vascular type channels. For a more detailed discussion see paper (25).

The mammographic accreditation phantom RMI 156 from the Gammex in Wisconsin comprises 16 blocks each of which has a 20 mm x 20 mm and 7 mm thick dimension. Each contains a variety of pseudo cancer tissue structure. Since the beam size available with X-ray optics was only 18 mm x 18 mm Fig. 5 shows the piece # 7 which contains a nylon fiber. This picture shows bubbles which may have been embedded. For a more detailed discussion see paper (26) in this volume. An early very precision work of the the mammographic accreditation phantom RMI 160 was done by the Italian group[27]. The work using the phantom RMI 156 is under way at the Grenoble[28]. Some groups, one at Trieste[29] and the other at St. Petersburg[30] have imaged breast cancer using excised tissues.

Discussion and conclusion

The X-ray dark field imaging needs only thickness control of A. By adoption of energy tuning alternatively one can obtain effectively the same X-ray dark field imaging. This new technique has capability to visualize the internal fine structures of any material in a wide range of discipline, such as medicine, biology, palaentology[31], material science and probably physics.

As shown in the previous paper[32] one can simultaneously take three images, phase-interference contrast[33,34], refraction contrast and absorption contrast.

Development of a 3D reconstruction technique applicable to

medicine, using absorption-based contrast, is currently under intensive development. The technique of 3D reconstruction for images using the phase-interference contrast[35] is also under way. The corresponding pioneering technique for refraction contrast has been initiated by Dilmanian et al[36] using a simple phantom; Progress in 3D reconstruction, and its application to medical specimens in vitro, is likely to result in major imaging advances. We have initiated attempt at making a computer program also using the concept of filtered back-projection algorithms[37].

Radiation dose also in case of clinical use will have to be considered very carefully as in the intravenous coronary angiography[38,39,40,41].
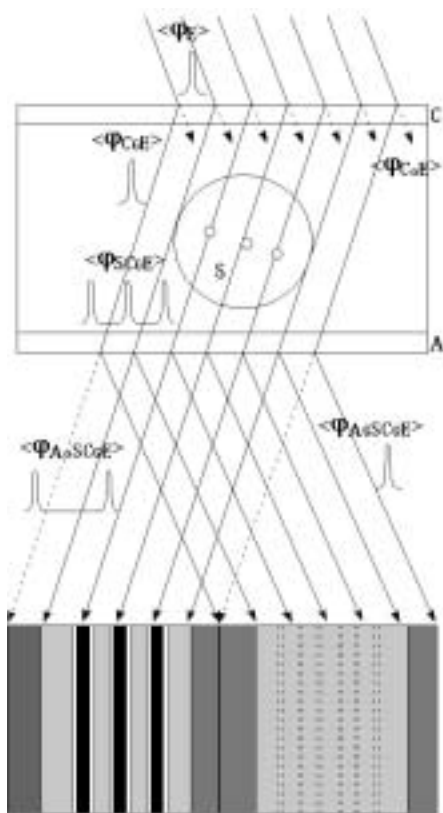
Acknowledgement

Figures

Fig. 1. Geometry of X-ray dark field imaging 'Owl'. Collimator C and analyzer A is a part of a monolithic block which keeps their angular relationship quite stable in between these. S means a sample. The incident beam $<\varphi_E>$ with 0.3 μrad beam divergence from an asymmetric monochromator excites $<\varphi_{CGE}>$ that passes through a sample S. The bright field image $<\varphi_{SCGE}>$ which is formed by a beam with beam divergence of 0.3 μrad is incident on analyzer A. This A holds acceptance in the angular range only outside ± 0.15 μrad so that $<\varphi_{AoSCGE}>$ containing refraction information is forward diffracted to bring us dark field imaging. See schematic the diffraction profiles shown as inset. A rocking curve $<\varphi_{CGE}>$ is shown by a solid line which corresponds to the H-beam and the other rocking curve $<\varphi_{COE}>$ is drawn by a broken line which corresponds to the O-beam. Thickness of silicon slabs C or A was chosen as 1.08 mm in this experiment. Their central peaks range ± 0.15 μrad which coincide with that of the incident beam $<\varphi_E>$. At the center of the profiles $<\varphi_{CGE}>$ has a maximum reflectivity and $<\varphi_{COE}>$ has a minimum value. As shown in inset of Fig. 1 the beam profile $<\varphi_{CGE}>$ does not have X-ray intensity practically outside the angular range ± 0.15 μrad while R_o has reasonable reflectivity outside ± 0.15 μrad so that only information due to refraction from S can be visualized in $<\varphi_{AOSCGE}>$. Thus this can be called 'X-ray dark field imaging'. The diffraction index and the X-ray energy used was 4,4,0 and 35 keV, respectively. As a model sample light element material contains lighter element inside such as tubes.
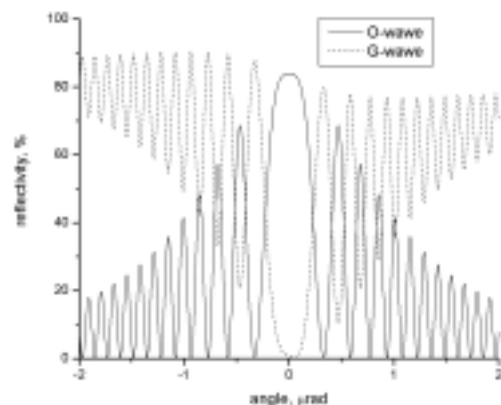
Fig. 2. Percent reflection of I_o for O-beam and I_G for G-beam. The O-beam and H-beam corresponds to the forward diffracted I_o and the diffracted beam I_G from the crystal wafer A, respectively. Under the special conditions these curves show the minimum value for I_O while the highest for I_G at W = 0. The corresponding four conditions are a Si plate, its diffraction index, its thickness and the X-ray photon energy. The wafer thickness of silicon is 1.08 mm, reflexion index 4,4,0 and the X-ray photon energy 36 keV. This relation may appear approximately every 67.5 μm of change of a wafer thickness. The profile I_O keeps its high percent reflection in average outside |W| = 1 while I_G shows rapid decreasing of its potential reflectivity. One can easily understand that the profile I_O in the angular range |W| > 1 may have high acceptance of scattering X-rays from a sample, while the I_G shows low reflectivity for the angular range |W| > 1 so that the signal level corresponding to the scattering from a sample will be relatively low compared to that corresponding to the I_O. Based on this consideration I_O may give a dark field imaging which has relatively low level of illumination light and I_G a conventional bright field imaging

with high level of illumination light.

Fig. 3. A human dried proximal phalanx showing vertical bony trabeculae taken by the method shown in Fig. 1. Its field is 7 mm by 14 mm in size. Several black solid circles on the picture are radiation marks with Pb. Horizontal lines seen over the picture are the replication of crystallographic defects such as growth striations from a crystal of the double crystal monochromator at the beamline BL 14B.

Fig. 4. A human malleus containing multiple intra-osseous channels, parallel to its long axis, which have the appearance of vascular structures. The branching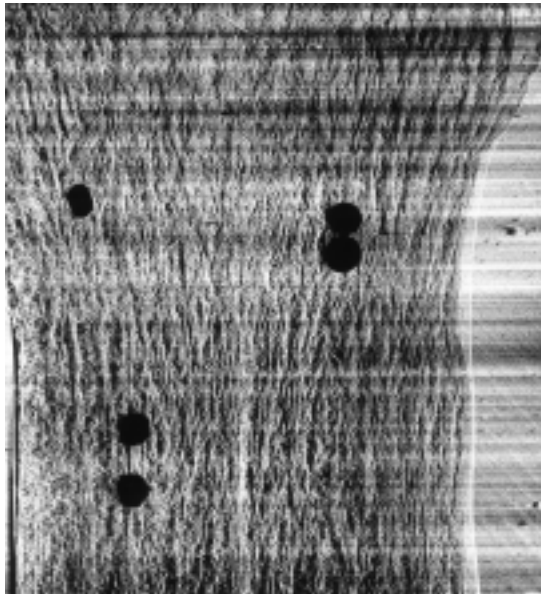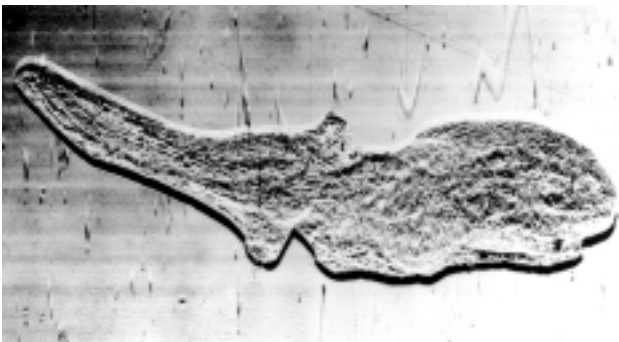 pattern suggests that the blood flow arises in the body of the incus and proceeds toward the lenticular process. Some crystallographic defects probably striations of a crystal of the X-ray optics used are visible in the background. The experiment was done at BL20B.
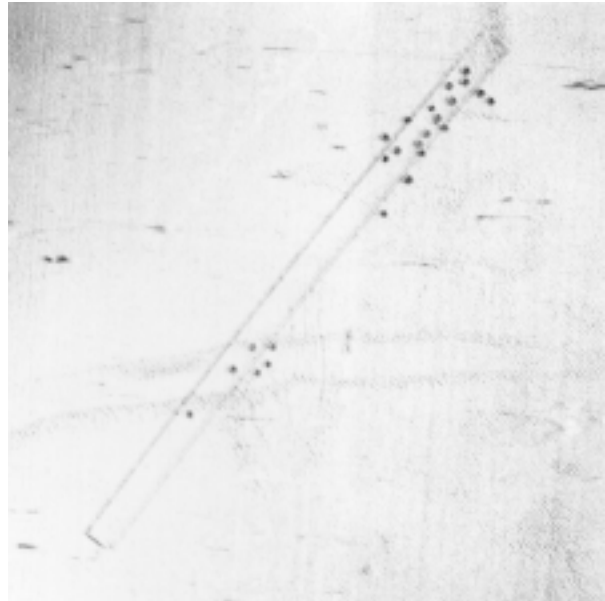
Fi.g 5. A breast cancer phantom piece #7 containing a nylon fiber with diameter of 400 µm molded in a wax block. This is a commercially available mammography phantom called "The mammographic accreditation phantom RMI 156" from Gammex. Its thickness is 7 mm. Not only the nylon fiber but also bubbles which might have been introduced during the fabrication process are very clearly shown. This object can be seen with only poor contrast by a normal projection of plane wave X-rays. The field size is approximately 2 mm by 2 mm. The experiment was performed at BL24XU.

References

[1] M. Ando, H. Sugiyama, A. Maksimenko, W. Pattansiriwisawa, K. Hyodo and Zhang X., "A new optics for dark-field imaging in X-ray region 'Owl,'" *Jpn. J. Appl. Phys.,* vol. 40, pp. L844-L846, August 2001.
[2] V.E. Cosslett and W.C. Nixon, "X-ray shadow microscope," *Nature*, vol. 168, pp. 24-25, July 1951.
[3] V.E. Cosslett and W.C. Nixon, "The X-ray shadow microscope," *J. Appl. Phys.*, vol. 24, pp. 616-623, May 1953.
[4] M. Born and E. Wolf, *Principles of Optics,* 5 th ed. Oxford, New York, Toronto, Sydney, Braunschweig: Pergamon Press, 1975.
[5] K.M. Podurets, V.A. Somenkov and S.Sh. Shil'shtein, "Refraction-contrast radiography," *Zh. Tekh. Fiz.* vol. 59, pp 115-121, June 1989; *Sov. Phys. Tech. Phys.,* vol. 34, pp. 654-657, June 1989.
[6] K.M. Podurets, V.A. Somenkov and S.Sh. Shil'shtein, "Neutron radiography with refraction contrast," *Physica B,* 156 & 157, pp. 691-693, 1989.
[7] K.M. Podurets, V.A. Somenkov, R.R. Chistyakov and S.Sh. Shil'shtein, "Visualization of internal domain structure of silicon iron crystals by using neutron radiography with refraction contrast," *Physica B,* vol. 156 & 157, pp. 694-697, 1989.
[8] V.A. Somenkov, A.K. Tkalich and S.Sh. Shil'stein, "Refraction contrast in X-ray introscopy," *Zh. Tech. Fiz.* vol. 61, pp.197-201; November 1991; *Sov. Phys. Tech. Phys.*, vol. 36-11, pp. 1309-1311, November 1991.

[9] A. Snigirev, I. Snigireva, V. Kohn, S. Kuznetsov, I. Schelokov, "On the possibilities of X-ray phase contrast microimaging by coherent high-energy synchrotron radiation," *R. Sci. Instrum.,* vol. 66-12, pp. 5486-5492, December 1995.

[10] V.N. Ingal, E.A. Beliaevskaya, "X-ray plane-wave topography observation of the phase contrast from a non-crsytalline object," *J. Phys. D* 28, pp. 2314-2317, 1995.

[11] T.J. Davis, D. Gao, T.E. Gureyev, A.W. Stevenson, S.W. Wilkins, "Phase-contrast imaging of weakly absorbing materials using hard X-rays," *Nature,* vol. 373-16, pp. 595-598, February 1995.

[12] T.J. Davis, T.E. Gureyev, D. Gao, A.W. Stevenson, S.W. Wilkins, "X-ray image contrast from a simple phase object," *Phys. Rev. Lett.,* vol. 74-16, pp. 3173-3176, April 1995.

[13] K.A. Nugent, T.E. Gureyev, D.F. Cookson, D. Paganin, Z. Barnea, "Quantative phase imaging using hard X-rays," *Phys. Rev. Lett.,* vol. 77-14, pp. 2961-2964, September 1996.

[14] S.W. Wilkins, T.E. Gureyev, D. Gao, A. Pogany, A.W. Stevenson, "Phase-contrast imaging using polychromatic hard X-rays," *Nature,* vol. 384, pp. 335-338, 1996.

[15] P. Clotens, R. Barrett, J. Bruchel, J.-P. Guigay, M. Shlenker, "Phase objects in synchrotron radiation hard x-ray imaging," *J. Phys. D,* vol. 29, pp. 133,-146, 1996.

[16] D. Gao, T.E. Gureyev, A. Pogany, A.W. Stevenson, S.W. Wilkins, "New methods of X-ray imaging based on phase contrast," in *Medical Applications of Synchrotron Radiation*, M. Ando and C. Uyama, Eds. Tokyo: Springer-Verlag, Tokyo, 1998, pp. 63-71.

[17] D. Chapman, W. Thomlinson, F. Arfelli, N. Gmuer, Z. Zhong, R. Menk. R. E. Johnson, D. Washburn, E. Pisano, D. Sayers, "Mammography imaging studies using a Laue crystal analyzer," *Rev. Sci. Instrum.* vol. 67, pp. 3360, 1996.

[18] W. Thomlinson, D. Chapman, Z. Zhong, R.E. Johnston, D. Sayers,"Diffraction enhanced X-ray imaging," in *Medical Applications of Synchrotron Radiation*, M. Ando and C. Uyama, Eds. Tokyo: Springer-Verlag, Tokyo, 1998, pp. 72-77.

[19] K. Kohra, "An application of asymmetric reflection for obtaining X-ray beams of extremely narrow angular spread," *J. Phys. Soc. Jpn*, vol. 17, pp. 589-590, 1962.

[20] M. Ando, Y. Satow, H. Kawata, T. Ishikawa, P. Spieker, S. Suzuki, "Design of beamline-14 for the PF vertical wiggler and its operation," *Nucl. Instr. & Meth*, vol. A264, pp. 144-148, 1986.

[21] K. Umetani, Y. Suzuki, N. Yagi, "On the construction of a medium length beamline BL20B2 for medical use from a bending magnet," *Spring-8 Information* (in Japanese) vol. 4, pp. 50-52, May 1999. S. Goto, K. Takeshita, Y. Suzuki, H. Ohashi, Y. Asano, H. Kimura, T. Matsushita, N. Yagi, M. Isshiki, H. Yamazaki, Y. Yoneda, K.Umetani, T. Ishikawa, "Construction and commissioning of a 215-m-long beamline at SPring-8," *Nucl. Instrum. and Meth*. vol. A467-468, pp 682-685, 2001.

[22] J. Matsui, Y. Kagoshima, Y. Tsusaka, Y. Katsuya, M. Motoyama, Y. Watanabe, K. Yokoyama, K. Takai, S. Takeda, J. Chikawa, "," *SPring-8 Annual Report 1997*, pp. 125.

[23] K. Mori, K. Hyodo, N. Shikano, M. Ando, "First Observation of small fractures on a human dried proximal phalanx by synchrotron X-ray interference radiography," *Jpn. J. Apply. Phys.*, vol. 38, pp. L1339-L1341, October 1999.

[24] T.E. Gureyev, A.W.Stevenson, D. Paganin, S.C. Mayo, A. Pogany, D. Gao, S.W. Wilkins, "Quantative methods in phase-contrast X-ray imaging," *J. Digital Imaging*, vol. 13, pp. 121-126, May 2000.

[25] M. Ando, J. Roberson, E. Rubenstein W. Pattanasiriwisawa, A. Maksimenko, H. Sugiyama, K. Hyodo, "Imaging of the microanatomy of the internal vascular channels in human ossicles using a synchrotron radiation based dark field optics system, "Owl," in preparation.

[26] W. Pattanasiriwisawa, A. Maksimenko, H. Sugiyama, K. Hyodo and M. Ando, "Visual observation of biological and medical specimen by a newly developed X-ray dark field imaing method," *Collected Abstracts of the Joint Symposium on Bio-Sensing and Bio-Imaging at Yamagata TERRSA, Yamagata*, pp. 16, 2001*; in this volume of the Proceedings of of the Joint Symposium on Bio-Sensing and Bio-Imaging*

[27] F. Arfelli, V. Bonvicini, A. Bravin, G. Cantatore, E. Castelli, L.Dalla Palma, M.Di. Michiel, M. Fabrizioli, R. Longo, R.H. Menk, A. Olivo, S. Pani, D. Pontoni, P. Poropat, M. Prest, A. Rashevsky, M. Patti, L. Rigon, G. Tromba, A. Vacchi, E. Vallazza, F. Zanconati, "Mammography with synchrotron radiation: phase-detection techniques," *Radiology*, vol. 215, pp. 286-293, 2000.

[28] S. Fiedler, A. Bravin, W. Thomlinson, J. Keyrilainen, P. Suortti, "Prospects for diffraction enhanced imaging mammography," *Collected Abstracts of the Joint Symposium on Bio-Sensing and Bio-Imaging at Yamagata TERRSA, Yamagata*, pp. 17, 2001*; in this volume of the Proceedings of of the Joint Symposium on Bio-Sensing and Bio-Imaging.*

[29] M.Di. Michiel, A. Olivo, G. Tromba, F. Arfelli, V. Bonvicini, A. Bravin, G. Cantatore, E. Castelli, L.Dalla Palma, R. Longo, S. Pani, D. Pontoni, P. Poropat, M. Prest, A. Rashevsky, A. Vacchi, E. Vallazza, "Phase-contrast imaging in the field of mammography," in *Medical Applications of Synchrotron Radiation*, M. Ando and C. Uyama, Eds. Tokyo: Springer-Verlag, Tokyo, 1998, pp. 78-82.

[30] V.N. Ingal, E.A. Beliaevskaya, A.P. Brianskaya, R.D. Merkurieva, "Phase mammography—a new technique for breast investigation," *Phys.Med. Biol.,* 43, pp. 2555-2567, 1998.

[31] M. Ando, J. Chen, K. Hyodo, K. Mori, H. Sugiyama, D. Xian, X. Zhang, "Nondestructive visual search for fossils in rock using X-ray interferometry imaging,". *Jpn. J. Appl. Phys.* vol. 39, pp. L1009-L1011, October 2000.

[32] M. Ando, H. Sugiyama, Zhang X., K. Hyodo, A. Maksimenko, W. Pattansiriwisawa, "An X-ray trichrome imaging 'Trinity' absorption, phase-interference and angle-resolved contrast," *Jpn. J. Appl. Phys.*, vol. 40, pp. L298-L301, March 2001.

[33] U. Bonse, M. Hart, "X-ray Interferometer with long separated interfering beam paths," *Appl. Phys. Lett.*, vol. 7, pp. 99-100, August 1965.

[34] M. Ando, S. Hosoya, "An attempt at X-ray phase-contrast microscopy"" in *Proc. 6th Int. Conf X-Ray Optics & Microanalysis, Osaka, 1971*,. G. Shinoda, K. Kohra and T. Ichinokawa, Eds. Tokyo: Univ. of Tokyo Press, 1972, pp. 63-68.

[35] A. Momose, T. Takeda, Y. Itai, A. Yoneyama and K. Hirano, "Perspective for medical applications of phase-contrast X-ray Imaging," in *Medical Applications of Synchrotron Radiation*, M. Ando, C. Uyama, Eds. Tokyo: Springer-Verlag, Tokyo, 1998, pp. 54-62.

[36] F. A. Dilmanian, Z. Zhong, B. Rent, X.Y. Wu, I.D. Chapman, I. Orion, W. C. Thomlinson,"Computed tomography of X-ray index of refraction using the diffraction enhanced imaging method," *Phys. Med. Biol*., vol. 45, pp. 933-946, 2000.

[37] A. Maksimenko, M. Ando, T. Yuasa "Reconstruction of 2D imaging due to refraction," *Collected Abstracts of the Joint Symposium on Bio-Sensing and Bio-Imaging at Yamagata TERRSA, Yamagata*, pp. 16, 2001*; in this volume of the Proceedings of of the Joint Symposium on Bio-Sensing and Bio-Imaging*

[38] W.-R. Dix, "Intravenous coronary angiography and competing methods," *Collected Abstract of Workshop on Medical Applications of Synchrotron Radiation at Grenoble on March 1-2, 2001*.pp. 35-36, 2001.

[39] K. Hyodo, M. Ando, S. Yamamoto, S. Ohtsuka, I. Yamaguchi, T. Takeda, Y. Itai, "Two-dimensional intravenous coronary angiography system II at PF-AR, KEK," *Collected Abstracts of Workshop on Medical Applications of Synchrotron Radiation at Grenoble on March 1-2, 2001*.pp. 37, 2001.

[40] S. Ohtsuka, I. Yamaguchi, W. Jin, T. Takeda, Y. Itai, A. Maruhashi, K. Hyodo, M. Ando, "SR angiography in Japan," *Collected Abstracts of Workshop on Medical Applications of Synchrotron Radiation at Grenoble on March 1-2, 2001*.pp. 38, 2001.

[41] B. Bertrand, P. Berkvens, G. Berruyer, A. Bravin, T. Brochard, Y. Dabin A. Draperi, H. Elleaume, F. Esteve, S. Fiedler, L. Hammer, G.Le Duc, S. Michelland, C. Nemoz, M. Perez, E. Pierrard, M. Renier, P. Suortti, W. Thomlinson, J. F.Le Bas, "Coronary angiography in France," *Collected Abstracts of Workshop on Medical Applications of Synchrotron Radiation at Grenoble on March 1-2, 2001*.pp. 39, 2001.

Visualization of Biomedical Specimens by X-Ray Dark Field Imaging

Wanwisa PATTANASIRIWISAWA,[1] Hiroshi SUGIYAMA,[1,2] Kazuyuki HYODO,[2,3] Anton MAKSIMENKO,[1] Seiji MURATSU,[4] and Masami ANDO, [†,1,2,3]

1   *Department of Photon Science, School of Advanced Studies, Graduate University for Advanced Studies (GUAS), Shonan International Village, Hayama, Miura, Kanagawa 240-0193, Japan*
2   *Photon Factory, Institute of Materials Structure Science, High Energy Accelerator Research Organization (KEK), Oho 1-1, Tsukuba, Ibaraki 305-0801, Japan*
3   *Department of Materials Structure Science, Institute of Materials Structure Science, Graduate University for Advanced Studies (GUAS), Oho 1-1, Tsukuba, Ibaraki 305-0801, Japan*
4   *Forensic Science Laboratory, Hyogo Prefecture Police Headquarters, Yamate-dori 5-4-1, Hyogo   Japan.*

A new X-ray dark field imaging technique using a monolithic X-ray optics comprising two Laue case diffraction wafers working with 35 keV has been successfully applied to some biomedical samples such as ivory, tusk, horn, tooth and a phantom of breast cancer. Images of ivory and others have shown very clear and informative inside structure. All pieces of the breast cancer phantom shows very promising and attractive images being capable of viewing excised tissue as a next step.

† all correspondence should be addressed to *masami.ando@kek.jp*.

Introduction

An X-ray optics called' Trinity' [1] simultaneously capable of viewing three kinds of imaging   absorption contrast   phase contrast [2-5] and refraction contrast [6-12] is under development. It has been proven that the refraction contrast has a power of revealing clearly any fiber structure inside material unless otherwise not clearly visible by any other techniques in X-ray region. If only refraction contrast is appreciated among the above three contrast the X-ray optics 'Trinity' can be simplified to an 'Owl' [13] which involves a monolithic X-ray optics comprising two wafers with certain thickness that splits the forward diffracted O-wave with almost no intensity and the diffracted H-wave with full intensity. Nevertheless the forward diffracted O-wave has high potential capability of receiving scattered and refracted signal from samples. In this paper visual application of this technique is shown; one elephant tusk that are highly appreciated as a seal and its related specimens in use as substitute of ivory and second a phantom of breast cancer as a candidate of medical application of the above X-ray optics. Also one may read another two papers in this proceedings: one on principle of the 'Owl' and its experimental evidence [14] and the other on its associated consideration on algorithm for CT in a future [15].

There still remain a fear of poaching of elephants in their habitats in Africa and Asia. Most of the reasons of their illegal capture is believed to be their ivories that may bring poaches and their associated brokers enormous profit. More than half of the ivories in the commercial market are consumed in Japan where seals are in use as signature especially in official

documents and those made of ivories are highly appreciated because of their popularity comprising long life, comfort in use and their high prestige. Further they have been used as raw materials of some art and crafts such as carved or scrimshawed, and '*netsuk*e' which had been used to secure a cord carrying personal belonging to the sash (*obi*) that acts as a belt on traditional Japanese dress. Traditional Japanese dress for men and women had very few places in which to keep small personal objects. Women kept things in their sleeves, but men had no equivalent in which to carry essentials such as seal cases (*inro*), tobacco pouches, purses, pipes in cases, and small writing kits, known as *yadat*e.

This study is of particular importance from the viewpoint of forensic science in order to examine visually ivory and its similar material nondestructively. For example, in Japan, seal impressions have been traditionally used as a certification means in official document together with hand-writing signature. African elephant ivory is a most supreme and expensive one among seal materials and used as an artifact. Now, the trade of elephant ivory and its product is prohibited under the control of the Convention on International Trade in Endangered Species (CITES), known well as the 'Washington convention'.

In spite of the above internationally established convention on comprehensive ban of export and import of ivories their smuggling is still rampant. In order to suppress smuggle on the claim as mammoth tusk in the attached document technical development of distinguishing ivories either by isotopes that could primarily distinguish even locality in South Africa [16,17] or by X-ray fluorescence [18,19] are under way. Since these methods may need substantial measuring time both

cannot be a practical method. Nevertheless no trial of development of visual technique that could save measurement time has been done before. We have collected material in use for seals in Japan, a hard ivory in Central and West of Africa, a soft ivory in East and South Africa, horn of water buffalo, teeth of sperm whale, teeth of hippopotamus and their associated artificial alternatives. Visualization of these have been attempted to study their internal structure by the above non-destructive technique.

In order to eradicate smuggle of ivory in Japan due to its strong demand a research to distinguish ivory from other similar material we have been requested, by the forensic science laboratory in Kobe, to develop a visual and confirmative technique. Ivory of African elephant can be smuggled as claim of mammoth tusk or even can be imported in a package of mammoth tusk. Since it seems worthwhile to find out a visual way to distinguish each we also took pictures of other samples such as horn of Dutch water buffalo, teeth of sperm whale and hippo and some industrialized seal material.

Cancer is a term for diseases in which abnormal cells divide without control. Cancer cells can invade nearly tissues and can spread through the bloodstream and lymphatic systems to other parts of body. Body is making up with many cells and sometimes it makes extra cells more than body needs. These extra cells can be benign tumours or malignant tumours (*cancer*). Now breast cancer is most significant cancer in woman. That is depending on many conditions;

First genetic alterations are in breast cancer genes (*BRCA1 and BRCA2*) and it is around 0.1% in population.

Second condition is family history. Women will be risky for getting breast cancer if her mother or sister has had breast cancer.

Third condition is age. Women can be at high risk in developing breast cancer, its risk is likely to be 0.5% if her age is around 40 and 10% for 80.

Fourth is estrogen and woman who has start of menstruation at early age and late menopause and include diethylstilbestrol during pregnancy will be risk.

Fifth is the woman who has first baby late after age 30.

Based on the evidence of above condition any age of woman can be at risk for developing breast cancer. Breast cancer is still difficult to find out from beginning. Everyone wishes that one can find it when it has just begun cancer. Technology now can find cancer with a certain size. Surgery is effective for primary breast cancer. Radiotherapy is to use high energy photons for killing cancer cells. Chemotherapy is use of drugs for killing cancer on patient who want to choose and that works effectively in case of big breast cancer.

What is ideal for woman is to develop a way to detect primary breast cancer. In view of this we have been developing a new X-ray visual technique called "X-ray dark field imaging". Breast cancer phantom has been used as a first step to check its capability.

Theory of refraction based imaging

Refraction contrast based dark field imaging [13-15] could reveal cancer part effectively. Our new technique can be simple in implementation because that will not request an operator to take a series of refracted X-ray photos so that all internal structure will be shown up by only one exposure. See its technical details in the paper by Ando *et al* in this proceedings

[14]. We have made an experiment to make sure that the dark field imaging can provide us with more information than other techniques.

Material

Ivories: The word "ivory" was traditionally applied to the tusks of elephants. However chemical structure of the teeth and tusks of mammals is the same regardless the species of origin, and the trade of certain teeth and tusks other than elephant is also well established and widespread. Therefore, "*ivory*" can correctly be together with any other mammalian tooth or tusk. Teeth and tusks have same origin. Teeth are specialized structure adapted for food mastication. Tusk, which are extremely large teeth projecting beyond lips, have evolved from teeth and give certain species an evolutionary advantage. The teeth of mammal consist of root and tusk proper. It has been reported that Sr, C and N in African elephant ivory was influenced by local geology [16,17]. That was studied by isotope effect. Another approach was by a group in Japan which is deeply involved in attempting at suppression of smuggling of ivory using X-ray fluorescence [18,19].

Breast cancer: Mammography is best to find breast cancer when the symptom appears. Nevertheless that has some limitations. A mammogram may miss some cancers that are present (false negative) or may find things that it is not be a cancer (false positive). Detecting tumour early does not necessarily guarantee that woman's life will be saved. Since everyone wishes early discovery of breast cancer when symptom appears intensive development of detecting breast cancer visually using synchrotron radiation is under development all over the world. Various types of breast phantom are in use [20-25]. The mammography accreditation phantom RMI 156 has been designed to test performance of a mammography s

ystem by quantitative evaluation of image of small structures similar to those found clinically. Objects within the phantom simulate micro-calcifications, fibrous structure in ducts and tumor-like masses. This RMI 156 has been chosen to determine if our mammography system can detect small structures that are important in the early detection of breast cancer.

Experimental

An experiment was performed at beamline BL 14B at Photon Factory KEK and at BL 20B and BL 20XU at Spring-8. First in order to collimate monochromatic X-rays and to expand the beam cross section a collimation crystal with asymmetry geometry which receives monochromatic X-rays from the double crystal monochromator at the beamline has been properly aligned. Further the 'Owl' which comprises a monolithic X-ray optics has been installed. A specimen has been put into a channel in between two wafers of the 'Owl'. The X-ray photon energy of 35 keV has been chosen because the higher X-ray photon energy may give the less pressure over breast when this will reach a clinical trial by that means female can be less painful due to pressurization if needed at that energy when comparing with the current energy of 20-25 keV at hospital. Images have been stored on electron microscopy films with spatial resolution of 5 μm. The exposure time for each picture was approximately 1-2 min.

The same geometry was adopted to the experiment of ivories.

First specimen was the accreditation phantom RMI 156 comprising sixteen types of cancerous fibers, speck and discs which are embedded in wax. Each size has dimension of 20 mm x 20 mm and its thickness of 7 mm as shown in Fig. 1. In Fig. 2 is shown an X-ray photograph taken by a supplier under the best exposure condition without an acryl plate. Phantom X-ray pictures were also taken without acrylic plate (see Fig. 3).

Second specimens were a variety of seal material with diameter of approximately 20 mm: hard ivory available from Central and Western Africa, soft ivory in East and Southern Africa, mammoth tusk, teeth of Dutch water buffalo, teeth of sperm whale and teeth of hippo.

Result

X-ray pictures of breast phantom showed very clear inner images of three kinds of inclusions such as fibers, speck and discs in all fifteen pieces. The piece #16 was not taken. Even some of the discs show additional contrast which might show how each was formed. If compared between Fig. 2 and 3 pieces of #7, #8, #10, #11, #12, and #13 which have not been clearly visible in Fig. 2 are very clearly in Fig.3. The dose rate of exposure is 0.0114 mSv/sec.

Ivory and others also show very clear internal structure as shown in Fig.4(a), (b), (c), (d), (e) and (f). The quality of each picture is good enough to distinguish each. The internal structure of hard ivory (a) shows very periodic lines, while soft ivory and mammoth tusk shows less regular lines compared with (a). The latter even shows further additional structure with which one distinguish clearly. Dutch water buffalo (d) has many tree like structure in the center. Sperm whale (e) and Hippo (f) shows slant lines extending from edge to center. The slant lines in hippo is smoother than sperm whale.

Discussion and conclusion

We have been successful to distinguish ivories and other similar materials by a new technique – dark field imaging. Each piece of 16 breast cancer phantom showed very clear element. Every detailed structure such as fiber structure, disc type and speck shape has been successfully revealed. Because of the mechanism of refraction contrast available in this X-ray optics edges of any inclusions are emphasized too much. Nevertheless this has been taken only without additional acryl so that as a next step the phantom together with the acryl which simulates a real breast thickness of 45mm has to be imaged. A whole phantom can be taken by a single shot if using the fairly large size monochromatic X-rays available at BL 20B at SPring-8. That each element in a phantom piece showed so clear edge encourages us to try to see realistic cancer in excised tissue. In other words unless applied to human tissue excised we can not say a decisive conclusion if our system works properly.

At last but not the least a lot of fringes seen in the background may bother quality of images a lot. This is probably due to growth striations which may correspond to a rotation and pulling speed of a grown crystal. Basically one can subtract this by a computational technique but looks much

better if the quality control of the crystal itself is possible.
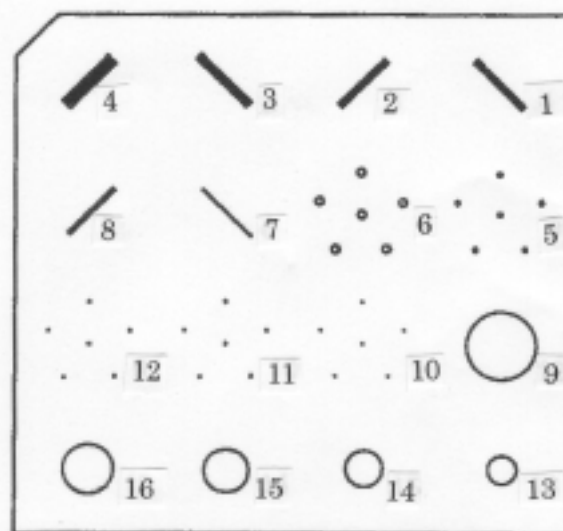
Figures

Fig. 1. Sketch of the accreditation phantom RMI156. This comprises three kinds of inclusions, nylon fibers #1-#4, #7 and #8 for fibrous structure, Al_2O_3 speck #5, #6, #10 and #12 for calcification and nylon discs #9 and #13-#16 for tumour. Each size is as follows: #1: 0.75mm in diameter , #2: 0.89mm in diameter , #3: 1.12mm in diameter, #4: 1.56mm in diameter, #5: 0.40mm in size, #6: 0.54mm in size, #7: 0.40mm in diameter, #8: 0.54mm in diameter, #9: 2.00mm in thickness, #10: 0.16mm in size , #11: 0.24mm in size , #12: 0.32mm in size , #13: 0.25mm in thickness , #14: 0.50mm in thickness , #15: 0.75mm in thickness , #16: 1.00mm in thickness. Each has a dimension of 20mm by 20mm and 6mm in thickness. All inclusion is embedded in wax.
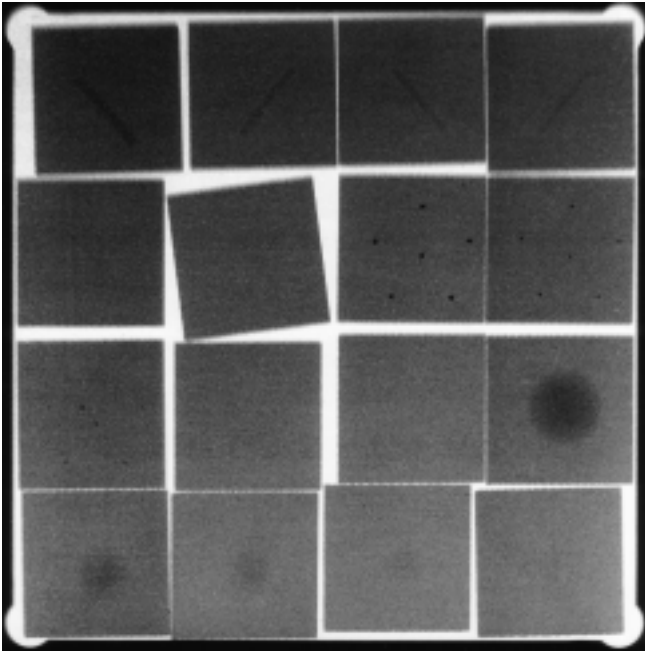
Fig. 2 X-ray picture of each piece in Fig.1 was taken by conventional mammography stystem
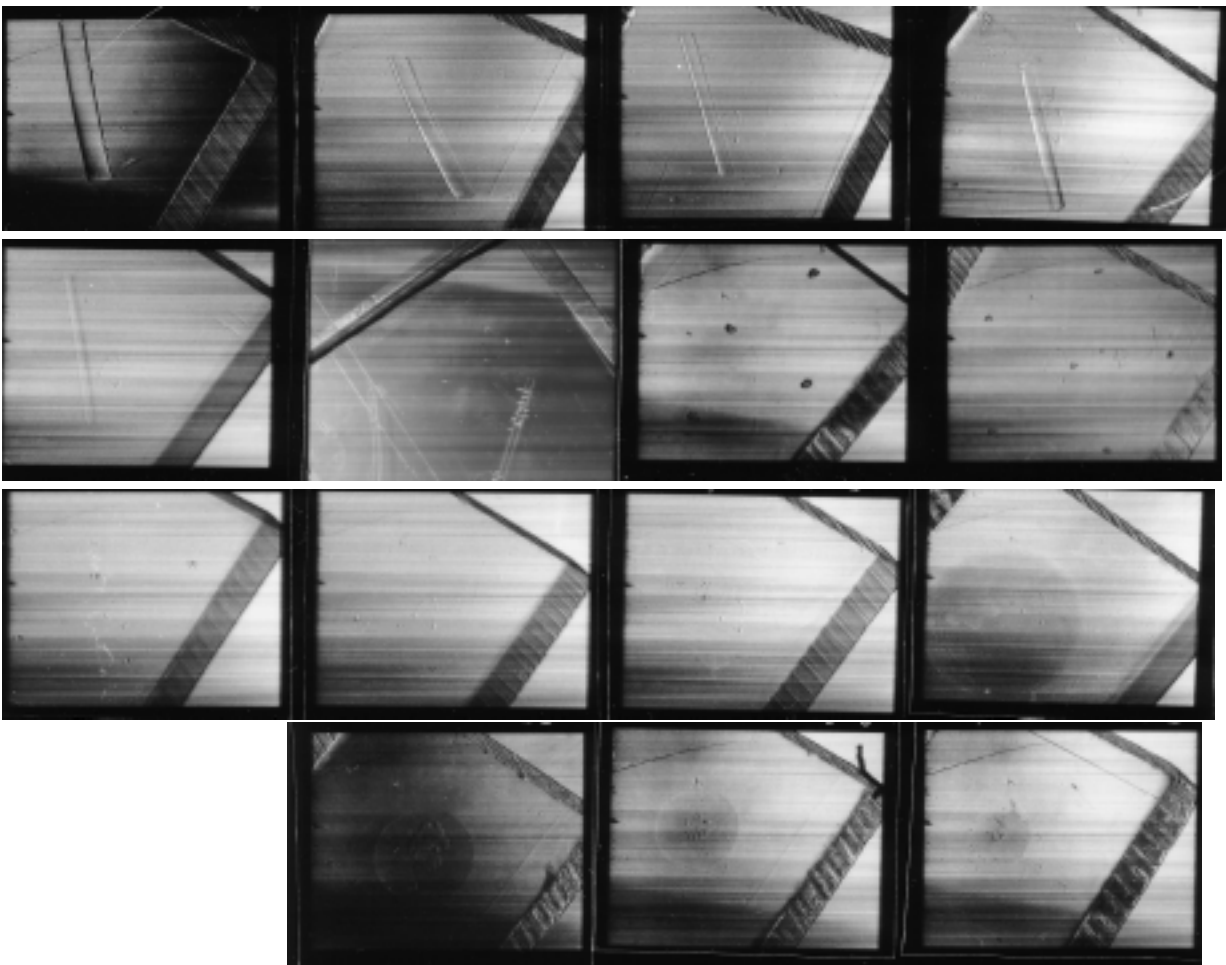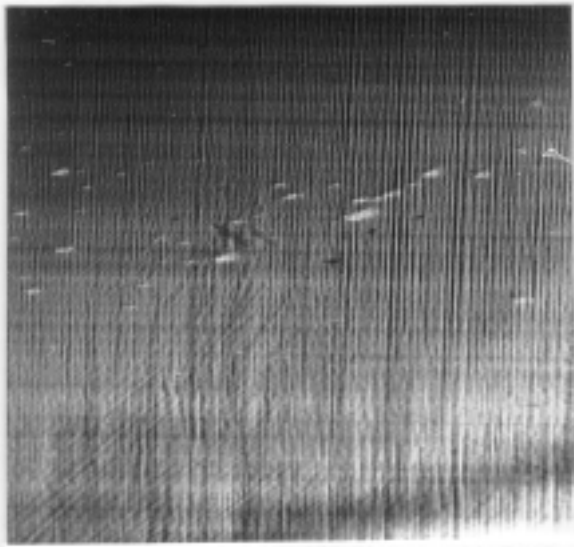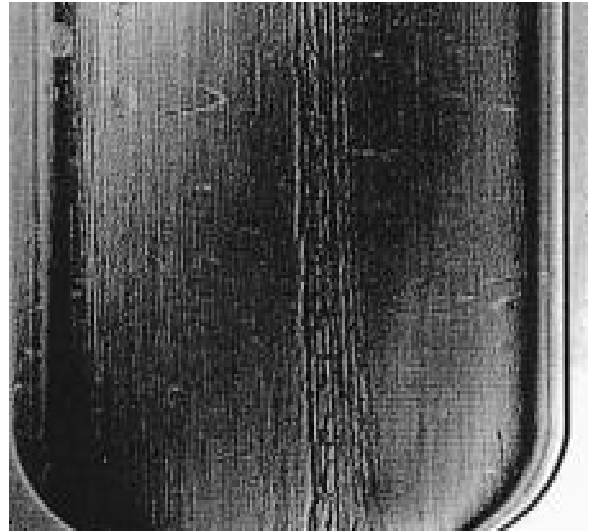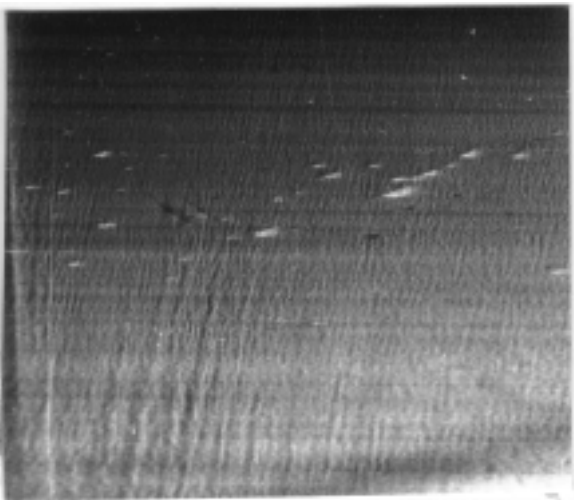

Fig. 3 X-ray picture of each piece in Fig.1 was taken by monochromatic X-ray beam with size of 15 mm by 15 mm. The edge of its piece is also clearly shown due to refraction
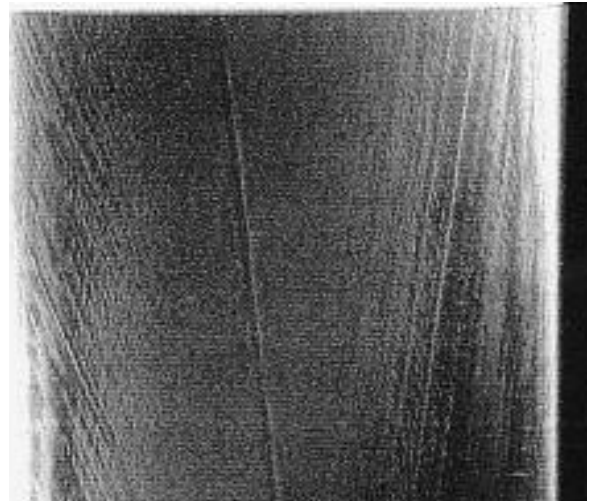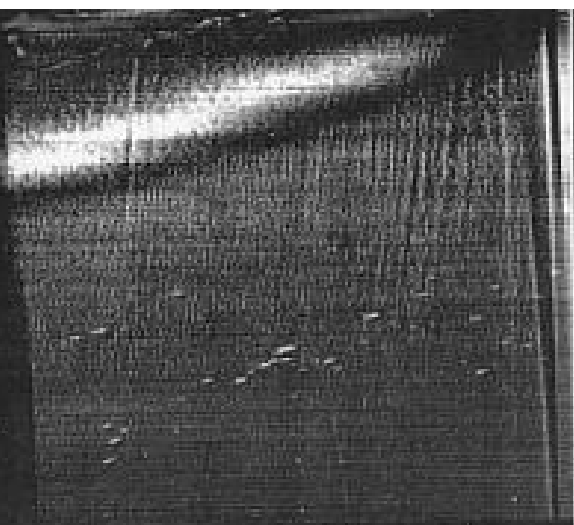
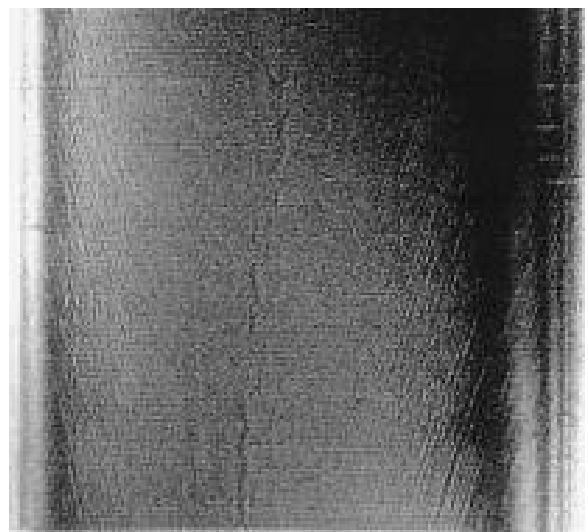(a)   hard ivory

(d)   horn of Dutch water buffalo

(b)   soft ivory

(e)   teeth of sperm whale

(c)   tusk of mammoth tusk

(f)   teeth of hippo

Fig. 4. Fibrous structure of (a) hard ivory, (b) soft ivory, (c) mammoth tusk, (d) teeth of Dutch water buffalo, (e) teeth of sperm whale and (f) teeth of hippo taken by the 'Owl' with photon energy of 35 keV. These are projection of 20 mm diameter seal material. One can relatively easily recognize each specimen in a nondestructive way.

References

[1] M. Ando H. Sugiyama Zhang X. K. Hyodo A. Maksimenko and W Pattanasiriwisawa," An X-ray trichrome imaging 'Trinity': absorption, phase-interference and angle-resolved contrast," *Jpn. J. Appl. Phys.*, vol. 40, pp. L298-L301, March 2001.

[2] M. Ando and S. Hosoya, "An Attempt at X-ray phase contrast microscopy," *Proc. 6th Int.Conf on X-Ray Optics & Microanalysis*, Osaka,1971, eds. G. Shinoda, K. Kohra, and T. Ichinokawa, Univ. of Tokyo Press, Tokyo, 1972, pp. 63-68.

[3] A. Momose, T. Takeda, Y. Itai, and K. Hirano, "Phase-contrast X-ray computed tomography for observating biological soft tissues," *Nature Medicine*, vol. 2, pp. 473-475,.February 1996.

[4] A. Momose, T. Takeda, Y. Itai, A. Yoneyama, and K. Hirano, "Perspective for medical applications of phase-contrast X-ray imaging," *Medical Applications of Synchrotron Radiation*, eds. M. Ando. and C. Uyama. Springer-Verlag, Tokyo, 1998, pp. 54-61.

[5] A. Momose, T. Takeda, Y. Itai, A. Yoneyama, and K. Hirano, "Phase-contrast tomographic imaging using an X-ray interferometer," *J. Synchrotron Rad.*, vol. 5, pp. 309-314, May 1998.

[6] K.M. Podurets, V.A. Somenkov, and S. Shil'stein, "Refraction-contrast radiology," *Sov. Phys. Thech. Phys.*, vol. 34(6), pp. 654-657, June 1989.

[7] V.N. Ingal and E.A. Beliavskaya, "X-ray plane-wave topography observation of the Phase contrast from a non-crystalline object," *J. Phys. D*, vol. 28, pp. 2314-2317, November 1995.

[8] S.W. Wilkins, T.E. Gureyev, D. Gao, A. Pogany, and A.W. Stevenson, "Phase-contrast imaging using polychromatic hard X-rays," *Nature*, vol. 384, pp. 335-338, November 1996.

[9] D. Chapman, W. Thomlinson, F. Arfelli, N. Gmuer, Z. Zhong, R. Menk, R.E. Jonston, D. Washburnn, E. Pisano, and D. Sayers, "Mammography imaging studies using a Laue crystal analzer," *Rev. Sci. Instr.*, vol. 67, pp. 3360, September 1996.

[10] P. Clotens, R. Barrett, J.R. Guigay, and M. Shlenker, "Phase objects in synchrotron radiation hard X-ray imaging," *J. Phys. D*, vol. 29, pp. 133-146, January 1996.

[11] W. Thomlinson, D. Chapman, Z. Zhong, R.E. Johnston, and D. Sayers, "Diffraction enhanced X-ray imaging," *Medical Applications of Synchrotron Radiation*, eds. M. Ando, and C. Uyama, Springer-Verlag, Tokyo, 1998, pp. 72-77.

[12] D. Gao, T.E. Gureyev, A. Pogany, A.W. Stevenson, and S.W. Wilkins, "New methods of X-ray imaging based on phase contrast," *Medical Applications of Synchrotron Radiation, eds*. M. Ando, and C. Uyama, Springer-Verlag, Tokyo, 1998, pp. 63-71.

[13] M. Ando H. Sugiyama A. Maksimenko, W. Pattanasiriwisawa K. Hyodo, and Zhang X, "A new optics for dark-field imaging in X-ray region 'Owl' ," *Jpn. J .Appl. Phys.*, vol.40, pp. L844-L846. August 2001

[14] M. Ando, J. Roberson, E. Rubenstein, W. Pattanasiriwisawa, A. Maksimenko, H. Sugiyama, K. Hyodo, C. Uyama, "Possible detection of bony trabeculae, vascular channels in auditory ossicles and breast cancer by means of X-ray dark field imaging," *in this Proceedings*.

[15] A. Maksimenko, M. Ando and T. Yuasa, Reconstruction of 2D imaging due to refraction, *in this Proceedings*.

[16] N.J. Van der Merwe, J.A. Lee-Throp, J.F. Thackeray, A. Hall-Martin, F.J. Kruger, H. Coetzee, R.H.V. Bell, and M. Lindeque, "Source-area determination of elephant ivory by isotopic analysis," *Nature*, vol. 346, pp. 744-746, August 1990.

[17] J.C. Vogel, B. Eglington, and J.M. Auret, "Isotope fingerprints in elephant bone and ivory," *Nature*, vol. 346, pp. 747-749, August 1990.

[18] M. Shimoyama, H. Maeda, H. Sato, T. Ninomiya, and Y. Ozaki, "Nondestructive discrimination of biological materials by near-infrared fourier transform Raman spectroscopy and chemometrics: discrimination and mammoth tusks and prediction of specific gravity of the ivories," *Applied. Spectroscopy*, vol. 51, pp. 1154-1158, August 1997.

[19] M. Shimoyama, T. Nakanishi, Y. Hamanaga, T. Ninomiya, and Y. Ozaki, "Non-destructive discrimination between elephant ivory products and mammoth tusk products by glancing incidence X-ray fluorescence spectroscopy," *J. Trace and Microprobe Techniques*, vol. 16 (2), pp. 175-182, February 1998.

[20] F. Arfelli, V. Bonvicini, A. Bravin, G. Cantatore, E. Castelli, L.D. Palma, M.D. Michiel, M. Fabrizioli, R. Longo, R.H. Menk, A. Olivo, S. Pani, D. Pontoni, P. Poropat, M. Prest, A. Rashevsky, M. Ratti, L. Rigon, G. Tromba, A. Vacchi, E. Vallazza, and F. Zanconati, "Mammography with synchrotron radiation: phase-detection techniques," *Radiology*, vol. 215, pp. 286-298, April 2000.

[21] F. Arfelli, A. Bravin, G. Barbiellini, G. Cantatore, E. Castelli, M.D. Michiel, P. Poropat, R. Rosei, M. Sessa, A. Vacchi, L.D. Palma, R. Longo, S. Bernstorff, A. Savoia, and G. Tromba, "Digital mammography with synchrotron radiation," *Rev. Sci. Instrum.*, vol. 66, pp. 1325-1328, February 1995.

[22] F. Arfelli, V. Bonvicini, A. Bravin, G. Cantatore, E. Castelli, L.D. Palma, M.D. Michiel, R. Longo, A. Olivo, S. Pani, D. Pontoni, P. Poropat, M. Prest, A. Rashevsky, G. Tromba, and A. Vacchi, "Mammography of a phantom and breast tissue with synchrotron radiation and linear-array silicon detector," *Radiology*, vol. 208, pp. 709-715, September 1998.

[23] J. Law, "A new phantom for mammography," *Br. J. Radiol.*, vol. 64 , pp.116-120, February 1991.

[24] A. Krol, A. Ikhlef, J.C. Kieffer, D.A. Bassano, C.C. Chamberlain, Z. Jiang, H. Pepin, and S.C. Prasad, "Laser-based microfocused X-ray source for mammography feasibility," *Med. Phys.*, vol. 24, pp. 725-732, May 1997.

[25] D.R. Dance, "Monte Carlo calculation of conversion factors for the estimation of mean glandular breast dose," *Phys. Med. Biol.*, vol. 35, pp. 1211-1219, September 1990.

A Test of an X-Ray Quatrochrome Interferometer for Simultaneous Observation of Images Due to Dark- and Bright-Field, Phase-Interference and Absorption Contrasts

Anton MAKSIMENKO[1,*], Masami ANDO[1,2], Hiroshi SUGIYAMA[1,2],
Wanwisa PATTANASIRIWISAWA[1] and Kazuyuki HYODO[1,3]

[1]*Department of Photo-Science, School of Advanced Studies, Graduate University for Advanced Studies (GUAS), Shonan International Village, Hayama, Miura, Kanagawa 240-0193, Japan*

[2]*Photon Factory, Institute of Materials Structure Science, High Energy Accelerator Research Organization (KEK), 1-1 Oho, Tsukuba, Ibaraki 305-0801, Japan*

[3]*Department of Material Structure Science, School of Physical Mathematics, Graduate University for Advanced Studies (GUAS), 1-1 Oho, Tsukuba, Ibaraki 305-0801, Japan*

We developed new notdestructive observation method that simultaneously provides four different types of contrast: dark- and bright-fields and absorption and phase-interferences. The first two contrasts originate from the deflection of X-ray on the boundaries of the object and nonhomogeneities of its internal structure. Although the first two contrasts are different manifestations of the so-called angle-resolved contrast they proved to be interesting independent of each other. A new X-ray optical device was realized. The device had dimensions of approximately 60 mm x 40 mm x 30 mm so that the view size available was approximately 4 mm x 10 mm. The X-ray energy used was 36.0 keV at Photon Factory's BL14B using the vertically polarized synchrotron radiation from the vertical wiggler that runs at 5 T. The exposure for each picture was approximately 60 s. [DOI: 10.1143/JJAP.42.L1096]

Recently, an X-ray interferometer that can produce simultaneous images due to not only phase-interference contrast[1–3] but also angle-resolved (or refraction) contrast[4,5] has been proposed. One year later, another X-ray interferometer called the "Trinity" was designed to be able to obtain three kinds of X-ray contrast, namely, phase-interference, refraction and absorption, was reported.[6] The refraction contrast become the base for the X-ray optics device called the "Owl" which was developed for producing angle-resolved contrast only.[7–9] Now it is clear that the angle-resolved contrast can become dark- or bright-field contrast depending on the thickness of the analyzer,[5] so that in this paper we present a new kind of X-ray optics, depicted in Fig. 1, that can produce simultaneously four kinds of contrast. The first two contrasts coincide with the ones mentioned above: phase-interference, which appears due to interference of two beams. The first beam travels from the reflector R to the mirror M1 and then to the analyzer A possessing no information about the object. The second beam, after reflection on R, penetrates through the object to collect information about it in terms of phase shifts, which are proportional to the light path. After the reflection on the M2, the second beam interferes with the first one on the analyzer. The absorption contrast is the result of the absorption and scattering of the X-ray on the object under investigation. The absorption and phase-interference contrasts are not described in detail in this paper because their description has been presented in ref. 6. The dark- and bright-field contrasts are different types of angle-resolved contrast.[10] In Fig. 1, one can see a schematic of the new X-ray optics. As is shown on the scheme, the optics has four blades. The first three blades are the same as in the interferometer described in ref. 6 while the fourth one has an additional element depicted in a grey box which is not present in the 'Trinity'.[6] Please note that this additional
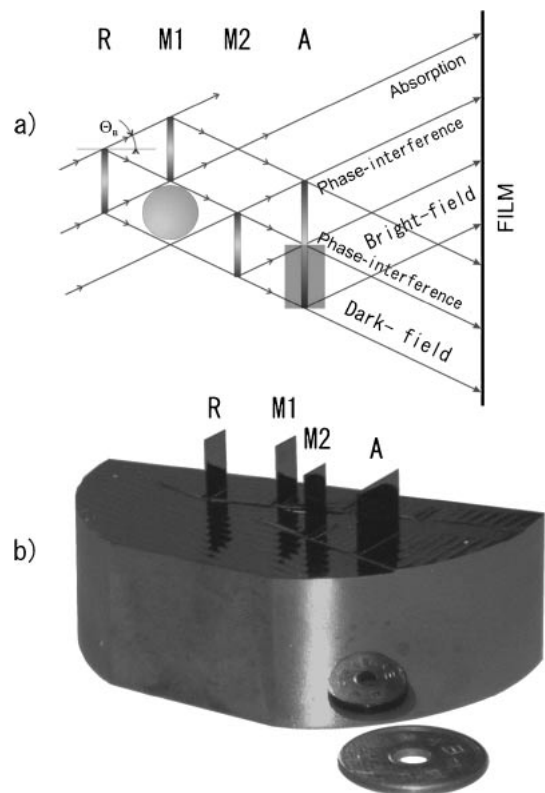
Fig. 1. a) Schematic of X-ray optics. The grey box shows the element responsible for the formation of dark- and bright-field images. b) photo of the device used in experiment together with a 5-yen coin for the reference. Capital letters mark reflector (R), mirror 1 (M1), mirror 2 (M2) and analyzer (A).

blade allows the X-ray coming from 3rd blade to diffract so that the diffracted and forward-diffracted beams form bright- and dark-field contrasts described in detail below.

The dark- and bright-field contrasts are two different types of the angle-resolved contrast obtained due to the Laue

*E-mail address: antonmx@post.kek.jp

diffraction of the X-ray beam deflected on an object. The Laue analyzer reflects the deflected component of the X-ray beam in the forward diffraction direction (dark-field contrast image) and the undeflected component in the diffraction direction (bright-field contrast image). The Laue diffraction profile is strongly dependent on the thickness of the analyzer and energy of the photons. The normalized intensities of the forward-diffracted and diffracted beams can be described as

$$I_{f-d} = \frac{\sin^2(t\pi\Lambda^{-1}\sqrt{1+W^2})}{1+W^2} \qquad (1)$$

for the forward diffracted beam and

$$I_d = \frac{W^2 + \cos^2(t\pi\Lambda^{-1}\sqrt{1+W^2})}{1+W^2} \qquad (2)$$

for the diffracted beam so that $I_{f-d} + I_d = 1$. In these equations, t is the thickness of the analyzing crystal, W is the deviation of angle from the Bragg angle measured in terms of the half-width of the Bragg peak, and $\Lambda = c\cos(\Theta_B)/(\nu|P||\chi_G|)$ with $h\nu$ as the X-ray photon energy, c as the light speed and Θ_B as the Bragg angle, while P and χ_G are the polarization factor and electric susceptibility, respectively (see ref. 11 for example). One can see from eq. (2) that the intensity under the Bragg condition ($W = 0$) can take any values between 0 and 1 depending on analyzer thickness and photon energy like it is presented in Fig. 2. When it is equal to 1, the whole deflected component of the X-ray beam is diffracted toward the dark-field image while the undeflected component are reflected toward the bright-field contrast. The dark- and bright-field contrasts can be called *exact* dark- and bright-field contrasts when the Laue analyzer is configured so that the the undeflected component is completely diffracted toward the bright-field image.

In order to obtain the exact contrasts one needs to choose the appropriate thickness and/or X-ray photon energy conditions for the most appropriate diffraction profile. Please note that according to eqs. (1) and (2), principally

there are some possible ways of controlling the shape of the rocking curves so that one can obtain the desired conditions of the exact contrasts. The shape of the rocking curve strongly depends on the thickness of the Laue analyzer, but sometimes it can be difficult to produce an analyzer with a necessary thickness within admissible accuracy ($\pm 5\,\mu$m). Another problem is that it is impossible to control thickness after the production is completed. Another way of obtaining the exact dark- and bright-field conditions is the tuning of the X-ray wavelength within close limits. Due to the energy tuning within a thin range of some keV (the exact range width depends on the diffraction conditions), one can change the shape of the rocking curves at a constant thickness to determine the particular energy of the X-ray beam that provides the desired shape of the rocking curve for a particular analyzer. Thus, the process of energy tuning solves the problem of obtaining exact dark-field and bright-field contrasts.

One can apply the above-described theory to achieve the exact dark- and bright- field contrasts from the blade marked with the grey box in Fig. 1 if energy tuning is performed only on that particular blade. Thus, the first step of the experiment should be the energy tuning of the analyzer so that other wafers of the device are not touched by the X-ray, as is shown in Fig. 3(a). Only after this procedure can the images be stored in accordance with the scheme in Fig. 3(b). A very reasonable question appears regarding the influence of mirror M2 on the final contrast. On one hand, this mirror is necessary to form the phase-interference contrast on the analyzer. On the other hand, the beam that passed through
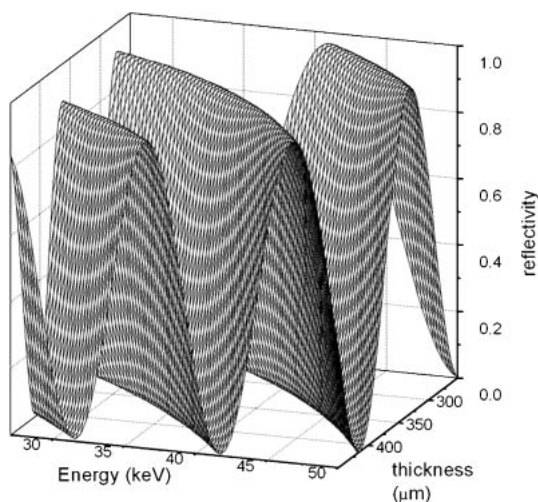

Fig. 2. Dependency of the reflectivity of the diffracted wave under the Bragg condition ($W = 0$) on photon energy and crystal thickness. One can see that the conditions of the exact contrasts at a certain analyzer thickness can be achieved at different photon energies. For the case of 417 μm, these energies are 36.0 keV, 49.95 keV and others which differs from each other for the whole number of 4.05 keV steps.
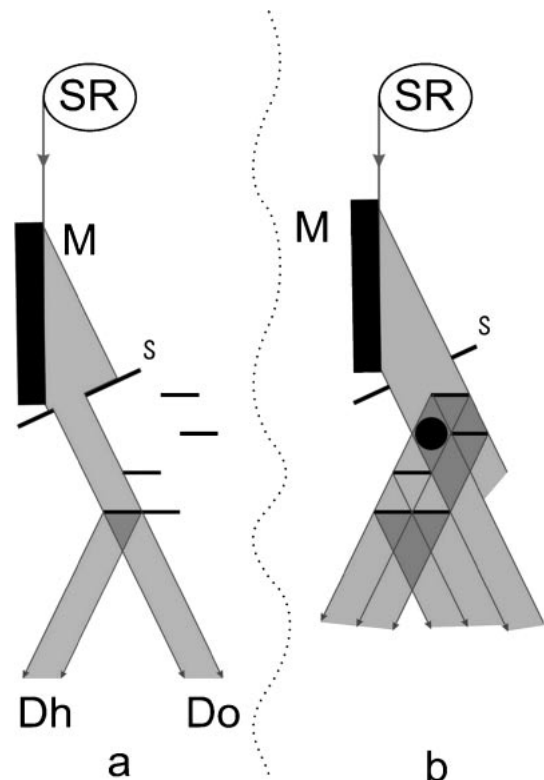

Fig. 3. Two steps of the experiment are a) energy tuning of the analyzer and b) storing the images. Here Do and Dh are the positions of the X-ray detectors for the forward-diffracted and diffracted beams, respectively, M is the asymmetrical monochromator which was cut 10° off the Si(4,4,0) reflecting planes, and S is the slit.

the mirror has a portion of angular contrast which depends on its thickness according to eqs. (1) and (2). In the case that the thickness of the mirror is equal to the that of the analyzer one loses the bright-field contrast because all undeflected components are deflected on M2 and do not reach A. Thus, the thicknesses of the M2 and analyzer should be different. The best case is the difference designed so that the mirror M2 gives 50% reflectance and 50% transmission under Bragg conditions.

The above-described theory was realized experimentally. The interferometer was designed to be used at photon energies between 33 and 37 keV for the Si(2,2,0) diffraction in order to be able to cover the X-ray photon energy discussed above. The beam monochromotized on the asymmetrically cut monochromator with an angular divergence of 0.058 arcsec was used. In accordance with the theory, the experiments included four steps: i) the first step is the taking rocking curves of the analyzer which is responsible for forming dark- and bright-field images at different photon energies of the X-ray beam, as is shown in Fig. 3(a). We find that the energy at which the reflectivities of the forward-diffracted wave under Bragg conditions is minimal and the diffracted one is maximal. The tuning of the X-ray energy has brought the optimum energy for the particular analyzer used at 36.0 keV. The energy tuning was performed with step of 0.1 keV in the range between 35.5 keV and 36.3 keV. The experimental rocking curve at this energy is presented in Fig. 4 with thin lines. As one can see from the figure, the maximum reflectivity does not reach 100 percent. The reasons for this is the absorption effect not taken into account in the theoretical calculations. ii) The second step is the determination of the analyzer's thickness from the thickness-energy dependency of reflection shown in Fig. 2. From this dependency, we found that thickness of the analyzer is 417 microns. iii) The third step is the theoretical calculations of the rocking curve of the analyzer with thickness determined in the previous step. The theoretical curves are presented in Fig. 4 with thick lines. The calculations were performed on the basis of eqs. (1) and (2). The rocking curves of the analyzer, asymmetrical cut

monochromator installed before the device, and symmetrical upstream monochromator of the beamline were convoluted together. The comparison of the theoretical and experimental curves showed a very good agreement. One can see from the experimental and theoretical graphs in Fig. 4 that the peak positions almost coincide. iv) The fourth step is the performing the experiments of storing images as is shown in Fig. 1.

The experiment was performed at beamline BL14B using a radiation source from a 5T vertical wiggler at the 2.5 GeV Photon Factory, KEK, Tsukuba. To decrease the angular divergence of the beam to 0.058 arcsec we used an asymmetrically cut monochromator installed in front of the interferometer. The important property of the synchrotron source is its broad continuous spectrum in a wide range of energies, which allows one to perform energy tuning with high precision. The estimation of the spatial resolution of the method was performed using Cu#1000 and Cu#2000 copper meshes. We could see the elements of the Cu#1000 mesh but could not see any structure for the Cu#2000 mesh. A photograph of the Cu#1000 mesh is shown in Fig. 5. Thus, we can state that the spatial resolution of the method is approximately 24 μm. The limitation of the spatial resolution comes from the Borrmann triangle formed by the forward-diffracted and diffracted beams inside the analyzing blade but due to the source characteristics. Another possibility of increasing the resolution is the use of the Bragg case based dark-field image which has some advantages owing to the weak effect of the Borrmann triangle since the penetration depth of X-ray is of some ten micron order and the independence of transmission on the thickness of the analyzer. This method is described in details in ref. 7.

Images were stored on an X-ray film. Its exposure time was approximately 60 s. The results are presented in Fig. 6 with the composite material consisting of an aluminum matrix with 149 μm in diameter carbon fibers as a sample object. Figure 6 shows the four contrasts, namely, dark-field, phase-interference, bright-field and phase-interference from left to right. The example shows good agreement with theoretical predictions. Please note that the background of
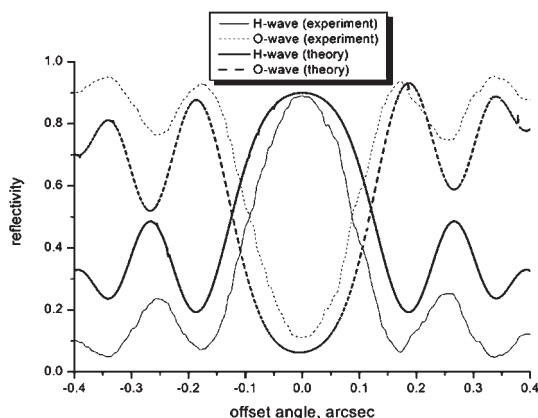

Fig. 4. Thin lines: experimentally obtained rocking curves at a photon energy 36.0 keV. The straight line represents the diffracted wave and the dotted line the forward-diffracted one. The rocking curves at this energy showed the sharpest shape of the main peaks. Thick lines: theoretical calculation of the rocking curves which shows good agreement with the experimental ones.
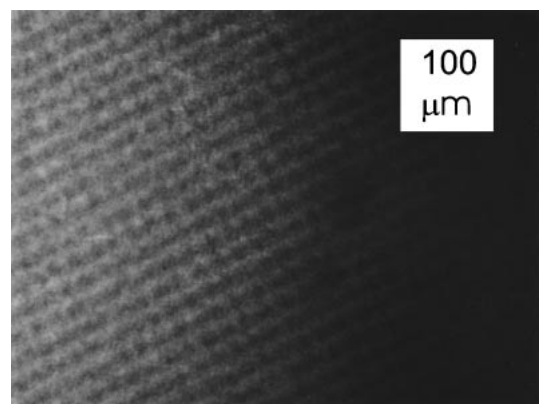

Fig. 5. Test of the spatial resolution limitations of the method due to the dark-field contrast of the Cu#1000 mesh which is used in electron microscope as a test sample. Please note that although we cannot see the structure of the wires composing the sample, the periodical structure of the object can be easily recognized in both directions. On this and all other photos, bright parts correspond to the higher X-ray intensity while darker one to the lower X-ray intensity.
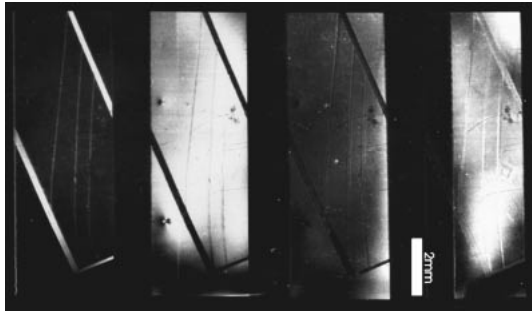
Fig. 6. From left to right: dark-field, phase-interference, bright-field, phase-interference contrasts image of composite material consisting of an aluminum matrix with 149 μm diameter carbon fibers.

the dark-field contrast is really dark. The intensity of the bright-field contrast proves to be low in comparison with the phase-interference contrast. This is due to the partial reflectance of the beam on the M2 so that part of it forms the bright-field contrast. One can note that two phase contrasts (second and fourth in Fig. 6) differ from each other. That can be understood by taking into account the fact that the analyzer where the two beams interfere divides both beams into unequal portions which are determined by the conditions of the reflection on all preceding blades. However both of the phase-interference contrasts have the same nature and origin.

Finally, we can state that the newly designed device works as expected and gives good result which agrees well with the theoretical consideration. The spatial resolution was determined and found to be approximately 24 μm. This limitation we do not consider as being the best possible and in the future we hope to improve it one order better.

1) M. Ando and S. Hosoya: *Proc. 6th Int. Conf. X-Ray Optics & Microanalysis, Osaka, 1971,* eds. G. Shinoda, K. Kohra and T. Ichinokawa (Univ. of Tokyo, Tokyo, 1972) p. 63.
2) A. Momose, T. Takeda, Y. Itai and K. Hirano: Nat. Med. **2** (1996) 473.
3) A. Momose, T. Takeda, Y. Itai, A. Yoneyama and K. Hirano: *Medical Applications of Synchrotron Radiation,* eds. M. Ando and C. Uyama (Springer-Verlag, Tokyo, 1998) p. 54.
4) D. Chapman, W. Thomlinson, F. Arfelli, N. Gmuer, Z. Zhong, R. Menk, R. E. Johnson, D. Washburn, E. Pisano and D. Sayers: Rev. Sci. Instrum. **67** (1996) 3360.
5) M. Ando, J. Chen, K. Hyodo, K. Mori, H. Sugiyama, D. Xian and X. Zhang: Jpn. J. Appl. Phys. **39** (2000) L1009.
6) M. Ando, H. Sugiyama, X. Zhang, K. Hyodo, A. Maksimenko and W. Pattanasiriwisawa: Jpn. J. Appl. Phys. **40** (2001) L298.
7) A. Maksimenko, K. Hirano, M. Ando, H. Sugiyama, K. Hyodo and W. Pattanasiriwisawa: in preparation for publication.
8) U. Bonse and M. Hart: Appl. Phys. Lett. **6** (1965) 155.
9) U. Bonse and M. Hart: Appl. Phys. Lett. **7** (1965) 99.
10) M. Ando, A. Maksimenko, H. Sugiyama, W. Pattanasiriwisawa and K. Hyodo: Jpn. J. Appl. Phys. **41** (2002) 4742.
11) W. H. Zachariasen: *Theory Of X-Ray Diffraction in Crystals* (Dover Publication Inc., New York, 1994) Sec. III-11, pp. 123–124.
12) M. Ando, H. Sugiyama, A. Maksimenko, K. Hyodo, K. Hirano and W. Pattanasiriwisawa: *16th Annual Meet. Japanese Society for Synchrotron Radiation Research, Igure Himeji, 2003.*

Development of X-ray dark-field imaging

towards clinical application

ANDO Masami,[1,2,3] HASHIMOTO Eiko,[2] HASHIZUME Hiroyuki,[4] HYODO Kazuyuki,[1,3] INOUE Hajime,[4]
ISHIKAWA Tetsuya,[5] KUNISADA Toshiyuki,[4] MAKSIMENKO Anton,[2] PATTANASIRIWISAWA Wanwisa,[6]
RUBENSTEIN Edward,[7] ROBERSON Joseph,[8] SHIMAO Daisuke,[3] SUGIYAMA Hiroshi,[1,2] TAKEDA Ken,[4] UENO Ei,[9]
WADA Hiroshi[10]

([1]Photon Factory, KEK, Oho 1-1, Tsukuba, Ibaraki 305-0801, Japan; [2]Department of Photo-Science, Graduate University for Advanced Studies, Hayama, Miura, Kanagawa 240-0193, Japan; [3]Department of Material Structural Sciences, Graduate University for Advanced Studies, Oho 1-1, Tsukuba, Ibaraki 305-0801, Japan; [4]Department of Orthopaedic Surgery, Okayama University Graduate School of Medicine and Dentistry 2-5-1, Shikata-cho, Okayama 700-8558, Japan; [5]RIKEN Harima, Koto 1-1-1, Mikazuki-cho, Sayo-gun, Hyogo-ken 679-5198, Japan; [6]Suranaree University of Technology, Muang District, University Avenue 1111, Nakhon Rachasima 30000, Thailand; [7]Department of Medicine, Stanford University School of Medicine, Stanford, CA 94305, USA; [8]California Ear Institute, Stanford, CA 94304, USA; [9]Department of Breast-Thyroid-Endorine Surgery, Institute of Clinical Medicine, Tsukuba University, Tsukuba, Ibaraki 305-0006, Japan; [10]Dept of Biorobotics, School of Engineering, Tohoku University, Aobayama 01, Sendai 980-8579, Japan)

Abstract   Review of X-ray dark-field imaging under development is presented. Its goal is its application to clinical diagnosis of organs that have been invisible by the ordinary techniques. In order to clinically visualize tissues in detail one needs high contrast and high spatial resolution say ~50 μm. This X-ray optics comprises a Bragg asymmetric monochro-collimator and a Bragg case or a Laue case filter with capability of analyzing angle in a parallel position. Their diffraction index is 4,4,0 and the X-ray energy 35 keV (λ= 0.0354 nm). The filter has 0.6 mm thickness in the Bragg case or 1.075 mm or 2.15 mm thickness in the Laue case. Under this condition only the refracted X-rays from object can transmit through the filter while the beam that may receive absorption and/or phase change will not. Soft tissues at human joints thus taken show high contrast images so that the DFI is promising for clinical diagnosis. Preliminary X-ray absorption images of another clinical candidates of ear bones are also shown.

Keywords   X-ray dark-field imaging, X-ray bright-field imaging, Bragg asymmetric monochro-collimator, Bragg case filter, Laue case filter, Clinical diagnosis

CLC numbers   R814, O436

1   Introduction—history of development of DFI (Dark-Field Imaging)

One can visualize internal structure by major three X-ray contrasts, absorption, phase change and refraction. Since discovery of X-rays by Roentgen in 1895 absorption based contrast imaging including computed tomography has delivered major popularity in clinical X-ray imaging. Another phase contrast imaging applied to mineralogical and biological object was first attempted by Ando and Hosoya in 1971[1]

using X-ray interferometry devised by Bonse and Hart in 1965.[2] Its 3D imaging was introduced in 1996 by Momose *et al*.[3] Another pioneering imaging technique due to refraction at internal boundaries of object was proposed by Pudorets *et al* in neutron imaging[4] and in X-ray imaging.[5-7] These can be categorized as X-ray bright-field imaging (BFI) where the refraction based image as well as absorption based image together with the illuminating light are recorded.

Starting from utilization of the X-ray interferometer[2] we have reached the concept of X-ray

dark-field imaging (DFI).[8] A certain thickness Laue case filter capable of analyzing angle can produce both DFI (X-ray dark-field imaging)[8] that can suppress the illumination background and the BFI. Plane-wave X-ray incident beam is required in this X-ray optics. Adoption of asymmetric diffraction[9] (see the monochro-collimator seen left in Fig.1) with 4,4,0 diffraction and E = 35 keV can give narrower beam divergence ~0.3 μrad than that incident onto a monochro-collimator and simultaneously provide with a larger beam cross section than that incident onto the monochro-collimator. This is an idea of extension of "Trinity"[10] (see Fig.1~3). Fig.1 shows the system of the "Trinity" comprising the monochro-collimator and the Trinity itself that can simultaneously provide three contrasts, absorption, phase retardation and refraction. Fig.1 shows the Trinity part made of silicon. Its dimension has approximately 100 mm in length as
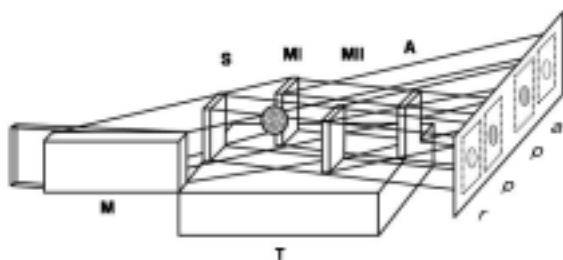

Fig.1 Sketch of "Trinity" that comprises M for an asymmetric monochro-collimator and T for a monolithic four blade S, MI, MII and A X-ray optics. "Trinity" simultaneously provides three types of X-ray images, *r* for angular resolved one, *p*'s for 2 phase-retarded ones and *a* for an absorption one.
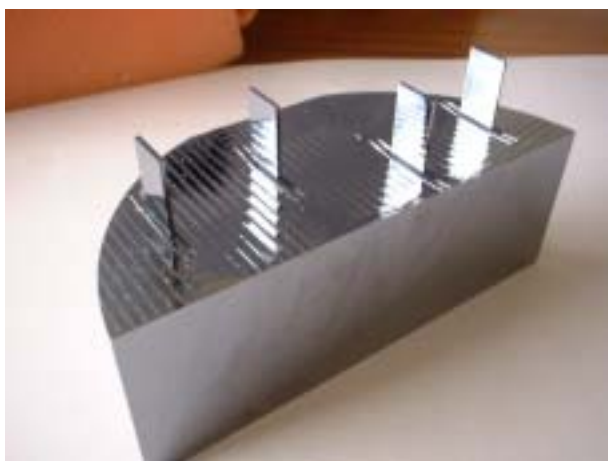

Fig.2 A fabricated "Trinity". The whole piece was home made. Each of four blades was cut out from a 50-mm-thick boule with the orientation of <1,0,0> of a floating-zone silicon crystal. The thickness of each wafer was 1.1 mm in design for the (4,4,0) diffracting planes. This size of 70 mm for 3D can provide a sample with a beam of 7 mm in size. The entire X-ray optics including an additional guard space is 100 mm long and 42 mm wide.
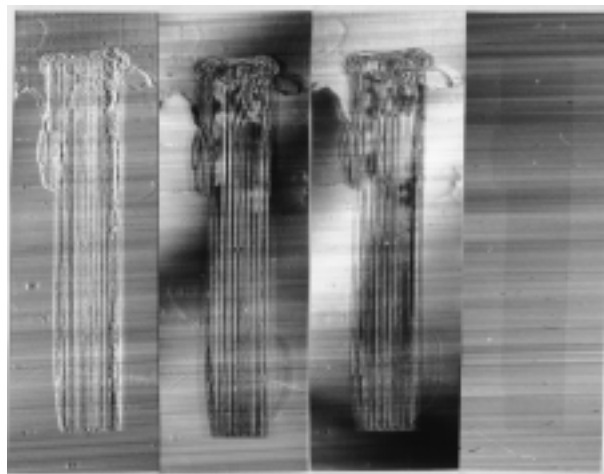

Fig.3 Images taken by the Trinity. A sample used as demonstration was a composite material comprising boron fibres with 140 μm in diameter embedded in a 1 mm thick Ti plate. Four images predicted in Fig.1 were obtained.

shown in Fig.2. In Fig.3 is shown an image taken with this optics: from left to right angular resolved, two phase-retarded and absorption contrast. It is clear that refraction and phase-retardation can show boron fibres with diameter of 140 μm imbedded in a composite material of Ti.

Later its another improvement named "Quadruple"[11] (see Fig.4 and Fig.5) was proposed by Maksimenko. This could provide not only three contrasts simultaneously but four simultaneously: the refraction
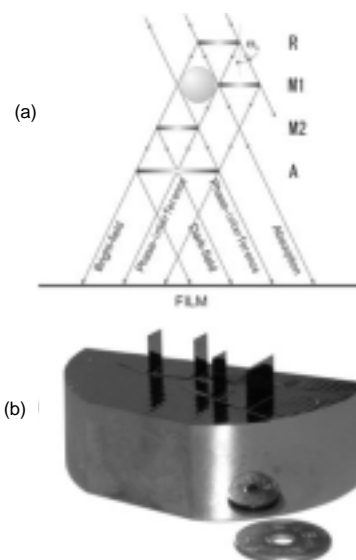
Fig.4 Another X-ray optics named "Quadruple" that has a dimension of 60 mm x 40 mm x 30 mm. The field size available was 4 mm (width) x 10 mm (height). Each wafer has thickness of 417 μm. As shown in (a) the angular analyzer has a twice width dimension of others. On an X-ray film one can see from left to right the bright-field imaging, phase-retarded imaging, dark-field imaging, phase-retarded imaging and absorption imaging. (b) shows a home made "Quadruple".
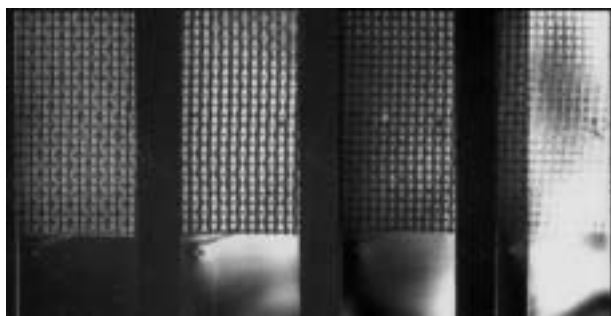
Fig.5 The X-ray images corresponding to the sketch shown in Fig.4(a). A sample used was a copper mesh $^{\#}$1000.

contrast is divided into DFI and BFI that will be precisely described later in this text. In this paper the X-ray energy used was primarily 35 keV. This energy is the intermediate energy, in other words a bit higher for a breast, appropriate for articular cartilage at knee, hand, shoulder and others, a bit low for thick trabecular bones, lung, stomach and others and too low for head and others, so that the basic development will be performed mainly at this X-ray energy. After usefulness of this method is proven we would like to go further.

Also our group proposed another idea of extracting the component of refraction contrast by adoption of the Bragg or the Laue filter. The DFI using the Bragg filter is shown in Fig.6. The mechanism of the contrast is described in Fig.7. This Bragg crystal filter has two functions, one is $B_r I_G(W)$ that produces the beam along the direction toward the diffraction and the other $B_r I_o(W)$ for the straight forward diffraction. The forward beam from object without interacting the object in Fig.6 will be diffracted towards the direction of diffraction named $B_r B(W)$ due to the function of $B_r I_G(W)$. That can be the image called BFI, while the forward beam interacting with the object will produce the beam $B_r D(W)$ due to the function of $B_r I_o(W)$. In Fig.7 the reflection profile drawn with the line corresponds to $B_r I_G(W)$, while the dotted line to $B_r I_o(W)$ that is indicated as the transmitted beam in the figure. According to the profile $B_r I_o(W)$ the image will be produced as shown in Fig.8. This can be called the DFI using a Bragg case analyzer. A sample image of copper mesh #100 is clearly visible. If the Bragg filter does not exist one will obtain a very faint absorption contrast image of the material. If the sample is not located in the sample position no X-ray intensity appears. Nevertheless due to the energy flow occurring

inside the Bragg filter crystal the image blurring may occur. That is shown in the inset.
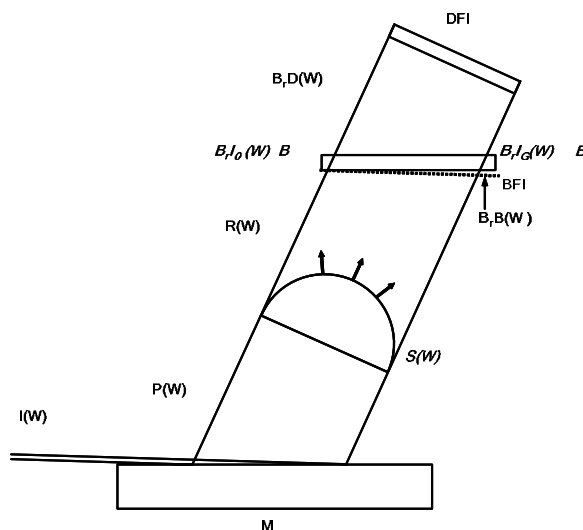

Fig.6 The DFI (dark-field imaging) X-ray optics using the Bragg case angular analyzer. A monochro-collimator M makes the angular spread of the incident beam I(W) sharper as indicated with P(W). The incident beam P(W) with divergence of 0.3 μrad available from an asymmetric monochro-collimator M is incident onto object S(W). In the sample position $S(W)$ having plano-convex shape is shown. The beam from the object is described with R(W). The modulated beam R(W) containing information on refraction involved in $S(W)$ is angularly analyzed by a Bragg case analyzer B that has transmission reflection capability BI_o (W). R(W) is thus transformed into BD(W). Due to the Bragg analyzer that has the reflection (diffraction) power $B_r I_G(W)$ towards the diffraction direction and transmission (forward diffraction) power $B_r I_o(W)$ towards the straight forward direction each produces $B_r B(W)$ bright-field image and $B_r D(W)$ dark-field image, respectively. As a result at the position indicated with DFI image is stored in a 2D imaging device. The X-ray energy used was 35 keV, the diffraction index of M and L 4,4,0. Under these conditions BD (0) = 0 is available.
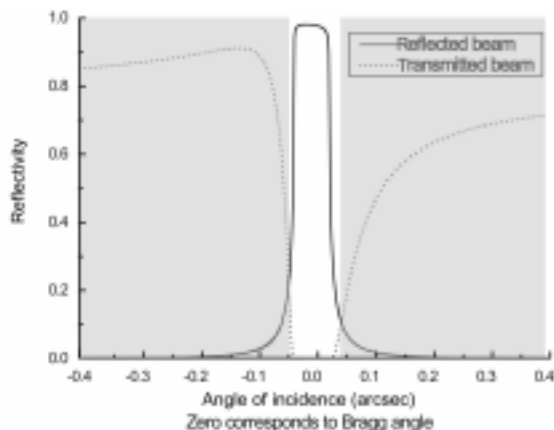
Fig.7 Two reflection curves showing how one can obtain dark-field images in the Bragg case analyzer. The central part indicated with the line "reflected beam" may occur by the Bragg analyzer. In other words the straight forward beam from object without interacting with the object will be diffracted towards the direction of diffraction. The dotted line labeled with the "transmitted beam" in the inset corresponds to the probability of transmission versus the refracted angle from the object.

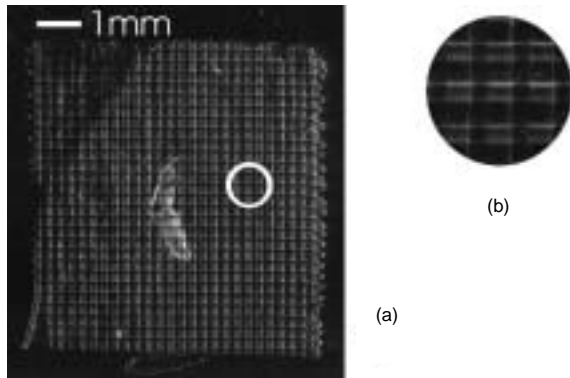**Fig.8**   The picture taken by the method shown in Fig.6 and Fig.7. A sample of copper mesh with #100 was used. One can see effect due to X-ray energy flow. This is shown in the inset with magnification.

The DFI using a Laue analyzer is shown in Fig.9. This scheme reminds a way of viewing internal defects by X-ray topography called KIT (kinematical image technique) by Chikawa et al.[12] This KIT can visualize weak signal from small internal defects in the diffracted beam while suppressing the illuminating light by letting that flow along the edge of the Borrmann fan. This can be almost the first X-ray dark-field image.
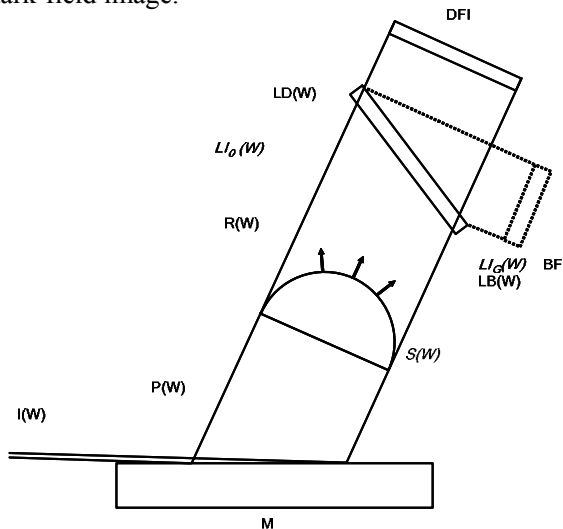

Fig.9   The DFI (dark-field imaging) X-ray optics using the Laue case angular analyzer. A monochro-collimator M makes the angular spread of the incident beam I(W) sharper as indicated with P(W). In the sample position is shown an object S(*W*) having plano-convex shape. The beam from the object is described with R(W). Due to the Laue analyzer that has the reflection (diffraction) power $LI_G(W)$ towards the diffraction direction and transmission (forward diffraction) power $LI_o(W)$ towards the straight forward direction. Each produces LB(W) bright-field image and LD(W) dark-field image, respectively. At the position indicated with DFI image is stored by a 2D imaging device.

BFI, where images together with the illuminating light are available, has been developed by many.[4-7] If one wants to extract DFI from BFI the mathematical

procedure has been proposed by Chapman et al.[7] A trial of 2D reconstruction on a basis of refraction contrast has been also initiated by Dilmanian.[13]

The so-called phase contrast imaging[14-17] involves all possible imaging contrasts such as absorption, phase change, refraction and even illumination light. This is summarized in Table 1. BFI involves three types of contrast mechanism. DFI[8] is only based on refraction contrast. Detailed discussion on the contrast mechanism of a variety of imaging will be done in another paper in a near future.

Table 1   A summary of various types of imaging mechanism

Imaging	Absorption	Phase change	Refraction	Illumination light
Phase-contrast	○	○	○	○
Bright-field	○	×	○	○
Dark-field	×	×	○	×

2   Theory and experiment

In Fig.1 the monochro-collimator is found at left. It is in the asymmetric diffraction geometry. The asymmetric diffraction is characterized by '*b*' the asymmetric factor in equations $\omega_0 = \sqrt{b}\ \omega_t$ and $b = \sin(\theta_B - \alpha) / \sin(\theta_B + \alpha)$, where ω_0 is the angular width of the beam coming out from the asymmetric crystal and ω_t the theoretical intrinsic diffraction width, θ_B denotes the Bragg angle and α the angle between the diffracting planes and surface. Thus if *b* is taken smaller than 1, which means the incoming angle ($\theta_B - \alpha$) of the beam is smaller than the outgoing angle ($\theta_B + \alpha$) of the beam, ω_0 is smaller than ω_t by a factor of $\sqrt{b}$. The incident X-ray beam can be expressed as *I*(*W*), while *W* is expressed as

$$W = 2\Lambda \sin\theta_B\ (\theta - \theta_B - \Delta\theta_0)\ /\lambda \qquad (1)$$

where $\Lambda = \lambda\cos\theta_B\ /\ |P||\chi_G|$ is defined as the extinction distance, λ the X-ray wavelength, *P* the polarization factor, 1 or $\cos 2\theta_B$, $\chi_G = -r_e\lambda^2 F_G\ /\pi V_C$ the susceptibility, r_e is the classical radius of electron, F_G the crystal structure form factor, V_C the volume of unit cell, θ the angle that deviates from the Bragg angle θ_B and $\Delta\theta_0$ the correction of the Bragg angle due to refraction expressed as $\Delta\theta_0 = 2\ (1-n)\ /\sin 2\theta_B$. ω_0 for

4,4,0 at E = 35 keV is 0.3 µrad at b = 0.2. The size of the outgoing X-ray beam is expanded by a factor of 1/b that means 5 in this case.

For refraction contrast let's take the propagation of X-rays along z-axis and refraction along x-axis so that the refraction $\Delta\alpha (x,y: k)$ as shown in Eq.(2)

$$\Delta\alpha(x,y) \propto -\frac{\lambda^2 r_e}{2\pi} \frac{\partial}{\partial x} \int_{z_0}^{z_1} N(x,y,z)\,\mathrm{d}z \qquad (2)$$

takes place in the (x,z) plane, where z_0 and z_1 are the z axis coordinates of the object where X-rays enter and exit. $N(x,y,z)$ is the density of electrons (number of electrons per unit volume) of the object. Since the value of $\Delta\alpha(x,y: k)$ should be on the order of 1 µrad or larger this value is much larger than the angular width of the incident beam $P(W)$ in Fig.8. Both the diffracting planes (4,4,0) in M and L are in a (+,-) parallel arrangement.

The analyzer crystal L in Fig.9 working as an angular analyzer has a transmission function $LI_0\ (W)$ along the transmission direction. The DFI will be suitable for visualizing objects containing light elements such as biomedical materials and reinforced composite material. A well established absorption contrast will hardly give contrast to these items.

Fig.10 shows how the DFI contrast using the Laue geometry analyzer comes. In Fig.10 the horizontal axis indicates deflection angle in W scale while X-ray power is plotted on the vertical axis. This shows the mechanism of imaging contrast in the Laue case filter. The refracted beam from object will be filtered by the Laue filter. The straight forward beam of no interaction with the matter will be diffracted towards the direction of diffraction, while the refracted beam will be forward diffracted. The beam P(W) described with (a) in Fig.10 is incident onto a sample $S(W)$ shown with (b) in a plano-convex lens that is indicated with angular form (c) S(W). This sample shape was adopted as a simple model. According to Eq.(1) a small angular change of X-rays takes place from the propagation direction along the z direction of the incident X-rays P(W). If $S(W)$ has a distribution of refractive index, indicated with (c), due to local electron density mapping $N(x,y,z)$ this can be separated clearly without blurring due to the wavelength spread. One

can recognize that this profile P(W) has the very narrow reflection curve with ~ 0.3 µrad and very high reflectivity ~ over 90 %. We need fix the thickness of the filter of silicon at 1.075 mm or its double 2.15 mm if holding the diffraction index at 4,4,0 and X-ray energy at 35 keV. By this transmission procedure R(W) containing information on internal structure of the object S(W) will be transformed into LD(W) that carry visual information on S(W) while suppressing the illumination light P(W). Since the angular full width of P(W) as shown is ±0.15 µrad that corresponds to ±1 in W scale and the whole angular range covers up to approximately ±2 µrad, the function S(W) sketched in (c) shows how the initial X-rays P(W) will be modified into R(W) by the object $S(W)$ as shown in (d). This R(W) will be analyzed by L in Fig.2. Angular analysis undertakes inside the crystal slab with reflectivity of $LI_0(W)$ in (e). They have zero transmission in the angular range $|W|$ 1. Finally the angular information LD(W) on the $S(W)$ is available as shown in (f).
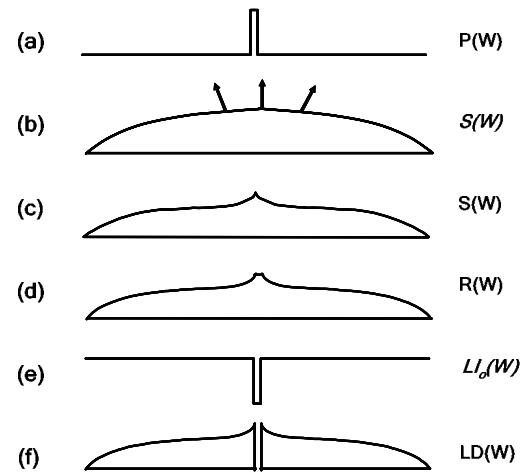

Fig.10 Diagram showing how DFI can be formed. The horizontal axis W represents the angular scale of the beam, while the vertical axis X-ray reflectivity. (a) shows a profile of an incident beam P(W); (b) a model of object $S(W)$; (c) angular distribution of the object $S(W)$; (d) the angular distribution of the outgoing beam R(W) from $S(W)$ when (a) was incident on; (e) represents a transmission function $LI_0(W)$ of a filter crystal L along the forward diffraction direction; (f) the result of passing through the filter $LI_0(W)$ of the beam R(W) from the object. This shows clearly the image LD(W) called DFI formed by the Laue type filter $LI_0(W)$.

The reflectivity function $LI_0(W)$ which is indicated with dotted lines in Fig.11 can be expressed as follows[18] if X-ray absorption is considered:

$$LI_0(W) = 1/4 \left[(1+W/\sqrt{1+W^2})^2 \cdot \right.$$

$$\exp\{-t\pi / [\sqrt{1+W^2} \cdot \cos\theta_B (1-|P|\,\varepsilon/\sqrt{1+W^2})]\}$$

$$+(1-W/\sqrt{1+W^2})^2 \cdot$$

$$\left. \exp\{-t\pi / [\sqrt{1+W^2} \cdot \cos\theta_B (1+|P|\varepsilon/\sqrt{1+W^2})]\} \right]$$

$$\text{(3)}$$

where t is thickness of L, $\varepsilon = \chi_g"/\chi_0"$ where $\chi_g" = r_e\lambda^2 F_G"$ and $\chi_0" = r_e\lambda^2 F_0"$. $F_G"$ and $F_0"$ indicates the crystal form factor corresponding to anomalous atomic form factor $f_g"$ and $f_0"$, respectively. This can be a simple function in case of no absorption:

$$LI_0(W) = [\sin^2(\pi H \sqrt{1+W^2} / \Lambda)]/(1+W^2) \quad \text{(4)}$$

Actually this is a function of the angular scale W, the analyzer thickness H, and the extinction distance Λ. All these parameters have been explained in Eq.(1). Eq.(4) can be further simplified as

$$LI_0(0) = \sin^2(t\pi/\Lambda) = 0 \quad \text{(5)}$$

At every $t = p\Lambda$, where p is integer, we have chosen $t = 1.075$ mm for $E = 35$ keV ($\lambda = 0.0354$ nm) that gives $LI_0(0)$. Since $LD(0) = LI_0(0)$ after L along the forward diffraction direction, $R(0) = 0$ in (g) will be available. At $|W| > 1$ all refracted X-rays which pass through L will form DFI reflecting the object $S(W)$. Since $LI_0(W)$ at $|W|>1$ has a significant value in average, all refracted X-rays may survive so that $LD(W)$ at $|W|>1$ will form DFI reflecting the object $S(W)$. This is mechanism of the DFI. Since this mechanism accepts any scattering that may occur at $|W|>1$, not only refraction but also other mechanism such as diffraction and/or small angle scattering should be able to make imaging as well.

Also in Fig.11 the curve BFI which is indicated with solid lines has a relation with $LI_G(W)=1- LI_0(W)$. Since the angular full width of P(W) as shown is ±0.15 µrad and the whole angular range in each covers up to approximately ±2 µrad, the function S(W) shows how the initial X-rays P(W) will be modified into R(W) by the object $S(W)$. This R(W) will be analyzed by L in Fig.1. Angular analysis undertakes inside the crystal slab with reflectivity of LI_0(W). They have zero transmission in the angular range at the central position $|W| < 1$ which corresponds to no deflection of the incident beam.
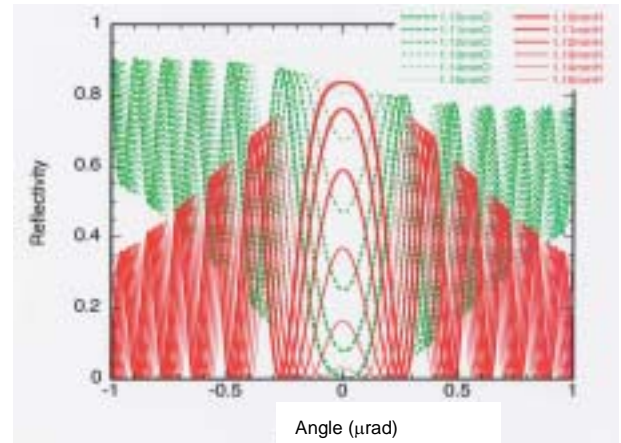

Fig.11 Thickness dependence of $LI_0(W)$ (shown with dotted line) and $LI_G(W)$ (shown with solid line). Change of thickness only by 50 µm may lead to complete change of the central part of the profile. One learns that the thickness control is quite essential in order to keep the DFI condition.

Exposure time for each was approximately 60 sec at 100 mA at 8 GeV SPring-8 or at 500 mA at the Photon Factory 2.5 GeV. The 35 keV X-ray energy was adopted because this has been utilized for intravenous coronary angiography (IVCAG) programme in Japan[19-21] where we have not introduced energy subtraction but fixed just above the absorption edge of iodine 33.17 keV for the contrast agent. Application of synchrotron radiation to IVCAG was initiated by Rubenstein et al[22] at Stanford Synchrotron Radiation Laboratory and later other synchrotron labs adopted this programme as a first clinical application.[19-21,23-27]

There are another variety of trials that are likely to reach clinical level in the medical application with synchrotron radiation. One is attempt at mammography,[28-30] and the other is osteoarthritis.[31-36] We have almost fixed the X-ray energy at 35 keV because transmission of even such X-ray energy is not high enough, say at the order of 0.1 % for the thickness of approximately 20 cm. On the other hand higher X-ray energy when applying the system under development to clinical issue will not produce enough photons even at the world largest storage ring. One may need compromise. Also we could save manpower to develop the X-ray optics if the X-ray energy will be almost the same as for the IVCAG.

Changing thickness of the analyzer crystal by only 50 microns can easily change the function of DFI to BFI because every 10 µm of change of the analyzer thickness brings 20% of reflection change as is obvious in Fig.11. Thus control of thickness of the Laue

filter crystal is required with the order of 1 μm. However it is not easy to realize this in case of home made filter so that in order to keep either functioning one has to fall in control difficulty of the analyzer thickness within say ~a few microns. If it will be possible to make both sides of the filter parallel it will not be easy to control the thickness. We can propose two ideas. One is to tune the X-ray energy as shown in Fig.12, because, as described in Eq.(3)~(5), each of which is a function of analyzer thickness H and wavelength λ or X-ray energy E. The other is to change the effective thickness as shown in Fig.13, which means the beam path of the analyzer. See more details in Ref.[36]. Instead of precision control of the analyzer thickness one can consider change the X-ray energy.

In this paper an attempt at visualizing articular cartilage of human excised joints is described. In order to bring organs with certain size into clinical test using the DFI and the BFI one needs a certain view size say ~ 80 mm × 80 mm. The articular cartilage provides joint surfaces with the low friction, lubrication and wear characteristics required for repetitive gliding motion. Once articular cartilage is damaged, the joint function is impaired with clinical symptom of redness, swelling and pain. For example, osteoarthritis is a chronic joint disorder in which there is a progressive softening and disintegration of articular cartilage. At the end stage of osteoarthritis, articular cartilage totally disappeared. It is of great importance to assess how much articular cartilage of the joint is remaining, because clinical treatment is often indicated by how much cartilage is damaged. There have been a few imaging methods to evaluate the articular cartilage and its grade of disorder. Thus there has been a long term strong requirement on the technique to visualize the articular cartilage. X-ray technique in hospital that has convenience in use and its less invasiveness on daily clinical use. However, it is unable to visualize the articular cartilage. One can visualize the articular cartilage only when injecting the contrast media into the joint. This may lead to the risk of joint infection. Magnetic Resonance Imaging (MRI) can now be the only technique to represent the articular cartilage, but its spatial resolution is not particularly good enough to clinical use.
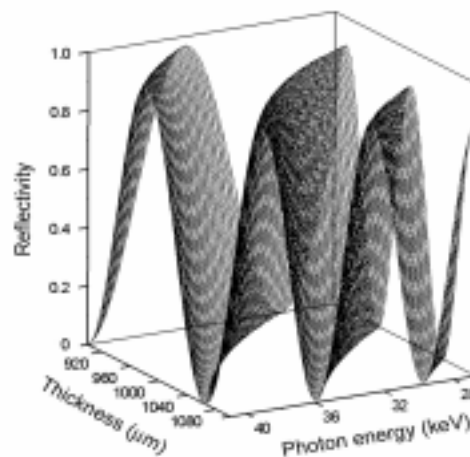

Fig.12 $LI_0(W)$ shown as a function of the analyzer thickness and the X-ray energy. In order to keep the same reflectivity one can tune the X-ray energy if the thickness has been fixed by fabrication.
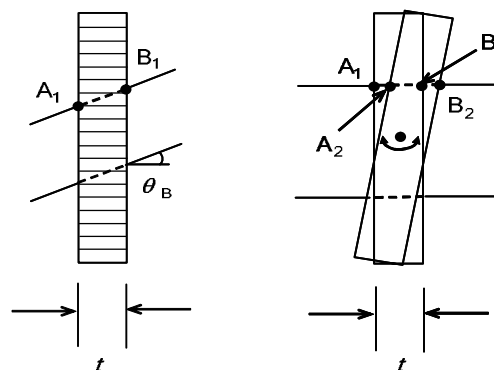

Fig.13 An alternative way to tune effective thickness H in $LI_0(W=0) = \sin^2(\ H / \ )$ for the fixed thickness and the fixed X-ray energy. The left shows the projection of the filter crystal. A_1 and B_1 corresponds to the point where the X-rays come in and out of the analyzer so that A_1B_1 means the beam path inside the analyzer. In order to change the beam path one can rotate this analyzer around the normal to its diffracting planes. This process is shown in the right. By rotating this analyzer by ω the effective beam path A_2B_2 is available as $A_1B_1 / \cos\omega$.

Fig.14 and Fig.15 show an object observed by this method. The object used was a 8 mm thick sliced distal end of a human femur that covers a medial (left in each figure) and lateral (right in each figure) femoral condyle. Its whole part was embedded in an acrylic box with formalin with thickness of 28 mm. All of the images were stored on imaging plate (FUJIFilm, BAS-SR 2025) and read out by an imaging plate reader (FUJIFILM, BAS-2500) with 50 μm pixel sizes. For dose estimation, entrance surface dose of the air regardless of backscatter factor: D_{es} was measured by a 3 mL ion chamber; 10× 5-6 with a model 9015 monitor (Radcal Corporation). The experiment was

performed at beamline BL14C1 at the Photon Factory (Tsukuba Japan) where the synchrotron X-ray with vertical polarization is only available in the world from the 5 T superconducting wiggler at the 2.5GeV Photon Factory storage ring. Our machine time was allocated in a single bunch mode where the initial stored current was 70 mA. Its inner structure will not be visible by the ordinary absorption contrast as shown in Fig.16. This picture clearly indicates horizontal holes so that the system has the refraction resolution capability along the vertical direction which corresponds to the vertical incidence plane. Their theoretical curves are nothing special but quite ordinary (see for example Ref.[18]) so that their formula is not described in this note.
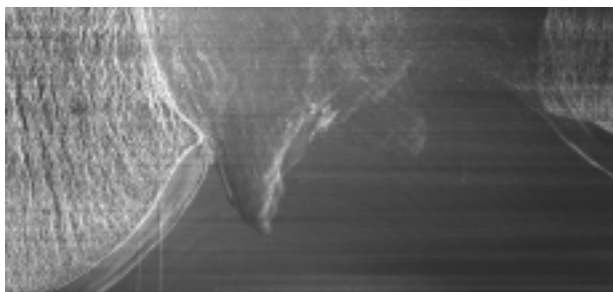

Fig.14   The DFI view of the object 8 mm thick sliced distal end of a human femur that covers a medial (left in each figure) and lateral (right in each figure) femoral condyle. Not only the articular cartilage but also ligament in intercondylar fossa are clearly visible. These have not been visible by any means so far.
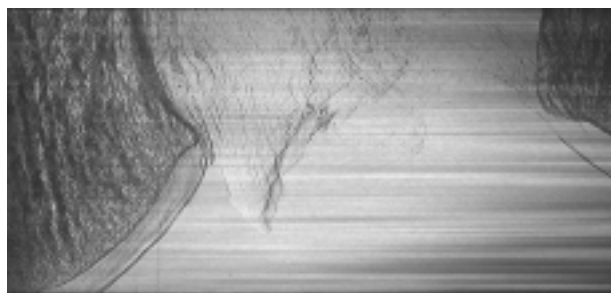

Fig.15   The BFI view of the same object in Fig.14. Almost similar view is available to the DFI.
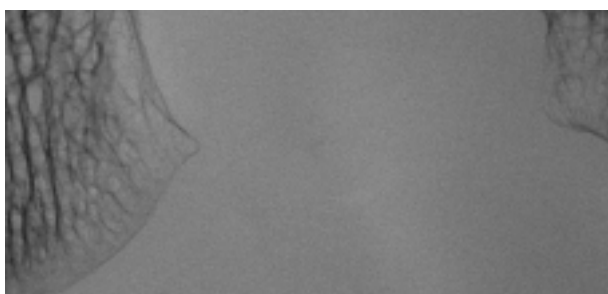

Fig.16   A picture ordinarily taken at hospital. This is due to absorption. No such contrast as seen in Fig.14 and 15 is visible.

We have been trying to expand the view size for a larger clinical object[36] such as joints of shoulder, knee and others by adopting larger silicon crystals. Fig.17 shows its system. That was taken from downstream of the system in the experimental hutch at BL20B2 at SPring-8. From the upstream to downstream one can see the asymmetric cut mono-chro-collimator (its surface shines) on a holder, the sample in a vinyl bag that is hung by crane, the Laue type filter crystal (its both surfaces shine) fitted in a aluminum frame, a Polaroid film and the 2D detector flat panel (Hamamatsu Photonics). The image can be read out by an electrode electronically. One can also see the precision goniometers that need to drive two crystals with a precision of the order of 0.05 arc seconds. In order to stabilize the crystal system the temperature of both crystals were controlled indirectly by the temperature regulated water. Its precision was at the order of 1/100 degrees. One can see the water pipes comprising vinyl and black colour polyurethane. The primary monochromated beam comes from the left in Fig.17. These are in a line with the offset angle of 21.2° from the horizontal plane because of the $2\theta_B$ angle. The sample was in water as seen in this figure. This simulates the sample condition on clinics. Exposure time was approximately 60 sec at 100 mA.

In the X-ray picture the signal corresponds to white and the background black. In Fig.18 one can clearly see the articular cartilage of an excised human femoral head. This sample was removed from the patient with a vascular necrosis at femoral head. In Fig.19 taken with the ordinary contrast the equivalent and necessary information on the articular cartilage was not attained.

Fig.17   The system for taking an excised human femur joint.

In Fig.20 a phantom of breast cancer is clearly shown. By the ordinary X-ray technique such fine details can not be seen. We have adopted this subject as a most intensive goal of application of our DFI. As a next step we would like to proceed to excised human breast tissue with cancer.

In order to estimate the spatial resolution of DFI a 20 nm thick carbon film called microgrid for elec-
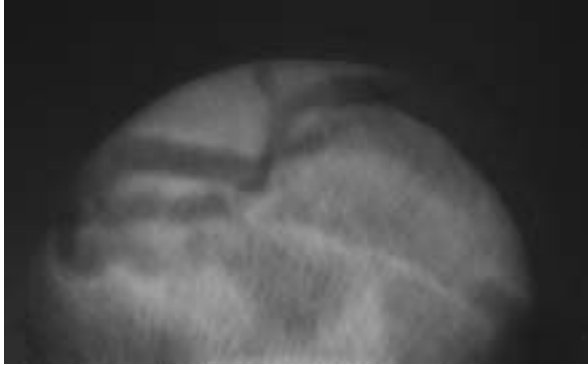

Fig.18   A picture taken by the DFI at BL20B2 at SPring-8. One can clearly see the articular cartilage of an excised human femur joint.
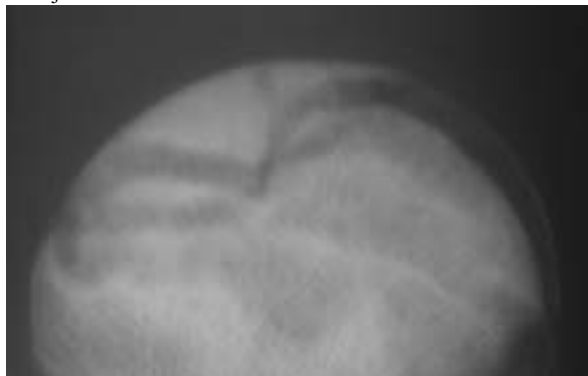

Fig.19   The same specimen taken by a hospital X-ray machine. The corresponding articular cartilage is not visible.
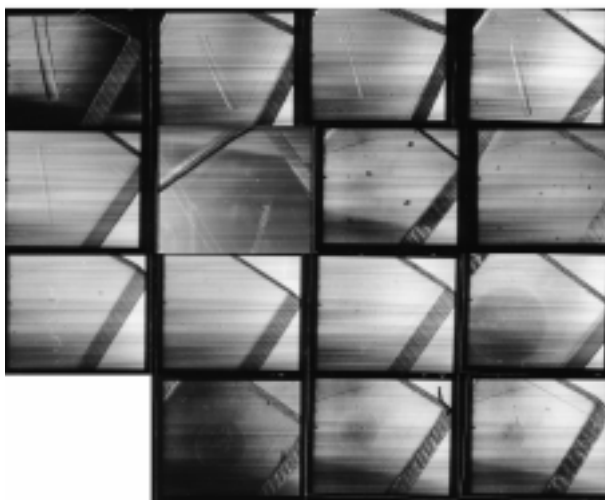

Fig.20   A 16 piece breast phantom labeled with ACR #156 made in Wisconsin. Details of each piece are visible. Each has the dimension of 20 mm × 20 mm. The pictures were taken at BL14B at Photon Factory. 15 pictures (one in lack) were collected to make a single image.

tron microscopy having a variety of randomly distributed holes ranging approximately 5~10 μm in size was used. Its result is shown in Fig.21. One can significantly see their holes. One can say that the system has the spatial resolution of approximately 5 μm. Since the 1.075 mm thick filter can provide the above spatial resolution one could anticipate the improvement up to nm region by thinning the filter down at best. Inside the Laue analyzer the diffracting planes run perpendicular to the surface where the X-ray comes in at one side and out at the other side. The X-ray energy is believed to flow along the diffracting planes. This may lead to the spatial resolution of the system. The X-ray energy used in this experiment was 35 keV. Thus the $2\Theta_B$ is 21.2°. The FWHM of the angular divergence 2α of the beam P(W) in Fig.9 incident onto a sample is approximately 0.6 μrad. According to the X-ray dynamical theory the X-rays corresponding to either the left wing or the right one of the FWHM is likely to flow parallel to the Borrmann fan so that the angular amplitude ranges approximately $21.2°/0.6$ μrad $= 6.2 \times 10^5$. $2\beta \times d$ should correspond to the current spatial resolution of 5 μm. However the value β is too small (~ the order of nano radian) so that not a simple expansion of the Borrmann fan but almost all X-ray energy may flow along the lattice planes. Precision discussion in order to interpret this discrepancy can be made by the computer calculation.
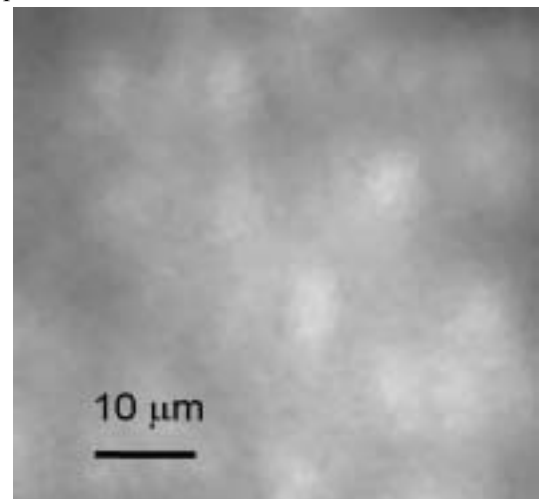

Fig.21   A view of a 50nm thick micro-grid made of carbon that has randomly distributed holes. This grid is usually for a sample substrate of electron microscopy. The holes have diameter of approximately 10 μm in average. That is for letting electron beams pass through sample which is over holes. The spatial resolution of the current system based on this photo can be ~5 μm. The X-ray energy used was 35 keV.

As another application of the above mentioned DFI we hope to be able to see auditory ossicles in a clinical mode. The structure of the ear bones was first performed by anatomical sketch. A non-destructive observation method described here in this note gives advantage in case of diagnosis over the destructive way. Nevertheless we have only initiated a test observation for obtaining 3D image due to absorption contrast. In a future we look forward to applying X-ray imaging technique to diagnosis. See, for instance, Fig.22 and Fig.23 for a reconstructed 3D malleus, one of human middle ear bones and a reconstructed 2D slice image of an inner ear of a mouse, respectively. The former shows a frontal, sagittal, axial cross section and 3D configuration in Fig.22. In Fig.23 a cochlea is clearly shown although the fine 1 micron region of sound sensing hair cell is not revealed. As a next step we would like to see their internal structure by the DFI contrast. We do hope the DFI will bring out some new structure of the above middle and inner ear. Interruption of the vascular perfusion of the ossicles from infection, cholesteatoma, trauma, and foreign-body reaction produces necrosis, fracture, and ossicular discontinuity with resultant conductive hearing loss. Additionally, with the advent of bio-integrating prostheses used in reconstruction of the human ossicular chain the information obtained here can become paramount to appropriate prosthesis design and construction. As a next step we would like to visualize
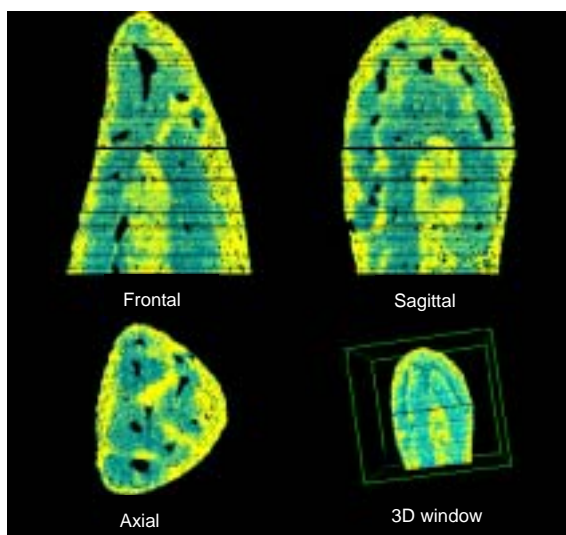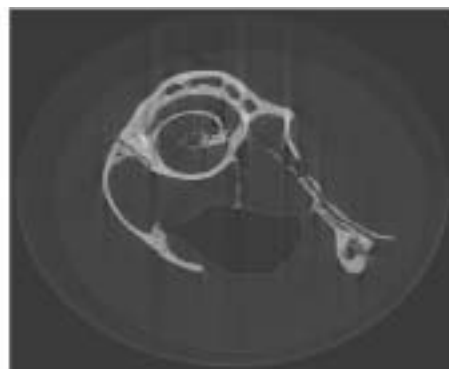

Fig.23 2D reconstruction of a mouse inner ear bone which shows a sliced cochlea. This was taken with a conventional absorption contrast at SPring-8 BL29XU.The spatial resolution was a few microns. The view size is approximately 5 mm × 5 mm. The X-ray energy used was 18 keV.

their internal structure in a 3D mode using DFI method.

3   Conclusions

Our new technique of X-ray DFI (dark-field imaging) can clearly depict the articular cartilage. This clearly indicates that the DFI can provide us with clinically accurate assessment for the condition of articular cartilage and the grade of its disorder. Another articular cartilage at shoulder very close to a clinical mode was successfully performed quite recently.[37] In applying the above-mentioned technique to joint clinical diagnosis in the nearest future photographing should be along the favourable direction so that the X-rays may suffer less absorption by the acetabulum and its surrounding soft tissue. The X-ray energy at 35 keV seems high enough. As a next step we would like to go closer to a clinical mode in order to collect clinically suitable objects. Radiation dose of 6.7 mGy is needed to take an ordinary absorption contrast image of knee joint, while 13.1 mGy by in-line imaging and 20.4 mGy by DFI. Still this radiation level seems acceptable.

Fig.22 3D reconstruction of human malleus taken with a conventional absorption contrast at SPring-8 BL47XU. It is shown by three projections. The view size is approximately 1 mm × 1mm × 1 mm because of the beam size. The X-ray energy used was 15 keV.

References

1   Ando M, Hosoya S. Proc of the 6th International Conference on X-Ray Optics and Microanalysis 63-68, Shinoda G, Kohra K, Ichinokawa T ed, Tokyo: University of Tokyo Press, 1972

2   Momose A, Takeda T, Itai Y *et al*. Nat Med, 1995, **2**: 473-475

3   Bonse U, Hart M. Appl Phys Lett, 1965, **7**: 99-101

4   Podurets KM, Somenkov VA, Shil'shtein SSh. Physica **B**, 1989, **156 & 157**: 691-693

5   Ingal VN, Beliaevskaya EA. J Phys **D**: Appl Phys, 1995, **28**: 2314-2317

6   Davis TJ, Gao D, Gureyev TE *et al*. Nature, 1995, **373**: 595-598

7   Chapman D, Thomlinson W, Johnston RE *et al*. Phys Med Biol, 1997, **42**: 2015-2025

8   Ando M, Sugiyama H, Maksimenko A *et al*. Jpn J Appl Phys, 2002, **41**: L1016-L1018

9   Kohra K. J Phys Soc Jpn, 1962, **17**: 589-590

10 Chikawa J, Asada Y, Fujimoto I. J Appl Phys, 1970, **41**: 1922-1925

11 Dilmanian FA, Zhong Z, Rent B *et al*. Phys Med Biol, 2000, **45**: 933-946

12 Snigirev A, Snigireva I, Kohn V *et al*. Rev Sci Instrum 1995, **66-12**: 5486-5492

13 Cloetens P, Barrett R, Baruchel J *et al*. J Phys **D**: Appl Phys, 1996, **29**: 133-146

14 Margaritondo G, Tromba G. J Appl Phys, 1999, **85(7)**: 3406-3408

15 Yagi N, Suzuki Y, Umetani K *et al*. Med Phys, 1999, **26**: 2190-2193

16 Ando M, Sugiyama H, Xiaowei Z *et al*. Jpn J Appl Phys, 2001, **40(3B)**: L298-L301

17 Maksimenko A, Sugiyama H, Pattanasiriwisawa W *et al*. Jpn J Appl Phys 2003, **42(9AB)**: L1096-L1099

18 Ishikawa T, Kohra K. Perfect crystal methods, Handbook on synchrotron radiation, Brown GS, Moncton DE, ed. Amsterdam: North-Holland, 1991, 63-104

19 Rubenstein E, Hofstadter R, Zeman HD *et al*. Proc Natl Acad Sci USA, 1987, **83**: 9724

20 Thomlinson W. Proceedings of the International School of Physics "Enrico Fermi," Course CXXVIII, Biomedical applications of synchrotron radiation, Burattini E, Balerna A, eds. IOS Press, 1996, 127-153

21 Dix W-R, Graeff W, Heuer J *et al*. Rev Sci Instrum, 1989, **60**: 2260

22 Dementiev EN, Dolbnya IP, Zagorodnikov EI *et al*. Rev Sci Instrum, 1989, **60**: 2264

23 Elleaume H, Fiedler S, Estève F *et al*. Phys Med Biol, 2000, **45**: L39-L43

24 Dix W-R, Kupper W, Dill T *et al*. J Synch Rad, 2003, **10**: 219-227

25 Akisada M, Ando M, Hyodo K *et al*. Nucl Instr Meth, 1986, **A264-1**: 713-718

26 Hyodo K, Nishimura K, Ando M. Handbook on synchrotron radiation Vol 4, Ebashi S, Koch M, Rubenstein E, ed. Amsterdam: Elsevier Science Publishers, 1991, 55

27 Ohtsuka S, Sugishita Y, Takeda T *et al*. Jpn Circ J, 1997, **61-5**: 432

28 Burattini E, Cossu E, Di Maggio C *et al*. Radiology, 1995, **159**: 239-244

29 Johnston RE, Washburn D, Posano E *et al*. Radiology, 1996, **200**: 659-663

30 Kim HJ, Hong JO, Lee KH *et al*. IEEE Trans on Nucl Sci, 2001, **48(3)**: 837-842

31 Shimao D, Mori, K, Sugiyama H *et al*. Jpn J Appl Phys, 2003, **42**: 5874-5875

32 Li J, Zhong Z, Litdke R *et al*. Radiography of soft tissue of the foot and ankle with diffraction enhanced imaging, J Am Podiatric Med Assoc, in press

33 Gureyev TE, Stevenson AW, Paganin D *et al*. J of Digital Imaging, 2000, **13**(2): 121-126

34 Shimao D, Mori K, Hyodo K *et al*. Application of X-ray refraction-contrast to medical joint imaging, Proceedings of the 8th International Conference on Synchrotron Radiation Instrumentation at San Francisco, 2003, in press

35 Shimao D *et al*. a draft in preparation

36 Sugiyama H, Kunisada T, Shimao D *et al*. Attempt at field size expansion in X-ray dark-field imaging with 35 keV for clinical application – Visualization of human excised articular cartilage of femoral head, submitted to JSR

37 Kunisada T *et al*. a draft in preparation

38 Wada H, Koike T, Kobayashi T *et al*. Ear and Hearing, 1998, **19**(3): 240-249

Curriculum Vitae

Miss Wanwisa Pattanasiriwisawa

Date of birth :   June 1, 1977

Nationality :   Thai

Address :   99/70 Pruksachart, 15 Ramkhamhaeng 118Rd., Sapansoong

                       Bangkok 10240, Thailand

Education

Academic year

1995-1998   Bachelor of Science (Physics)

                       Kasetsart University, Bangkok, Thailand.

1999-2004   Ph.D. in Physics.

                       Suranaree University of Technology.

                       Nakhon Ratchasima, Thailand.